UAB
Universitat Autònoma de Barcelona

Understanding plant immunity through the identification of immunogenic cell death indicators and the characterization of plant metacaspases in Arabidopsis thaliana

Jose Manuel Salguero Linares

Understanding plant immunity through the identification of immunogenic cell death indicators and the characterization of plant metacaspases in *Arabidopsis thaliana*

Jose Manuel Salguero Linares

PhD thesis

Understanding plant immunity through the identification of immunogenic cell death indicators and the characterization of plant metacaspases in *Arabidopsis thaliana*

Thesis submitted for the fulfilment of the requirements for the doctoral degree (PhD) in plant biology and biotechnology

Jose Manuel Salguero Linares

Supervisor: Dr. Núria Sánchez Coll

ACKNOWLEDGMENTS

To my supervisor Núria Sánchez Coll: I would like to explicitly thank her for exploiting my full potential as scientist during my PhD. Her great mentoring throughout these five years has enabled me not only to be awarded a PhD but to learn the basics of critical thinking and productivity as a scientist. I will always be grateful for the opportunity she gave me to work in her lab, participate in different projects, write review articles, and disseminate my work at international conferences. The positive impact she has made on my scientific career has been extremely profound.

To my second supervisor Marc Valls Matheu I thank him for endless and fruitful discussions on my project and for co-guiding me throughout my PhD.

To past and present members of the bacterial plant disease and cell death lab. Thank you for the great times in the lab and outside of the lab. Thank you for the scientific discussions. Without your support, the research presented in this thesis would not have been possible. I will miss guys. **To Alex, Saul, Eugenia, Pau and Marc Planas**. Since my very first day at CRAG, you made me feel like I always had belonged to the lab. It means a lot to me to have people like you forever.

To Nerea Ruiz-Solaní and Laia Armengot. Thank you for all the ideas discussed at “cell death” meetings and for catapulting the research presented in all chapters of this PhD thesis with your expertise at the confocal microscope. Nerea, we have truly been team players during our time in the lab. I wish you all the best for the end of your PhD and your future. Laia, thank you for hours and hours of interesting discussions about autoimmunity, crosses, pathways and/or fractionation protocols. Your arrival was crucial to improve Chapter 2 and 3.

To Joel Ayet Gómez, Marta Salas Gómez, and Jenna Krumbach. It has been a pleasure to mentor you during your time in the lab. I would like to thank you guys for your contribution to the works presented in Chapter 2. I would like to give a special mention to Joel for his dedication and efforts during his time as an undergraduate student that enabled a lot of the experiments presented in Chapter 2 to be done. Also, special shout-out for putting together the cover of this thesis.

To the collaborators. Thank you for adding value to the research presented in this thesis with your ideas and suggestions. Special mention to Simon Stael and Marina Klemenčič for supervising and hosting me during my international stays at the VIB and University of Ljubljana. I would like to extend my gratitude to Alvaro Fernandez and Katarina Petra for hosting and assisting me during the international stays at VIB and the University of Ljubljana, respectively.

A mi pareja, novia, amiga y compañera de vida Carlota Martín Tamargo. Te agradezco cada día que hemos pasado juntos durante esta larga etapa de mi doctorado. Has estado involucrada en esto de principio a fin. Tu comprensión, paciencia, actitud positiva ante los problemas y tu afecto hacia a mí en el día a día han sido elementos clave de todos mis éxitos. Te estaré siempre eternamente agradecido.

A mi grupo de amigos de Almería, gracias por aguantarme día a día dando mi opinión sobre absolutamente todo. En especial a Alberto por responderme a todas las opiniones.

A mis padres y hermana, Soledad Linares Linares y Jose Manuel Salguero Illescas, y Soledad Salguero Linares. Gracias por vuestro ánimo y apoyo durante estos cinco años de doctorado.

SYNOPSIS

Losses to plant pathogens pose a major threat to food security, bringing about serious economic and societal burdens across the globe. The Food Agriculture Organization of the United Nations (FAO) predicts a global economic loss of around 220 billion dollars per year, with around 20-40% of crop production lost to plant diseases (FAO - News Article: Climate change fans spread of pests and threatens plants and crops). In the face of climate change, rapidly evolving pathogens can easily overcome resistance provided by traditional pesticides. Consequently, a thorough understanding of the plant immune system is of paramount importance to breed disease-resistant crops.

As a strategy to counteract pathogen invasion, infected plant cells “die in self-defence” eliciting a type of cell death known as the hypersensitive response (HR) (Mur et al., 2008). Tight regulation of HR is critical for confinement of the immune response exclusively to the pathogen ingress site. However, our understanding of how cell death zonation is achieved and how by-stander cells respond to infection remains fragmentary. In the **first chapter** of my PhD thesis, we explored how HR triggered by pathogenic bacteria is spatiotemporally regulated at the transcriptional level in the plant model *Arabidopsis thaliana*. Results from this data set allowed us to identify *bona fide* transcriptional indicators of HR. Moreover, we provide for the community a fluorescent reporter transgenic line that displays a strong spatiotemporally resolved signal specifically in cells destined to undergo HR (Salguero-Linares et al., 2022). Use of this reporter line for specific and-or high-throughput techniques involving single-cell “omics” will enable further dissection of the spatial aspect of plant immunity.

Over the last decade, accumulating evidence suggests that plant proteases play crucial roles during HR (Salguero-Linares & Coll, 2019). While animal caspases are major regulators and executioners of animal programmed-cell death, plants lack caspases and instead, their genomes encode for an ancient, structurally related group of proteases termed metacaspases (Tsiatsiani et al., 2011; Uren et al., 2000). In the **second chapter** of my PhD, we analyzed in detail the role of Arabidopsis metacaspase 1 (*At*MC1) in plant immunity. In this study, we report that the lack of *At*MC1 results in autoimmunity, exacerbated by introducing a point mutation in the catalytic cysteine of the protease. Through a combination of genetic, biochemical and cell biology experiments we show that catalytically inactive *At*MC1 may act as a sticky docking platform for immune-related components, including immune receptors, possibly preventing their timely turnover. Based on these data and previous findings, we infer that *At*MC1 might directly or indirectly control the homeostasis of immune receptors and therefore, interfering with the wild-type function of the protease has negative impacts on plant growth.

Finally, in **Chapter 3** we biochemically characterized *At*MC1 as part of a study of the group showing that the protein is dynamically recruited into stress granules during various forms of proteotoxic stress (Ruiz-Solaní N. et al., 2023 unpublished). Our laboratory and others have long been trying recombinant isolation of *At*MC1 *in vitro*. However, previous efforts to express and isolate this protease in heterologous systems proved unsuccessful due to the high insolubility of its full-length version. To circumvent this issue, we removed certain domains predicted to be intrinsically disordered and aggregation-prone and successfully expressed and isolated the protease (van Midden et al., 2021).

This major step forward allowed us to prove that *At*MC1 exhibits a strong and evolutionary conserved capacity to clear protein aggregates, including those formed by pathological protein forms that cause a diversity of life-threatening diseases in humans. The implementation of recombinant proteins with high aggregate-clearance activity may open new avenues for therapeutic intervention in diseases caused by misfolded proteins.

In the last five years, the plant science community has particularly witnessed a quantum leap in our understanding of the plant immune system thanks to mechanistic studies on plant immune receptors and signalling pathways regulating and leading to HR. Leveraging this knowledge to engineer disease resistance in staples and economically important crops will be a priority in the years to come. I hope that the works and conclusions drawn from this thesis can contribute to future endeavours to achieve such an ambitious goal.

REFERENCES SYNOPSIS

FAO - News Article: Climate change fans spread of pests and threatens plants and crops, n. F. s. https://www.fao.org/news/story/en/item/1402920/icode/

Mur, L. A. J., Kenton, P., Lloyd, A. J., Ougham, H., & Prats, E. (2008). The hypersensitive response; the centenary is upon us but how much do we know? *Journal of Experimental Botany*, *59*(3), 501-520. https://doi.org/10.1093/jxb/erm239

Salguero-Linares, J., & Coll, N. S. (2019). Plant proteases in the control of the hypersensitive response. *Journal of Experimental Botany*, *70*(7), 2087-2095. https://doi.org/10.1093/jxb/erz030

Salguero-Linares, J., Serrano, I., Ruiz-Solani, N., Salas-Gomez, M., Phukan, U. J., Gonzalez, V. M., . . . Coll, N. S. (2022). Robust transcriptional indicators of immune cell death revealed by spatiotemporal transcriptome analyses [Article]. *Molecular Plant*, *15*(6), 1059-1075. https://doi.org/10.1016/j.molp.2022.04.010

Tsiatsiani, L., Van Breusegem, F., Gallois, P., Zavialov, A., Lam, E., & Bozhkov, P. V. (2011). Metacaspases. *Cell Death and Differentiation*, *18*(8), 1279-1288. https://doi.org/10.1038/cdd.2011.66

Uren, A. G., O'Rourke, K., Aravind, L., Pisabarro, M. T., Seshagiri, S., Koonin, E. V., & Dixit, V. M. (2000). Identification of paracaspases and metacaspases: Two ancient families of caspase-like proteins, one of which plays a key role in MALT lymphoma [Article]. *Molecular Cell*, *6*(4), 961-967. https://doi.org/10.1016/s1097-2765(00)00094-0

van Midden, K. P., Peric, T., & Klemencic, M. (2021). Plant type I metacaspases are proteolytically active proteases despite their hydrophobic nature [Article]. *Febs Letters*, *595*(17), 2237-2247. https://doi.org/10.1002/1873-3468.14165

RESUMEN EN ESPAÑOL

Los patógenos vegetales representan una gran amenaza para la seguridad alimentaria, causando alrededor del 20-40% de pérdidas en la producción de cultivos. En un contexto de cambio climático, los patógenos que evolucionan rápidamente pueden superar fácilmente la resistencia proporcionada por los pesticidas tradicionales. En consecuencia, comprender exhaustivamente el sistema inmune de las plantas es de suma importancia para generar cultivos resistentes.

Como estrategia para contrarrestar la invasión de patógenos, las células vegetales infectadas desencadenan un tipo de muerte celular regulada conocida como la respuesta hipersensible (HR). La regulación de la HR es esencial para confinar la respuesta inmune exclusivamente al lugar de ingreso del patógeno. Sin embargo, nuestra comprensión de cómo se logra la zonificación de la muerte celular y cómo las células vecinas responden a la infección es fragmentaria. En el primer capítulo de mi tesis, exploro cómo la HR se regula espacio-temporalmente a nivel transcripcional en la planta modelo *Arabidopsis thaliana*. Estos resultados nos permitieron identificar indicadores transcripcionales genuinos de la HR. Además, proporcionamos a la comunidad una línea transgénica reportera fluorescente que muestra un fuerte señal espacio-temporal en células destinadas a sufrir HR. El uso de esta línea reportera para técnicas específicas que involucren estudios "ómicos" de células individuales permitirá una mayor disección del aspecto espacial de la inmunidad vegetal.

En la última década, evidencias crecientes sugieren que las proteasas desempeñan papeles cruciales durante la HR. En el segundo capítulo de mi tesis, intento desentrañar el papel de la metacaspasa 1 (*At*MC1) de Arabidopsis, un tipo de cisteína proteasa, en la inmunidad vegetal. Aunque originalmente se describió como un regulador positivo de la HR en plantas jóvenes, plantas adultas que carecen de *At*MC1 exhiben una activación constitutiva de la inmunidad en condiciones basales, actuando por consiguiente como un regulador negativo de la inmunidad. Mutaciones en el sito catalítico de la proteasa desencadenan una autoinmunidad grave. A través de una combinación de experimentos genéticos, bioquímicos y de biología celular, mostramos que la versión cataliticamente inactiva de *At*MC1 actúa como un sitio de acoplamiento pegajoso para componentes relacionados con la inmunidad, incluidos receptores inmunes, posiblemente evitando su oportuna degradación. En base a estos datos y a la literatura previa, inferimos que *At*MC1 podría controlar directa o indirectamente la homeostasis de los receptores inmunes. Por lo tanto, interferir con la función de la proteasa wild-type tiene impactos negativos en el crecimiento de la planta.

Finalmente, participé en una segunda línea de investigación en la que intentamos entender la función de *At*MC1 ante el estrés proteotóxico. *At*MC1 es dinámicamente reclutada a condensados citoplásmicos altamente conservados, conocidos como granulos de estrés, regulando la senescencia (Capítulo 3). Para caracterizar bioquímicamente esta función, eliminamos ciertos dominios previstos de ser altamente propensos a la agregación y logramos expresar e aislar la proteasa de forma recombinante. Esto nos permitió demostrar que *At*MC1 tiene una gran capacidad, evolutivamente

conservada, de limpiar agregados de proteínas, incluidos los formados por formas de proteínas patológicas que causan enfermedades mortales en los humanos. La implementación de proteínas recombinantes con alta actividad de limpieza de agregados puede abrir nuevas vías para la intervención terapéutica en enfermedades causadas por proteínas mal plegadas.

En los últimos cinco años, la comunidad científica de plantas ha presenciado un gran avance en nuestra comprensión del sistema inmune vegetal gracias a estudios mecanísticos en receptores inmunes y vías de señalización que regulan y conducen a la HR. Aprovechar este conocimiento para lograr resistencia a enfermedades en cultivos básicos y económicamente importantes será una prioridad en los próximos años. Espero que los trabajos presentados en esta tesis puedan contribuir a futuros esfuerzos para lograr esos ambiciosos objetivos.

RESUM EN CATALÀ

Els patògens vegetals representen una gran amenaça per la seguretat alimentària, causant al voltant del 20-40% de pèrdues en la producció de cultius. En el context actual de canvi climàtic, els patògens, que evolucionen ràpidament, poden superar fàcilment la resistència proporcionada pels pesticides tradicionals. Per tant, entendre exhaustivament el sistema immunitari de les plantes és de gran importància per generar cultius resistents.

Com a estratègia per combatre la invasió de patògens, les cèl·lules vegetals infectades desencadenen un tipus de mort cel·lular regulada coneguda com a resposta hipersensible (HR). La regulació de la HR és essencial per confinar la resposta immunitària exclusivament al lloc d'entrada del patogen. Actualment, el nostre coneixement de com es produeix la zonació de la mort cel·lular i com responen les cèl·lules veïnes a l'infecció és escàs. En el primer capítol de la meva tesi, he explorat com la HR es regula de manera espaciotemporal a nivell transcripcional a la planta model *Arabidopsis thaliana*. Aquests resultats ens van permetre identificar marcadors transcripcionals específics de la HR. A més, proporcionem a la comunitat una línia transgènica reportera fluorescent que mostra una forta senyal espaciotemporal en cèl·lules destinades a patir HR. L'ús d'aquesta línia reportera per tècniques específiques que involucrin estudis "òmics" de cèl·lules individuals permetrà una major comprensió del caracter zonal de la immunitat vegetal.

En la darrera dècada, un nombre creixent d'estudis suggereixen que les proteases desenvolupen papers fonamentals durant la HR. En el segon capítol de la meva tesi, he estudiat el paper de la metacaspasa 1 (*At*MC1) d'Arabidopsis, un tipus de cisteïna proteasa, en la immunitat vegetal. Originalment, es va descriure a la *At*MC1 com un regulador positiu de la HR en plantes joves, per contra, les plantes adultes que no tenen *At*MC1 mostren una activació constitutiva de la immunitat en condicions basals, actuant així com un regulador negatiu de la immunitat. Les mutacions en el lloc catalític de la proteasa desencadenen una autoimmunitat greu. A través d'una combinació d'experiments genètics, bioquímics i de biologia cel·lular, mostrem que la versió catalíticament inactiva d'*At*MC1 actua com una plataforma d'acoblament per a components relacionats amb la immunitat, inclosos receptors i.possiblement, evita la seva correcta degradació. Basant-nos en aquestes dades i en la literatura anterior, inferim que l'*At*MC1 podria controlar directa o indirectament l'homeostasi dels receptors d'immunitat. Per tant, interferir amb la funció de la proteasa wild-type té un impacte negatiu en el creixement de la planta.

Finalment, he participat en una segona línia d'investigació on hem intentat entendre la funció d'*At*MC1 en condicions d'estrés proteotòxic. *At*MC1 és dinàmicament reclutada a condensats citoplasmàtics, coneguts com granuls d'estrés, regulant la senescència (Capítol 3). Per caracteritzar bioquímicament aquesta funció, vam eliminar alguns dominis predits com a altament propensos a l'agregació i vam aconseguir expressar i aïllar la proteasa de forma recombinant. Això ens va permetre demostrar que *At*MC1 té una gran capacitat, evolutivament conservada, de netejar agregats de proteïnes, inclosos els formats per formes de proteïnes patològiques que causen malalties mortals en humans. La

implementació de proteïnes recombinants amb alta activitat de neteja d'agregats pot obrir noves vies per a la intervenció terapèutica en malalties causades per proteïnes mal plegades.

En els darrers cinc anys, la comunitat científica de plantes ha presenciat un gran progrés en la nostra comprensió del sistema immunitari vegetal gràcies a estudis mecanístics dels receptors d'immunitat i vies de senyalització que regulen i condueixen la HR. Aprofitar aquest coneixement per aconseguir resistència a malalties en cultius bàsics i econòmicament importants serà una prioritat en els pròxims anys. Espero que els treballs presentats en aquesta tesi puguin contribuir a aconseguir aquests ambiciosos objectius.

INDEX

LIST OF KEY ABBREVIATIONS

Abbreviation	Description of term
ADR1	Activated disease resistance 1
*At*MC1/MC1	Metacaspase-1
CNL	Coiled-coil-NLR
DAMP	Danger-associated molecular pattern
DN-NLR	Dominant negative NLR
EDS1	Enhanced disease susceptibility 1
ETI	Effector-triggered immunity
hNLR	Helper NLR
HR	Hypersensitive response
JA	Jasmonic acid
LRR	Leucine-rich repeat
NAD+	Nicotinamide adenine dinucleotide
NLR	Nucleotide-binding leucine rich repeat
NOD	Nucleotide oligomerization domain
NRG1	N-required gene 1
PAD4	Phytoalexin deficient 4
PAMP	Pathogen-associated molecular pattern
PM	Plasma membrane
PRR	Pattern-recognition receptors
PTI	PAMP-triggered immunity
RNL	Resistance to powdery mildew 8 NLR
ROS	Reactive oxygen species
SA	Salicylic acid
SAG101	Senescence-associated gene 101
sNLR	Sensor NLR
TNL	Toll Interleukin 1 receptor-NLR
Wt	Wild type

1.INTRODUCTION

Cell death as a defence strategy against pathogens in plants and animals

(Publication 1)

Cell death as a defense strategy against pathogens in plants and animals

Running title: Immunogenic cell death plants vs animals

Jose Salguero-Linares[1] and Núria S. Coll[1,2,*]

[1] *Centre for Research in Agricultural Genomics (CRAG), CSIC-IRTA-UAB-UB, Campus UAB, Bellaterra, Barcelona, 08193, Spain*

[2] *Consejo Superior de Investigaciones Científicas (CSIC), Barcelona, Spain.*

[*] *To whom correspondence should be addressed:*

e-mail: nuria.sanchez-coll@cragenomica.es

Centre for Research in Agricultural Genomics (CRAG), CSIC-IRTA-UAB-UB

Campus UAB

Bellaterrra, 08193

Barcelona, Spain

Abstract

Eukaryotes are endowed with sophisticated innate immune systems to recognize non-self and halt pathogen proliferation. Activation of cell death at the site of attempted pathogen ingress is a common strategy used by plants and animals to restrict pathogen proliferation and trigger immune responses in the surrounding tissues. As such, immunogenic cell death shares several features in both plants and animals that will be discussed in this article, namely: i) it is triggered by activation of NLR immune receptors -often through oligomerization-, ii) it results in disruption of the plasma membrane (PM)/endomembrane integrity driving an imbalance in ion fluxes and iii) it results in the release of signalling molecules from dying cells.

Keywords: cell death, immunity, pathogen, NLR, PAMPs, DAMPs

1. Pathogens are perceived by immune receptors

Immune receptors of the nucleotide-binding leucine rich-repeat (NLR)-type constitute fundamental elements of the plant and animal innate immune systems. Animal NLRs respond to and mediate interaction with pathogen- or danger-associated molecular patterns (PAMPs or DAMPs) (*1*). In plants, the task of pathogen recognition is divided between intracellular NLRs and cell surface pattern-recognition receptors (PRRs). While plant NLRs recognize secreted pathogen effectors or their activity within the host cells, PRRs recognize PAMPs (*2*). Animal and plant NLRs share a similar multidomain architecture within the core nucleotide-binding and oligomerization domain (NOD) and the leucine-rich repeat (LRR) domains. However, there is substantial diversity at the C- and N-terminal accessory domains (*3*).

In plants, NLRs are categorized based on their domain composition at the N-terminus and their function during the immune response. NLRs carrying a coiled-coil (CNLs) or a Toll/Interleukin 1-receptor (TIR)-type domain (TNLs) can act as sensor NLRs by perceiving effectors, whereas a subset of CNLs function as helper NLRs by amplifying the downstream immune signal emanating from sensor NLRs or PRRs (*4-7*). In animal NLRs, N-terminal domains belong to the death-fold superfamily and mainly include Pyrin and CARD domains (*8*) **(Fig 1)**.

2. NLRs are activated by oligomerization

NLR activation in both plants and animals involves oligomerization through their N-terminal domains. In mammals, PAMP or DAMP-triggered NLR oligomerization leads to the assembly of the so called “inflammasomes”. These supramolecular structures are comprised of a varying number of NLR molecules depending on the nature of molecule trigger and provide a platform for recruitment and activation of caspases either directly or indirectly through the adaptor protein apoptosis-associated speck-like protein containing a caspase recruitment domain (ASC) (*11*). Caspase-dependent processing of pro-interleukins (ILs) and gasdermins (GSDMs) ultimately results in pyroptosis (**Fig 1**) (described in section 3).

Upon pathogen effector perception, plant NLRs also assemble into multimeric protein complexes termed “resistosomes” (*12-15*). In the case of CNLs, pentameric oligomerization leads to resistosome activation and a concomitant structural switch that results in a funnel-shaped structure that acts as a PM localized cation-selective channel permeable to Ca^{2+} (*12, 13, 16, 17*). Altered ion fluxes may act as an important determinant of pathogen-triggered cell death. This indicates that whilst certain plant immune receptors (sensor CNLs) can act as both sensors and executors of cell death, most animal NLRs require accessory molecules to drive cell death (*18*) (**Fig 1**).

Plant TIR-NLRs oligomerize into tetrameric protein complexes exhibiting NADase activity (nicotinamide adenine dinucleotide hydrolases) in their TIR domains (*19*). By-products or “info-chemicals” derived from TNL-mediated hydrolysis of the metabolic co-factor NAD^+ can directly

bind to heterodimers formed by plant lipase-like proteins with ENHANCED DISEASE SUSEPTIBILITY 1 (EDS1), promoting interactions with helper NLRs (*9, 10*). Certain helper NLRs can oligomerize into a pentameric resistosome capable of forming pores at the PM and driving ion flux imbalances in a similar way to sensor CNLs (*20-22*) (**Fig 1**).

While activated plant resistosomes/NLRs in plants are executors of cell death and localize at the PM membrane (CNLs and hNLRs) where they exert its pore-forming activities, activated animal NLRs (NLRP3 inflammasome) remain cytoplasmic acting as molecular scaffolds for recruitment and activation of accessory molecules that ultimate mediate plasma membrane disruption (**Fig 1**).

3. Immunogenic cell death exists in different flavors

In plants, the term **hypersensitive response (HR)** is used to define a local, pathogen-triggered type of cell death mediated by NLR activation. HR restricts pathogen growth and hence it is an important component of plant immunity (*23, 24*). Broadly, HR involves production of reactive oxygen species, nitric oxide and an increase of intracellular calcium, likely mediated by formation of PM pores by resistosomes (*12-15, 17*) (**Fig 2**). Still, how NLR activation and calcium influxes connects to downstream cell death programs as well as the role of proteolytic enzymes and organelles such as the chloroplast, mitochondria and the vacuole in this process remains largely unknown.

In animals, **pyroptosis**, **necroptosis** and **ferroptosis**, unlike apoptosis, are pro-inflammatory cell death programs that involve release of lytic content to the extracellular space and rupture of the plasma membrane prior to cellular demise (**Fig 2**). Besides their morphological resemblance, their triggers and biochemical executors of the cell death pathways differ (*25*).

Pyroptosis is activated upon detection of PAMPs or DAMPs by inflammasomes. These multi-protein complexes act as platforms for the activation of caspases that cleave GSDM unleashing its pore-forming domain to form an oligomeric pore at the PM (*11*). Pore formation through GSDMD results in cell size increase and subsequent burst, releasing intracellular proteins to the extracellular space.

Necroptosis involves ligand-mediated activation of RECEPTOR-INTERACTING PROTEIN KINASE 3 (RIPK3) that phosphorylates the pseudo-kinase MIXED LINEAGE KINASE DOMAIN-LIKE (MLKL) (*26*). Phosphorylation drives interaction of MLKL with the PM where it oligomerizes and forms a necroptotic pore (*26*). Pore formation also results in the release of intracellular content, including pro-inflammatory ILs, eventually leading to cellular demise. Interestingly, plants possess a conserved protein family resembling animal MLKLs that participate in immunity, indicating a potentially common mode of action with animal MLKLs (*27*).

Ferroptosis is a lytic, pro-inflammatory cell death that involves iron-dependent peroxidation of lipids associated with loss of PM integrity and ion influxes (*28*) (**Fig 2**). In plants, a ferroptosis-like process has been reported in response to NLR-mediated recognition of a fungal pathogen (*29*). Conservation between plant and animal ferroptosis may unfold as the mechanisms and players of the process become fully elucidated.

Apoptosis is an immunologically silent form of cell death in which gradual dismantling of the cell content leads to morphological features such as cytoplasmic shrinkage, chromatin condensation and DNA fragmentation (*30*). As opposed to other cell death programs, PM integrity is retained throughout the cell death process. Eventually, membrane blebbing results in cell fragmentation giving rise to "apoptotic bodies" that are engulfed and eliminated by phagocytes (**Fig 2**). Apoptosis initiation culminates in activation of effector caspases and concomitant cell death (*25*). Inhibition of caspases is an important target for pathogens to prevent apoptosis and maintain their replicative niche. It is thus not surprising that caspases have evolved as versatile molecular switches that can resort to pro-inflammatory cell death when apoptosis is blocked. In fact, an increasing number of immunogenic cell death modalities, deeply interlinked between them, is emerging as a central determinant of tissular/systemic responses (*31*).

4. Loss of plasma membrane/endomembrane integrity is a key step of immunogenic cell death

Loss of plasma membrane/endomembrane integrity is a common hallmark between plant and animal immunogenic cell death. In animals, pore formation at the PM constitutes an execution step of pro-inflammatory cell death and it involves GSDMD and MLKL in pyroptosis and necroptosis, respectively. During pyroptosis, the N-terminal portion of GSDMD, cleaved by caspase-1, directly inserts into the PM, where it self-associates and forms ring-shaped pores (~20 nm) (*32*). These large pores allow the release of pro-inflammatory molecules (cytokines, alarmins) and cause cell lysis. In the case of necroptosis, phosphorylated MLKL interacts with the PM, although the pore structure remains unresolved. Therefore, its oligomeric state in membranes and how it mediates permeabilization remain not fully elucidated. MLKL pores drive calcium and sodium influx and potassium efflux from the cell followed by water influx, resulting in a cell burst typical of necroptosis (*33, 34*). Ferroptosis also involves loss of integrity and partial rupture of the PM, which has been associated with iron-dependent peroxidation of phospholipids (*28*).

In plants it has been demonstrated that CNL pentameric resistosomes can drive membrane pore formation. Oligomerization of CNLs results in a structural switch of the N-terminus of each monomer that then projects out of the resistosome plane. The funnel-shaped structure can insert into membranes forming a small pore (~1 nm) that can act as a cation-selective channel permeable to Ca^{2+} (*16, 17, 20*). Pore formation and subsequent Ca^{2+} influx may activate a cell death programme as described for ferroptosis. In sum, current evidence suggests that transient

or permanent pore formation at the PM and permeabilization constitutes a common mechanism to execute cell death both in plant and animal cells.

5. Dying cells release signalling molecules important for immunity

Immunogenic cell death results in the release of signalling molecules, which activate immunity in surrounding/distal tissues and is therefore an important mechanism to counteract invading agents. In animals, immunogenically dying cells release DAMPs such as nuclear HIGH MOBILITY GROUP BOX 1 PROTEINS (HMGB1), ATP or circulating free DNA (cfDNA), among others. In addition, pyroptotic and necroptotic cells release pro-inflammatory cytokines. DAMP release appears tightly controlled and not a mere consequence of cell lysis as originally considered. In this sense, a growing body of evidence indicates that different types of lytic cell death will release a distinct signature of pro-inflammatory molecules (*29, 35*).

During plant immune responses a broad range of DAMPs and phytocytokines are released from infected/damaged cells and activate defence responses locally and in surrounding tissues (*36, 37*). DAMPs include nucleotides, sugars, and amino acids, whilst phytocytokines comprise endogenous signalling peptides actively generated upon maturation of the propeptide by a protease and subsequently perceived by cell surface receptors. Expression of phytocytokine precursors is in fact upregulated upon MAMP treatments or pathogen attack, constituting an early immune response (*38*). Among phytocytokines, those peptides that do not contain a secretory signal may reach the extracellular space after cell lysis or via not yet identified mechanisms. Research in recent years has evidenced that multitude of phytocytokines may in fact regulate immune responses, although very few have been characterized to date, such as some PLANT ELICITOR PEPTIDES (PEPs) or RAPID ALCALINIZATION FACTORS (RALFs) (*37*).

An exciting avenue for future research is whether specific DAMPs/phytocytokines emanate from dying cells and if so, how do they communicate with neighbouring cells and whether specific signatures exist depending on the particular plant-pathogen interaction. Also, it remains unclear what is the exact effect of phytocytokines in neighbouring cells: do they promote cell death or they are rather acting as pro-survival molecules acting for example in tissue repair? In coming years we may witness how increasing knowledge on plant HR is translated into disease resistance in the field, in the same way that basic knowledge on pro-inflammatory cell death in animals is leading to novel therapeutics.

Acknowledgements

We kindly thank Johana Misas-Villamil, Laia Armengot and Marc Valls for sharing thoughts and ideas and critically reviewing the manuscript.

References

1. J. D. G. Jones, J. L. Dangl, The plant immune system. *Nature* **444**, 323-329 (2006).

2. T. Griebel, T. Maekawa, J. E. Parker, NOD-like receptor cooperativity in effector-triggered immunity. *Trends in Immunology* **35**, 562-570 (2014).
3. J. D. G. Jones, R. E. Vance, J. L. Dangl, Intracellular innate immune surveillance devices in plants and animals. *Science* **354**, (2016).
4. J. Kourelis *et al.*, The helper NLR immune protein NRC3 mediates the hypersensitive cell death caused by the cell-surface receptor Cf-4. *PLoS Genet* **18**, e1010414 (2022).
5. R. N. Pruitt *et al.*, The EDS1-PAD4-ADR1 node mediates Arabidopsis pattern-triggered immunity. *Nature*, (2021).
6. V. Bonardi *et al.*, Expanded functions for a family of plant intracellular immune receptors beyond specific recognition of pathogen effectors. *Proceedings of the National Academy of Sciences of the United States of America* **108**, 16463-16468 (2011).
7. S. M. Collier, L. P. Hamel, P. Moffett, Cell Death Mediated by the N-Terminal Domains of a Unique and Highly Conserved Class of NB-LRR Protein. *Molecular Plant-Microbe Interactions* **24**, 918-931 (2011).
8. Z. Duxbury, C. H. Wu, P. T. Ding, A Comparative Overview of the Intracellular Guardians of Plants and Animals: NLRs in Innate Immunity and Beyond. *Annual Review of Plant Biology, Vol 72, 2021* **72**, 155-184 (2021).
9. S. Huang *et al.*, Identification and receptor mechanism of TIR-catalyzed small molecules in plant immunity. *Science* **377**, 487-+ (2022).
10. A. Jia *et al.*, TIR-catalyzed ADP-ribosylation reactions produce signaling molecules for plant immunity. *Science* **377**, 488-+ (2022).
11. K. Newton, V. M. Dixit, N. Kayagaki, Dying cells fan the flames of inflammation. *Science* **374**, 1076-+ (2021).
12. J. Z. Wang *et al.*, Ligand-triggered allosteric ADP release primes a plant NLR complex. *Science* **364**, 43-+ (2019).
13. J. Wang *et al.*, Reconstitution and structure of a plant NLR resistosome conferring immunity. *Science* **364**, 44-+ (2019).
14. R. Martin *et al.*, Structure of the activated ROQ1 resistosome directly recognizing the pathogen effector XopQ. *Science* **370**, 1185-+ (2020).
15. S. Ma *et al.*, Direct pathogen-induced assembly of an NLR immune receptor complex to form a holoenzyme. *Science* **370**, 1184-+ (2020).
16. G. Bi *et al.*, The ZAR1 resistosome is a calcium-permeable channel triggering plant immune signaling. *Cell* **184**, 3528-+ (2021).
17. A. Förderer *et al.*, A wheat resistosome defines common principles of immune receptor channels. *Nature*, (2022).
18. I. M. L. Saur, R. Panstruga, P. Schulze-Lefert, NOD-like receptor-mediated plant immunity: from structure to cell death. *Nature Reviews Immunology* **21**, 305-318 (2021).
19. L. Wan *et al.*, TIR domains of plant immune receptors are NAD(+)-cleaving enzymes that promote cell death. *Science* **365**, 799-+ (2019).
20. P. Jacob *et al.*, Plant "helper" immune receptors are Ca2+-permeable nonselective cation channels. *Science* **373**, 420-+ (2021).
21. M. P. Contreras *et al.*, Sensor NLR immune proteins activate oligomerization of their NRC helper. *bioRxiv*, 2022.2004.2025.489342 (2022).
22. H.-K. Ahn *et al.*, Effector-dependent activation and oligomerization of NRC helper NLRs by Rpi-amr3 and Rpi-amr1. *bioRxiv*, 2022.2004.2025.489359 (2022).
23. P. Balint-Kurti, The plant hypersensitive response: concepts, control and consequences. *Molecular Plant Pathology* **20**, 1163-1178 (2019).
24. E. Pitsili, U. J. Phukan, N. S. Coll, Cell Death in Plant Immunity. *Cold Spring Harbor Perspectives in Biology* **12**, (2020).
25. I. Jorgensen, M. Rayamajhi, E. A. Miao, Programmed cell death as a defence against infection. *Nature Reviews Immunology* **17**, 151-164 (2017).
26. L. Sun *et al.*, Mixed Lineage Kinase Domain-like Protein Mediates Necrosis Signaling Downstream of RIP3 Kinase. *Cell* **148**, 213-227 (2012).
27. L. K. Mahdi *et al.*, Discovery of a Family of Mixed Lineage Kinase Domain-like Proteins in Plants and Their Role in Innate Immune Signaling. *Cell Host & Microbe* **28**, 813-+ (2020).
28. X. J. Jiang, B. R. Stockwell, M. Conrad, Ferroptosis: mechanisms, biology and role in disease. *Nature Reviews Molecular Cell Biology* **22**, 266-282 (2021).

29. S. Dangol, Y. F. Chen, B. K. Hwang, N. S. Jwa, Iron- and Reactive Oxygen Species-Dependent Ferroptotic Cell Death in Rice-Magnaporthe oryzae Interactions. *Plant Cell* **31**, 189-209 (2019).
30. E. A. Minina *et al.*, Apoptosis is not conserved in plants as revealed by critical examination of a model for plant apoptosis-like cell death. *Bmc Biology* **19**, (2021).
31. T. Maekawa, H. Kashkar, N. S. Coll, Dying in self-defence: a comparative overview of immunogenic cell death signalling in animals and plants. *Cell Death Differ*, (2022).
32. S. Y. Xia *et al.*, Gasdermin D pore structure reveals preferential release of mature interleukin-1. *Nature* **593**, 607-+ (2021).
33. B. Q. Xia *et al.*, MLKL forms cation channels. *Cell Research* **26**, 517-528 (2016).
34. X. Chen *et al.*, Pyroptosis is driven by non-selective gasdermin-D pore and its morphology is different from MLKL channel-mediated necroptosis. *Cell Research* **26**, 1007-1020 (2016).
35. A. Murao, M. Aziz, H. C. Wang, M. Brenner, P. Wang, Release mechanisms of major DAMPs. *Apoptosis* **26**, 152-162 (2021).
36. S. Hou, D. Liu, P. He, Phytocytokines function as immunological modulators of plant immunity. *Stress Biol* **1**, 8 (2021).
37. J. Rzemieniewski, M. Stegmann, Regulation of pattern-triggered immunity and growth by phytocytokines. *Current Opinion in Plant Biology* **68**, (2022).
38. B. Li, X. Z. Meng, L. B. Shan, P. He, Transcriptional Regulation of Pattern-Triggered Immunity in Plants. *Cell Host & Microbe* **19**, 641-650 (2016).

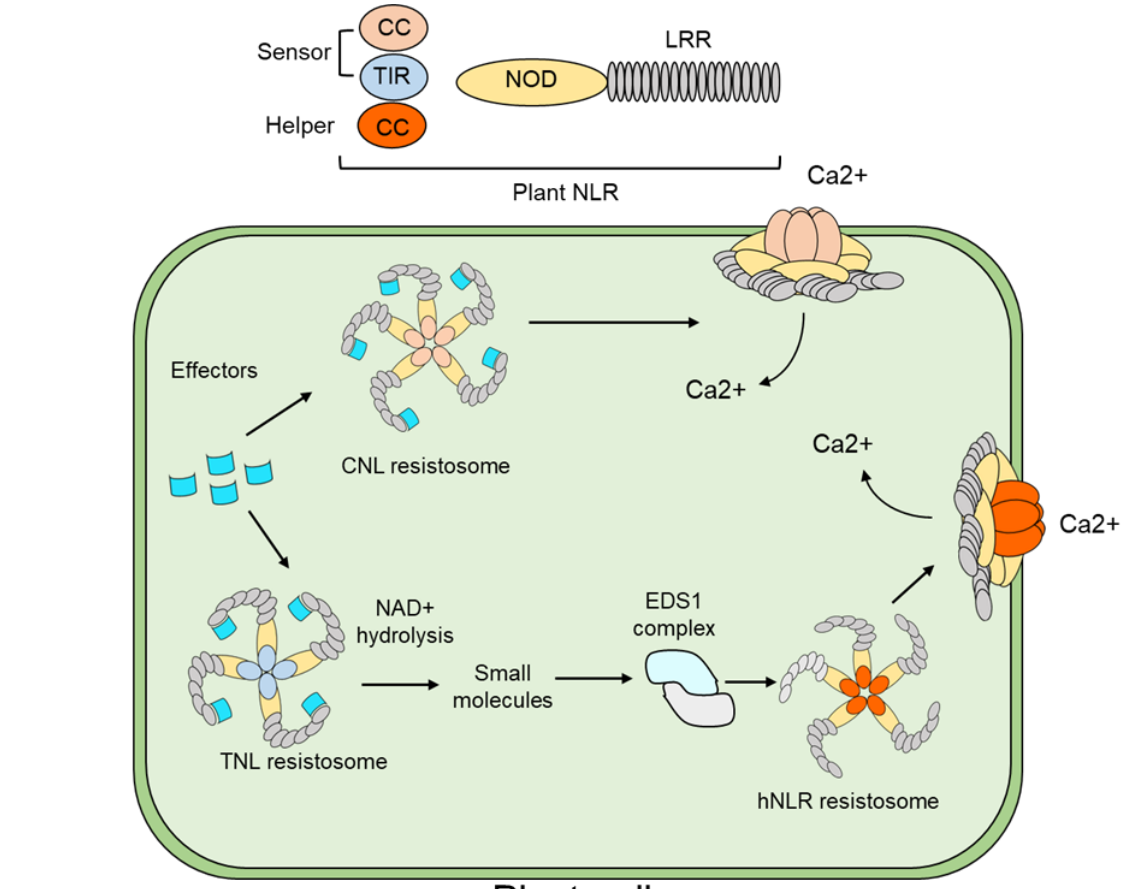

Plant cell

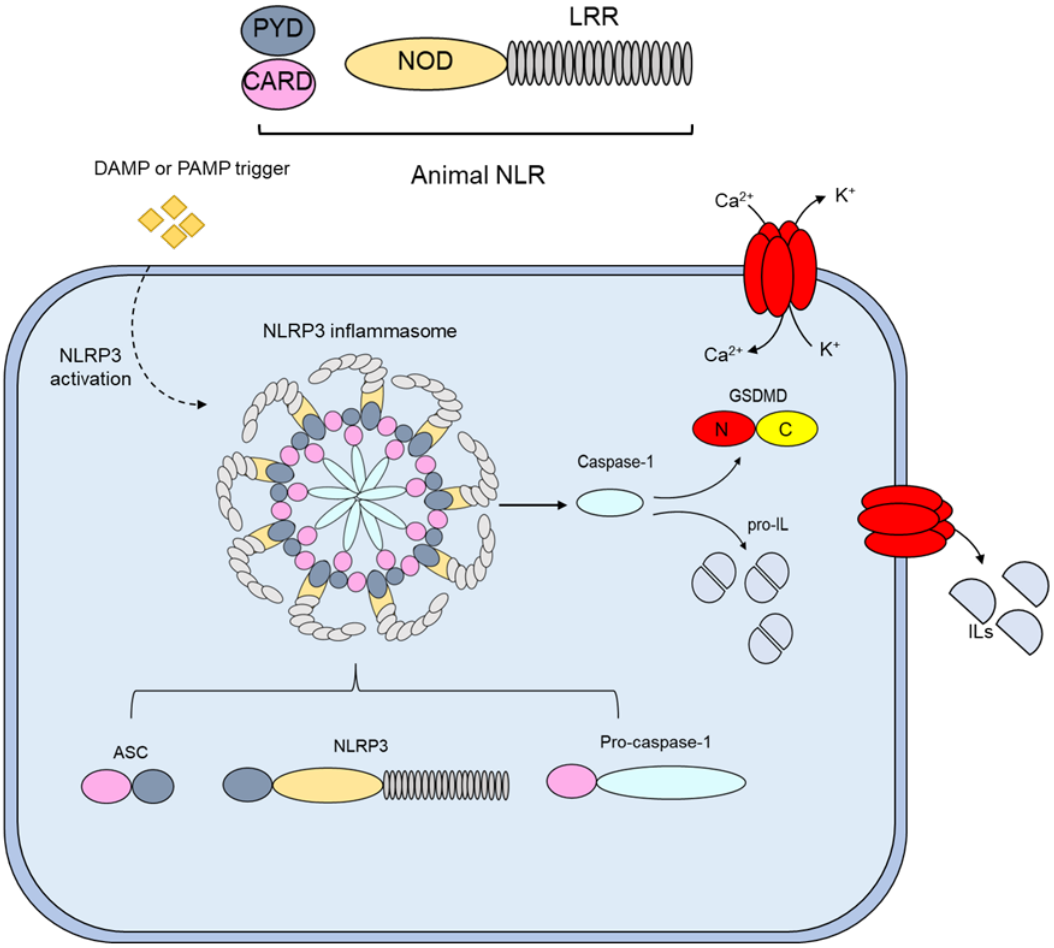

Animal cell

Figure 1. Domain architecture of NLR immune receptors and general activation mechanisms of resistosomes and inflammasomes in plants and animals, respectively. NLRs are modular tripartite immune receptors comprised of a N-terminal signalling domain, a NOD and LRR domain. In plants, NLRs are broadly classified into sNLRs and hNLRs based on their function during the immune response. Sensors are divided into CC- or TIR-NLR whereas helpers carry a CC domain at their N-terminus. Upon pathogen perception, CNLs oligomerize into a pentameric wheel-like structure whereas TNLs oligomerize into a tetrameric structure collectively known as resistosomes. Whilst CNLs can sense pathogen effectors and execute cell death by acting as permeable Ca^{2+} channels with no need of hNLRs, TIR domains from TNLs act as NAD+ hydrolases generating by-products or small molecules that bind to EDS1 complexes. Allosteric changes in EDS1 complexes allow interaction with hNLRs. Oligomerization of certain hNLRs into a pentameric resistosome with Ca^{2+}channel activity at the PM drive ion flux imbalances that resultin HR-cell death (*9, 10*).
In animals, the N-terminal domain of NLRs generally harbor either a CARD or a PYRIN domain. Upon recognition of DAMPs or PAMPs, animal NLRs nucleate into heteromeric inflammasome complexes. For instance, the pyrin-containing NLRP3 inflammasome is comprised of a sensor NLR (NLRP3), the adaptor protein ASC and caspase-1. Oligomerization of NLRP3 through homotypic interactions at the NOD recruits the ASC through a PYD-PYD interactions. Conformational changes in ASC allows recruitment of caspase-1 through CARD-CARD interactions, enabling caspase-1 activation. Proteolytically active caspase-1 subsequently cleaves GSDMD and pro-ILs which are released into the extracellular space. Insertion of the N-terminal pore-forming domain of GSDMD into the PM leads to nonselective ion fluxes that ultimately results in cellular demise.

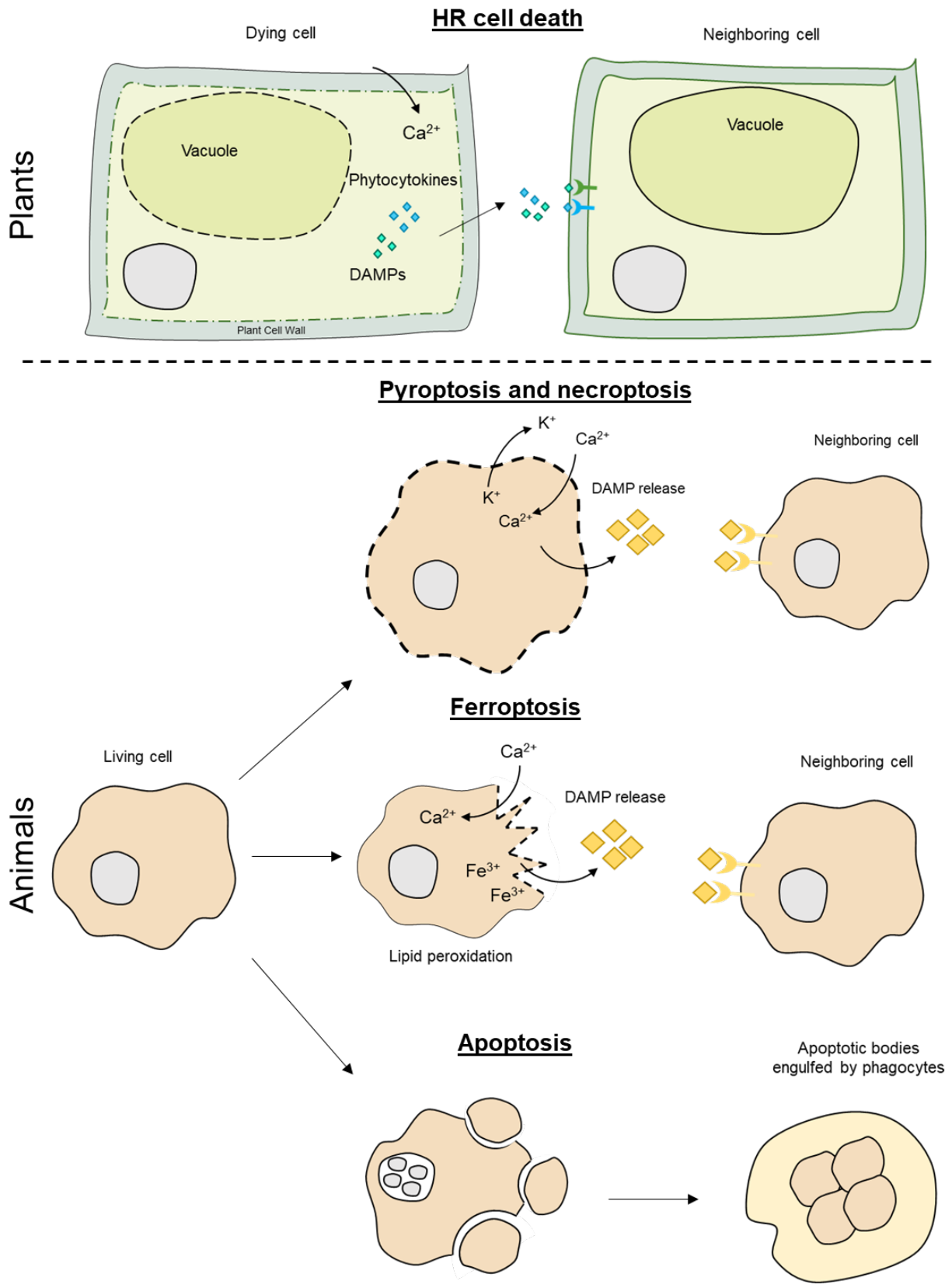
HR cell death
Dying cell
Neighboring cell
Plants
Vacuole
Ca2+
Phytocytokines
DAMPs
Plant Cell Wall
Vacuole
Pyroptosis and necroptosis
K+
Ca2+
K+
Ca2+
DAMP release
Neighboring cell
Ferroptosis
Living cell
Ca2+
Ca2+
DAMP release
Fe3+
Fe3+
Lipid peroxidation
Neighboring cell
Animals
Apoptosis
Apoptotic bodies
engulfed by phagocytes

Figure 2. Overview of cell death types and their general features in plants and animals. During HR cell death in plants, ROS accumulation and calcium channel activity exerted by plant resistosomes drive Ca^{2+} entry into the cytoplasm. How intracellular Ca^{2+} spikes lead to downstream cell death features such as loss of chloroplast and mitochondrial and eventually cellular demise is currently unknown. DAMPs and phytocytokines are released from infected/damaged cells and activate defence responses in neighboring cells via perception by surface receptors. Although differentially regulated at the molecular level, pyroptosis and necroptosis are both pro-inflammatory forms of cell death that involve release of cellular content to the extracellular space (DAMP release and inflammatory cytokines). In both cell death modalities, rupture of the plasma allows for the influx and efflux of ions altering homeostasis in the cell. Ferroptosis is an iron-dependent mode of cell death in which peroxidation of lipids cause plasma membrane damage with partial rupture allowing entry of Ca^{2+} ions and release of DAMPs to the extracellular space. Apoptosis is a non-inflammatory and silent form of cell death in which membrane integrity is maintained during cellular dismantling. Cell shrinkage, chromatin condensation and DNA fragmentation are typical hallmarks of apoptosis. Importantly, plasma membrane blebbing leads to apoptotic bodies that are eventually engulfed and eliminated by phagocytes.

Plant proteases in the control of the hypersensitive response

(Publication 2)

Journal of Experimental Botany, Vol. 70, No. 7 pp. 2087–2095, 2019
doi:10.1093/jxb/erz030 Advance Access Publication 4 February, 2019

REVIEW PAPER

Plant proteases in the control of the hypersensitive response

Jose Salguero-Linares and Núria S. Coll*

Centre for Research in Agricultural Genomics (CRAG), CSIC-IRTA-UAB-UB, Campus UAB, Bellaterra, Barcelona, 08193, Spain

* Correspondence: nuria.sanchez-coll@cragenomica.es

Received 30 October 2018; Editorial decision 7 January 2019; Accepted 7 January 2019

Editor: Moritz Nowack, VIB - Flemish Institute for Biotechnology/University of Gent, Belgium

Abstract

The hypersensitive response (HR) is a plant defence reaction triggered by activation of immune receptors upon pathogen recognition. It results in rapid cell death at the attempted invasion site, confining the pathogen and sending signals to distal parts of the plant that can in turn activate defences for subsequent attacks. HR cell death is a highly controlled phenomenon, requiring the concerted action of diverse plant proteases and regulatory mechanisms to keep it efficient yet confined. Research in the last decade has significantly contributed to a better understanding of the mechanisms leading to HR, although our knowledge about the pathways that regulate this form of programmed cell death (PCD) still remains incomplete. In this review, we explore current knowledge of plant proteases as HR regulators. Proteases are key regulatory enzymes that not only serve degradative purposes, but also have very important signalling roles. In animals, caspases have been shown to be the major regulators and executioners of PCD. Plants do not have caspases, and instead PCD is carried out by the activities of caspase-like and other protease belonging to different protease classes. We summarise the mechanistic roles of plant proteases whose roles in HR regulation are relatively well understood, which includes members of the cysteine, threonine, and serine protease families.

Keywords: Defence, hypersensitive response, immunity, pathogens, programmed cell death, proteases.

Introduction

Due to their lack of physical mobility, plants must defend themselves against rapidly evolving pathogens. Unlike animals, plants do not possess an adaptive immune system with mobile defender cells, and thus they rely on the innate immunity of each cell for effective defence responses (Jones and Dangl, 2006). In what is known as gene-for-gene interactions, plant resistance (*R*) gene products, such as surface-localised and intracellular nucleotide-binding leucine-rich repeat (NB-LRR) immune receptors, perceive avirulent (*avr*) pathogen-derived gene products, also known as effector proteins, often leading to a form of confined programmed cell death (PCD, also known as regulated cell death), known as the hypersensitive response (HR).

The first reports of HR date back to the beginning of the 20th century when H. Marshall Ward described a variable discoloration of leaves that turned from yellow to brown/black when infected with the leaf rust *Puccinia dispersa* (Ward, 1902). Additional studies at the time on the plant pathosystems *Chrysanthemum–Uredo* (*Puccinia*) *chrysanthemi* and wheat–*P. glumarum* (leaf yellow rust) also reported a similar cell death phenomenon upon pathogen infection (Gibson, 1904; Marryat, 1907). However, it was not until 1915 that the term 'hypersensitiveness' was used by Elvin C. Stackman to convey an 'abnormal rapid cell death' in cereal crops when attacked by black stem rust fungus (*P. graminis*) (Stakman, 1915). Since the plant exhibited hypersensitiveness at the fungal entry sites, the fungus was unable to develop normally, and thus the plant was deemed resistant. This phenotypic definition of HR has remained largely unchanged over the years, though in certain

pathosystems we now know that HR is often uncoupled from resistance (Coll *et al.*, 2011).

Defining HR cell death has not been an easy task due to its mixed morphological and biochemical features, which partly resemble several other forms of cell death in both plants and animals (Mur *et al.*, 2008). In mammals, up to 12 types of PCD modalities have been described so far (Galluzzi *et al.*, 2018). Amongst them, the best characterised is apoptosis, which is a non-inflammatory process mainly regulated by caspases, in which the following features are observed: cytoplasmic shrinkage, chromatin condensation, nuclear fragmentation, and plasma membrane blebbing; these ultimately lead to the formation of intact vesicles (apoptotic bodies) that are engulfed and digested by phagocytes (Galluzzi *et al.*, 2018). Whilst certain features such as cytoplasmic shrinkage and chromatin condensation are also observed during HR, other events such as phagocytosis of apoptotic bodies after cellular death do not occur in plants (Table 1). As a result, the resemblance of specific aspects of HR to apoptosis is not sufficient to consider HR as an apoptotic-like cell death. On the other hand, HR presents the majority of morphological features of plant regulated-necrosis cell death in which mitochondrial swelling, shrinkage of the protoplast, and early rupture of the plasma membrane are observed, and these features can also be found in other types of mammalian PCD such as pyroptosis and necroptosis (Table 1) (Galluzzi *et al.*, 2018). However, characteristics reminiscent of plant vacuolar-cell death such as enlargement of the vacuole and rupture of the tonoplast are also exhibited during HR (van Doorn *et al.*, 2011). When considering the cytological features of HR, it is also of great importance to consider the nature of the invading pathogen. For instance, vacuolar rupture can be an effective measure to restrict viruses that proliferate in the host cytoplasm (Hatsugai *et al.*, 2004). By contrast, fusion of the tonoplast with the plasma membrane allows discharge of antimicrobial compounds to the intercellular space where bacterial pathogens tend to proliferate (Hatsugai *et al.*, 2009). In summary, HR is an atypical and confined plant cell death modality that occurs at the site of successful recognition of pathogens, and it generally displays the following hallmarks: cytoplasmic shrinkage, mitochondrial swelling, chromatin condensation, chloroplast and plasma membrane disruption, and vacuolisation (Table 1). Interestingly, necrotrophic pathogens such as the fungus *Cochliobolus victoriae* can hijack the HR machinery through the delivery of toxins that target the plant cell in order to kill it and feed on cell remnants (Lorang *et al.*, 2012). In the course of this cell death, expected features that resemble necrosis (protoplast shrinkage and a transition of mitochondrial permeability) are displayed, although membrane and tonoplast integrity is maintained (Curtis and Wolpert, 2004).

Despite its discovery more than a century ago, a thorough understanding of the mechanisms regulating HR is lacking. In the last few decades, a growing body of evidence has indicated that plant proteases are involved in pathogen perception and in the induction of effective local and systemic defence responses, which are often accompanied by a HR-related cell death confined to the site of the attempted pathogen ingression (Rooney *et al.*, 2005; Coll *et al.*, 2010; Bozkurt *et al.*, 2011).

Proteases are ubiquitous enzymes required for the correct functioning of living cells. Operating at the post-translational level, proteases catalyse irreversible hydrolytic reactions in which peptide bonds of target substrates are cleaved, giving rise to new protein products (van der Hoorn, 2008). Whilst originally believed to act solely as destructive enzymes, we now know that proteases can also influence the activity of other proteins, regulate protein fate and localisation, modulate protein–protein interactions, and contribute to processing of cellular information through signal transduction (Turk, 2006).

Based on the *MEROPS* database, an integrated information resource of proteases (http://merops.sanger.ac.uk), there are five mechanistic classes of proteases found in living organisms according to the catalytic residue involved in the cleavage of the substrate peptide bond, namely cysteine, aspartate, threonine, serine, and metalloproteases (Rawlings *et al.*, 2018). In the case of cysteine, threonine, and serine proteases, the orchestrated action of a catalytic triad comprised of a nucleophile (Cys, Thr, or Ser), a base (usually His), and in certain cases an acid (Asp), allows cleavage of the peptide bond (López-Otin and Bond, 2008). A second classification in the *MEROPS* database

Table 1. *Hallmarks of PCD in animals (apoptosis, necroptosis and pyroptosis) and plants (HR, regulated necrosis and vacuolar) , based on Mur et al., (2008)*

Characteristics	Animal PCD			Plant PCD		Vacuolar cell death
	Apoptosis	Necroptosis	Pyroptosis	HR	Regulated necrosis	
Cytoplasmic shrinkage	✓	✗	✗	✓	✗	✓
Cytoplasmic swelling	✗	✓	✓	✗	✓	✗
Chromatin condensation	✓	✗	✓	✓	✗	✓
Mitochondrial swelling	✗	✓	✓	✓	✓	✗
Vacuolization	✗	✗	✗	✓	✗	✓
Chloroplast rupture	na	na	na	✓	✓	✗
Plasma membrane blebbing	✓	✗	✗	✗	✗	✗
Plasma membrane rupture	✗	✓	✓	✓	✓	✗
Tonoplast rupture	✗	✗	✗	✓	✗	✓
Nuclear fragmentation	✓	✗	✓	✗	✗	✓
Apoptotic bodies	✓	✗	✗	✗	✗	✗

Although additional cell death modalities exist in animals, we considered the three types listed to be the most representative for conveying comparisons with HR in plants. na, not applicable.

discriminates between clan types (usually denoted by a letter), where proteases fall into distinct categories depending on their protein tertiary structure. Within each clan, a third and final subdivision is made into distinct families of proteases based on their evolutionary relationships (Rawlings *et al.*, 2018).

As occurs in animals, plant proteases are directly implicated in the regulation of host responses to pathogen infection, including PCD. This review is intended to highlight the crucial functions of the distinct classes of plant proteases in the regulation of HR. Due to space limitations, we only concentrate on proteases whose mechanistic roles in HR regulation are well understood, namely members of the cysteine, threonine, and serine protease classes.

Cysteine proteases: PLCPs, VPEs, and metacaspases

In mammals, apoptosis requires an evolutionarily conserved group of cysteine proteases termed caspases. Since particular characteristics are shared between animal apoptosis and defence-related hypersensitive cell death in plants, it was reasoned in the past that a certain level of conservation of the molecular components involved in PCD should be present across kingdoms (del Pozo and Lam, 1998). However, although certain structurally unrelated plant proteases have been shown to exhibit caspase-like activities in the course of defence-related HR (del Pozo and Lam, 1998; Chichkova *et al.*, 2004; Hatsugai *et al.*, 2004), no caspase homologues are found within plant genomes. Plant genomes encode approximately 140 cysteine proteases, which fall into five distinct clans. In the context of plant–pathogen interactions, the CA clan, comprising proteases with a papain-like fold named papain-like cysteine proteases (PLCPs), and the CD clan, comprising proteases with a caspase-like fold, have been well documented (Misas-Villamil *et al.*, 2016). Biochemical tools such as specific protease inhibitors as well as activity-based probes have been pivotal in the discovery of many cysteine proteases implicated in plant defence by monitoring their protease activity (van der Hoorn and Kaiser, 2012). Here, we will discuss the role in HR of three PLCPs (Cathepsin B, Rcr3, Pip1), three metacaspases (AtMC1, AtMC2 and AtMC4), and the vacuolar processing enzymes (VPEs).

PLCPs

PLCPs are released as pre-proteases bearing a signal peptide at the N-terminal end, an auto-inhibitory domain or pro-domain, and the catalytic domain (bearing the catalytic triad Cys, His, and Asn). A granulin domain with unknown function is usually present at the C-terminus. PLCPs are predominately secreted into the apoplast, a major battleground in which the fate of either a successful pathogen infection or an effective plant defence response is dictated (Fig. 1) (Du *et al.*, 2016).

Early evidence for a role of Cathepsin B (CathB) in PCD came from studies in animals where it was shown to activate caspases (Kingham and Pocock, 2001) and CathB knock-out mice exhibited impaired apoptosis (Guicciardi *et al.*, 2001). Plant CathB was subsequently shown to be involved in the regulation of defence-related HR and basal disease resistance (Gilroy *et al.*, 2007; McLellan *et al.*, 2009). In plants, CathB is activated upon secretion in the apoplast. Through the use of specific animal CathB inhibitors and virus-induced gene silencing (VIGS) in potato CathB (*StCathB*), Gilroy *et al.* (2007) demonstrated that the HR elicited by two bacterial pathogens, *Erwinia amylovora* and *Pseudomonas syringae* pv. tomato (*Pst*) DC3000, was remarkably impaired in the absence of CathB, resulting in enhanced disease susceptibility in *Nicotiana benthamiana* (Fig. 1). Likewise, transient co-expression of the pathogen-derived effector Avr3a from *Phytophthora infestans* and the potato NB-LRR R3a resulted in compromised HR when CathB transcript levels were reduced (Table 2) (Armstrong *et al.*, 2005) Conversely, VIGS of CathB in *N. benthamiana* did not attenuate HR following perception of *Cladosporium fulvum* effector Avr4 by the plant receptor-like protein Cf-4 (Gilroy *et al.*, 2007). In Arabidopsis, although required for basal resistance to *Pst*, *AtCathB1-3* genes are dispensable for avirulent *R*-gene mediated resistance to strains carrying the effectors AvrB and AvrRps4. Interestingly, *AtCathB1-3* genes act redundantly to positively regulate HR development triggered by *Pst* strains expressing AvrB, owing to the fact that *atcathb* triple-mutants, but not double- or single-mutant *atcathb* lines, exhibit nullified HR (Fig. 1 and Table 2) (McLellan *et al.*, 2009). Taken together, these observations indicate that CathB is not a universal HR regulator and its role in defence-related HR seems to be pathogen-specific.

The tomato cysteine proteases, Rcr3 and PHYTOPTHORA INHIBITED PROTEASE 1 (Pip1), are two interesting examples of secreted PLCPs that mediate pathogen perception in the apoplast. These pathogenesis-related proteases are targeted by phylogenetically unrelated pathogens and appear to be under strong diversifying selection (Shabab *et al.*, 2008). The fungal pathogen *C. fulvum* secretes the effector Avr2 into the apoplast. Avr2 binds to and inhibits Rcr3 and Pip1, forming Avr2-Rcr3 and Avr2-Pip1 complexes, respectively (Fig. 1) (Rooney *et al.*, 2005; Shabab *et al.*, 2008). Avr2-mediated perturbations of Rcr3 are perceived by the LRR-containing receptor-like protein (RLP) Cf-2, triggering HR which, in this case, results in full resistance to *C. fulvum* (Fig. 1, Table 2) (Rooney *et al.*, 2005). Interestingly, *rcr3* mutant lines do not exhibit higher susceptibility compared with tomato lines missing the *Cf-2* gene cluster, implying that Rcr3 inhibition does not contribute to virulence (Dixon *et al.*, 2000). Moreover, Pip1 accumulates to higher levels compared to Rcr3 in the apoplast upon treatment with salicylic acid or in response to diverse pathogen infections. Hence, in agreement with the 'decoy' model, it can be hypothesised that Rcr3 evolved as a decoy to perceive effector-mediated perturbations and that the original operational target of Avr2 is Pip1 (Shabab *et al.*, 2008; van der Hoorn and Kamoun, 2008). In addition to *C. fulvum*, the oomycete *Phytophthora infestans* and the root parasitic nematode *Globodera rostochiensis* are also able to inhibit Rcr3 via secretion of apoplastic effectors, namely EPIC1 and EPIC2B, and Gr-VAP1, respectively (Lozano-Torres *et al.*, 2012; Song *et al.*, 2009). However, whilst the weak interaction between EPICs and Rcr3 is not sufficient to trigger HR,

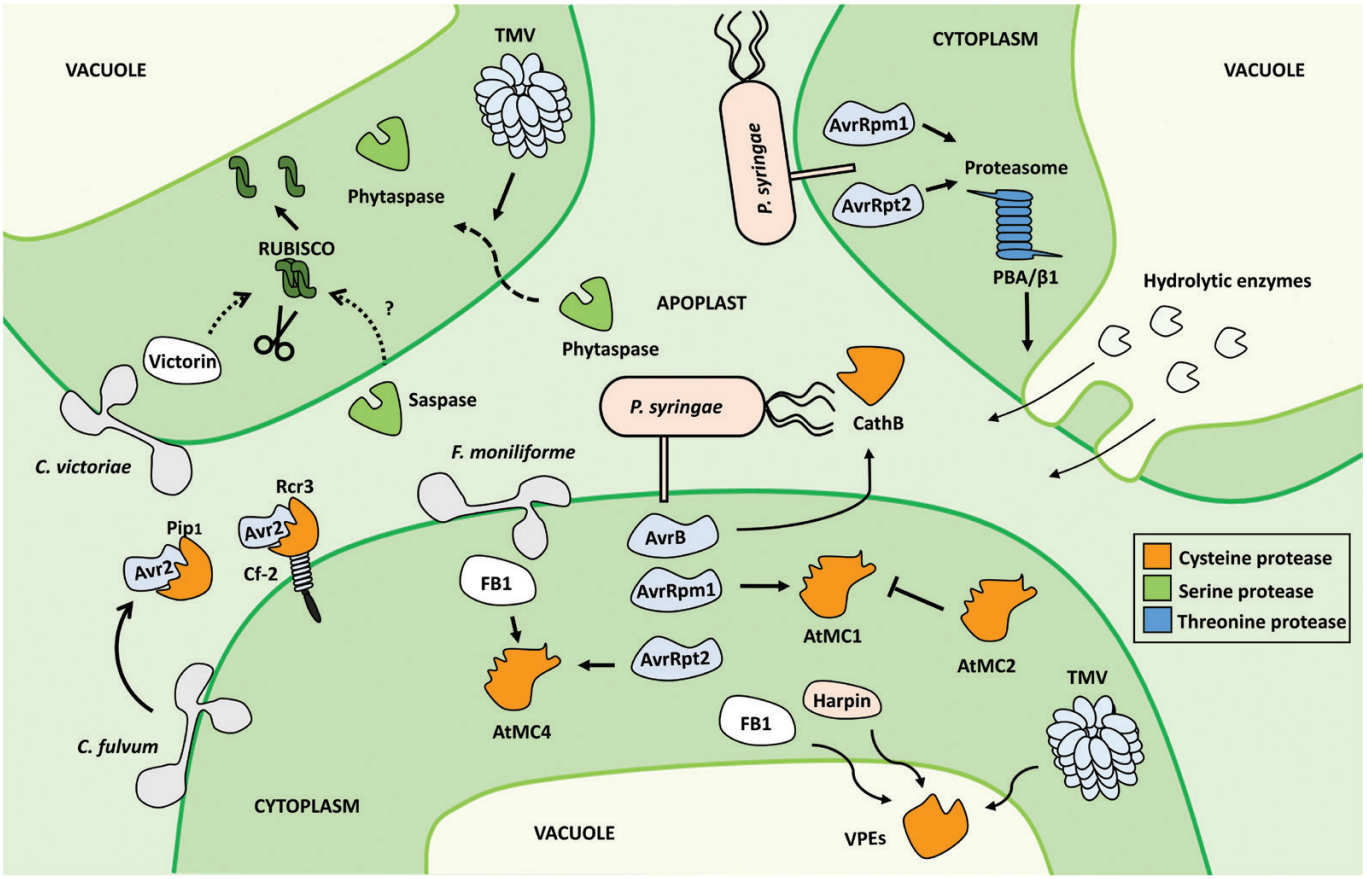

Fig. 1. Mechanistic roles of cysteine, serine, and theronine proteases in the regulation of hypersensitive response (HR) cell death in plants. The cysteine (orange), serine (green), and threonine (blue) protease activities highlighted in this review are represented separately in three schematic cells. Bacteria are represented in light pink, viruses in light grey, and fungi in white. **Cysteine proteases** (bottom cell). Papain-like cysteine proteases (PLCPs): the Avr2 effector from *C. fulvum* binds to its virulence-host target Pip1 and the host decoy cysteine protease Rcr3. The formation of the Avr2–Rcr3 complex is sensed by the immune receptor Cf-2, leading to HR. CathB is necessary for HR cell death induced by *P. syringae* carrying the effector *AvrB*. Metacaspases: *P. syringae* carrying the *AvrRpm1* effector is perceived by intracellular immune receptors, which trigger activation of AtMC1 and HR. This AtMC1-mediated cell death event is genetically inhibited by AtMC2. AtMC4 is required for HR triggered by *P. syringae* carrying the *AvrRpt2* effector and by *F. moniliforme* mycotoxin FB1. Vacuolar processing enzymes (VPEs) are involved in TMV-induced HR, and in fungal mycotoxin FM1 and bacterial harpin-triggered HR. **Serine proteases** (upper left cell). Saspases are thought to be constituents of a proteolytic cascade upstream of Rubisco cleavage and victorin-induced cell death in response to treatment of *A. sativa* leaves with victorin. Phytaspases are imported from the apoplast to the cytosol upon TMV-induced cell death and are required for HR. **Threonine protease** (upper right cell). The PBA1/β1 subunit of the proteasome is required for fusion of the vacuolar membrane with the plasma membrane upon infection with avirulent *P. syringae* carrying the AvrRpm1 or AvrRpt2 effectors. This membrane fusion facilitates discharge of anti-microbial hydrolytic enzymes, ultimately leading to HR.

formation of a complex between the allergen-like effector Gr-VAP1 and Rcr3 is sensed by the guardian Cf-2, which ultimately induces HR at the attempted site of infection (Table 2) (Rooney *et al.*, 2005; Song *et al.*, 2009; Lozano-Torres *et al.*, 2012). Consequently, Rcr3 provides a striking example of an antagonistic evolutionary arms race in which a plant PLCP has evolved as a decoy to trap diverse pathogen effectors into a recognition event.

VPEs

VACUOLAR PROCESSING ENZYMEs (VPEs) are cysteine proteases of the CD clan C13 family that cleave their substrate after asparagine or aspartate residues (Thomas and van der Hoorn, 2018). Despite their low sequence similarities, VPEs are evolutionarily related and share structural homology to caspases (Misas-Villamil *et al.*, 2013). Moreover, they exhibit caspase 1-like activity. By means of VPE inhibitors and VIGS experiments, it has been shown that the HR triggered by tobacco mosaic virus (TMV) in *N. benthamiana* carrying an *N* resistance gene requires active VPEs (Fig. 1, Table 2) (Hatsugai *et al.*, 2004). A prerequisite of HR is the rupture of the tonoplast through vacuolar collapse and the subsequent release of hydrolytic enzymes to the cytoplasm. Notably, vacuoles of TMV-infected plants deficient in VPEs are similar to wild-type plants, suggesting that VPEs are necessary for tonoplast disruption (Hatsugai *et al.*, 2004). Besides their role in TMV-triggered cell death, VPEs are also required for a HR-like cell death triggered by the bacterial elicitor harpin and by fumonisin B1 (FB1), a toxin naturally produced by the maize necrotrophic fungal pathogen *Fusarium moniliforme* (Fig. 1, Table 2) (Kuroyanagi *et al.*, 2005; Zhang *et al.*, 2010). Remarkably, a necrotrophic pathogenic strategy to induce cell death and a HR-like cell death response mediated by the host as a plant defence strategy are both mediated by VPEs. However, VPEs are not universal HR regulators. HR-like cell death induced by elicitors such

Table 2. *Plant proteases involved in HR and HR-like cell death*

Class	Protease	Protein ID (UNIPROT)	Clan and family	Plant species	HR or HR-like cell death trigger	Subcellular localisation	Regulatory role in HR	References
CYSTEINE	Cathepsin B	Q40413, F4HVZ1, Q93VC9, Q94K85	CA/PLCP,C1	*N. bethamiana*, *A. thaliana*	*Pst (AvrB)*; *E. amylovora*; *Pst DC3000*	Apoplast	Positive	Gilroy *et al.* (2007); McLellan *et al.* (2009)
	Rcr3	Q8S333	CA/PLCP,C1	*Solanum lycopersicum*	*C. fulvum*; *G. rostochiensis*	Apoplast	Positive	Rooney *et al.* (2005); Lozano-Torres *et al.* 2012)
	Pip1	Q156I2	CA/PLCP,C1	*S. lycopersicum*	*C. fulvum*	Apoplast	Positive	Shabab *et al.* (2008)
	VPE	Q39119, Q60G64, Q60G63	CD/ Legumain,C13	*N. bethamiana*, *A. thaliana*	TMV; Mycotoxin FB1; Bacterial harpin	Vacuole	Positive	Hatsugai *et al.* (2004); Kuroyanagi *et al.* (2005); Zhang *et al.* (2010)
	AtMC1	Q7XJE6	CD,C14	*A. thaliana*	*Pst* (*AvrRPM1*); *H. arabidopsis*	Cytoplasm	Positive	Coll *et al.* (2010)
	AtMC2	Q7XJE5	CD,C14	*A. thaliana*	*Pst* (*AvrRPM1*); *H. arabidopsis*	Cystoplasm	Negative	Coll *et al.* (2010)
	AtMC4	O64517	CD,C14	*A. thaliana*	*P.m.a*(*AvrRpt2*); Mycotoxin FB1	Cystoplasm	Positive	Watanabe and Lam (2005)
THREONINE	PBA1	F4JRY2	PB,T1	*A. thaliana*	*Pst* (*AvrRPM1*); *Pst* (*AvrRpt22*)	Cystoplasm	Positive	Hatsugai *et al.* (2009)
SERINE	Saspase	-	SB,S8A	*A. sativa*	Victorin	Apoplast	Positive	Coffeen and Wolpert (2004)
	Phytaspase	C7E4J6	SB,S8A	*N. tabacum*, *Oryza sativa*	TMV	Apoplast/ Cytoplasm	Positive	Chichkova *et al.* (2010)

as fungal nep1 and oomycete boehmerin do not require VPE activity (Zhang *et al.*, 2010). Moreover, in the course of compatible interactions between the oomycete obligate biotroph *Hyaloperosnospora arabidopsis* (*Hpa*) and Arabidopsis, the activity of a host VPE (γVPE) is increased upon infection, leading to enhanced disease susceptibility. Since sporulation of *Hpa* on *vpe* mutant plants is significantly reduced, it can be hypothesised that VPEs play a role during compatible interactions that is independent of cell death (Misas-Villamil *et al.*, 2013). Collectively, it can be concluded that the role of VPEs in host pathogen-triggered PCD also appears to be dependent on the pathosystem.

Metacaspases

Together with VPEs in the CD clan, and belonging to the C14 family, are metacaspases (Rawlings *et al.*, 2018). Metacaspases are an ancient group of cysteine proteases found in protozoa, fungi, plants, and bacteria, and they are predominantly known for their pivotal roles in PCD in non-metazoan organisms (Minina *et al.*, 2017). From an evolutionary point of view, metacaspases are distantly related to animal caspases, although bioinformatic analyses predict close structural homology to animal caspases at the catalytic domain, which harbours a caspase-like His-Cys catalytic dyad and a caspase-hemoglobinase fold (Tsiatsiani *et al.*, 2011). With regards to their biochemical features, metacaspases are quite distinct compared to caspases, owing to their lack of aspartate specificity and their preference for substrate cleavage after Arg or Lys residues (Vercammen *et al.*, 2004; Watanabe and Lam, 2005; González *et al.*, 2007). Metacaspases are classified into type I and type II based on their domain architecture. In plants, type I metacaspases bear an N-terminal pro-domain extension that is absent in type II metacaspases. Type II metacaspases, on the other hand, possess an extended linker region between catalytic subunits and the C-terminus (Tsiatsiani *et al.*, 2011). Evidence for a direct role of metacaspases in HR have come mainly from studies in Arabidopsis, in which an up-regulation of type I metacaspase 1 (AtMC1) upon pathogen infection was initially reported (Zimmermann *et al.*, 2004). Subsequently, genetic analysis of the function of AtMC1 through knock-out mutants revealed that it is required for the HR-like runaway cell death phenotype of the lesion mimic mutant *lesion stimulating disease 1* (*lsd1*) (Coll *et al.*, 2010). In parallel, *atmc1* plants exhibit suppression of HR triggered by infection with an avirulent strain of *Pst* DC3000 (*AvrRpm1*) (see Fig. 1) or an avirulent strain of the oomycete *Hyaloperonospora arabidopsidis* (*Hpa*) (Table 2). Of note, pathogen growth is unaffected in *atmc1* plants, providing another example of HR uncoupled from disease resistance. Interestingly, AtMC2, a closely related type I metacaspase in Arabidopsis, genetically serves the opposite function of AtMC1 by negatively regulating HR, as *AtMC2* overexpression phenocopies the nullified HR phenotype of *atmc1* mutant plants, whereas *atmc2* mutants show exacerbated HR (Fig. 1, Table 2).

Remarkably, whilst the function of AtMC1 is dependent on its catalytic activity, AtMC2 exerts its negative HR regulation in spite of the presence or absence of its cysteine catalytic residue (Coll *et al.*, 2010).

Given that it is such a potent HR mediator, plant cells must ensure appropriate AtMC1 activation under different stress scenarios. Consequently, besides the negative regulation of AtMC1 mediated by AtMC2, plants have evolved alternative means to keep AtMC1 at bay under basal conditions. LSD1 negatively regulates AtMC1 by directly interacting with the LSD1-like zinc finger region of the N-terminal pro-domain of AtMC1 (Coll *et al.*, 2010). Presumably, this interaction with the pro-domain impedes autoprocessing of AtMC1, thus preventing its activation. Furthermore, AtSERPIN1 functions as a 'suicide inhibitor' by covalently and irreversibly inhibiting AtMC1 (Asqui *et al.*, 2018).

In parallel to type I metacaspases, the constitutively expressed Arabidopsis type II metacaspase AtMC4 has been found to contribute to the HR-like cell death response triggered by fungal mycotoxin FB1 and avirulent *Pseudomonas syringae* pv. maculicola ES4326 carrying AvrRpt2 (*Pma AvrRpt2*) (Fig. 1, Table 2) (Watanabe and Lam, 2005). Two independent knock-out mutant lines of AtMC4 display attenuated and delayed HR-like cell death upon mycotoxin treatment and *Pma* (*AvrRpt2*) infection, respectively. Conversely, AtMC4 overexpressor lines treated with mycotoxin FB1 induce a more pronounced HR-like cell death when compared to wild-type plants. Notably, during mycotoxin FB1-induced HR-like cell death, catalytic activity and self-processing of AtMC4 in the cytosol is of critical importance to exert a wild type-like cell death response (Watanabe and Lam, 2011).

Although solid evidence for the implication of AtMC1, AtMC2, and AtMC4 in HR regulation exists, the molecular mechanisms by which metacaspases exert their pro-death function during mycotoxin FB1 treatment and downstream of NB-LRR activation is far from clear. Future determination of the physiological substrates of metacaspases during the course of pathogen infection by means of protein degradomics studies will be of critical importance to enhancing our fragmented knowledge of HR.

Threonine proteases: PBA1 subunit of the proteasome

The ubiquitin–proteasome system (UPS) is a protein degradation system that has long been known for its role in many fundamental cellular processes, including plant immunity (Ustun *et al.*, 2016). Ubiquitinated proteins destined for degradation are recognised and degraded by the 26S proteasome, an ATP-dependent protease complex comprised of 31 subunits that are further subdivided into two subcomplexes, the 20S core protease (CP) and the 19S regulatory particles (RPs). Owing to its caspase 3-like activity, one of the subunits of the CP subcomplex, PBA1/β1, has been heavily scrutinised in the context of HR (Hatsugai *et al.*, 2009). PBA1/β1 is a threonine protease that belongs to the PB clan and T1 family of cysteine proteases in Arabidopsis (Thomas and van der Hoorn, 2018). In the course of an avirulent bacterial infection, the central vacuole of plant cells fuses with the plasma membrane. By doing so, anti-microbial hydrolytic enzymes can be released to the apoplast where bacteria proliferate (Hatsugai *et al.*, 2009). Upon infection of Arabidopsis with avirulent *Pst* DC3000 carrying AvrRpt2 or AvrRpm1, inhibition of the PBA1/β1 subunit of the proteasome through caspase 3 and proteasome specific inhibitors impedes the fusion of the vacuolar membrane with the plasma membrane, which is believed to prevent discharge of anti-microbial enzymes into the apoplast (Fig. 1, Table 2). In the same manner, Arabidopsis *PBA1/β1*-silenced plants exhibit the exact same phenotype. Consequently, HR is remarkably reduced in Arabidopsis PBA1/β1-defective plants compared to wild-type controls, and such impairment is dependent on the caspase 3-like activity of PBA1/β1 (Fig. 1, Table 2). Of note, concomitant with the reduction of HR is an increase in plant susceptibility to the avirulent bacterial strains (Hatsugai *et al.*, 2009). Other catalytic subunits of the proteasome such as PBB and PBE do not exhibit caspase-3 like activity, although silencing of *PBB* and *PBE* replicates the HR suppression observed in PBA1/β1-deficient plants (Hatsugai *et al.*, 2009). Finally, a subunit of the RP subcomplex, RPN1a, is required for effective resistance to powdery mildew and mildew-induced cell death. Perturbation of other subunits of the proteasome such as RPT2a and RPN8a also impair powdery mildew resistance and mildew-induced cell death (Yao *et al.*, 2012). However, *rpn1a* mutant Arabidopsis plants infected with avirulent *Pst* (*AvrRpt2*) and *Pst* (*AvrRPS4*) display normal HR induction compared to the wild-type, suggesting a function of the RPN1a subunit during induced cell death that is specific to powdery mildew (Yao *et al.*, 2012).

Subtilisin-like proteases: saspases and phytaspases

Given the importance of caspases in animal PCD processes, over the past few decades there has been a considerable effort to find caspase-like proteases in plants. A thorough examination of caspase-like activities in plants has led to the conclusion that, although they share a minor structural resemblance to animal caspases, the majority of caspase-like activities displayed in plants can be attributed to subtilisin-like proteins or subtilases (Vartapetian *et al.*, 2011). Subtilases are serine proteases, belonging to the SB clan and S8A family, which rely on the catalytic triad aspartate, histidine, and serine for execution of their catalytic activity (Rawlings *et al.*, 2018). In the context of HR, saspases and phytaspases represent two examples of serine proteases that might play indirect and direct roles, respectively, in the regulation of cell death upon biotic attacks (Coffeen and Wolpert, 2004; Chichkova *et al.*, 2010).

Saspases

The necrotrophic fungus *Cochliobolus victoriae*, the causative agent of Victoria Blight of oats (*Avena sativa*), produces the host-selective toxin victorin. Acting in a gene-specific manner, victorin triggers a form of cell death reminiscent of

HR. Proteolysis of Rubisco, an *in vitro* substrate of victorin, has been demonstrated to be inhibited by caspase-specific and general inhibitors of cysteine and serine proteases (Navarre and Wolpert, 1999). In parallel, purification of two specific caspase-like activities of protein extracts from victorin-treated *A. sativa* followed by substrate cleavage assays of caspase-like synthetic tretrapeptides has suggested the existence of a proteolytic signalling cascade upstream of Rubisco cleavage (Coffeen and Wolpert, 2004). Purification of active proteolytic enzymes followed by N-terminal sequencing has revealed two peptidases that share extensive homology to diverse plant subtilases, in particular rice subtilisin-like serine proteases. As a result, the term 'saspases' was coined, referring to its serine catalytic residue and their 'aspase' activity (Coffeen and Wolpert, 2004). Alike animal caspases, saspases appear to serve a processing enzymatic function rather than a degradative one, owing to their low activity towards general protease substrates, including Rubisco. Collectively, it appears likely that, in the presence of victorin sensitivity, saspases may be constituents of a proteolytic cascade that leads to Rubisco cleavage and PCD. Interestingly, saspases localise to the extracellular fluid at the early stages of victorin-induced PCD, in what appears to be a tightly regulated secretion event rather than a consequence of PCD (Fig. 1). As a result, the subcellular localisation of saspases and Rubisco makes it unlikely that they cleave Rubisco directly (Coffeen and Wolpert, 2004; Vartapetian *et al.*, 2011). Unfortunately, besides the intriguing biochemical data on saspases, no direct genetic evidence for their involvement in HR has been identified to date.

Phytaspases

An alternative approach to search for caspase-like proteases was based on the previous knowledge that the *Agrobacterium tumefaciens*-encoded protein VirD2 is cleaved by human caspase 3 at D^{400} within a TATD motif (Chichkova *et al.*, 2004). VirD2 from *A. tumefaciens* harbours a nuclear-localisation signal (NLS) and assists in the transfer of single-stranded DNA fragments (T-DNA) into the genome of the plant (Tinland *et al.*, 1995). Since the NLS of Vir2D is essential for successful nuclear uptake of foreign DNA, Chichkova *et al.* (2004) hypothesised the existence of a plant protease capable of cleaving VirD2 in a caspase 3-like manner. In order to test this hypothesis, Vir2D was utilised as a substrate to detect a 'plant caspase' that operates in the course of a TMV infection in *N. tabacum* plants carrying an *N* resistance gene, and they found a caspase 3-like activity that was exclusively present in plants undergoing TMV-induced PCD. Subsequent purification of the protein responsible for the activity in tobacco and rice followed by mass spectrophotometry analysis suggested that the protein was a subtilisin-like protease of the S8 family, which was thereafter named phytaspase (Chichkova *et al.*, 2010). This enzyme is comprised of a signal peptide, a pro-domain, and a protease-associated domain within its peptidase domain (Vartapetian *et al.*, 2011). *In vitro* cleavage assays further demonstrated the aspartate specificity of phytaspases. Moreover, mutational analysis on the catalytic Ser^{537} of recombinant protein corroborated a Ser^{537}-dependence for substrate cleavage and maturation of the protease, thus demonstrating autocatalytic processing of the pro-enzyme (Chichkova *et al.*, 2010).

With regards to their role in HR and defence, several lines of evidence suggest that phytaspases are required for TMV-triggered HR in tobacco plants harbouring an *N* resistance gene (Chichkova *et al.*, 2010). Transgenic tobacco plants overproducing phytaspases exhibit enhanced HR upon TMV infection. By contrast, impairment of phytaspase production in silenced plants results in an attenuation of HR triggered by TMV (Fig. 1, Table 2). Notably, this latter phenotype can be restored by heterologous expression of rice wild-type phytaspase but not by its catalytically inactive mutant (Chichkova *et al.*, 2010). In this pathosystem, HR triggered by phytaspases appears to serve a protective function, as demonstrated by the fact that in contrast to phytaspase-silenced plants, which tend to accumulate high levels of TMV, phytaspase-overproducing plants have reduced TMV accumulation compared to wild-type control plants (Chichkova *et al.*, 2010).

In contrast to animal caspases that retain an intracellular localisation, phytaspases seem to be constitutively synthesised as zymogens and processed into pro-domainless mature forms that are secreted to the apoplast (Fig. 1). Intriguingly, upon viral infection, phytaspases shuttle their subcellular localisation into the cytoplasm where they may cleave intracellular substrates required to induce HR, pointing towards a spatial regulation of their activity (Chichkova *et al.*, 2010). This re-entry into the cytoplasm would be needed to explain the observed VirD2 cleavage by *N. tabacum* phytaspase. Such protease redistribution is exclusive to phythaspases since other apoplastic proteases that exhibit caspase-like activities, such as CathB, are confined in the apoplast throughout the entire course of a viral infection (Gilroy *et al.*, 2007; Vartapetian *et al.*, 2011).

Concluding remarks

More than a century since the discovery of HR, we are still far from understanding the mechanisms by which this type of PCD is carried out. However, research over the last decade has significantly contributed to a better understanding of the proteases involved in this phenomenon, largely due to the successful efforts of the expanding plant protease community, which has developed many tools and methods to efficiently examine their functions, modes of action, and substrates.

We now know that plants do not have caspases. Their structural relatives in plants are important both for HR and for other types of PCD, but they have a different mode of action. Plants have evolved several different caspase-like activities catalysed by other families or even by classes of proteases. These caspase-like activities in plants are not only involved in HR, but also in processes not related to cell death. In this review, we have only considered the functions of a few proteases in HR belonging to the cysteine, threonine, and serine protease families, which are the best characterized. Even so, for most of them we still do not know the substrates or their upstream regulators. In addition, several other plant proteases that have been directly or indirectly linked to HR await characterisation. Our current knowledge of the process of HR consists

of various protease activities in different cell compartments of different plant species infected by different pathogens. These diverse pieces of the HR puzzle will hopefully be brought together over the coming years, thanks to the concerted efforts of the plant protease community.

Acknowledgements

We acknowledge financial support from the Spanish Ministry of Economy and Competitiveness with grant numbers RyC 2014-16158 and AGL2016-78002-R (NSC), and through the "Severo Ochoa Programme for Centres of Excellence in R&D" (SEV-2015-0533 and SEV-2015-0496). We also acknowledge financial support from an FPI fellowship from the Spanish Ministry of Education awarded to JSL. and by the CERCA Programme/Generalitat de Catalunya.

References

Armstrong MR, Whisson SC, Pritchard L, *et al*. 2005. An ancestral oomycete locus contains late blight avirulence gene *Avr3a*, encoding a protein that is recognized in the host cytoplasm. Proceedings of the National Academy of Sciences, USA **102,** 7766–7771.

Asqui SL, Vercammen D, Serrano I, Valls M, Rivas S, Van Breusegem F, Conlon FL, Dangl JL, Coll NS. 2018. AtSERPIN1 is an inhibitor of the metacaspase AtMC1-mediated cell death and autocatalytic processing in planta. New Phytologist **218,** 1156–1166.

Bozkurt TO, Schornack S, Win J, *et al*. 2011. *Phytophthora infestans* effector AVRblb2 prevents secretion of a plant immune protease at the haustorial interface. Proceedings of the National Academy of Sciences, USA **108,** 20832–20837.

Chichkova NV, Kim SH, Titova ES, Kalkum M, Morozov VS, Rubtsov YP, Kalinina NO, Taliansky ME, Vartapetian AB. 2004. A plant caspase-like protease activated during the hypersensitive response. Plant Cell **16,** 157–171.

Chichkova NV, Shaw J, Galiullina RA, *et al*. 2010. Phytaspase, a relocalisable cell death promoting plant protease with caspase specificity. EMBO Journal **29,** 1149–1161.

Coffeen WC, Wolpert TJ. 2004. Purification and characterization of serine proteases that exhibit caspase-like activity and are associated with programmed cell death in *Avena sativa*. The Plant Cell **16,** 857–873.

Coll NS, Epple P, Dangl JL. 2011. Programmed cell death in the plant immune system. Cell Death and Differentiation **18**, 1247–1256.

Coll NS, Vercammen D, Smidler A, Clover C, Van Breusegem F, Dangl JL, Epple P. 2010. Arabidopsis type I metacaspases control cell death. Science **330,** 1393–1397.

Curtis MJ, Wolpert TJ. 2004. The victorin-induced mitochondrial permeability transition precedes cell shrinkage and biochemical markers of cell death, and shrinkage occurs without loss of membrane integrity. The Plant Journal **38,** 244–259.

del Pozo O, Lam E. 1998. Caspases and programmed cell death in the hypersensitive response of plants to pathogens. Current Biology **8,** 1129–1132.

Dixon MS, Golstein C, Thomas CM, van der Biezen EA, Jones JDG. 2000. Genetic complexity of pathogen perception by plants: the example of *Rcr3*, a tomato gene required specifically by *Cf-2*. Proceedings of the National Academy of Sciences, USA **97,** 8807–8814.

Du Y, Stegmann M, Misas Villamil JC. 2016. The apoplast as battleground for plant–microbe interactions. New Phytologist **209,** 34–38.

Galluzzi L, Vitale I, Aaronson SA, *et al*. 2018. Molecular mechanisms of cell death: recommendations of the Nomenclature Committee on Cell Death 2018. Cell Death and Differentiation **25,** 486–541.

Gibson CM. 1904. Notes on infection experiments with various uredineae. New Phytologist **3,** 184–191.

Gilroy EM, Hein I, van der Hoorn R, *et al*. 2007. Involvement of cathepsin B in the plant disease resistance hypersensitive response. The Plant Journal **52,** 1–13.

González IJ, Desponds C, Schaff C, Mottram JC, Fasel N. 2007. *Leishmania major* metacaspase can replace yeast metacaspase in programmed cell death and has arginine-specific cysteine peptidase activity. International Journal for Parasitology **37,** 161–172.

Guicciardi ME, Miyoshi H, Bronk SF, Gores GJ. 2001. Cathepsin B knockout mice are resistant to tumor necrosis factor-alpha-mediated hepatocyte apoptosis and liver injury: implications for therapeutic applications. The American Journal of Pathology **159,** 2045–2054.

Hatsugai N, Iwasaki S, Tamura K, Kondo M, Fuji K, Ogasawara K, Nishimura M, Hara-Nishimura I. 2009. A novel membrane fusion-mediated plant immunity against bacterial pathogens. Genes & Development **23,** 2496–2506.

Hatsugai N, Kuroyanagi M, Yamada K, Meshi T, Tsuda S, Kondo M, Nishimura M, Hara-Nishimura I. 2004. A plant vacuolar protease, VPE, mediates virus-induced hypersensitive cell death. Science **305,** 855–858.

Jones JD, Dangl JL. 2006. The plant immune system. Nature **444,** 323–329.

Kingham PJ, Pocock JM. 2001. Microglial secreted cathepsin B induces neuronal apoptosis. Journal of Neurochemistry **76,** 1475–1484.

Kuroyanagi M, Yamada K, Hatsugai N, Kondo M, Nishimura M, Hara-Nishimura I. 2005. Vacuolar processing enzyme is essential for mycotoxin-induced cell death in *Arabidopsis thaliana*. The Journal of Biological Chemistry **280,** 32914–32920.

López-Otín C, Bond JS. 2008. Proteases: multifunctional enzymes in life and disease. The Journal of Biological Chemistry **283,** 30433–30437.

Lorang J, Kidarsa T, Bradford CS, Gilbert B, Curtis M, Tzeng SC, Maier CS, Wolpert TJ. 2012. Tricking the guard: exploiting plant defense for disease susceptibility. Science **338,** 659–662.

Lozano-Torres JL, Wilbers RHP, Gawronski P, *et al*. 2012. Dual disease resistance mediated by the immune receptor Cf-2 in tomato requires a common virulence target of a fungus and a nematode. Proceedings of the National Academy of Sciences, USA **109,** 10119–10124.

Marryat DCE. 1907. Notes on the infection and histology of two wheats immune to the attacks of *Puccinia glumarum*, yellow rust. Journal of Agricultural Science **2,** 129-U125.

McLellan H, Gilroy EM, Yun BW, Birch PR, Loake GJ. 2009. Functional redundancy in the *Arabidopsis Cathepsin B* gene family contributes to basal defence, the hypersensitive response and senescence. New Phytologist **183,** 408–418.

Minina EA, Coll NS, Tuominen H, Bozhkov PV. 2017. Metacaspases versus caspases in development and cell fate regulation. Cell Death and Differentiation **24,** 1314–1325.

Misas-Villamil JC, Toenges G, Kolodziejek I, Sadaghiani AM, Kaschani F, Colby T, Bogyo M, van der Hoorn RA. 2013. Activity profiling of vacuolar processing enzymes reveals a role for VPE during oomycete infection. The Plant Journal **73,** 689–700.

Misas-Villamil JC, van der Hoorn RA, Doehlemann G. 2016. Papain-like cysteine proteases as hubs in plant immunity. New Phytologist **212,** 902–907.

Mur LA, Kenton P Lloyd A, Ougham H, Prats E. 2008. The hypersensitive response; the centenary is upon us but how much do we know? Journal of Experimental Botany **59**, 501–520.

Navarre DA, Wolpert TJ. 1999. Victorin induction of an apoptotic/senescence-like response in oats. The Plant Cell **11,** 237–249.

Rawlings ND, Barrett AJ, Thomas PD, Huang X, Bateman A, Finn RD. 2018. The *MEROPS* database of proteolytic enzymes, their substrates and inhibitors in 2017 and a comparison with peptidases in the PANTHER database. Nucleic Acids Research **46,** D624–D632.

Rooney HC, Van't Klooster JW, van der Hoorn RA, Joosten MH, Jones JD, de Wit PJ. 2005. Cladosporium Avr2 inhibits tomato Rcr3 protease required for Cf-2-dependent disease resistance. Science **308,** 1783–1786.

Shabab M, Shindo T, Gu C, Kaschani F, Pansuriya T, Chintha R, Harzen A, Colby T, Kamoun S, van der Hoorn RA. 2008. Fungal effector protein AVR2 targets diversifying defense-related Cys proteases of tomato. The Plant Cell **20,** 1169–1183.

Song J, Win J, Tian MY, Schornack S, Kaschani F, Ilyas M, van der Hoorn RAL, Kamoun S. 2009. Apoplastic effectors secreted by two unrelated eukaryotic plant pathogens target the tomato defense protease Rcr3. Proceedings of the National Academy of Sciences, USA **106,** 1654–1659.

Stakman EC. 1915. Relation between *Puccinia graminis* and plants highly resistant to its attack. Journal of Agricultural Research **4,** 193–199.

Thomas EL, van der Hoorn RAL. 2018. Ten prominent host proteases in plant–pathogen interactions. International Journal of Molecular Sciences **19,** 639.

Tinland B, Schoumacher F, Gloeckler V, Bravoangel AM, Hohn B. 1995. the *Agrobacterium tumefaciens* virulence D2 protein is responsible for precise integration of T-DNA into the plant genome. EMBO Journal **14,** 3585–3595.

Tsiatsiani L, Van Breusegem F, Gallois P, Zavialov A, Lam E, Bozhkov PV. 2011. Metacaspases. Cell Death and Differentiation **18,** 1279–1288.

Turk B. 2006. Targeting proteases: successes, failures and future prospects. Nature Reviews Drug Discovery **5,** 785–799.

Ustun S, Sheikh A, Gimenez-Ibanez S, Jones A, Ntoukakis V, Bornke F. 2016. The proteasome acts as a hub for plant immunity and is targeted by *Pseudomonas* type III effectors. Plant Physiology **172,** 1941–1958.

van der Hoorn RAL. 2008. Plant proteases: from phenotypes to molecular mechanisms. Annual Review of Plant Biology **59,** 191–223.

van der Hoorn RA, Kaiser M. 2012. Probes for activity-based profiling of plant proteases. Physiologia Plantarum **145,** 18–27.

van der Hoorn RA, Kamoun S. 2008. From Guard to Decoy: a new model for perception of plant pathogen effectors. The Plant Cell **20,** 2009–2017.

van Doorn WG, Beers EP, Dangl JL, *et al*. 2011. Morphological classification of plant cell deaths. Cell Death and Differentiation **18,** 1241–1246.

Vartapetian AB, Tuzhikov AI, Chichkova NV, Taliansky M, Wolpert TJ. 2011. A plant alternative to animal caspases: subtilisin-like proteases. Cell Death and Differentiation **18,** 1289–1297.

Vercammen D, van de Cotte B, De Jaeger G, Eeckhout D, Casteels P, Vandepoele K, Vandenberghe I, Van Beeumen J, Inzé D, Van Breusegem F. 2004. Type II metacaspases Atmc4 and Atmc9 of *Arabidopsis thaliana* cleave substrates after arginine and lysine. The Journal of Biological Chemistry **279,** 45329–45336.

Ward HM. 1902. On the relations between host and parasite in the Bromes and their Brown Rust, *Puccinia dispersa* (Erikss.). Annals of Botany **16,** 233–315.

Watanabe N, Lam E. 2005. Two Arabidopsis metacaspases AtMCP1b and AtMCP2b are arginine/lysine-specific cysteine proteases and activate apoptosis-like cell death in yeast. The Journal of Biological Chemistry **280,** 14691–14699.

Watanabe N, Lam E. 2011. Arabidopsis metacaspase 2d is a positive mediator of cell death induced during biotic and abiotic stresses. The Plant Journal **66,** 969–982.

Yao C, Wu Y, Nie H, Tang D. 2012. RPN1a, a 26S proteasome subunit, is required for innate immunity in Arabidopsis. The Plant Journal **71,** 1015–1028.

Zhang H, Dong S, Wang M, Wang W, Song W, Dou X, Zheng X, Zhang Z. 2010. The role of vacuolar processing enzyme (VPE) from *Nicotiana benthamiana* in the elicitor-triggered hypersensitive response and stomatal closure. Journal of Experimental Botany **61,** 3799–3812.

Zimmermann P, Hirsch-Hoffmann M, Hennig L, Gruissem W. 2004. GENEVESTIGATOR. Arabidopsis microarray database and analysis toolbox. Plant Physiology **136,** 2621–2632.

2. OBJECTIVES

The main objectives of my PhD thesis are presented below.

OBJECTIVE 1

Identify robust transcriptional indicators of immune-cell death through spatiotemporal transcriptome analyses in *Arabidopsis thaliana*

OBJECTIVE 2

Identify the role of metacaspase 1 (*At*MC1) in plant immunity through genetic, biochemical and cell biology studies of autoimmune mutants

OBJECTIVE 3

Express, isolate, and characterize recombinant *At*MC1

3. RESULTS/RESEARCH ARTICLES

CHAPTER 1

Robust transcriptional indicators of plant immune cell death revealed by spatio-temporal transcriptome analyses

(Publication 3)

Molecular Plant
Resource Article

CellPress
Partner Journal

Robust transcriptional indicators of immune cell death revealed by spatiotemporal transcriptome analyses

Jose Salguero-Linares[1,5,8], Irene Serrano[2,6,8], Nerea Ruiz-Solani[1], Marta Salas-Gómez[1], Ujjal Jyoti Phukan[1], Victor Manuel González[1], Martí Bernardo-Faura[1], Marc Valls[1,2], David Rengel[2,3,7,8,*] and Nuria S. Coll[1,4,8,*]

[1]Centre for Research in Agricultural Genomics (CRAG), CSIC-IRTA-UAB-UB, Campus UAB, Bellaterra, 08193 Barcelona, Spain

[2]LIPM, Université de Toulouse, INRA, CNRS, 84195 Castanet-Tolosan, France

[3]INRAE, GeT-PlaGe, Genotoul, 31326 Castanet-Tolosan, France

[4]Department of Genetics, Universitat de Barcelona, 08028 Barcelona, Spain

[5]Consejo Superior de Investigaciones Científicas (CSIC), Barcelona, Spain

[6]Present address: Department of Plant Molecular Biology and Physiology, Albrecht von Haller Institute for Plant Sciences, University of Göttingen, Julia-Lermontowa-Weg 3, 37077 Göttingen, Germany

[7]Present address: Institut de Pharmacologie et de Biologie Structurale, IPBS, Université de Toulouse, CNRS, UPS, BP 64182, 205 route de Narbonne, 31077 Toulouse Cedex 04, France

[8]These authors contributed equally to this article

***Correspondence: David Rengel (david.rengel@ipbs.fr), Nuria S. Coll (nuria.sanchez-coll@cragenomica.es)**

https://doi.org/10.1016/j.molp.2022.04.010

ABSTRACT

Recognition of a pathogen by the plant immune system often triggers a form of regulated cell death traditionally known as the hypersensitive response (HR). This type of cell death occurs precisely at the site of pathogen recognition, and it is restricted to a few cells. Extensive research has shed light on how plant immune receptors are mechanistically activated. However, two central key questions remain largely unresolved: how does cell death zonation take place, and what are the mechanisms that underpin this phenomenon? Consequently, *bona fide* transcriptional indicators of HR are lacking, which prevents deeper insight into its mechanisms before cell death becomes macroscopic and precludes early or live observation. In this study, to identify the transcriptional indicators of HR we used the paradigmatic *Arabidopsis thaliana–Pseudomonas syringae* pathosystem and performed a spatiotemporally resolved gene expression analysis that compared infected cells that will undergo HR upon pathogen recognition with bystander cells that will stay alive and activate immunity. Our data revealed unique and time-dependent differences in the repertoire of differentially expressed genes, expression profiles, and biological processes derived from tissue undergoing HR and that of its surroundings. Furthermore, we generated a pipeline based on concatenated pairwise comparisons between time, zone, and treatment that enabled us to define 13 robust transcriptional HR markers. Among these genes, the promoter of an uncharacterized AAA-ATPase was used to obtain a fluorescent reporter transgenic line that displays a strong spatiotemporally resolved signal specifically in cells that will later undergo pathogen-triggered cell death. This valuable set of genes can be used to define cells that are destined to die upon infection with HR-triggering bacteria, opening new avenues for specific and/or high-throughput techniques to study HR processes at a single-cell level.

Key words: *Arabidopsis thaliana*, cell death indicator, effector-triggered immunity, hypersensitive response, pattern-triggered immunity, plant immunity, *Pseudomonas syringae*

Salguero-Linares J., Serrano I., Ruiz-Solani N., Salas-Gómez M., Phukan U.J., González V.M., Bernardo-Faura M., Valls M., Rengel D., and Coll N.S. (2022). Robust transcriptional indicators of immune cell death revealed by spatiotemporal transcriptome analyses. Mol. Plant. **15**, 1059–1075.

Published by the Molecular Plant Shanghai Editorial Office in association with Cell Press, an imprint of Elsevier Inc., on behalf of CSPB and CEMPS, CAS.

INTRODUCTION

Plants are rich sources of nutrients for pathogens with contrasting lifestyles (Dangl et al., 2013). As opposed to animals, plants do not possess a circulatory system with mobile cells specialized in pathogen defense (Jones and Dangl, 2006). Because their cells are fixed by their cell walls, plants rely on each cell's autonomous immunity and on systemic signals emanating from infection sites to distal cells to prime the plant for future pathogen encounters (Ausubel, 2005). Instead of a somatic adaptive immune system that produces antigen receptors on demand, plant cells are equipped with extracellular pattern recognition receptors and intracellular nucleotide-binding leucine-rich repeat immune receptors (NLRs) that recognize microbe-associated microbial patterns and pathogen effectors required for virulence, respectively (Couto and Zipfel, 2016). Pattern recognition receptor activation brings about a broad defense response called pattern-triggered immunity (PTI), whereas NLR activation triggers a potentiated and prolonged immune response called effector-triggered immunity (ETI) that reinforces defense outputs observed during PTI (Yuan et al., 2021a; Ngou et al., 2021b). ETI often culminates in macroscopic localized cell death at the attempted pathogen ingress site, known as hypersensitive response (HR) cell death or immune-related cell death (Olvera-Carrillo et al., 2015; Balint-Kurti, 2019; Salguero-Linares and Coll, 2019).

Regulated cell death has a crucial role in animal and plant immune responses. Extensive research in the animal field supports the notion that the immune system is highly dependent on cell death for a robust and tightly controlled immune response to occur (Lu et al., 2014; Nagata and Tanaka, 2017). In plants, our knowledge about the biochemical and genetic pathways regulating cell death, particularly in the context of immunity, is still very limited. To shed light on how HR is orchestrated in plants, most efforts have been directed towards understanding how NLRs are mechanistically activated and identifying molecular components upstream or downstream of NLRs that are required for HR to occur (Wang et al., 2019a, 2019b; Dangl and Jones, 2019; Ma et al., 2020; Ngou et al., 2021a).

Plant NLRs can be broadly classified into TNLs (toll/interleukin receptor-nucleotide binding site-type leucine rich-repeat) and CNLs (coiled coil domain-nucleotide binding site-type leucine rich-repeat)based on their domain composition; TNLs contain a Toll/interleukin-1 receptor, whereas CNLs harbor a coiled-coiled domain at their N-terminal end (Jones et al., 2016). Groundbreaking research has shown that, in plants, pathogen perception leads to NLR oligomerization, which ultimately results in cell death and immunity (Wang et al., 2019a, 2019b; Ma et al., 2020; Förderer et al., 2022). Oligomerized forms of CNLs can form pores at the plasma membrane that act as Ca^{2+}-permeable channels (Wang et al., 2019a, 2019b; Jacob et al., 2021). Some TNLs, in turn, can oligomerize upon activation to reconstitute a holoenzyme that triggers cell death by a mechanism that is not fully elucidated but may involve their nicotinamide adenine dinucleotide^{+} hydrolase and their 2′,3′-cyclic adenosine/guanosine monophosphate synthetase activities (Ma et al., 2020; Martin et al., 2020; Yu et al., 2021). How oligomerization translates to immune signaling and HR remains to be defined.

In the context of signaling downstream NLR activation or ETI, large-scale transcriptional studies have highlighted the importance of phytohormone networks for high-amplitude transcriptional reprogramming to mount a fast and efficient response (Mine et al., 2018). Comparisons of host transcriptional responses elicited by PTI and ETI suggest minor qualitative differences in the repertoire of differentially expressed genes (Navarro et al., 2004; Mine et al., 2018). These studies also support the recently evidenced assumption that ETI and PTI share immune signaling components (Yuan et al., 2021a; Ngou et al., 2021b; Pruitt et al., 2021). However, a central key question remains unexplored: which early transcriptional signatures differentiate cells that recognize the pathogen and will undergo HR from bystander cells that will remain alive and will activate defenses to fight the pathogen? A few studies underscore the importance of zonation during HR (Betsuyaku et al., 2018; Giolai et al., 2019; Lukan et al., 2020). At the hormonal level, it has been shown that salicylic acid (SA) plays a major role at pathogen-inoculated spots that will later undergo HR, whereas the jasmonic acid (JA) signaling pathway is activated in cells surrounding the central SA-active cells (Dorey et al., 1997; Betsuyaku et al., 2018). Precision transcriptomics during the immune response elicited by the potato Ny-1 gene against potato virus Y revealed the importance of SA accumulation and genes involved in generation of reactive oxygen species for efficient confinement of macroscopic cell death lesions caused by potato virus Y (Lukan et al., 2020). The cell wall polymer lignin has also been shown to participate in HR zonation by forming a physical barrier around the infection site upon pathogen recognition that presumably contributes to confining the invading agents and restricting colonization (Lee et al., 2019). A transcriptional meta-analysis of developmental versus HR cell death in plants could only reveal robust indicators of developmental cell death but not HR cell death (Olvera-Carrillo et al., 2015). We realized that the limitation of previous large-scale transcriptomic analyses lacked the spatial dimension of HR (Lewis et al., 2015; Mine et al., 2018) because dying cells were not compared with bystander cells, and the focus was not on identifying specific cell death markers but, rather, on bulk-analyzing the ETI response at the inoculated area.

A systematic gene expression analysis of the zonation of HR overtime would help us to understand the process of HR at the molecular level and, importantly, would allow definition of *bona fide* transcriptional markers of the process. With this purpose, we generated RNA sequencing (RNA-seq) data to systematically analyze and compare the transcriptional programs taking place at the zone of inoculation/pathogen recognition that will undergo HR versus the surrounding area that will stay alive and activate immunity. We show unique and time-dependent differences in the repertoire of differentially expressed genes (DEGs) and expression profiles derived from tissue undergoing HR and that of its surrounding tissues. We generated a pipeline based on pairwise comparisons between time, zone, and treatment that enabled us to define 13 robust transcriptional HR markers and a fluorescent transgenic

reporter line. These valuable sets of genes can be used to define cells that are destined to die upon pathogen recognition before onset of cell death becomes macroscopically visible, opening new methods to study the involved processes by live, cell-specific, and/or high-throughput techniques.

RESULTS

Zonally dissected *Arabidopsis* transcriptomes upon *Pto AvrRpm1* infection reveal unique spatiotemporal gene expression

In our experiments, we used the paradigmatic interaction between *Arabidopsis thaliana* Col-0 (hereafter *Arabidopsis*) and the bacterial pathogen *Pseudomonas syringae* pathovar tomato (*Pto*) carrying the effector *AvrRpm1* (hereafter *Pto AvrRpm1*), which triggers restricted HR at the site of inoculation upon recognition by the CNL RPM1 (RESISTANCE TO PSEUDOMONAS SYRINGAE PV MACULICOLA 1) (Mackey et al., 2002). To zonally dissect HR and its surroundings, we syringe-infiltrated a limited area (roughly 3–4 mm) at the side edge of *Arabidopsis* leaves with a mock solution or *Pto AvrRpm1*. Collected tissue from this area was designated as the "IN" zone. To ensure proper separation between IN and OUT zones, a buffer zone expanding 1 mm next to the IN area was discarded, and a parallel region expanding 1–2 mm toward the vein was designated as "OUT" (Figure 1A). We collected tissue 0, 1, 2, 4 and 6 h post-inoculation (hpi), extracted RNA, and assessed transcript abundance by RNA-seq. Under these conditions, macroscopic cell death started to appear at 4 hpi in the *Pto AvrRpm1*-inoculated samples, as visualized by trypan blue staining (Figure 1B). As expected, this cell death is concomitant with a dramatic drop in photosynthetic efficiency of photosystem II (Fv (variable fluorescence)/maximum fluorescence in the dark-adapted state [Fm] ratio) and electron transport rate (ETR) at the IN area (Figure 1C; Berger et al., 2007).

To determine whether the obtained RNA-seq data complied with our working hypothesis of spatiotemporal gene expression regulation, we performed a principal-component analysis (PCA) (Supplemental Figure 1A and 1B). We observed that, at the IN area, *Pto AvrRpm1*-treated samples separated from their mock controls from 2 hpi onward. At the OUT area, however, only *Pto AvrRpm1*-treated samples at 4 and 6 hpi separated from mock controls. Overall, the PCA confirms that the biggest changes in gene expression are produced at IN, particularly at 4 and 6 hpi, whereas at OUT, there is a subtler modulation that is most pronounced at 4 hpi.

Next we identified DEGs between bacteria and mock-inoculated samples (DEGs; false discovery rate [FDR] < 0.05 and $|\log2FC| > 2$), characterizing the transcriptional changes occurring at each tissue area at every time point. We found a total of 5495 DEGs at the IN zone and 1785 at the OUT zone (Figure 2A; Supplemental Table 1). Enrichment of Gene Ontology (GO) terms was examined in every group of DEGs at each specific time point (Supplemental Figure 2; Supplemental Table 2). Upregulated genes at the IN area were enriched in immunity- and phytohormone-associated processes (Supplemental Figure 2A). Immunity-related GO terms associated with PTI and ETI, such as "plant-type hypersensitive response" and "pattern recognition receptor signaling pathway," appeared at initial stages of infection (1 and 2 hpi), whereas at later stages (from 2 hpi onwards), there is enrichment of GO terms associated with more general defense and abiotic stress processes, such as "defense response to bacteria" and "response to wounding," respectively (Supplemental Figure 2A). Regarding phytohormone-related processes, we observed an enrichment in SA-related GO terms from 1 hpi onward, confirming the importance of SA at the HR/IN area (Dorey et al., 1997; Zheng et al., 2015). In contrast, GO terms associated with JA were particularly overrepresented at later time points (4 and 6 hpi), in accordance with previous findings demonstrating that SA can activate JA signaling through a non-canonical pathway promoting ETI (Liu et al., 2016). GO terms related to other defense/stress-related phytohormones, such as ethylene and abscisic acid, were also enriched at 4 and 6 hpi (Supplemental Figure 2A).

Among downregulated genes at the IN zone, an enrichment in GO terms related to photosynthesis and chloroplast biology occurred at late time points (4 and 6 hpi) (Supplemental Figure 2B). This correlates with the drop in photosynthetic efficiency shown in Figure 1C, which is part of the defense/yield trade-off to derive resources for immune responses and shut down production of sugars and nutrients because they might serve as a source for pathogen survival and multiplication (Lu and Yao, 2018).

Strikingly, at the OUT area, we only observed differential expression at late time points (4 and 6 hpi), with an overall reduction in the number of DEGs compared with the IN area (Figure 2A). Upregulated genes were enriched in GO terms associated with hormonal regulation, particularly the JA signaling pathway (Supplemental Figure 2C). Downregulated genes at the OUT area did not show any enriched GO term, possibly because of the low number of genes.

To identify genes exclusively upregulated (FDR <0.05 and $|\log2FC| > 2$) at the IN or OUT areas, we first generated Venn diagrams representing the number of genes modulated at each time point upon infection (Figure S3). This analysis confirmed that upregulation at IN and OUT mainly occurs at 4 or 6 hpi (Figure S3); therefore, we selected these two time points to identify genes that are exclusively upregulated at each tissue area (Figure 2B). Specifically, we found a total of 1840 genes being upregulated exclusively at IN, 1117 genes upregulated at IN and OUT, and 221 genes being exclusively upregulated at OUT (Figure 2B; Supplemental Table 3). Among the overrepresented GO terms found in genes exclusive to the IN area were "defense response to bacterium," "response to molecule of bacterial origin," and "response to salicylic acid." We also found various GO terms associated with responses to several other stresses, such as salt, oxygen-containing compounds, sulfur compounds, heat, and hydrogen peroxide (Figure 2C; Supplemental Table 4), which is not surprising considering that the tissue is undergoing cell death. In contrast, overrepresented GO terms in genes exclusively upregulated at the OUT area included "regulation of defense response" and, interestingly, "response to wounding" and "response to jasmonic acid" (Figure 2C; Supplemental Table 4). These JA-related genes follow a very distinct expression pattern with an

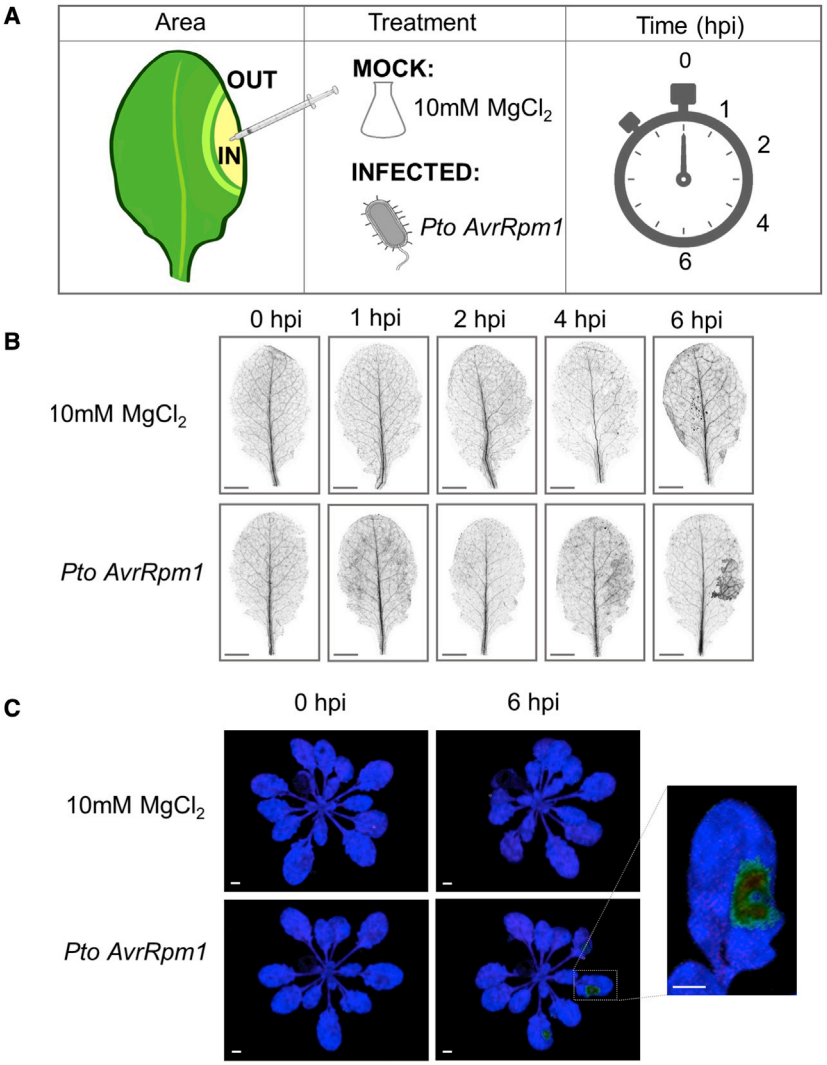

Figure 1. HR in plants can be spatiotemporally dissected.

(A) Experimental design of the study. A limited area (3–4 mm) at the side edge of 4-week-old *A. thaliana* Col-0 leaves was syringe infiltrated with *Pto AvrRpm1* at 2.5×10^7 CFU/ml (infected) or a 10 mM $MgCl_2$ solution (mock), and samples were collected at 5 different time points after infection: 0, 1, 2, 4 and 6 hpi. Upon infiltration, the edge of the infiltrated area was marked, and the total area infiltrated was designated IN. A 1-mm buffer zone right next to the IN zone ensured proper separation between the IN and OUT area, which was the parallel region that expanded from the edge of the buffer zone to 1–2 mm toward the vein. Three biological replicates per area, treatment, and time point were collected and subjected to RNA-seq analysis.

(B) Analysis of macroscopic cell death upon infection with *Pto AvrRpm1* or 10 mM $MgCl_2$ solution. Leaves were infected as described in **(A)** and subsequently stained with trypan blue. Scale bar, 3 mm.

(C) Representative images of mock- or *Pto AvrRm1*-treated plants subjected to pulse amplitude modulation (PAM) chlorophyll fluorescence measurement to monitor photosynthesis. Scale bar, 3 mm. Photosynthetic efficiency (Fv/Fm ratio) and electron transport rate (ETR) were measured in the infiltrated area (IN) and the neighboring tissue (OUT). Measurements were taken at 0, 1, 2, 4, and 6 hpi. Results are representative of 6 different measurements of each tissue area from 6 different plants. Letters indicate statistically significant differences in Fv/Fm ratio or ETR values following a two-way analysis of variance (ANOVA) with Tukey's honestly-significant-difference (HSD) test ($\alpha = 0.05$). Exact p values are provided in Supplemental Table 5.

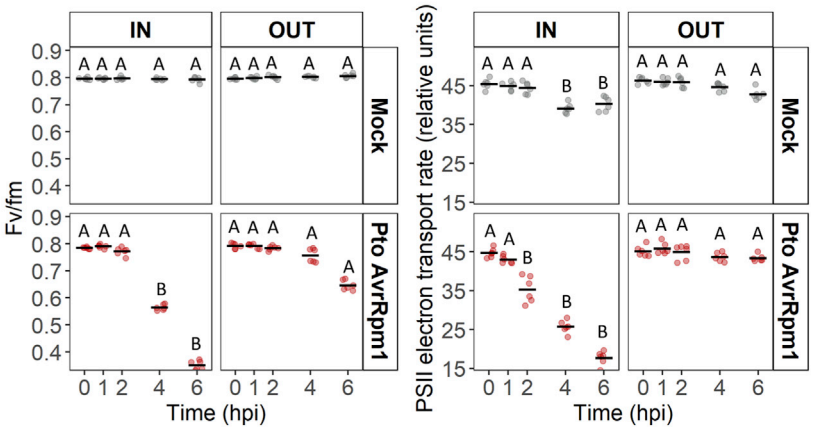

early peak at 1 hpi at the IN and OUT areas and a second peak at 4 hpi of higher intensity in the OUT zone (Supplemental Figure 5; Supplemental Table 4). Although further experimental validation would be required, these data reveal expression patterns of a set of genes that could potentially be used as OUT markers along with previously reported markers, such as VSP1 (Chung et al., 2008; Betsuyaku et al., 2018). To better visualize the behavior of the remaining OUT-specific genes throughout the course of the infection, we generated heatmaps representing their differential expression at IN and OUT areas (Supplemental Figure 4).

Clustering of gene expression profiles reveals distinct expression patterns at the IN and OUT areas over time

Next we set out to determine whether genes at the IN and OUT areas followed specific expression patterns and whether particular biological processes were associated with those patterns. We first analyzed gene expression profiles using Fuzzy c-means, a soft partitioning algorithm that offers robust clustering with regard to noise by variation of a fuzzification parameter that limits the contribution of ill-behaved profiles to the clustering process (Olsen et al., 2006; Kumar and Futschik, 2007). Based on this, we could define three and five distinct and non-overlapping clusters for *Pto AvrRpm1*-treated samples in the IN and OUT areas, respectively (Figure 3; Supplemental Figure 8; Supplemental Tables 6 and

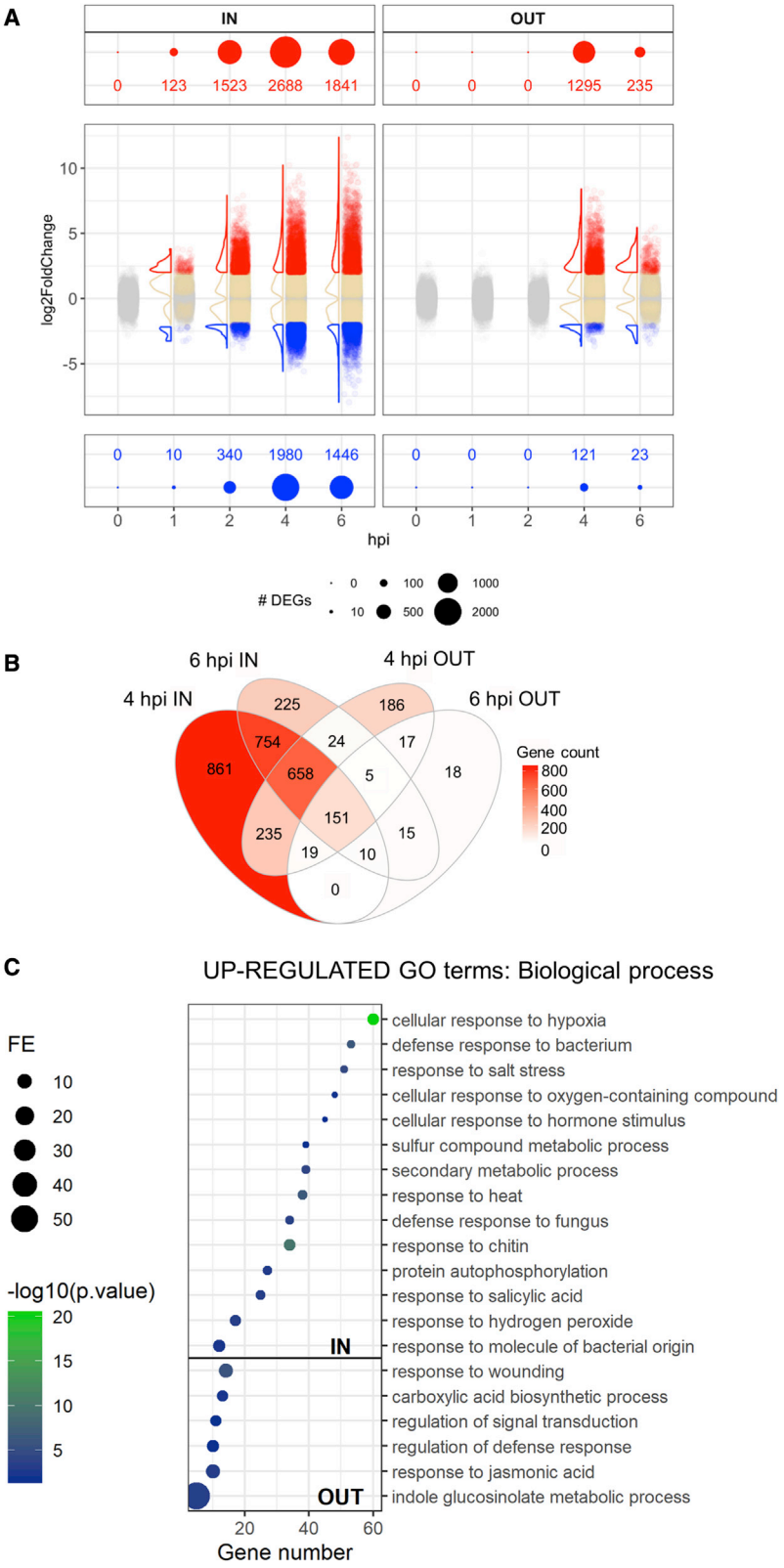

Figure 2. Spatiotemporal dynamics of the transcriptomes reveal time- and zone-dependent gene expression signatures upon infection.

(A) DEGs (FDR < 0.05 and |log2FC| > 2) in *Pto AvrRpm1*-infected plants compared with mock-treated plants at each time point at the IN (left) and OUT (right) areas. Red denotes upregulated genes, and blue indicates downregulated genes. Yellow indicates genes with an FDR of less than 0.05 but |log2FC| < 2, whereas gray indicates genes not complying with FDR or log2FC criteria.

(B and **C)** Genes exclusively upregulated (FDR <0.05 and log2FC > 2) at IN or OUT areas of infection at 4 and 6 hpi.

(B) Venn diagram showing sizes of gene sets that are upregulated (FDR < 0.05 and log2FC > 2) upon bacterial infection at 4 and/or 6 hpi at IN, OUT, or both areas.

(C) GO terms representing enriched biological processes derived from genes exclusively upregulated at IN or OUT areas at 4 and/or 6 hpi. The most specific term from each family term provided by PANTHER was plotted along with the corresponding gene number, fold enrichment (FE), and FDR (Bonferroni correction for multiple testing) represented as $\log_{10}$. Only GO terms with an FE above 2 and FDR below 0.05 were plotted.

7). Genes within each cluster were subsequently re-clustered in mock-treated samples, producing two distinct sub-clusters (Figure 3; Supplemental Figure 8; Supplemental Tables 6 and 7). This procedure provided a more detailed overview of the differences and similarities of trajectories between treatments over time and reflected the well-documented wound response that takes place in mock-treated tissue (Mine et al., 2018; Giolai et al., 2019; Vega-Munoz et al., 2020).

At the IN area of infection, cluster I exhibited a pattern of upregulation from 0–2 hpi and mild downregulation from 2–6 hpi (Figure 3A). Genes near its centroid (membership score value [MSV] > 0.7; see Methods) are mainly associated with immune-related GO terms (Supplemental Figure S6A; Supplemental Table 8). Genes in this cluster followed two distinct trajectories in the mock-treated samples. Mock sub-cluster 1.1 showed a steady increase throughout the experiment, and mock sub-cluster 1.2 exhibited a typical wounding immune-related response common in infected samples, peaking at 1 h and rapidly returning to steady-state levels (Savatin et al., 2014).

Cluster II-IN includes genes with a sharp increase in expression at 4 hpi (Figure 3A). Many of the genes following that trajectory are involved in protein degradation processes (autophagy, protein targeting to the vacuole, proteasome-mediated degradation) taking place in response to infection (Supplemental Figure S6A; Supplemental Table 8). Sub-clusters from mock-treated samples predominantly followed a similar steady trajectory throughout the experiment, which points to an infection-specific effect of upregulation on protein turnover because of infection at the IN area (Figure 3A; Supplemental Figure7A; Supplemental Table 10).

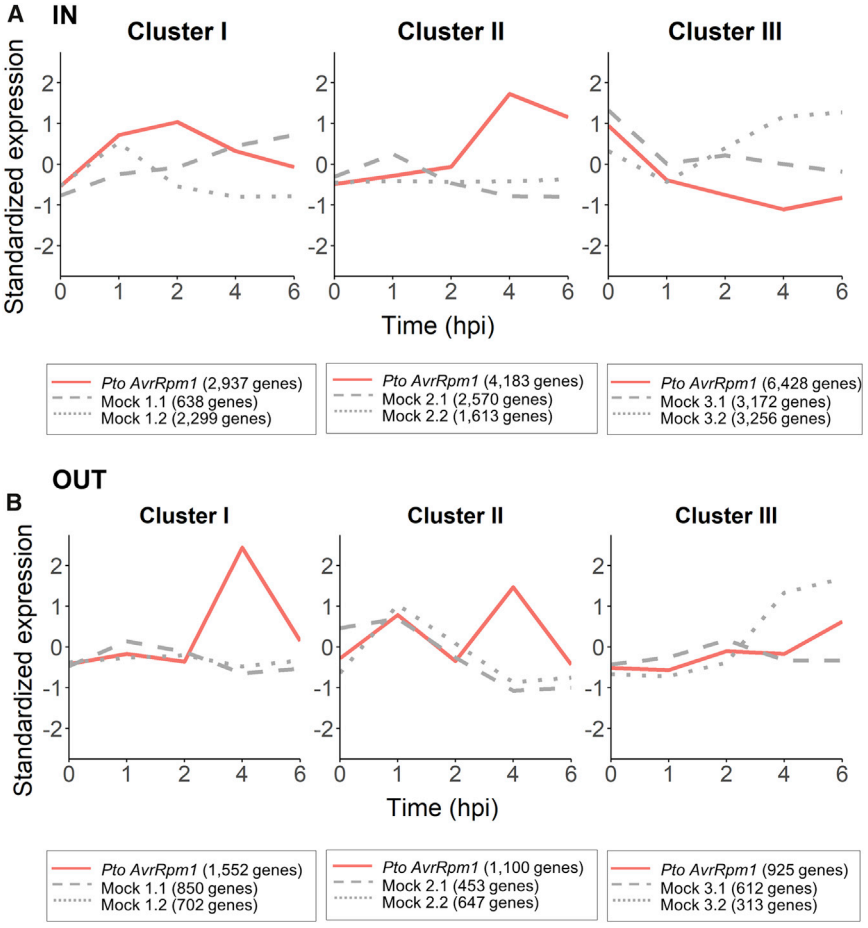

Figure 3. Gene expression profile clustering reveals three distinctive expression patterns at the IN and OUT areas of infection

(A and B) Non-overlapping clusters derived from *Pto AvrRpm1*- and mock-treated plants for IN **(A)** and OUT **(B)** areas. Standardized expression to *Z* scores (y axis) is calculated by subtracting the mean and normalizing to standard deviation. The trajectory that defines the overall expression profile of each cluster through the course of the infection is shown in red for *Pto AvrRpm1*-treated plants. Genes derived from *Pto AvrRpm1*-treated samples were re-clustered for mock-treated samples, and their trajectories are represented in gray. Because the expression profile of these genes in mock-treated samples was very distinct among the overall number of genes, they were divided into two sub-clusters represented as dotted or dashed gray lines. The number of genes that constitute each cluster is indicated below each cluster. Genes comprising each cluster along with their MSV can be found in Supplemental Tables 6 and 7.

Cluster III-IN exhibits an expression pattern of steady downregulation from 0–4 hpi, followed by a slight recovery of expression from 4–6 hpi (Figure 3A). This cluster includes mostly genes belonging to GO terms related to photosynthesis (Supplemental Figure 6A; Supplemental Table 8). In this case, mock-treated samples sub-cluster into two distinct patterns of expression. sub-cluster 3.1 follows a similar pattern as infected samples, and sub-cluster 3.2 shows a transient decrease of expression at 1 h, followed by a recovery phase from 2–6 hpi (Figure 3A). Our data show that only certain components of the photosynthetic machinery are specifically affected by the pathogen treatment (Supplemental Figures 6A and 7A; Supplemental Table 10).

At the OUT area of infection, cluster I includes genes that display a sharp peak of expression at 4 hpi (Figure 3B). From this cluster, genes near the centroid belong to GO terms associated with metabolism, hormonal regulation, and wounding response, among others (Supplemental Figure 6B; Supplemental Table 9). Interestingly, JA- and SA-responsive genes, which are known to act antagonistically and cooperatively during ETI (Liu et al., 2016; Betsuyaku et al., 2018), seem to be highly enriched in the OUT area. Genes comprising the mock-derived sub-clusters follow a similar trend of steady expression throughout the time course of the experiment, suggesting that the peak of high expression is a specific response to the bacterial infection in the surrounding area (Figure 3B; Supplemental Figure 7B; Supplemental Table 11).

Cluster II-OUT in *Pto AvrRpm1*-treated samples follows an expression pattern with two sharp upregulation peaks at 1 and 4 hpi (Figure 3B). These trajectories are followed by genes associated with JA-related processes and wounding, which is a very specific pattern exclusively found at the OUT zone (Figure 3; Supplemental Figure 6B; Supplemental Table 9). The early peak at 1 hpi shared between mock and infected samples could account for a wounding response elicited early at the area surrounding the syringe-infiltrated area, whereas the peak at 4 hpi appears as a late response that occurs specifically at the tissues surrounding the pathogen inoculation area (Figure 3; Supplemental Figure 6; Supplemental Table 11).

In cluster III-OUT, the trajectory of genes from *Pto AvrRpm1*-treated samples does not remarkably differ from mock treatment (Figure 3B). Genes that comprise this cluster mainly fall into GO terms associated with the photosynthetic machinery (Supplemental Figure 6B; Supplemental Table 9). These data indicate that photosynthesis at the OUT area of infection does not seem to be altered by pathogen infection as opposed to the IN area (Figure 3B; Supplemental Figures 6 and 7), correlating with the zonal photosynthesis efficiency values shown in Figure 1C and as reported previously (Berger et al., 2007).

Novel zonal HR transcriptional indicators can be elucidated from pairwise comparisons between time, treatment, and area

To identify robust HR markers that are exclusively upregulated at the site of cell death (IN area), we conducted a pipeline of differential expression analysis that consisted of concatenated

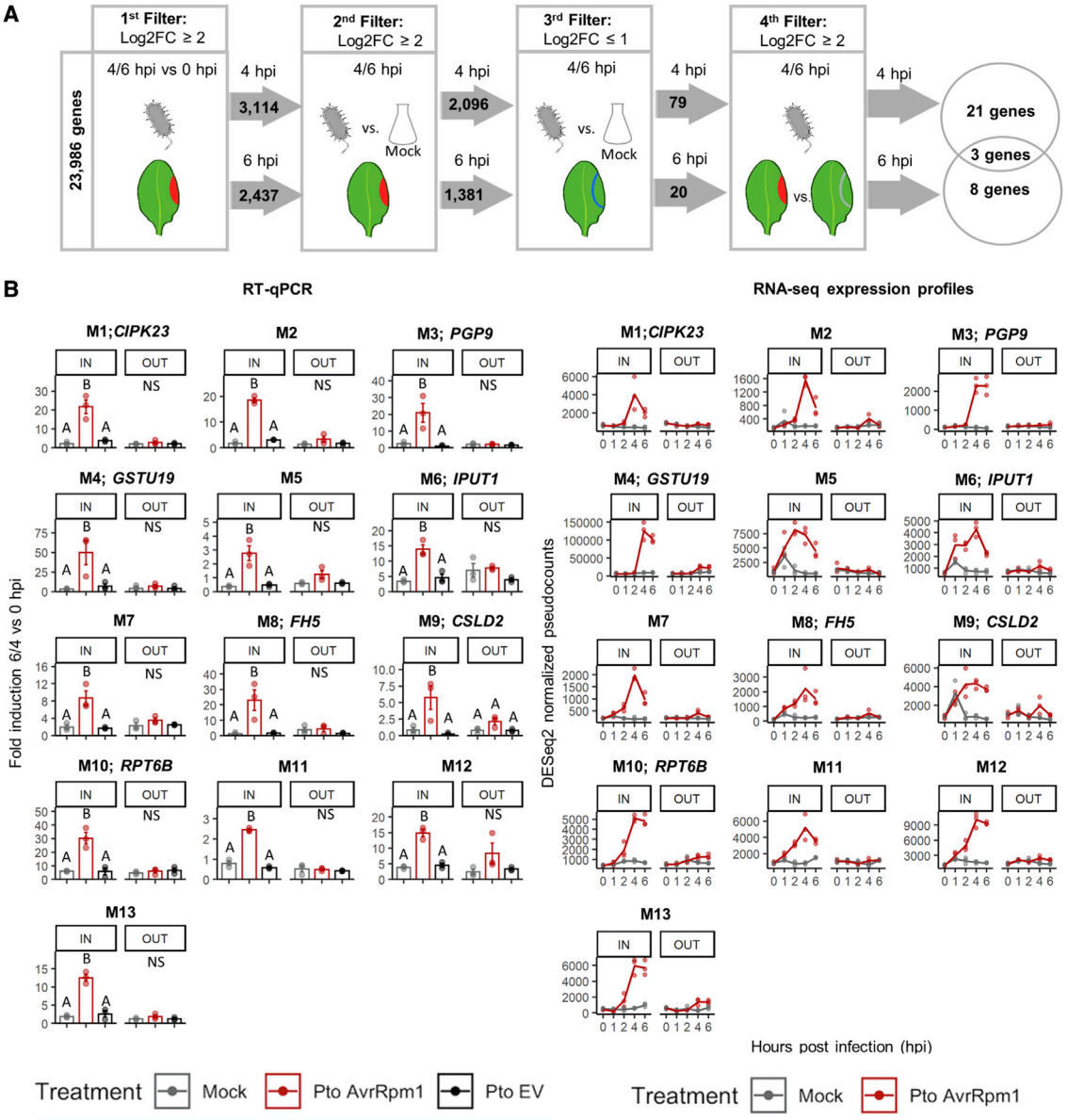

C

Marker ID	Gene ID	Gene	Description	Time point	Process
M1	AT1G30270	CIPK23	CBL-interacting serine/threonine-protein kinase 23	4 hpi	Ion transport PM
M2	AT1G79710		Probable folate-biopterin transporter 3	4 hpi	Cell detoxification
M3	AT4G18050	PGP9	P-glycoprotein 9	4 hpi	
M4	AT1G78380	GSTU19	Glutathione S-transferase U19	6 hpi	
M5	AT4G24160		1-acylglycerol-3-phosphate O-acyltransferase	4 hpi	Lipid metabolism
M6	AT5G18480	IPUT1	Inositol phosphorylceramide glucuronosyltransferase 1	4 hpi	
M7	AT4G30390		UDP-arabinopyranose mutase	4 hpi	Cell wall remodeling
M8	AT5G54650	FH5	Formin-like protein 5	4 hpi	
M9	AT5G16910	CSLD2	Cellulose synthase-like protein D2	6 hpi	
M10	AT5G20000	RPT6B	26S proteosome regulatory subunit 8 homolog B	4 hpi	Protein degradation
M11	AT2G36580		Pyruvate kinase	4 hpi	Uncharacterized
M12	AT5G56350		Pyruvate kinase	4/6 hpi	
M13	AT5G17760		AAA-ATPase	6 hpi	

Figure 4. Identification of HR markers specific for the IN area of infection.

(A) Schematic of the sequence of filters applied to identify indicators. Four filters were concatenated, considering the three variables of our experimental design: time, treatment, and tissue area. Briefly, in the first filter, we selected genes differentially upregulated from 0–4/6 hpi (FDR < 0.05 and log2FC > 2) at the IN area (red) upon bacterial infection. From the genes that passed this first filter, we selected those that were exclusively upregulated (FDR < 0.05 and log2FC > 2) because of bacterial infection at the IN area at 4/6 hpi. Subsequently, from the genes that made it into the third filter, we selected those

pairwise comparisons considering the three variables in our experimental design: time, treatment, and area (Figure 4A). Because the highest degree of differential expression between treatments took place at 4 and 6 hpi (Figure 2A), we carried out the comparisons at these two time points independently. First we focused on the time variable and selected genes that were confidently upregulated at the IN area of *Pto AvrRpm1*-infected plants at 4 and/or 6 hpi compared with 0 hpi (first filter: FDR < 0.05 and log2FC > 2). Then we removed genes also upregulated at 4 and/or 6 hpi at the IN area in mock controls (second filter: FDR < 0.05 and log2FC > 2). Because we aimed to find genes only upregulated at the IN/cell death area, we next removed genes that were upregulated by bacterial inoculation at the OUT area at least to half of the levels of the IN zone (third filter: FDR < 0.05 and log2FC < 1). Finally, from the genes that met those three criteria, we kept those that were differentially upregulated at the IN compared with the OUT area in *Pto AvrRpm1*-infected plants (fourth filter: FDR < 0.05 and log2FC > 2) (Figure 4A).

A total of 32 genes passed all 4 filters, constituting a set of potential HR indicators (Supplemental Figure 9). From these, 24 were extracted from the 4-hpi dataset, 11 from the 6-hpi dataset, and 3 from both time points (Supplemental Figure 9). Because of the stringency of the filters, none of these genes passed all filters at 1 or 2 hpi, although 7 of them were upregulated after infection at the IN zone at these early time points (M5, M6, M7, M8, M9, M11, and M12). The expression profiles of these putative HR indicators can be visualized as DESeq2 pseudocounts as a function of time at both areas of infection in Supplemental Figure 10. The expression patterns of these 32 genes at 0 and 4/6 hpi were validated by quantitative real-time PCR using newly obtained biological samples (Supplemental Figure 11). To ensure that the potential markers were exclusively upregulated as part of the HR response triggered by effector-mediated bacterial recognition and not as part of the defense responses triggered by disease-causing bacteria, we also included samples inoculated with *Pto* DC3000 empty vector (EV) (*Pto* EV), a strain that causes disease but does not trigger HR in *Arabidopsis* Col-0. Among the 32 genes tested, a total of 14 (10 of them at 4 hpi and 4 at 6 hpi, with one at both time points) behaved as *bona fide* HR indicators (Figure 4B and 4C), showing distinctive upregulation specifically triggered at the IN area by an HR-causing bacterium.

The *At5g17760* promoter specifically drives expression of GFP to the IN area of infection, constituting a robust transcriptional live marker of HR

To generate much-needed tools to extend our understanding of how HR unfolds at the infection site and its surrounding tissue, we generated stable transgenic *Arabidopsis* plants expressing green fluorescent protein (3×GFP) under control of the promoters of each of the 13 identified putative HR marker genes. A nuclear localization signal (NLS) was fused to GFP to concentrate the signal in the nucleus and facilitate detection, which enabled us to distinguish promoter-driven fluorescence from the autofluorescence derived from HR (Betsuyaku et al., 2018).

We focused our analysis on plants expressing *pAT5G17760:NLS-3xGFP* (corresponding to M13) because they showed high, cell-specific, robust, and clear GFP signals in the nuclei of the leaf regions infected with *Pto AvrRpm1* (Figure 5B; Supplemental Figure 12). In several independent transgenic lines, activation of *pAT5G17760* was limited to the syringe-infiltrated area and could not be detected in the surrounding tissue (Supplemental Figure 13). In all *pAT5G17760:NLS-3xGFP* marker lines, the GFP signal appeared concomitant with cell death, as shown by trypan blue staining (Figure 5B; Supplemental Figures 12 and 13). A clear GFP signal was not detected in all other marker lines tested.

In addition to *Pto AvrRpm1*, we also analyzed the response of *pAT5G17760:NLS-3xGFP* plants to *Pto* expressing *AvrRpt2* (*Pto AvrRpt2*), which induces HR in Col-0 plants via the CNL RESISTANT TO P. SYRINGAE 2 (RPS2) (Mackey et al., 2003) and to *Pto* expressing *AvrRps4 (Pto AvrRps4*), where HR is mediated by the TNL pair RPS4/RRS1 and requires helper NLRs (Gassmann et al., 1999; Narusaka et al., 2009). The same pattern was observed after infiltration with *Pto AvrRpt2* or *Pto AvrRps4* (Figure 5B), which indicates that *pAT5G17760* robustly responds to pathogen-mediated activation of different classes of NLR receptors. As controls, we included mock, *Pto* EV, and a non-pathogenic mutant strain secreting no effectors (*Pto hrcC*$^{-}$) (Alfano et al., 2000). Importantly, infiltration with the mock solution or with non-HR-causing bacterial strains did not activate *pAT5G17760*. For microscopy imaging experiments, we used a lower bacterial inoculum (optical density 600 [OD_{600}] 0.01) to mimic more natural infection conditions and delay the onset of HR and tissue collapse (Figure 5A), which was necessary for microscopic detection of GFP. At higher inoculum levels, rapid accumulation of phenolic compounds at the site of infection results in extremely high autofluorescence levels that hamper imaging.

Because pathogens with contrasting lifestyles can trigger HR or HR-like cell death in plants, we tested whether this reporter line can be employed in a broader sense. We infected adult *Arabidopsis* leaves by drop inoculation with *Botrytis cinerea*, a necrotrophic pathogen that kills plant tissue prior to feeding, using a range of toxic molecules (Muckenschnabel et al., 2002). At 3 days post-inoculation (dpi), we observed GFP expression in the nuclei of cells at the region inoculated with the pathogen as opposed to mock-inoculated plants (Supplemental Figure 14). Our observations indicate that *pAT5G17760* activity is spatially

that were not highly upregulated in the OUT area (blue) upon bacterial infection at 4/6 hpi (FDR < 0.05 and log2FC < 1). Finally, we applied a fourth filter to discard genes that could potentially be basally upregulated at the OUT area upon pathogen treatment at 4/6 hpi (FDR < 0.05 and log2FC > 2). The starting number of genes and the genes passing the different filtering criteria are indicated.

(B) Quantitative real-time PCR and RNA-seq expression profiles of marker genes that behave as *bona fide* HR indicators. Relative expression levels to the housekeeping gene *EIF4a* are represented as FE between 4/6 and 0 hpi. Error bars represent standard error of the mean from three independent experiments. Letters indicate statistically significant differences between treatments following one-way ANOVA with Tukey's HSD test ($\alpha = 0.05$) performed independently at IN and OUT. NS, non-significant after one-way ANOVA. Exact p values are provided in Supplemental Table 5.

(C) List of HR indicators along with their gene ID, gene name, and description.

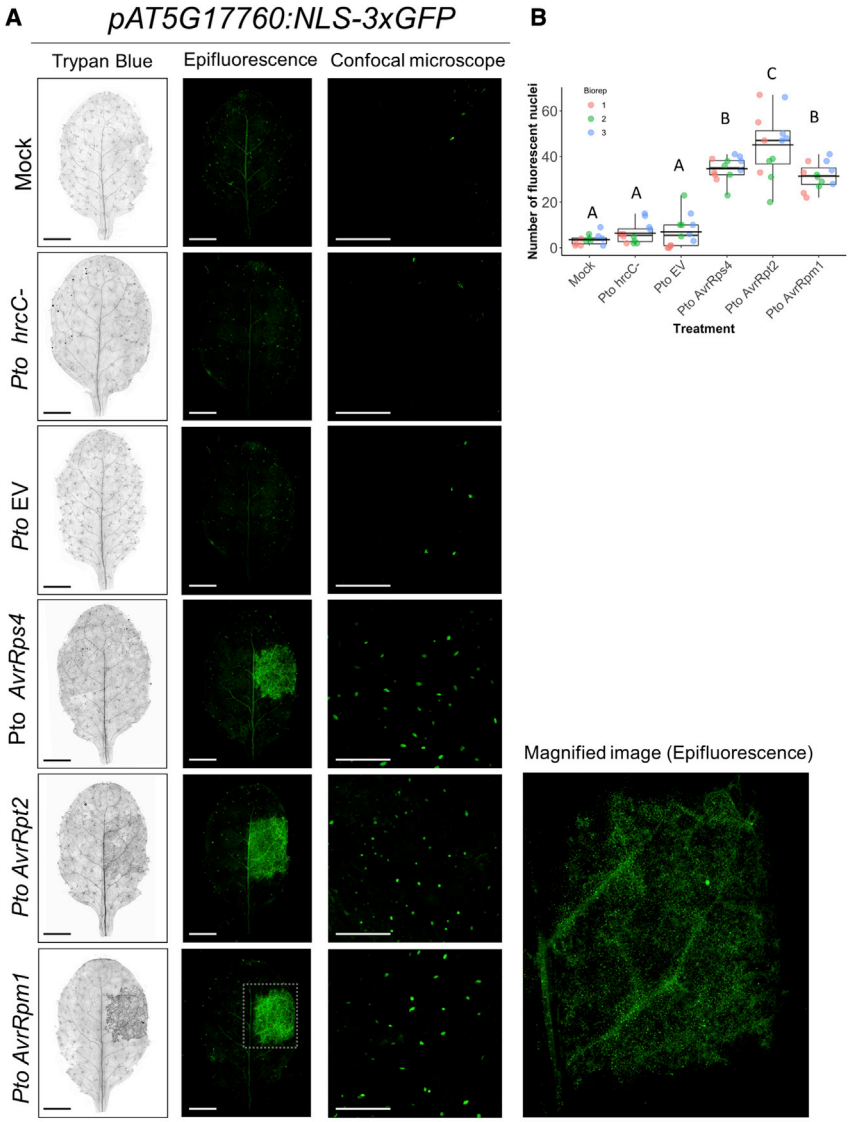

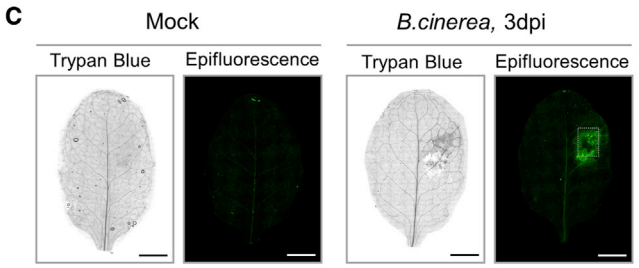

Figure 5. *AT5G17760* encodes an AAA-ATPase and is a reliable HR indicator specifically induced at the IN area by activation of different classes of NLR receptors.

(A) Representative images of trypan blue-stained leaves, epifluorescence microscopy, and confocal microscopy from *pAT5G17760:NLS-3xGFP Arabidopsis* transgenics. A small region of 4-week-old *pAT5G17760::NLS-3xGFP* leaves was syringe infiltrated with *Pto* expressing the effectors *AvrRpm1*, *AvrRpt2*, or *AvrRps4* at 1 × 10^7 CFU/ml (OD_{600} = 0.01). Besides mock treatment, the non-cell-death-causing bacterial strains *Pto* DC3000 EV and *Pto* DC3000 *hrcC*$^-$ were included as negative controls. Images were taken 16 hpi. Scale bar, 3 mm. Images were taken 16 hpi on a Leica DM6 microscope and a confocal microscope prior to trypan blue staining. Scale bar, 3 mm. Expression of p*AT5G17760* is detected as green dots corresponding to nuclei with a positive GFP signal. Scale bar, 100 μm. A representative magnified image of a *Pto AvrRpm1*-infected leaf expressing *pAT5G17760:NLS-3xGFP* at 16 hpi is also shown. Scale bar, 3 mm.

(B) Quantification of fluorescent nuclei from confocal microscopy pictures in **(A)**. Nucleus count was performed using ImageJ software. Data are representative of three independent experiments, each containing 4 leaves. Letters indicate statistically significant differences in the number of nuclei following one-way ANOVA with Tukey's HSD test (α = 0.05). Exact p values are provided in Supplemental Table 5.

(C) Activation of *pAT5G17760* occurred upon drop inoculation infection with the necrotrophic pathogen *B. cinerea* or a mock solution. Four- to five-week-old leaves from *pAT5G17760::*3xGFP transgenics were drop inoculated with *B. cinerea* at concentration of 1 × 10^5 spores/ml. Images in the left panels show trypan blue-stained leaves and in the right panels leaves imaged under an epifluorescence microscope at 3 days post-inoculation (dpi). Scale bars, 3 mm.

regulated and confined to the area undergoing HR elicited by hemibiotrophic (*P. syringae*) and necrotrophic (*B. cinerea*) pathogens. Thus, the transgenic reporter line *pAT5G17760:NLS-3xGFP* is a very useful tool to monitor this process *in planta*.

The *AT5G17760* gene encodes a putative ATPase associated with diverse cellular activities (AAA) ATPase of unknown function. A knockout mutant of this gene did not show any alteration in HR or pathogen growth restriction compared with wild-type plants (Supplemental Figure 14). The lack of phenotype could be due to functional redundancy/compensation, a very common masking phenomenon in plants.

HR markers and particularly *At5g17760* are highly upregulated in other RNA-seq datasets from plants undergoing ETI and autoimmunity

We looked at the behavior of *At5g17760* and the rest of the marker genes in already published RNA-seq datasets from plants undergoing ETI or autoimmune mutant plants displaying constitutive defense responses and runaway cell death (Supplemental Figure 16; Mine et al., 2018; Yang et al., 2020; Barragan et al., 2021; Chantarachot et al., 2020). Fold changes from marker genes with significant p values (FDR < 0.05) in these datasets were plotted as heatmaps to reveal their level of upregulation (Supplemental Figure 16). As expected, most gene markers are significantly (FDR < 0.05) upregulated during ETI triggered by *Pto AvrRpm1* and *Pto AvrRpt2* at 4, 6, and 9 hpi in Mine et al. (2018) (Supplemental Figure 16A). Interestingly, *At5g17760* is the

highest upregulated gene in *hos15-4* and *rh6812* mutant plants undergoing autoimmunity (Chantarachot et al., 2020; Yang et al., 2020). Likewise, upregulated genes from datasets of incompatible *Arabidopsis* F1 hybrids (*Cdm-0 x TueScha-9*) exhibiting autoimmunity comprised most HR markers found in this study, with *At5g17760* being the highest upregulated gene (Barragan et al., 2021; Supplemental Figure 16B).

DISCUSSION

Zonation of HR in plants is underscored by distinct gene expression patterns and processes in dying versus bystander cells

In plants, pathogen recognition via intracellular NLR receptors often results in an HR reaction that helps prevent pathogen proliferation (Pitsili et al., 2020). This is a highly zonal response that takes place at the site of infection, where dying cells send signals to the surrounding tissue to activate defenses and block pathogen invasion. Traditionally, the plant immune system has been considered strictly two branched, with PTI elicited by recognition of conserved pathogen patterns via cell surface receptors and ETI recognizing pathogen effector proteins secreted into the plant cell via intracellular NLR receptors (Jones and Dangl, 2006). Over the last decades, many efforts have been directed toward understanding the transcriptional reprogramming elicited during PTI and ETI (Tao et al., 2003; Lewis et al., 2015; Bozso et al., 2016; Mine et al., 2018; Duan et al., 2020). One of the major conclusions drawn from these studies is that, although the repertoire of DEGs in the host is largely similar, ETI leads to a faster and more robust transcriptional response than PTI (Tao et al., 2003; Mine et al., 2018; Yuan et al., 2021a, 2021b; Ngou et al., 2021b). These findings, together with emerging evidence showing additional levels of synergy and crosstalk between PTI and ETI, have somewhat blurred the traditional PTI-ETI dichotomy (Ngou et al., 2021a; Dongus and Parker, 2021; Pruitt et al., 2021). However, despite the large amount of time-resolved transcriptomics data (Tao et al., 2003; Lewis et al., 2015; Hillmer et al., 2017; Mine et al., 2018), the spatial consideration of HR upon ETI activation has been partly overlooked, with only few studies pointing to its importance in regulating the process (Dorey et al., 1997; Betsuyaku et al., 2018; Giolai et al., 2019; Lukan et al., 2020). It remains unclear whether and to what extent transcriptional reprogramming takes place in the vicinity of cell death compared with that occurring at the infected area upon bacterial infection.

Our experimental design (Figure 1A) considered the spatiotemporal angle of plant HR to gain a better understanding of how this process is restricted to a few cells upon pathogen recognition and to define robust markers of the dying area over time. This is particularly important because, in plants, cell death characterization has largely relied on biochemical and morphological hallmarks, most of which are postmortem and, in most cases, do not provide unequivocal criteria (van Doorn, 2011; van Doorn et al., 2011). We currently lack a set of genes that can be employed as gene indicators of cell death triggered by pathogens. *In silico* comparisons of transcriptome profiles at different developmental stages and upon environmental stresses leading to cell death enabled identification of cell death indicators of developmentally regulated programmed cell death that can be used to detect or even isolate cells that are ready to die (Olvera-Carrillo et al., 2015). The same approach did not lead to identification of reliable HR markers, partly because the available datasets were not obtained on zonally resolved samples (Olvera-Carrillo et al., 2015).

Here differential expression analysis and clustering of genes based on expression profiles over time enabled us to infer biological processes taking place at each tissue area (IN/OUT) upon bacterial infection, giving us hints about how HR can be spatially restricted. At the IN area, genes involved in a local immune response to ETI-triggering bacteria are greatly induced from 1 hpi onwards (cluster I) (Figure 2A; Supplemental Figure 2A; Figure 3A). Tissue from the IN area also contains a set of genes that show a peak of upregulation from 2–4 hpi (cluster II), involved in diverse biological processes ranging from regulation of immunity, responses to JA and SA, and protein turnover (Supplemental Figure 6A). It is now well established that proteasome activity is strongly induced during bacterial infection and that certain subunits of the proteasome are required for efficient fine-tuning of immune responses in plants (Misas-Villamil et al., 2013; Ustun et al., 2016, 2018). Finally, we identified strong transcriptional repression of photosynthetic genes at 4 hpi at the IN area (cluster III) (Figure 2B; Supplemental Figure 2B; Figure 3A; Supplemental Figure 6A), in accordance with the previously established notion that infection results in global downregulation of genes associated with the photosynthetic machinery (Bilgin et al., 2010). This specific decrease in photosynthesis is particularly interesting in light of recent reports of the interplay between bacterial effectors and the chloroplast, where certain effectors can suppress chloroplast functions and, in turn, chloroplasts can adopt immune functions to fight off pathogens (Kachroo et al., 2021; Littlejohn et al., 2021; Savage et al., 2021).

Our results also show that transcriptional reprogramming in host cells surrounding the infection area (OUT area) is less extensive, with a lower number of DEGs than at the IN area, and starts later, mostly from 4 hpi onward (Figure 2A). Remarkably, photosynthesis is not significantly affected at the OUT area, corroborating our *in vivo* measurements (Figure 1C) and previous findings (Bilgin et al., 2010). A relatively functional photosynthetic machinery may be key for maintaining effective defense mechanisms and preventing these cells from dying as their neighbors. This finding might have been masked in previous transcriptional studies that have not taken into account the zonal nature of HR and reveals that the defense–growth trade-off may also have a marked spatial component that needs to be taken into account in future research. Besides photosynthesis, the OUT zone was characterized by marked upregulation of wound/JA-related genes at 4 hpi (Figures 2C and 3B; Supplemental Figure 2C). This response can also be observed at the IN zone, but the level of upregulation at the OUT zone is remarkably higher (Supplemental Figure 4), indicating amplification of JA signaling at the cells surrounding the death zone. In addition, some of the JA-related genes are among genes exclusively upregulated at OUT at 4/6 hpi, which indicates that they could potentially be used as zonal markers of the surrounding area (Figure 2B and 2C; Supplemental Figure 5). *In vivo* imaging of marker gene promoter activities of SA and JA signaling during ETI discerned two spatially distinct domains around the infection site, where JA signaling is thought to be important for regulating overactivation

of SA signaling (Betsuyaku et al., 2018). Future studies that include mutants deficient in JA could provide mechanistic insights into how JA signaling contributes to confinement of plant HR. Our analysis also shows that some SA signaling genes are among the upregulated IN-specific genes at late time points (Figure 2B and 2C; Supplemental Table S4). Although originally considered antagonistic hormones required for immunity against pathogens with contrasting lifestyles (Spoel et al., 2007), the interplay and synergism of these two phytohormones during ETI is now well established (Liu et al., 2016).

Zonally resolved transcriptomic analysis allows identification of robust biomarkers of HR

Robust biomarkers are essential for gaining mechanistic knowledge of cell- or tissue-specific processes. The extensive mechanistic knowledge of molecular constituents underlying regulated cell death in mammals has enabled use of biomarkers for detection of tumor cells or aberrant cell death processes in individuals with cancer (Abu-Qare and Abou-Donia, 2001; Ward et al., 2008). The field of HR in plants is gaining momentum because of recent major discoveries that, on one hand, are leading to redefinition of the PTI-ETI relationship and on the other have provided mechanistic insight into how NLRs become activated and form supramolecular complexes that mediate cell death (Wang et al., 2019a, 2019b; Martin et al., 2020; Yuan et al., 2021a; Bi et al., 2021; Ngou et al., 2021b; Jacob et al., 2021; Pruitt et al., 2021; Tian et al., 2021; Förderer et al., 2022). However, the conceptual framework of HR zonation is scarcely defined and will be key for understanding its execution and spatial restriction mechanisms and define *bona fide* indicators of the process.

One of the main goals of our analysis was to define new markers of HR. We made use of the RNA-seq data generated from IN and OUT areas to pinpoint gene indicators of HR that can be used as transcriptional markers or gene promoter markers for *in planta* detection of cells destined to die using live imaging. Applying stringent filters to our dataset, we identified 13 genes that can be used as unequivocal transcriptional markers of zonally restricted cells that have activated a death program in response to pathogen perception via NLR activation (Figure 4C).

This marker set includes genes involved or putatively involved in various processes such as ion transport across the plasma membrane (M1), cell detoxification (M2 and M3), lipid metabolism (M5 and M6), cell wall remodeling (M7, M8, and M9), protein degradation (M10), and glycolysis (M11 and M12), but one of these genes remains largely uncharacterized (M13) and encodes an AAA-ATPase of unknown function. Interestingly, all of these predicted functions are consistent with processes expected to take place on cells destined to die or that have started dying, although the function of most of these genes remains to be fully determined. This set of genes provides a glimpse into transcriptional regulation of HR at the site of infection, the tip of the iceberg of the multi-level regulation of the process. For example, the fact that several genes are involved in cell wall remodeling highlights the importance of processes taking place in this extracellular compartment. In line with this, an increase in lignification at the edge of cells undergoing HR has been shown in the past and provides a clear picture of the zonal nature of this process (Lee et al., 2019). Interestingly, our transcriptome data clearly show that many lignin biosynthetic genes are strongly and specifically upregulated at the IN zone at certain time points (Supplemental Figure 15). How this cell wall lignification is regulated upon pathogen perception remains to be clarified and will be an interesting topic of future research.

Our data also reinforce the idea that the proteases involved in degradation of cell components during HR are not particularly regulated at the transcriptional level. We observe specific upregulation of degradative processes at the IN zone, such as autophagy, vacuolar degradation, and proteasome-mediated processes, and, in fact, one of the marker genes is a proteasome subunit (Figures 3 and 4B). However, we did not find any protease specifically upregulated at the IN zone, nor did any of them pass the filters that constitute a marker gene in our study.

In parallel, the changes observed in marker genes involved in ion transport across the plasma membrane or cell detoxification may be somewhat related to the predicted formation of a pore at the plasma membrane by pathogen-mediated activation of certain NLRs (Bi et al., 2021; Jacob et al., 2021; Förderer et al., 2022). Although crucial pieces of this mechanism have been unveiled, knowledge is still scattered, and we lack a more integrated picture that combines NLR activation with downstream processes, including cell death execution. Interestingly, 7 of the 32 gene markers (*M5*, *M6*, *M7*, *M8*, *M9*, *M11*, and *M12*) that pass our filters exhibit early upregulation at 2 hpi compared with mock controls according to the RNA-seq data (Supplemental Figure 10). Although these genes did not pass the stringent 4-tier filtering applied (Figure 4A) at 2 hpi, the expression profiles of these genes could be compatible with their potential use as earlier markers of HR at the IN area.

Our data provide a snapshot of how infected cells respond to pathogen recognition at the transcriptional level compared with their neighbors that are not directly exposed to the pathogen but respond to it. This analysis has revealed a set of genes that are specifically upregulated at the IN zone and constitute robust markers of HR, opening new paths to deepen our knowledge about the process.

We present an *Arabidopsis* HR reporter line stably expressing GFP under control of the AAA-ATPase *At5g17760* (M13), which shows extremely clear and strong expression exclusively at the inoculated area, where pathogen recognition takes place via ETI, before onset of cell death becomes apparent (Figure 5A and 5B; Supplemental Figure 12). The other genes (*M1–M12*) constituted very clear quantitative PCR markers, but GFP promoter fusions did not result in clear GFP expression. This can be attributed to the limitations from defining an active promoter sequence.

Expression of the marker p*At5g17760:NLS-3xGFP* is similarly regulated by different classes of NLRs (CNLs and TNLs), revealing conservation of the process (Figure 5A). The marker is also induced zonally by necrotrophic pathogens, such as *B. cinerea*, that cause an HR-like phenotype (Figure 5C). Thus, this transgenic line is a robust *in planta* biomarker of HR triggered by activation of different NLRs upon infection with pathogens with contrasting lifestyles.

Future in-depth analysis of all HR marker genes identified in this work, including combinatorial genetics, will contribute to a better understanding of HR. This set of genes is an invaluable tool to zonally discriminate cells undergoing pathogen-triggered cell death and mechanistically dissect this process. Of particular interest will be to sort GFP-expressing cells of the p*At5g17760:NLS-3xGFP* transgenic line upon infection and adapt high-throughput cell death monitoring equipment used so far for animal cell death to describe and quantify the features and regulatory networks that define HR in plants at a single-cell level.

METHODS

Plant and bacterial materials and growth

The *A. thaliana* accession Col-0 was used for all experiments carried out in this study expect for electrolyte leakage. For electrolyte leakage, Col-0, the *rpm1-3* (Grant et al., 1995) mutant of the NLR RPM1, and the *at5g17760* mutant (GABI-KAT line 592F04_1), which carries a T-DNA insertion in exon 2, were used. Primers used for identifying the T-DNA mutant and for corroboration null expression by quantitative real-time PCR are listed in Supplemental Table 12.

Seeds were sown on ½ Murashige and Skoog medium supplemented with 1% sucrose and stratified at 4°C for 2 days. Plants were grown in a controlled chamber with a photoperiod of 9 h light and 15 h dark with white fluorescent lamps under 65% relative humidity. Seeds were germinated on plates and grown for 10–7 days, individually transplanted to Jiffy pellets, and grown for 3 additional weeks.

The *Pto* strains *Pto AvrRpm1*, *Pto AvrRpt2*, *Pto AvrRps4*, *Pto hrpC*$^-$, and *Pto* EV pVSP61 were grown on selective King's B medium plates for 48 h at 28°C. Bacteria were then resuspended in 10 mM $MgCl_2$, and the OD_{600} was adjusted to the appropriate inoculum.

Bacterial inoculation and RNA-seq data collection

Bacteria were resuspended, and the concentration was adjusted at 5 $\times 10^7$ colony-forming units or to an OD_{600} of 0.05. Fully expanded seventh- or eighth-rosette leaves were used for infiltration with a mock solution (10 mM $MgCl_2$) or *Pto AvrRpm1*. We syringe-infiltrated an area of roughly 3–4 mm at the side edge of leaves. Upon infiltration, the edge of the infiltrated area was underlined using India ink, and the total area infiltrated was designated as "IN". A 1-mm buffer zone next to the IN area was discarded and used as a reference to properly separate the IN and the OUT zone, which expanded 1–2 mm toward the vein. Leaf tissue was collected separately from the IN and OUT area of infiltration at 5 different time points (0, 1, 2, 4, and 6 h) using a sterile scalpel. Leaf tissue was stored in 2-ml Eppendorf tubes and snap frozen in liquid nitrogen until RNA extraction. Each sample collected consisted of tissue from six leaves derived from three different plants. For generation of three biological replicates from each condition (area, treatment, and time), three independent experiments were performed. In total, 60 samples (2 treatments [mock/infected], 5 time points [0, 1, 2, 4, and 6 hpi], 2 areas [IN/OUT], and 3 biological replicates) were used for RNA-seq.

For RNA library preparation, 1 μg of RNA from each sample was isolated using the NucleoSpin RNA isolation kit (Macherey-Nagel, Hoerdt Cedex, France) following the manufacturer's instructions. RNA-seq was performed at the GeT-PlaGe core facility (INRA Toulouse). RNA-seq libraries were prepared according to Illumina's protocols using the Illumina TruSeq Stranded mRNA Sample Prep Kit to analyze mRNA. Briefly, mRNA was selected using poly-T beads. Then RNA was fragmented to generate double-stranded complementary DNA, and adaptors were ligated to be sequenced. Eleven cycles of PCR were applied to amplify libraries. Library quality was assessed using a fragment analyzer, and libraries were quantified by quantitative PCR using the Kapa Library Quantification Kit (Kapa Biosystems, Wilmington, MA, USA). RNA-seq experiments were performed on an Illumina HiSeq3000 using a paired-end read length of 2 × 150 bp with the Illumina HiSeq3000 sequencing kits.

Read mapping and differential expression analysis

FastQC and TrimGalore! software was used for raw Illumina read quality control analysis and trimming of reads containing adaptor- or vector-derived sequences, respectively (FastQC A Quality Control Tool for High Throughput Sequence Data, Babraham Bioinformatics, 2021). Ribosomal RNA was detected and removed using SortMeRNA 2.1b software (Kopylova et al., 2012). Cleaned reads together with the transcriptome of *A. thaliana* (as of August 30, 2018), including non-coding RNA, were used to quantify gene expression at the transcript level using the software Salmon v.0.11.3 (Patro et al., 2017). Raw counts aggregated by gene were obtained using tximport v.1.14.2, and the result was used as input to DESeq2 v.1.26.0 (Love et al., 2014; Soneson et al., 2015) to perform differential expression analysis. Then genes adding up to less than 10 counts across all 60 samples were removed. The pre-filtered DESeq2 object contained 32,865 rows that turned to 23,986 after filtering. Counts normalized for sample size and regularized logarithm transformed were used to produce PCAs.

Raw counts together with sample size information were used as input for DESeq2 differential expression analysis. Simple pairwise comparisons based on a single factor were performed using the DESeq2 Result function, and time course differential expression results were obtained using a likelihood ratio test as described previously (Love et al., 2015). Genes with an FDR below 0.05 and |log2FC| higher than 2 were considered differentially expressed. FDR was calculated according to the Benjamini and Hochberg method (Benjamini and Hochberg, 1995).

Gene clustering

Gene clustering was performed using the Mfuzz v.2.46.0 package under the R environment (Kumar and Futschik, 2007; RStudio, 2021) which is based on fuzzy c-means clustering algorithms. IN and OUT samples were independently analyzed. After time course differential expression analysis using DESeq2, only genes with an FDR of less than 0.05 in the likelihood ratio test were selected for clustering.

The optimal numbers of non-overlapping clusters with a correlation value below 0.85 were 3 and 6 for *Pto AvrRpm1*-treated samples at the IN and OUT areas of infection, respectively.

Subsequently, two highly redundant clusters were merged for OUT samples, yielding 5 final clusters. Genes that integrated each cluster derived from *Pto AvrRpm1*-treated samples were re-clustered for mock-treated samples to inspect the differences and similarities of trajectories between treatments over time. Between two and four mock-based sub-clusters were obtained for every infected cluster. To avoid overlap, we reduced the number of sub-clusters to two in mock-treated samples. Each gene belonging to a cluster returned an associated MSV that ranged from 0–1 depending on how well it fitted the expression profile dictated by the overall genes comprising the cluster. Genes that integrate each cluster in Figure 3 can be found in Supplemental Tables 6 and 7.

Enriched GO analysis

The sets of genes that belonged to expression profile clusters or that exhibited differential expression were entered into The Arabidopsis Information Resource for GO enrichment analysis for biological processes, which uses the PANTHER classification system containing up-to-date GO annotation data for *Arabidopsis* (Berardini et al., 2004). The most specific term belonging to a particular family of GO terms was always selected for plotting. Only GO terms exhibiting an FDR of less than 0.05 after Bonferroni correction for multiple testing and a fold enrichment above 2 were selected for representation in dot plots.

Identification of HR indicators

For identification of HR indicators, we concatenated four pairwise comparisons using DESeq2 in which we set different thresholds of log2FC while keeping a stringent cutoff of FDR of less than 0.05 throughout all comparisons. Briefly, we firstly selected genes that were upregulated (log2FC > 2) after *Pto AvrRpm1* infection at 4 or 6 hpi versus 0 hpi. From the genes that complied with this first filter, we selected those that were specifically upregulated in *Pto AvrRpm1*-infected versus mock-inoculated samples at 4 or 6 hpi (log2FC > 2). From the genes that passed these two filters, we kept those with a log2FC < 1 at the OUT area in *Pto AvrRpm1*-infected versus mock-inoculated samples at four or 6 hpi. Because genes with log2FC near 0 do not usually have a low FDR, we kept our stringent FDR threshold while setting the log2FC threshold below 1 to capture, with statistical confidence, downregulated and only mildly upregulated genes at this tissue area. Finally, from the genes that met these three criteria, we kept those that were differentially upregulated at the IN area compared with the OUT area in *Pto AvrRpm1*-infected plants.

Validation of gene expression by real-time qPCR

The same experimental setup used for RNA-seq data generation was followed for experimental validation by quantitative real-time PCR, including infections with *Pto AvrRpt2*, *Pto AvrRps4*, *Pto hrpC*$^-$, and *Pto* EV. Briefly, tissue was snap frozen and RNA isolated with the Maxwell RSC Plant RNA Kit (Promega). One microgram of RNA was reverse transcribed into complementary DNA with the High-Capacity cDNA Reverse Transcription Kit with RNase Inhibitor (Applied Biosystems). Quantitative real-time PCR was performed with LightCycler SYBRgreen I Master (Roche) in a LightCycler 480 System (Roche). Data were analyzed using the $\Delta\Delta CT$ method and represented as fold enrichment of the time point tested (4 or 6 hpi) relative to 0 hpi. Primers for quantitative real-time PCR used in this study are listed in Supplemental Table 12 along with primer concentrations. Quantitative real-time PCR results in numeric format along with Cp (crossing point) values of targets and Cp values of reference housekeeping gene are listed in Supplemental Table 13.

Cell death analysis

Trypan blue staining of *Arabidopsis* leaves was performed by collecting whole leaves in 50-ml tubes (each leaf in a separate tube) at the specified time points after treatment and covered with a 1:3 dilution of the stain. Tubes were incubated in previously boiled water for 15 min and then cleared overnight with chloral hydrate on an orbital shaker. After removal of staining solution, leaves were covered in a 50% glycerol solution and photographed using a Leica DM6 microscope.

Electrolyte leakage

Whole leaves from 4- to 5-week-old *Arabidopsis* Col-0, *rpm1-3*, or *at5g17760* (GABI-KAT: 592F04) grown under short-day conditions with a photoperiod of 9 h light and 15 h dark were infiltrated with *Pto AvrRpm1* at OD_{600} of 0.05 using a 1-ml needleless syringe. Leaf discs were dried and collected with a 0.8-cm-diameter cork borer from infiltrated leaves. Discs were washed in deionized water for 1 h before being floated on 2 ml deionized water. Electrolyte leakage was measured as water conductivity with a pocket water quality meter (LAQUAtwin-EC-11; Horiba, Kyoto, Japan) at the indicated time points.

Bacterial growth assay

Whole leaves from 4- to 5-week-old *Arabidopsis* Col-0, *rpm1-3*, or *at5g17760* (GABI-KAT: 592F04) grown under short-day conditions (9 h light and 15 h dark) were infiltrated with *Pto AvrRpm1* at OD_{600} of 0.001 using a 1-ml needleless syringe. Two leaf discs from two different leaves were collected using a 6 mm-diameter cork borer (disc area, 0.282 cm^2). Samples on day 0 and day 3 after infection were grounded in 10 mM $MgCl_2$ and serially diluted 5, 50, 500, 5000 and 50,000 times on a 96-well plate. Subsequently, dilutions were spotted (10 μl per spot) on King's B medium with antibiotics. The number of colony-forming units (CFUs) per drop was calculated and bacterial growth represented as log_{10} CFU per cm^2 of tissue.

Chlorophyll fluorescence imaging

An IMAGING-PAM (pulse amplitude modulation) M-Series Chlorophyll Fluorometer system (Heinz Walz, Effeltrich, Germany) was used to investigate spatiotemporal changes in photosynthetic parameters at the IN and OUT areas of infection (Schreiber, 2004). Plants were kept in the dark for 30 min before measurement. Plants were exposed to 2-Hz frequency light pulses for Fo (minimum fluorescence in the dark-adapted state) determination. Saturating pulses (800 ms) of white light (2400 mmol photons.m^{-2} s^{-1}) were applied for Fm (maximum fluorescence in the dark-adapted state) determination. The photosynthetic efficiency or maximum quantum yield of photosystem II (PSII) photochemistry (Fv/Fm) was determined as (Fm-Fo)/Fm. The relative PSII ETR was calculated by performing a kinetics analysis for 10 min with 60-s pulses (Schreiber et al., 2012). Areas of interest included IN and OUT to evaluate spatial heterogeneity. The measurements were taken 0, 1, 2, 4 and 6 hpi. Results from 6 different areas of interest are shown.

Generation of transgenic promoter reporter lines

Regions of approximately −2.5 kb upstream of the transcription starting site of *AT1G79710*, *AT4G18050*, *AT1G78380*, *AT4G24160*, *AT5G18480*, *AT4G30390*, *AT5G54650*, *AT5G16910*, *AT5G20000*, *AT2G36580*, *AT5G56350*, and *AT5G17760* were amplified from *Arabidopsis* Col-0 genomic DNA by PCR and cloned into the pGGA (plasmid Green Gate A) entry vector to generate pGGA-pMarkerGene. A region of approximately −1.5 kb upstream of the transcription start site of *AT1G30270* was synthetized by GENEWIZ (South Plainfield, NJ) and subsequently also cloned into the pGGA entry vector (Lampropoulos et al., 2013). Each entry vector was then recombined with the following plasmids: pGGB-SV40-NLS, pGGC-3xGFP, pGGD-RBCSt (D-F), pGGF-AlliYFP (seed coat selection cassette for transgenic seed selection), and pGGZ-empty destination vector. Primers used for cloning and sequencing the final constructs are listed in Supplemental Table 12. All plasmids were transfected by electroporation into the *Agrobacterium tumefaciens* GV3101 strain containing the plasmid pSoup and then transformed into *Arabidopsis* Col-0 by the floral dipping method (Clough and Bent, 1998). Transgenic seeds from transformed plants were identified as those displaying a clear fluorescence signal under the stereomicroscope (Olympus SZX18).

Pathogen inoculation and microscopy of reporter lines

For microscopy of the reporter line p*AT5G17760*:NLS-3xGFP, plants were grown as described previously. Leaves of Col-0 p*AT5G17760*:NLS-3xGFP were infiltrated in the IN area with a mock solution (10 mM $MgCl_2$) or different *Pto* strains. *Pto* strains expressing the following effectors were used: *AvrRpm1*, *AvrRpt2*, and *AvrRps4*. As controls, the *Pto* EV and *Pto hrcC*$^-$ strains were also used. All *Pto* strains were infiltrated at OD_{600} of 0.01 for microscopy imaging. For *B. cinerea* infection, the B05.10 strain was grown for 14 days in potato dextrose agar at 22°C under dark conditions. Spores were collected, washed in 5 ml of potato dextrose agar, and filtered through two layers of Miracloth (Merck Millipore). Subsequently, spores per cm^2 were counted under the microscope and diluted to 1×10^5 spores/ml. For inoculation, a 6-μl droplet was placed on the upper surface of the seventh or eighth leaf of an adult *Arabidopsis* plant grown under short-day conditions. A dome covered the plants throughout the course of *B. cinerea* infection.

Leaves were imaged at 16 hpi with *Pto* stains and at 3 dpi with *B. cinerea*. Whole leaves were photographed using a Leica DM6 microscope (Leica Microsystems) equipped with a DFC365 FX 1.4 MP monochrome digital camera. Bright-field and GFP filter pictures were taken of each leaf. Confocal images were obtained using a FV1000 Olympus confocal microscope with the following excitation/emission wavelengths for GFP: 488 nm/500–540 nm. Confocal microscopy images were taken of the epidermal layer (20 z stacks with a stack size of 1 μm), and fluorescent nuclei were counted using ImageJ software.

DATA AVAILABILITY

RNA-seq raw and processed data generated in this study can be found in GEO (GSE198022). All code used for analysis can be found at https://doi.org/10.34810/data174.

ETHICS STATEMENT

The present study did not require ethical approval.

SUPPLEMENTAL INFORMATION

Supplemental information can be found online at https://doi.org/10.1016/j.molp.2022.04.010.

FUNDING

Research at CRAG was supported by grants PID2019-108595RB-I00 funded by MCIN/AEI/10.13039/501100011033 and AGL2016-78002-R funded by MCIN/AEI/10.13039/501100011033 and by "ERDF A way of making Europe" (to N.S.C. and M.V.); fellowship PID2019-108595RB-I00 funded by Spanish MCIN/AEI/10.13039/501100011033 (to N.S.C. and M.V.); fellowship BES-2017-080210 funded by MCIN/AEI/10.13039/501100011033 and by "ESF Investing in your future" (to J.S.-L.); FPU19/03778 funded by MU (o Ministerio de Universidades) (to N.R.-S.); by the "Severo Ochoa Programme for Centres of Excellence in R&D" (SEV-2015-0533 and CEX2019-000902-S funded by MCIN/AEI/10.13039/501100011033); and by the CERCA Programme/Generalitat de Catalunya. Work at the LIPM was supported by the INRA SPE department (AAP2014), the Région Midi-Pyrénées (grant 13050322), and the French Laboratory of Excellence project "TULIP" (ANR-10-LABX-41; ANR-11-IDEX-0002-02). I.S. was supported by an AgreenSkills fellowship within the EU Marie-Curie FP7 COFUND People Programme (grant agreement 267196).

AUTHOR CONTRIBUTIONS

J.S.-L. designed and performed experiments, analyzed and interpreted data, and wrote the manuscript. I.S. and N.R.-S. designed and performed experiments, analyzed and interpreted data, and helped with writing the manuscript. M.S.-G. and U.J.P. performed experiments. V.M.G. and M.B.-F. performed analyses and interpreted data. M.V. interpreted data and helped with writing the manuscript. D.R. performed experiments, analyzed and interpreted data, and helped with writing the manuscript. N.S.C. conceptualized the research, designed the experiments, interpreted data, and wrote the manuscript.

ACKNOWLEDGMENTS

We thank Susana Rivas, who conceived and initiated the project but declined to be an author. Likewise, we thank Susana Rivas's team for help with the preliminary experiments and plant tissue harvest for RNA-seq. We thank Sebastien Carrère from the Bioinformatics facility at the LIPM for bioinformatics preliminary analysis. We also thank Simon Stael (VIB) for helpful comments and inspiring discussions and all members of the Bacterial plant diseases and cell death lab for insights and suggestions. We thank José Luis Riechman (CRAG) and Miguel Ángel Moreno-Risueño for help with analysis, Antoni Garcia-Molina for help with *B. cinerea* infections, and Montse Amenós for help with microscopy. We thank Kenichi Tsuda for sharing his RNA-seq data of previously published transcriptomics studies (Mine et al., 2018) and Ignacio Rubio-Somoza for providing us with the green gate plasmid pGGD-RBCSt (D–F). The authors declare no conflict of interest.

Received: October 26, 2021
Revised: April 1, 2022
Accepted: April 28, 2022
Published: May 1, 2022

REFERENCES

Abu-Qare, A.W., and Abou-Donia, M.B. (2001). Biomarkers of apoptosis: release of cytochrome c, activation of caspase-3, induction of 8-hydroxy-2 '-deoxyguanosine, increased 3-nitrotyrosine, and alteration of p53 gene. J. Toxicol. Environ. Health-B-Critical Rev. **4**:313–332. https://doi.org/10.1080/109374001301419737.

Alfano, J.R., Charkowski, A.O., Deng, W.L., Badel, J.L., Petnicki-Ocwieja, T., van Dijk, K., and Collmer, A. (2000). The *Pseudomonas syringae* Hrp pathogenicity island has a tripartite mosaic structure composed of a cluster of type III secretion genes bounded by exchangeable effector and conserved effector loci that contribute to parasitic fitness and pathogenicity in plants. Proc. Natl. Acad. Sci. U S A **97**:4856–4861. https://doi.org/10.1073/pnas.97.9.4856.

Ausubel, F.M. (2005). Are innate immune signaling pathways in plants and animals conserved? Nat. Immunol. **6**:973–979. https://doi.org/10.1038/ni1253.

Balint-Kurti, P. (2019). The plant hypersensitive response: concepts, control and consequences. Mol. Plant Pathol. **20**:1163–1178. https://doi.org/10.1111/mpp.12821.

Barragan, A.C., Collenberg, M., Wang, J., Lee, R.R.Q., Cher, W.Y., Rabanal, F.A., Ashkenazy, H., Weigel, D., and Chae, E. (2021). A truncated singleton NLR causes hybrid necrosis in Arabidopsis thaliana. Mol. Biol. Evol. **38**:557–574. https://doi.org/10.1093/molbev/msaa245.

Benjamini, Y., and Hochberg, Y. (1995). Controlling the false discovery rate - a practical and powerful approach to multiple testing. J. R. Stat. Soc. Ser. B-Statistical Methodol. **57**:289–300. https://doi.org/10.1111/j.2517-6161.1995.tb02031.x.

Berardini, T.Z., Mundodi, S., Reiser, L., Huala, E., Garcia-Hernandez, M., Zhang, P.F., Mueller, L.A., Yoon, J., Doyle, A., Lander, G., et al. (2004). Functional annotation of the Arabidopsis genome using controlled vocabularies. Plant Physiol. **135**:745–755. https://doi.org/10.1104/pp.104.040071.

Berger, S., Benediktyova, Z., Matous, K., Bonfig, K., Mueller, M.J., Nedbal, L., and Roitsch, T. (2007). Visualization of dynamics of plant-pathogen interaction by novel combination of chlorophyll fluorescence imaging and statistical analysis: differential effects of virulent and avirulent strains of P-syringae and of oxylipins on A-thaliana. J. Exp. Bot. **58**:797–806. https://doi.org/10.1093/jxb/erl208.

Betsuyaku, S., Katou, S., Takebayashi, Y., Sakakibara, H., Nomura, N., and Fukuda, H. (2018). Salicylic acid and jasmonic acid pathways are activated in spatially different domains around the infection site during effector-triggered immunity in Arabidopsis thaliana. Plant Cell Physiol. **59**:8–16. https://doi.org/10.1093/pcp/pcx181.

Bi, G., Su, M., Li, N., Liang, Y., Dang, S., Xu, J., Hu, M., Wang, J., Zou, M., Deng, Y., et al. (2021). The ZAR1 resistosome is a calcium-permeable channel triggering plant immune signaling. Cell **184**:3528–3541.e12. https://doi.org/10.1016/j.cell.2021.05.003.

Bilgin, D.D., Zavala, J.A., Zhu, J., Clough, S.J., Ort, D.R., and DeLucia, E.H. (2010). Biotic stress globally downregulates photosynthesis genes. Plant Cell Environ. **33**:1597–1613. https://doi.org/10.1111/j.1365-3040.2010.02167.x.

Bozso, Z., Ott, P.G., Kaman-Toth, E., Bognar, G.F., Pogany, M., and Szatmari, A. (2016). Overlapping yet response-specific transcriptome alterations characterize the nature of tobacco-Pseudomonas syringae interactions. Front. Plant Sci. **7**:251. https://doi.org/10.3389/fpls.2016.00251.

Chantarachot, T., Sorenson, R.S., Hummel, M., Ke, H., Kettenburg, A.T., Chen, D., Aiyetiwa, K., Dehesh, K., Eulgem, T., Sieburth, L.E., et al. (2020). DHH1/DDX6-like RNA helicases maintain ephemeral half-lives of stress-response mRNAs. Nat. Plants **6**:675–685. https://doi.org/10.1038/s41477-020-0681-8.

Chung, H.S., Koo, A.J.K., Gao, X., Jayanty, S., Thines, B., Jones, A.D., and Howe, G.A. (2008). Regulation and function of Arabidopsis JASMONATE ZIM-domain genes in response to wounding and herbivory. Plant Physiol. **146**:952–964. https://doi.org/10.1104/pp.107.115691.

Clough, S.J., and Bent, A.F. (1998). Floral dip: a simplified method for Agrobacterium-mediated transformation of Arabidopsis thaliana. Plant J. **16**:735–743. https://doi.org/10.1046/j.1365-313x.1998.00343.x.

Couto, D., and Zipfel, C. (2016). Regulation of pattern recognition receptor signalling in plants. Nat. Rev. Immunol. **16**:537–552. https://doi.org/10.1038/nri.2016.77.

Dangl, J.L., and Jones, J.D.G. (2019). A pentangular plant inflammasome. Science **364**:31–32. https://doi.org/10.1126/science.aax0174.

Dangl, J.L., Horvath, D.M., and Staskawicz, B.J. (2013). Pivoting the plant immune system from dissection to deployment. Science **341**:746–751. https://doi.org/10.1126/science.1236011.

Dongus, J.A., and Parker, J.E. (2021). EDS1 signalling: at the nexus of intracellular and surface receptor immunity. Curr. Opin. Plant Biol. **62**:102039. https://doi.org/10.1016/j.pbi.2021.102039.

Dorey, S., Baillieul, F., Pierrel, M.A., Saindrenan, P., Fritig, B., and Kauffmann, S. (1997). Spatial and temporal induction of cell death, defense genes, and accumulation of salicylic acid in tobacco leaves reacting hypersensitively to a fungal glycoprotein elicitor. Mol. Plant-Microbe Interactions **10**:646–655. https://doi.org/10.1094/mpmi.1997.10.5.646.

Duan, Y., Duan, S., Armstrong, M.R., Xu, J., Zheng, J., Hu, J., Chen, X., Hein, I., Li, G., and Jin, L. (2020). Comparative transcriptome profiling reveals compatible and incompatible patterns of potato toward phytophthora infestans. G3-Genes Genomes Genet. **10**:623–634. https://doi.org/10.1534/g3.119.400818.

Förderer, A., Li, E., Lawson, A., Deng, Y.-N., Sun, Y., Logemann, E., Zhang, X., Wen, J., Han, Z., Chang, J., et al. (2022). A wheat resistosome defines common principles of immune receptor channels. Preprint at bioRxiv, Advance Access published 2022. https://doi.org/10.1101/2022.03.23.485489.

Gassmann, W., Hinsch, M.E., and Staskawicz, B.J. (1999). The Arabidopsis RPS4 bacterial-resistance gene is a member of the TIR-NBS-LRR family of disease-resistance genes. Plant J. **20**:265–277. https://doi.org/10.1046/j.1365-313x.1999.t01-1-00600.x.

Giolai, M., Verweij, W., Lister, A., Heavens, D., Macaulay, I., and Clark, M.D. (2019). Spatially resolved transcriptomics reveals plant host responses to pathogens. Plant Methods **15**:114. https://doi.org/10.1186/s13007-019-0498-5.

Grant, M.R., Godiard, L., Straube, E., Ashfield, T., Lewald, J., Sattler, A., Innes, R.W., and Dangl, J.L. (1995). Structure of the Arabidopsis RPM1 gene enabling dual-specificity disease resistance. Science **269**:843–846. https://doi.org/10.1126/science.7638602.

Hillmer, R.A., Tsuda, K., Rallapalli, G., Asai, S., Truman, W., Papke, M.D., Sakakibara, H., Jones, J.D.G., Myers, C.L., and Katagiri, F. (2017). The highly buffered Arabidopsis immune signaling network conceals the functions of its components. PLoS Genet. **13**:e1006639. https://doi.org/10.1371/journal.pgen.1006639.

Jacob, P., Kim, N.H., Wu, F., El-Kasmi, F., Chi, Y., Walton, W.G., Furzer, O.J., Lietzan, A.D., Sunil, S., Kempthorn, K., et al. (2021). Plant "helper" immune receptors are Ca2+-permeable nonselective cation channels. Science **373**:420. https://doi.org/10.1126/science.abg7917.

Jones, J.D.G., and Dangl, J.L. (2006). The plant immune system. Nature **444**:323–329. https://doi.org/10.1038/nature05286.

Jones, J.D.G., Vance, R.E., and Dangl, J.L. (2016). Intracellular innate immune surveillance devices in plants and animals. Science, 354.

Kachroo, P., Burch-Smith, T.M., and Grant, M. (2021). An emerging role for chloroplasts in disease and defense. Annu. Rev. Phytopathology **59**:423–445. https://doi.org/10.1146/annurev-phyto-020620-115813.

Kopylova, E., Noé, L., and Touzet, H. (2012). SortMeRNA: fast and accurate filtering of ribosomal RNAs in metatranscriptomic data. Bioinformatics **28**:3211–3217.

Kumar, L., and Futschik, M.E. (2007). Mfuzz: a software package for soft clustering of microarray data. Bioinformation **2**:5–7. https://doi.org/10.6026/97320630002005.

Lampropoulos, A., Sutikovic, Z., Wenzl, C., Maegele, I., Lohmann, J.U., and Forner, J. (2013). GreenGate - a novel, versatile, and efficient cloning system for plant transgenesis. PLoS One **8**:e83043. https://doi.org/10.1371/journal.pone.0083043.

Lee, M.-H., Jeon, H.S., Kim, S.H., Chung, J.H., Roppolo, D., Lee, H.-J., Cho, H.J., Tobimatsu, Y., Ralph, J., and Park, O.K. (2019). Lignin-based barrier restricts pathogens to the infection site and confers resistance in plants. EMBO J. **38**, e101948. https://doi.org/10.15252/embj.2019101948.

Lewis, L.A., Polanski, K., de Torres-Zabala, M., Jayaraman, S., Bowden, L., Moore, J., Penfold, C.A., Jenkins, D.J., Hill, C., Baxter, L., et al. (2015). Transcriptional dynamics driving MAMP-triggered immunity and pathogen effector-mediated immunosuppression in Arabidopsis leaves following infection with Pseudomonas syringae pv tomato DC3000. Plant Cell **27**:3038–3064. https://doi.org/10.1105/tpc.15.00471.

Littlejohn, G.R., Breen, S., Smirnoff, N., and Grant, M. (2021). Chloroplast immunity illuminated. New Phytologist **229**:3088–3107.

Liu, L.J., Sonbol, F.M., Huot, B., Gu, Y.N., Withers, J., Mwimba, M., Yao, J., He, S.Y., and Dong, X.N. (2016). Salicylic acid receptors activate jasmonic acid signalling through a non-canonical pathway to promote effector-triggered immunity. Nat. Commun. **7**:13099. https://doi.org/10.1038/ncomms13099.

Love, M.I., Huber, W., and Anders, S. (2014). Moderated estimation of fold change and dispersion for RNA-seq data with DESeq2. Genome Biol. **15**:550. https://doi.org/10.1186/s13059-014-0550-8.

Love, M.I., Anders, S., Kim, V., and Huber, W. (2015). RNA-Seq workflow: gene-level exploratory analysis and differential expression. F1000Res **4**:1070. https://doi.org/10.12688/f1000research.7035.1.

Lu, Y., and Yao, J. (2018). Chloroplasts at the crossroad of photosynthesis, pathogen infection and plant defense. Int. J. Mol. Sci. **19**:3900. https://doi.org/10.3390/ijms19123900.

Lu, J. v., Chen, H.C., and Walsh, C.M. (2014). Necroptotic signaling in adaptive and innate immunity. Semin. Cell Develop. Biol. **35**:33–39. https://doi.org/10.1016/j.semcdb.2014.07.003.

Lukan, T., Pompe-Novak, M., Baebler, S., Tusek-Znidaric, M., Kladnik, A., Kriznik, M., Blejec, A., Zagorscak, M., Stare, K., Dusak, B., et al. (2020). Precision transcriptomics of viral foci reveals the spatial regulation of immune-signaling genes and identifiesRBOHDas an important player in the incompatible interaction between potato virus Y and potato. Plant J. **104**:645–661. https://doi.org/10.1111/tpj.14953.

Ma, S., Lapin, D., Liu, L., Sun, Y., Song, W., Zhang, X., Logemann, E., Yu, D., Wang, J., Jirschitzka, J., et al. (2020). Direct pathogen-induced assembly of an NLR immune receptor complex to form a holoenzyme. Science **370**:1184. https://doi.org/10.1126/science.abe3069.

Mackey, D., Holt, B.F., Wiig, A., and Dangl, J.L. (2002). RIN4 interacts with Pseudomonas syringae type III effector molecules and is required for RPM1-mediated resistance in Arabidopsis. Cell **108**:743–754. https://doi.org/10.1016/s0092-8674(02)00661-x.

Mackey, D., Belkhadir, Y., Alonso, J.M., Ecker, J.R., and Dangl, J.L. (2003). Arabidopsis RIN4 is a target of the type III virulence effector AvrRpt2 and modulates RPS2-mediated resistance. Cell **112**:379–389. https://doi.org/10.1016/s0092-8674(03)00040-0.

Martin, R., Qi, T., Zhang, H., Liu, F., King, M., Toth, C., Nogales, E., and Staskawicz, B.J. (2020). Structure of the activated ROQ1 resistosome directly recognizing the pathogen effector XopQ. Science **370**:1185. https://doi.org/10.1126/science.abd9993.

Mine, A., Seyfferth, C., Kracher, B., Berens, M.L., Becker, D., and Tsuda, K. (2018). The defense phytohormone signaling network enables rapid, high-amplitude transcriptional reprogramming during effector-triggered immunity. Plant Cell **30**:1199–1219. https://doi.org/10.1105/tpc.17.00970.

Misas-Villamil, J.C., Kolodziejek, I., Crabill, E., Kaschani, F., Niessen, S., Shindo, T., Kaiser, M., Alfano, J.R., and van der Hoorn, R.A.L. (2013). Pseudomonas syringae pv. syringae uses proteasome inhibitor syringolin A to colonize from wound infection sites. Plos Pathog. **9**:e1003281. https://doi.org/10.1371/journal.ppat.1003281.

Muckenschnabel, I., Goodman, B.A., Williamson, B., Lyon, G.D., and Deighton, N. (2002). Infection of leaves of Arabidopsis thaliana by Botrytis cinerea: changes in ascorbic acid, free radicals and lipid peroxidation products. J. Exp. Bot. **53**:207–214. https://doi.org/10.1093/jexbot/53.367.207.

Nagata, S., and Tanaka, M. (2017). Programmed cell death and the immune system. Nat. Rev. Immunol. **17**:333–340. https://doi.org/10.1038/nri.2016.153.

Narusaka, M., Shirasu, K., Noutoshi, Y., Kubo, Y., Shiraishi, T., Iwabuchi, M., and Narusaka, Y. (2009). RRS1 and RPS4 provide a dual Resistance-gene system against fungal and bacterial pathogens. Plant J. **60**:218–226. https://doi.org/10.1111/j.1365-313x.2009.03949.x.

Navarro, L., Zipfel, C., Rowland, O., Keller, I., Robatzek, S., Boller, T., and Jones, J.D.G. (2004). The transcriptional innate immune response to flg22. interplay and overlap with Avr gene-dependent defense responses and bacterial pathogenesis. Plant Physiol. **135**:1113–1128. https://doi.org/10.1104/pp.103.036749.

Ngou, B.P.M., Jones, J.D.G., and Ding, P. (2021a). Plant immune networks. Trends Plant Sci. Adv. **27**:255–273, Access published 2021. https://doi.org/10.1016/j.tplants.2021.08.012.

Ngou, B.P.M., Ahn, H.K., Ding, P., and Jones, J.D.G. (2021b). Mutual potentiation of plant immunity by cell-surface and intracellular receptors. Nature **592**:7852–8115. https://doi.org/10.1038/s41586-021-03315-7.

Olsen, J. v., Blagoev, B., Gnad, F., Macek, B., Kumar, C., Mortensen, P., and Mann, M. (2006). Global, in vivo, and site-specific phosphorylation dynamics in signaling networks. Cell **127**:635–648. https://doi.org/10.1016/j.cell.2006.09.026.

Olvera-Carrillo, Y., van Bel, M., van Hautegem, T., Fendrych, M., Huysmans, M., Simaskova, M., van Durme, M., Buscaill, P., Rivas, S., Coll, N.S., et al. (2015). A conserved core of programmed cell death indicator genes discriminates developmentally and environmentally induced programmed cell death in plants. Plant Physiol. **169**:2684–2699. https://doi.org/10.1104/pp.15.00769.

Patro, R., Duggal, G., Love, M.I., Irizarry, R.A., and Kingsford, C. (2017). Salmon provides fast and bias-aware quantification of transcript expression. Nat. Methods **14**:417–419. https://doi.org/10.1038/nmeth.4197.

Pitsili, E., Phukan, U.J., and Coll, N.S. (2020). Cell death in plant immunity. Cold Spring Harbor Perspect. Biol. **12**:a036483. https://doi.org/10.1101/cshperspect.a036483.

Pruitt, R.N., Locci, F., Wanke, F., Zhang, L., Saile, S.C., Joe, A., Karelina, D., Hua, C., Frohlich, K., Wan, W.-L., et al. (2021). The EDS1-PAD4-ADR1 node mediates Arabidopsis pattern-triggered immunity. *Nat.* Adv. **598**:495–499, Access published 2021. https://doi.org/10.1038/s41586-021-03829-0.

RStudio. (2021). Open source & professional software for data science teams. Advance Access published 2021.

Salguero-Linares, J., and Coll, N.S. (2019). Plant proteases in the control of the hypersensitive response. J. Exp. Bot. **70**:2087–2095. https://doi.org/10.1093/jxb/erz030.

Savage, Z., Duggan, C., Toufexi, A., Pandey, P., Liang, Y., Segretin, M.E., Yuen, L.H., Gaboriau, D.C.A., Leary, A.Y., Tumtas, Y., et al. (2021). Chloroplasts alter their morphology and accumulate at the pathogen interface during infection by Phytophthora infestans. *Plant J.* Adv. **107**: 1771–1787, Access published 2021. https://doi.org/10.1111/tpj.15416.

Savatin, D.V., Gramegna, G., Modesti, V., and Cervone, F. (2014). Wounding in the plant tissue: the defense of a dangerous passage. Front. Plant Sci. **5**:470. https://doi.org/10.3389/fpls.2014.00470.

Schreiber, U. (2004). Pulse-amplitude-modulation (PAM) fluorometry and saturation pulse method: an overview. Chlorophyll a Fluoerescence: Signature of Photosynthesis **19**:279–319. https://doi.org/10.1007/978-1-4020-3218-9_11.

Schreiber, U., Klughammer, C., and Kolbowski, J. (2012). Assessment of wavelength-dependent parameters of photosynthetic electron transport with a new type of multi-color PAM chlorophyll fluorometer. Photosynthesis Res. **113**:127–144. https://doi.org/10.1007/s11120-012-9758-1.

Soneson, C., Love, M.I., and Robinson, M.D. (2015). Differential analyses for RNA-seq: transcript-level estimates improve gene-level inferences. F1000Res **4**:1521. https://doi.org/10.12688/f1000research.7563.1.

Spoel, S.H., Johnson, J.S., and Dong, X. (2007). Regulation of tradeoffs between plant defenses against pathogens with different lifestyles. Proc. Natl. Acad. Sci. U S A **104**:18842–18847. https://doi.org/10.1073/pnas.0708139104.

Tao, Y., Xie, Z.Y., Chen, W.Q., Glazebrook, J., Chang, H.S., Han, B., Zhu, T., Zou, G.Z., and Katagiri, F. (2003). Quantitative nature of Arabidopsis responses during compatible and incompatible interactions with the bacterial pathogen Pseudomonas syringae. Plant Cell **15**:317–330. https://doi.org/10.1105/tpc.007591.

Tian, H., Wu, Z., Chen, S., Ao, K., Huang, W., Yaghmaiean, H., Sun, T., Xu, F., Zhang, Y., Wang, S., et al. (2021). Activation of TIR signalling boosts pattern-triggered immunity. *Nat.* Adv. **598**:500–503, Access published 2021. https://doi.org/10.1038/s41586-021-03987-1.

Ustun, S., Sheikh, A., Gimenez-Ibanez, S., Jones, A., Ntoukakis, V., and Bornke, F. (2016). The proteasome acts as a Hub for plant immunity and is targeted by Pseudomonas type III effectors. Plant Physiol. **172**:1941–1958. https://doi.org/10.1104/pp.16.00808.

Ustun, S., Hafren, A., Liu, Q.S., Marshall, R.S., Minina, E.A., Bozhkov, P. v., Vierstra, R.D., and Hofius, D. (2018). Bacteria exploit autophagy for proteasome degradation and enhanced virulence in plants. Plant Cell **30**:668–685. https://doi.org/10.1105/tpc.17.00815.

van Doorn, W.G. (2011). Classes of programmed cell death in plants, compared to those in animals. J. Exp. Bot. **62**:4749–4761. https://doi.org/10.1093/jxb/err196.

van Doorn, W.G., Beers, E.P., Dangl, J.L., Franklin-Tong, V.E., Gallois, P., Hara-Nishimura, I., Jones, A.M., Kawai-Yamada, M., Lam, E., Mundy, J., et al. (2011). Morphological classification of plant cell deaths. Cell Death Differ. **18**:1241–1246. https://doi.org/10.1038/cdd.2011.36.

Vega-Munoz, I., Duran-Flores, D., Fernandez-Fernandez, A.D., Heyman, J., Ritter, A., and Stael, S. (2020). Breaking bad news: dynamic molecular mechanisms of wound response in plants. Front. Plant Sci. **11**:610445. https://doi.org/10.3389/fpls.2020.610445.

Wang, J., Hu, M., Wang, J., Qi, J., Han, Z., Wang, G., Qi, Y., Wang, H.-W., Zhou, J.-M., and Chai, J. (2019). Reconstitution and structure of a plant NLR resistosome conferring immunity. Science **364**:44. https://doi.org/10.1126/science.aav5870.

Wang, J.Z., Wang, J., Hu, M.J., Wu, S., Qi, J.F., Wang, G.X., Han, Z.F., Qi, Y.J., Gao, N., Wang, H.W., et al. (2019). Ligand-triggered allosteric ADP release primes a plant NLR complex. Science **364**:43. https://doi.org/10.1126/science.aav5868.

Ward, T.H., Cummings, J., Dean, E., Greystoke, A., Hou, J.M., Backen, A., Ranson, M., and Dive, C. (2008). Biomarkers of apoptosis. Br. J. Cancer **99**:841–846. https://doi.org/10.1038/sj.bjc.6604519.

Yang, L., Chen, X., Wang, Z., Sun, Q., Hong, A., Zhang, A., Zhong, X., and Hua, J. (2020). HOS15 and HDA9 negatively regulate immunity through histone deacetylation of intracellular immune receptor NLR genes in Arabidopsis. New Phytol. **226**:507–522. https://doi.org/10.1111/nph.16380.

Yu, D., Song, W., Tan, E.Y.J., Tan, J., Liu, L., Cao, Y., Jirschitzka, J., Li, E., Logemann, E., Huang, S., et al. (2021). TIR domains of plant immune receptors are 2′,3′-cAMP/cGMP synthetases mediating cell death. Preprint at bioRxiv Adv., Access published November 10, 2021 https://doi.org/10.1101/2021.11.09.467869.

Yuan, M., Jiang, Z., Bi, G., Nomura, K., Liu, M., Wang, Y., Cai, B., Zhou, J.-M., He, S.Y., Xin, X.-F., et al. (2021a). Pattern-recognition receptors are required for NLR-mediated plant immunity Check for updates. Nature **592**:105–109. https://doi.org/10.1038/s41586-021-03316-6.

Yuan, M., Ngou, B.P.M., Ding, P., and Xin, X.-F. (2021b). PTI-ETI crosstalk: an integrative view of plant immunity. Curr. Opin. Plant Biol. **62**:102030. https://doi.org/10.1016/j.pbi.2021.102030.

Zheng, X.Y., Zhou, M., Yoo, H., Pruneda-Paz, J.L., Spivey, N.W., Kay, S.A., and Dong, X. (2015). Spatial and temporal regulation of biosynthesis of the plant immune signal salicylic acid. Proc. Natl. Acad. Sci. U S A **112**:9166–9173. https://doi.org/10.1073/pnas.1511182112.

Molecular Plant, Volume *15*

Supplemental information

Robust transcriptional indicators of immune cell death revealed by spatiotemporal transcriptome analyses

Jose Salguero-Linares, Irene Serrano, Nerea Ruiz-Solani, Marta Salas-Gómez, Ujjal Jyoti Phukan, Victor Manuel González, Martí Bernardo-Faura, Marc Valls, David Rengel, and Nuria S. Coll

Robust transcriptional indicators of immune cell death revealed by spatio-temporal transcriptome analyses

Jose Salguero-Linares[a,#], Irene Serrano[b, ,#,†], Nerea Ruiz-Solani[a], Marta Salas-Gómez[a], Ujjal Jyoti Phukan[a], Victor Manuel González[a], Martí Bernardo-Faura[a], Marc Valls[a,b], David Rengel[b,c,¥,§,*], Nuria S. Coll[a,d,§,*]

Supplemental Information

Supplementary figures and supplementary tables

Figure S1:

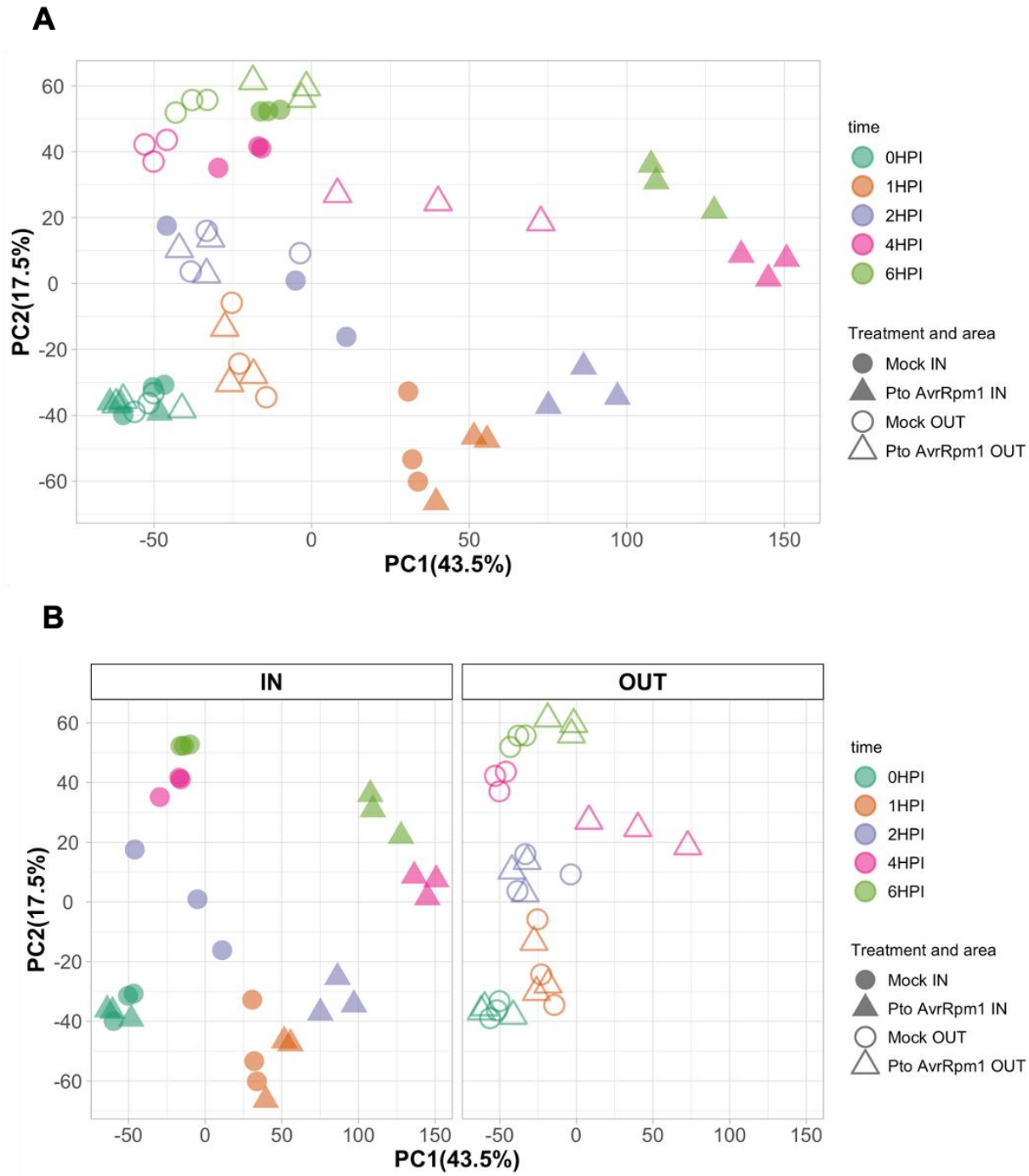

Figure S1. Principal component analysis (PCA) from the RNA seq-data. Circles represent mock-treated plants and triangles represent *Pto AvrRpm1*-infected plants. Different colors are assigned for each time point. **(A)** PCA comprising all data sets in our study (IN and OUT samples together). **(B)** PCA with IN and OUT data sets separated in order to ease visualization of the data.

Figure S2:

A

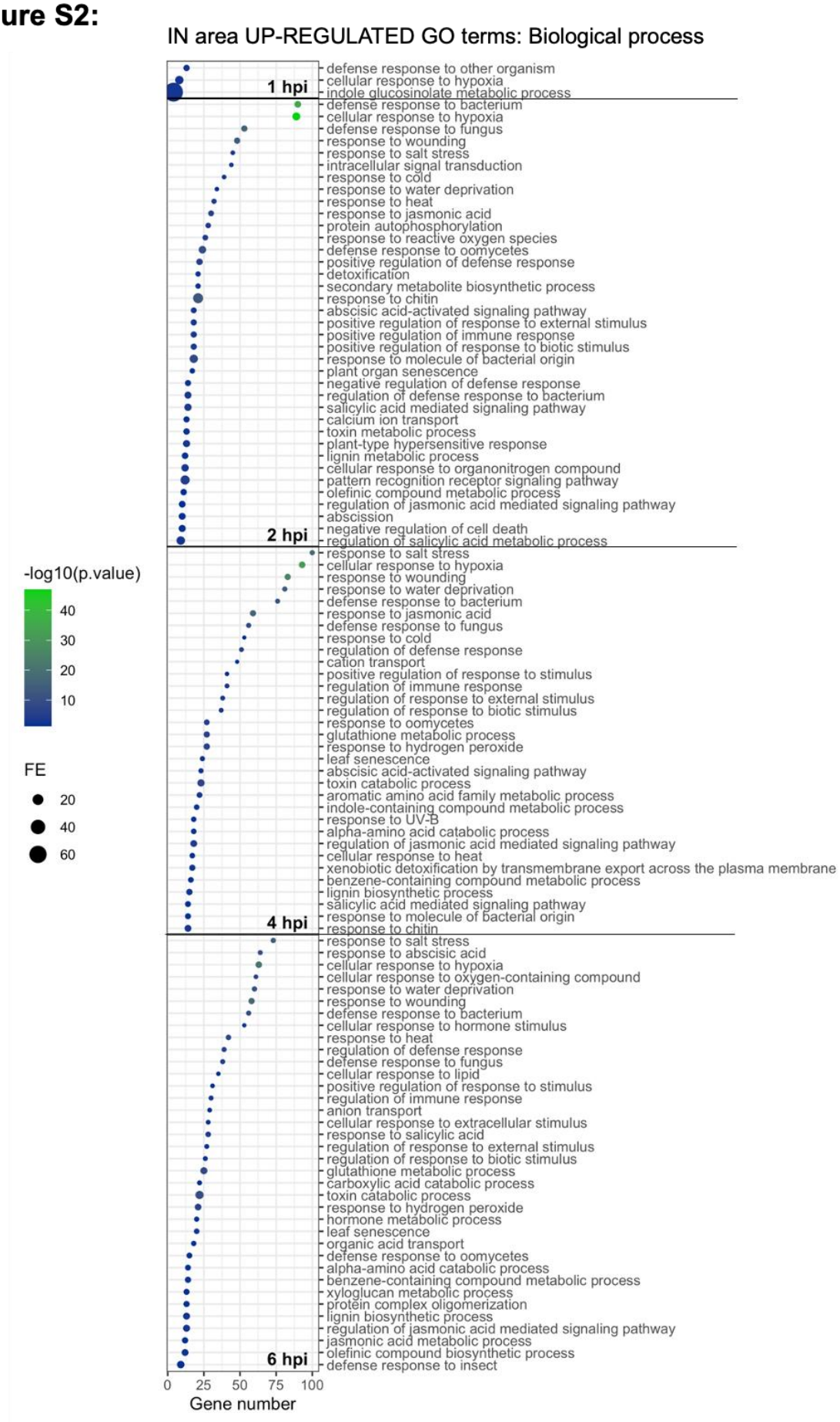
IN area UP-REGULATED GO terms: Biological process
1 hpi
defense response to other organism
cellular response to hypoxia
indole glucosinolate metabolic process
defense response to bacterium
cellular response to hypoxia
defense response to fungus
response to wounding
response to salt stress
intracellular signal transduction
response to cold
response to water deprivation
response to heat
response to jasmonic acid
protein autophosphorylation
response to reactive oxygen species
defense response to oomycetes
positive regulation of defense response
detoxification
secondary metabolite biosynthetic process
response to chitin
abscisic acid-activated signaling pathway
positive regulation of response to external stimulus
positive regulation of immune response
positive regulation of response to biotic stimulus
response to molecule of bacterial origin
plant organ senescence
negative regulation of defense response
regulation of defense response to bacterium
salicylic acid mediated signaling pathway
calcium ion transport
toxin metabolic process
plant-type hypersensitive response
lignin metabolic process
cellular response to organonitrogen compound
pattern recognition receptor signaling pathway
olefinic compound metabolic process
regulation of jasmonic acid mediated signaling pathway
abscission
negative regulation of cell death
2 hpi
regulation of salicylic acid metabolic process
response to salt stress
cellular response to hypoxia
response to wounding
response to water deprivation
defense response to bacterium
response to jasmonic acid
defense response to fungus
response to cold
regulation of defense response
cation transport
positive regulation of response to stimulus
regulation of immune response
regulation of response to external stimulus
regulation of response to biotic stimulus
response to oomycetes
glutathione metabolic process
response to hydrogen peroxide
leaf senescence
abscisic acid-activated signaling pathway
toxin catabolic process
aromatic amino acid family metabolic process
indole-containing compound metabolic process
response to UV-B
alpha-amino acid catabolic process
regulation of jasmonic acid mediated signaling pathway
cellular response to heat
xenobiotic detoxification by transmembrane export across the plasma membrane
benzene-containing compound metabolic process
lignin biosynthetic process
salicylic acid mediated signaling pathway
4 hpi
response to molecule of bacterial origin
response to chitin
response to salt stress
response to abscisic acid
cellular response to hypoxia
cellular response to oxygen-containing compound
response to water deprivation
response to wounding
defense response to bacterium
cellular response to hormone stimulus
response to heat
regulation of defense response
defense response to fungus
cellular response to lipid
positive regulation of response to stimulus
regulation of immune response
anion transport
cellular response to extracellular stimulus
response to salicylic acid
regulation of response to external stimulus
regulation of response to biotic stimulus
glutathione metabolic process
carboxylic acid catabolic process
toxin catabolic process
response to hydrogen peroxide
hormone metabolic process
leaf senescence
organic acid transport
defense response to oomycetes
alpha-amino acid catabolic process
benzene-containing compound metabolic process
xyloglucan metabolic process
protein complex oligomerization
lignin biosynthetic process
regulation of jasmonic acid mediated signaling pathway
jasmonic acid metabolic process
olefinic compound biosynthetic process
6 hpi
defense response to insect
0
25
50
75
100
Gene number
-log10(p.value)
40
30
20
10
FE
20
40
60

B

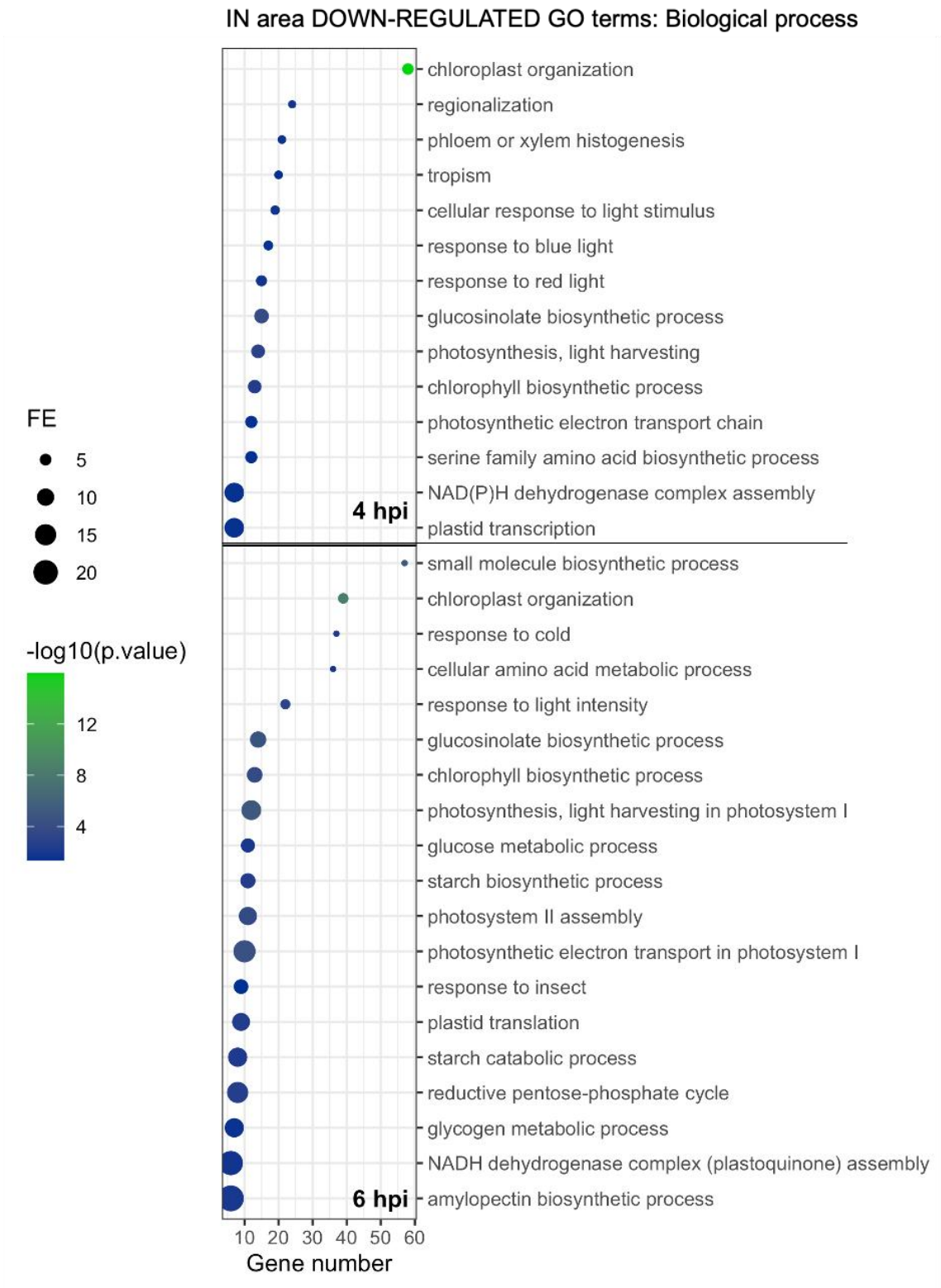
IN area DOWN-REGULATED GO terms: Biological process
chloroplast organization
regionalization
phloem or xylem histogenesis
tropism
cellular response to light stimulus
response to blue light
response to red light
glucosinolate biosynthetic process
photosynthesis, light harvesting
chlorophyll biosynthetic process
photosynthetic electron transport chain
serine family amino acid biosynthetic process
NAD(P)H dehydrogenase complex assembly
plastid transcription
4 hpi
small molecule biosynthetic process
chloroplast organization
response to cold
cellular amino acid metabolic process
response to light intensity
glucosinolate biosynthetic process
chlorophyll biosynthetic process
photosynthesis, light harvesting in photosystem I
glucose metabolic process
starch biosynthetic process
photosystem II assembly
photosynthetic electron transport in photosystem I
response to insect
plastid translation
starch catabolic process
reductive pentose-phosphate cycle
glycogen metabolic process
NADH dehydrogenase complex (plastoquinone) assembly
amylopectin biosynthetic process
6 hpi
10 20 30 40 50 60
Gene number
FE
5
10
15
20
-log10(p.value)
12
8
4

C

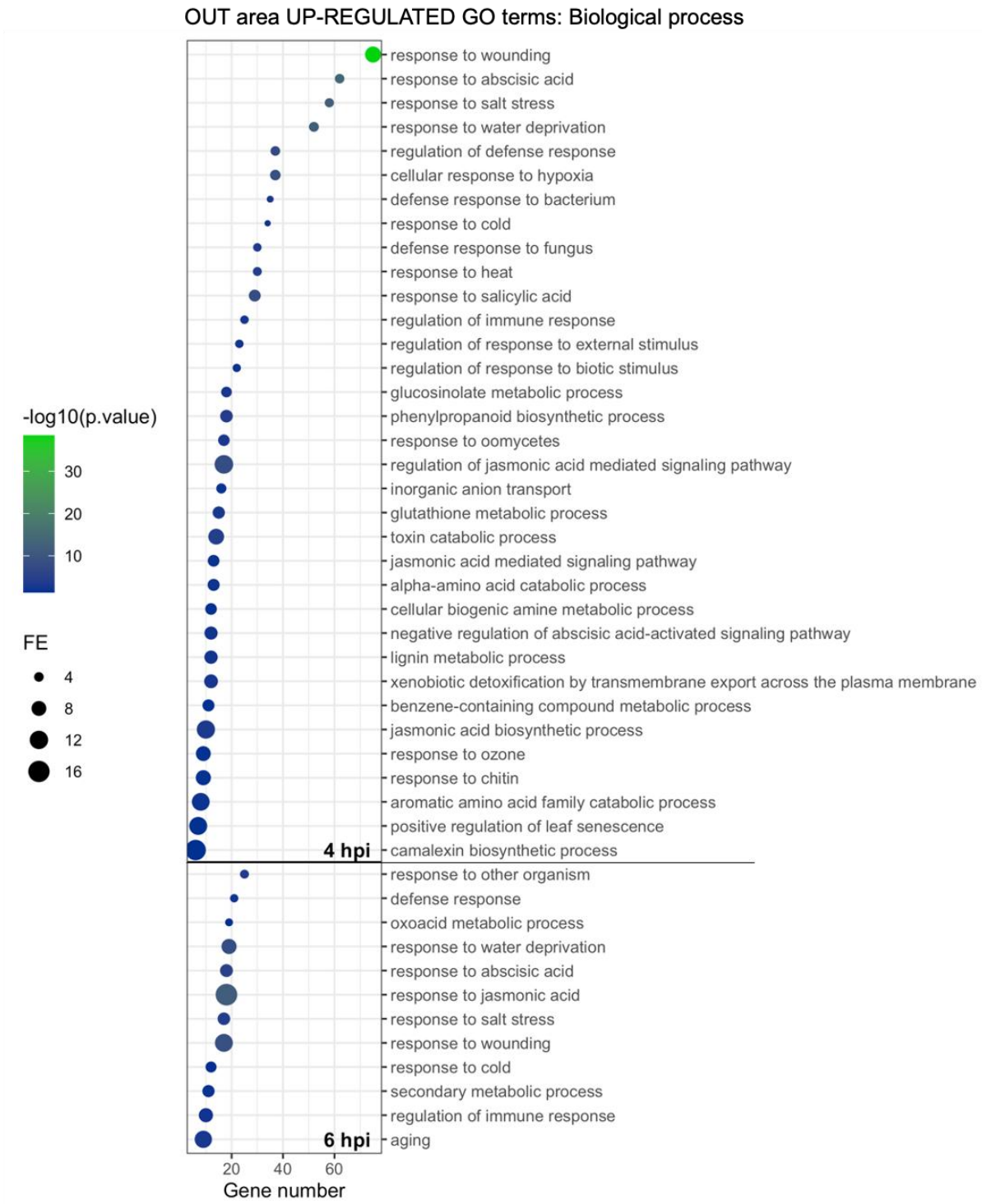
OUT area UP-REGULATED GO terms: Biological process
response to wounding
response to abscisic acid
response to salt stress
response to water deprivation
regulation of defense response
cellular response to hypoxia
defense response to bacterium
response to cold
defense response to fungus
response to heat
response to salicylic acid
regulation of immune response
regulation of response to external stimulus
regulation of response to biotic stimulus
glucosinolate metabolic process
phenylpropanoid biosynthetic process
response to oomycetes
regulation of jasmonic acid mediated signaling pathway
inorganic anion transport
glutathione metabolic process
toxin catabolic process
jasmonic acid mediated signaling pathway
alpha-amino acid catabolic process
cellular biogenic amine metabolic process
negative regulation of abscisic acid-activated signaling pathway
lignin metabolic process
xenobiotic detoxification by transmembrane export across the plasma membrane
benzene-containing compound metabolic process
jasmonic acid biosynthetic process
response to ozone
response to chitin
aromatic amino acid family catabolic process
positive regulation of leaf senescence
camalexin biosynthetic process
4 hpi
response to other organism
defense response
oxoacid metabolic process
response to water deprivation
response to abscisic acid
response to jasmonic acid
response to salt stress
response to wounding
response to cold
secondary metabolic process
regulation of immune response
aging
6 hpi
20
40
60
Gene number
-log10(p.value)
30
20
10
FE
4
8
12
16

Figure S2. GO term enrichment analysis of upregulated and downregulated genes at each time after infection at the IN **(A-B)** and OUT **(C)** areas. The most specific term from each family term provided by PANTHER was plotted along with their corresponding gene number, fold enrichment and adj p value (Bonferroni Correction for multiple testing) represented as $\log_{10}$. Only GO terms with a fold enrichment above 2 and adj p value below 0.05 were plotted.

Figure S3:

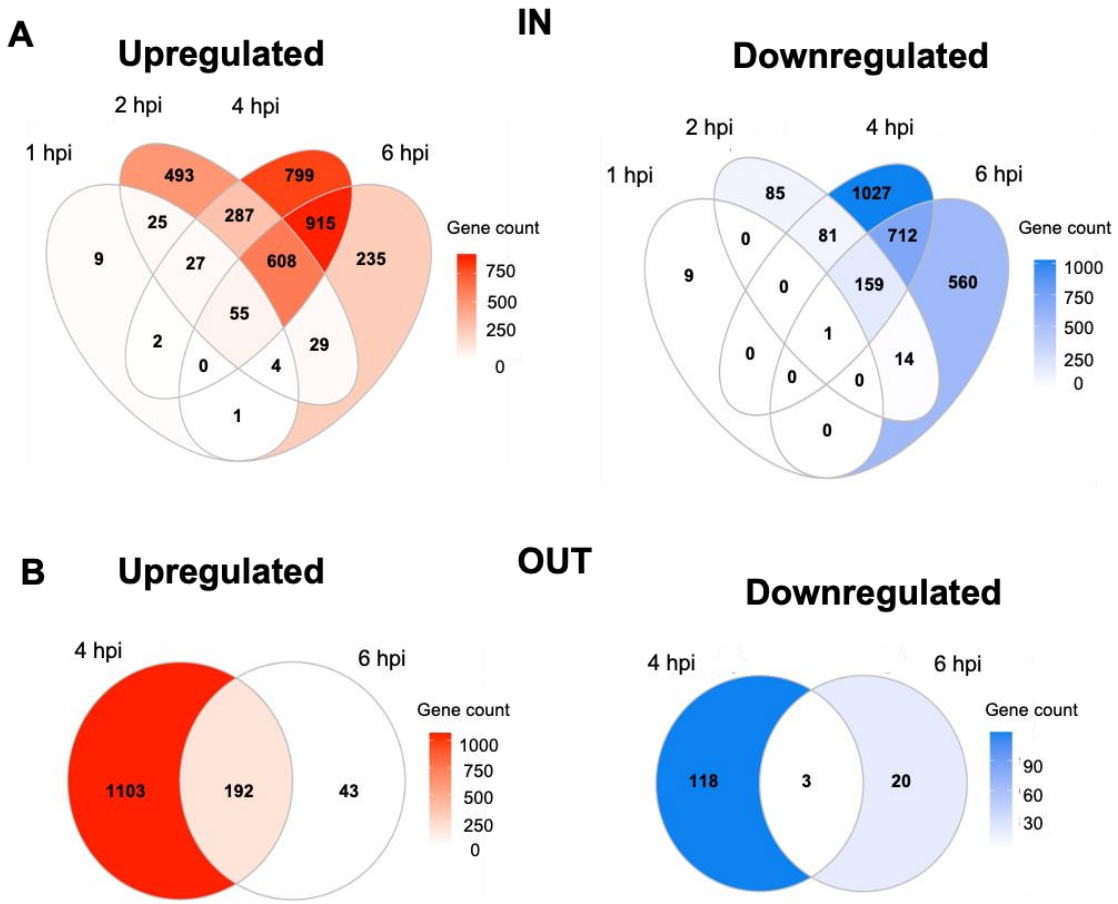

Figure S3. The majority of differentially expressed genes at both IN and OUT are specific to 4 and 6 hpi. Venn diagrams showing sizes of gene sets that are differentially expressed (red: upregulated and blue: downregulated) at IN **(A)** or OUT **(B)** at each time point.

Figure S4

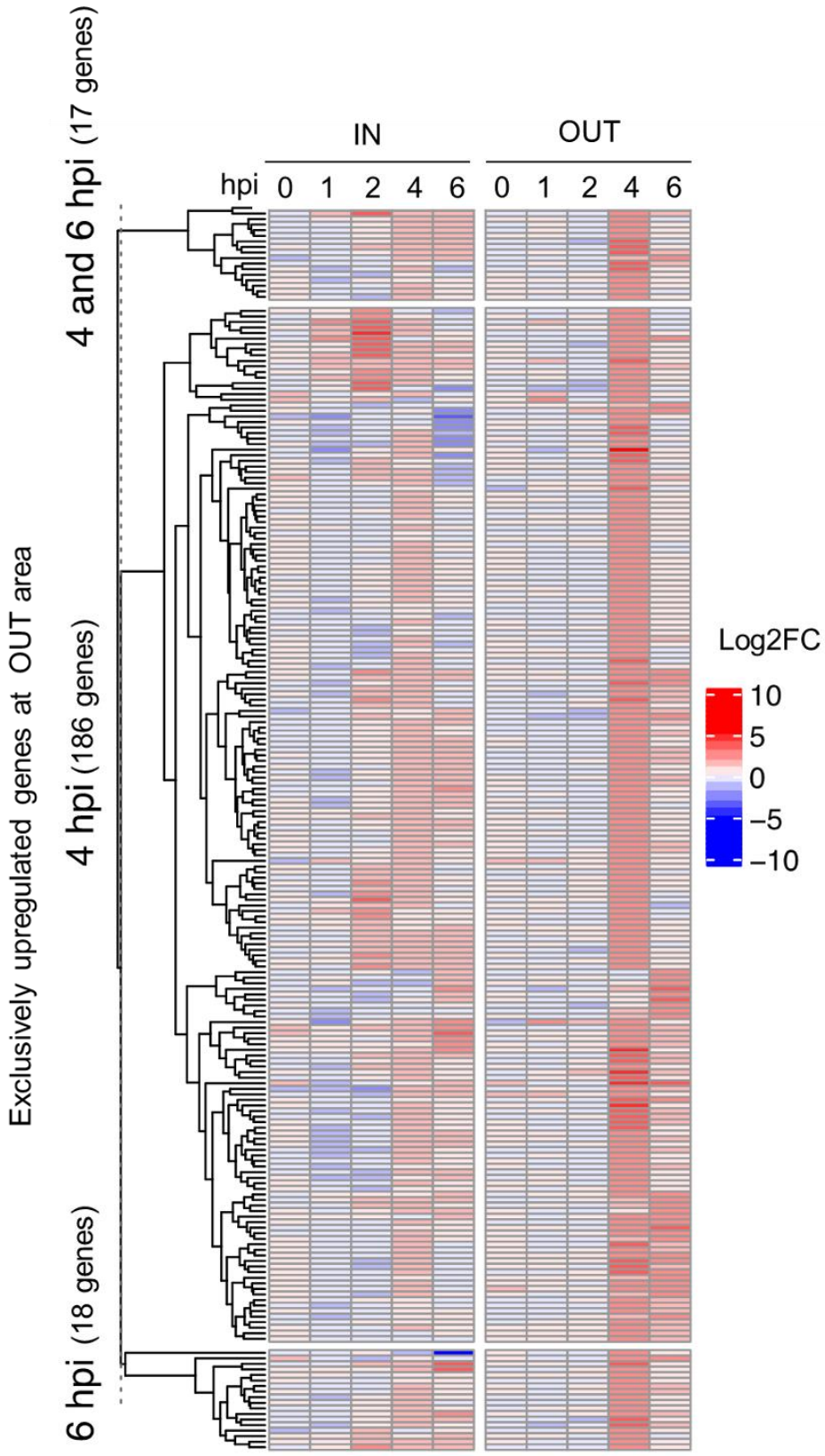
Exclusively upregulated genes at OUT area
6 hpi (18 genes)
4 hpi (186 genes)
4 and 6 hpi (17 genes)
hpi
IN
OUT
0 1 2 4 6
0 1 2 4 6
Log2FC
10
5
0
−5
−10

Figure S4. Heatmap representing differential expression of genes exclusively upregulated at 4 and/or 6 hpi at the OUT area (log2FC > 2 and BTH <0.05) throughout the course of the infection (0,1,2,4 and 6 hpi) at IN and OUT areas.

Figure S5

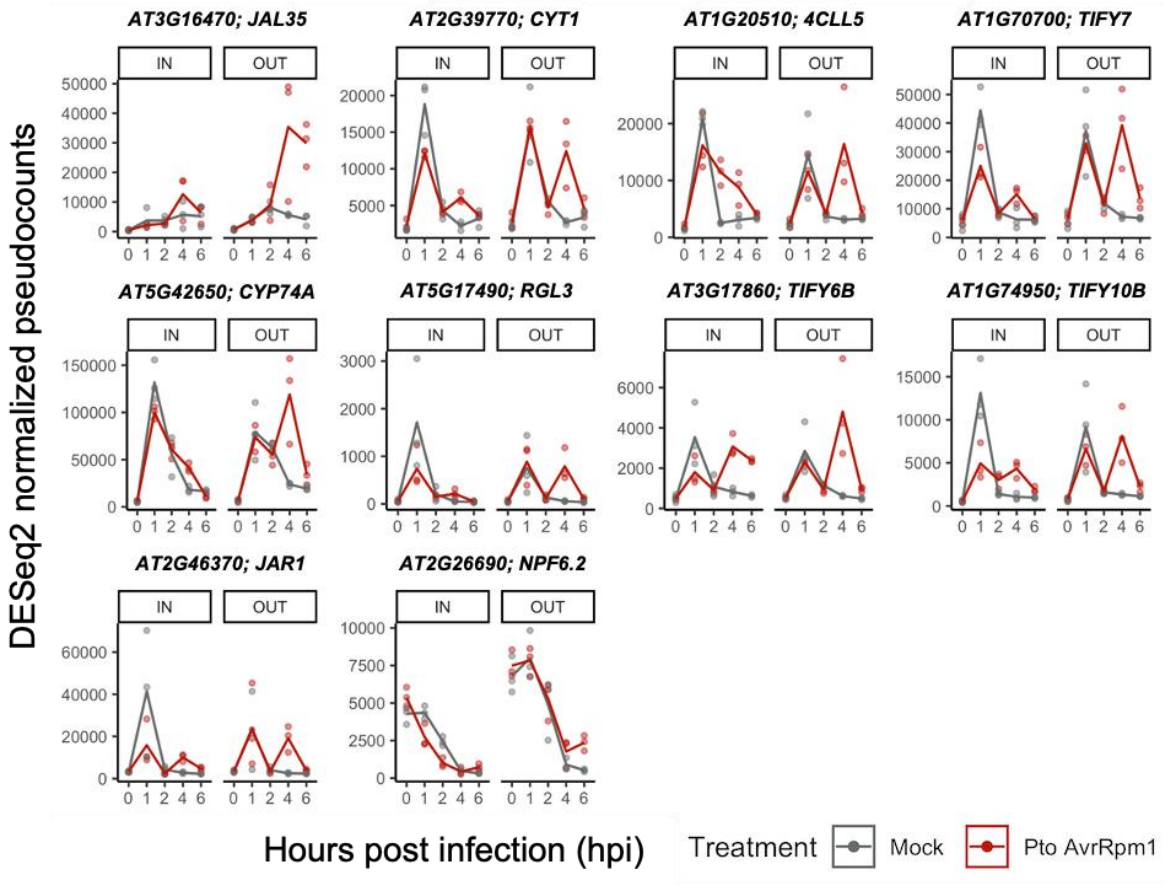

Figure S5. RNA-seq expression profiles of JA responsive genes exclusively upregulated at the OUT area upon *Pto AvrRpm1* infection. Gene expression of genes from *Pto-AvrRpm1* or mock-infected plants is represented as DESeq2 pseudocounts.

JAL35, Jacalin-related lectin 35; *CYT1,* Mannose-1-phosphate guanylyltransferase 1; *4CLL5,* 4-coumarate--CoA ligase-like 5; *TIFY7,* Protein TIFY 7; *CYP74A,* Allene oxide synthase, chloroplastic; *RGL3,,* DELLA protein RGL3; *TIFY6B,* Protein TIFY 6B; *TIFY10B,* Protein

TIFY 10B; *JAR1,* Jasmonoyl--L-amino acid synthetase JAR1; *NPF6.2,* Protein NRT1/ PTR FAMILY 6.2

Figure S6.

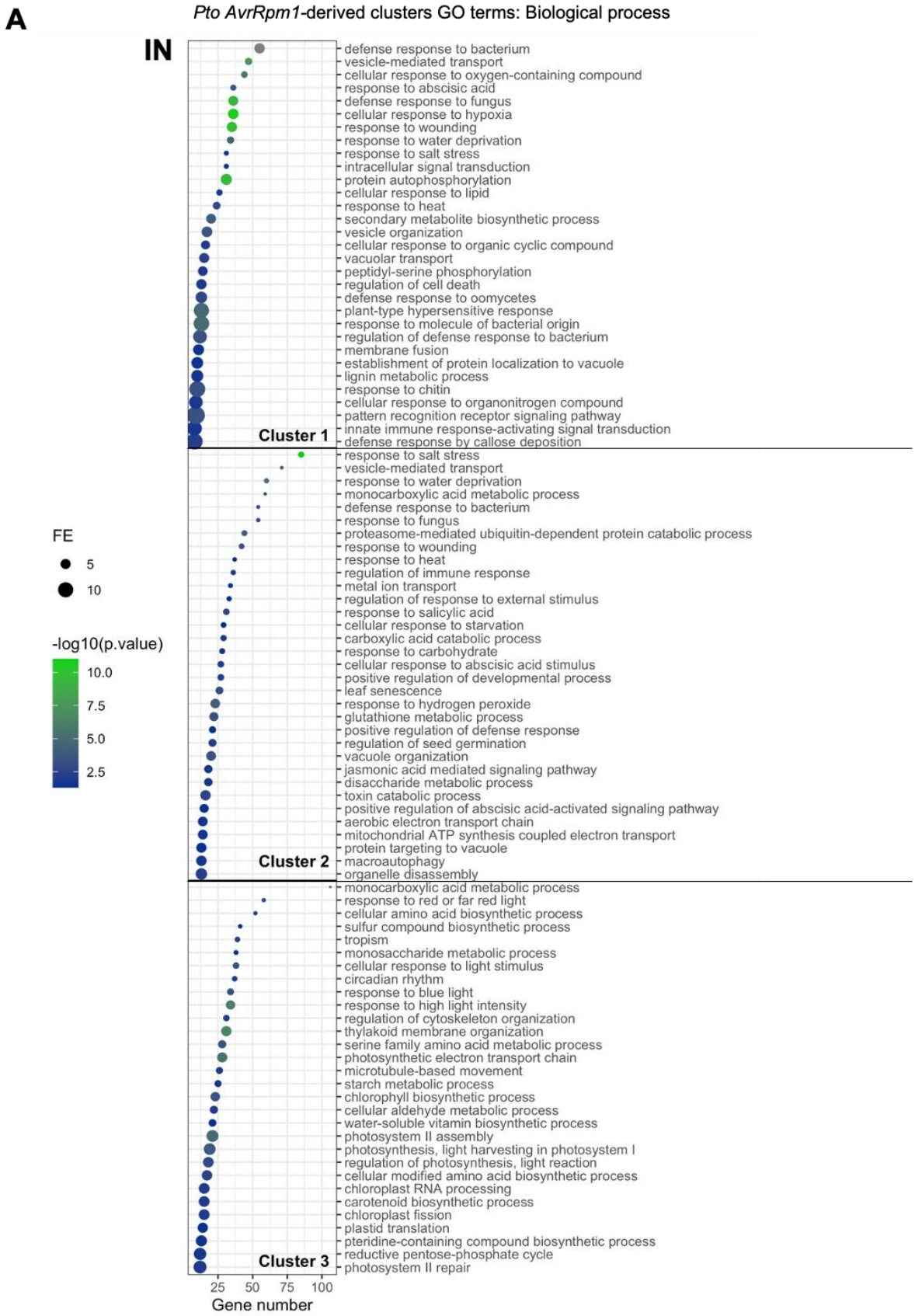
A
Pto AvrRpm1-derived clusters GO terms: Biological process
IN
defense response to bacterium
vesicle-mediated transport
cellular response to oxygen-containing compound
response to abscisic acid
defense response to fungus
cellular response to hypoxia
response to wounding
response to water deprivation
response to salt stress
intracellular signal transduction
protein autophosphorylation
cellular response to lipid
response to heat
secondary metabolite biosynthetic process
vesicle organization
cellular response to organic cyclic compound
vacuolar transport
peptidyl-serine phosphorylation
regulation of cell death
defense response to oomycetes
plant-type hypersensitive response
response to molecule of bacterial origin
regulation of defense response to bacterium
membrane fusion
establishment of protein localization to vacuole
lignin metabolic process
response to chitin
cellular response to organonitrogen compound
pattern recognition receptor signaling pathway
innate immune response-activating signal transduction
defense response by callose deposition
Cluster 1
response to salt stress
vesicle-mediated transport
response to water deprivation
monocarboxylic acid metabolic process
defense response to bacterium
response to fungus
proteasome-mediated ubiquitin-dependent protein catabolic process
response to wounding
response to heat
regulation of immune response
metal ion transport
regulation of response to external stimulus
response to salicylic acid
cellular response to starvation
carboxylic acid catabolic process
response to carbohydrate
cellular response to abscisic acid stimulus
positive regulation of developmental process
leaf senescence
response to hydrogen peroxide
glutathione metabolic process
positive regulation of defense response
regulation of seed germination
vacuole organization
jasmonic acid mediated signaling pathway
disaccharide metabolic process
toxin catabolic process
positive regulation of abscisic acid-activated signaling pathway
aerobic electron transport chain
mitochondrial ATP synthesis coupled electron transport
protein targeting to vacuole
macroautophagy
organelle disassembly
Cluster 2
monocarboxylic acid metabolic process
response to red or far red light
cellular amino acid biosynthetic process
sulfur compound biosynthetic process
tropism
monosaccharide metabolic process
cellular response to light stimulus
circadian rhythm
response to blue light
response to high light intensity
regulation of cytoskeleton organization
thylakoid membrane organization
serine family amino acid metabolic process
photosynthetic electron transport chain
microtubule-based movement
starch metabolic process
chlorophyll biosynthetic process
cellular aldehyde metabolic process
water-soluble vitamin biosynthetic process
photosystem II assembly
photosynthesis, light harvesting in photosystem I
regulation of photosynthesis, light reaction
cellular modified amino acid biosynthetic process
chloroplast RNA processing
carotenoid biosynthetic process
chloroplast fission
plastid translation
pteridine-containing compound biosynthetic process
reductive pentose-phosphate cycle
photosystem II repair
Cluster 3
25
50
75
100
Gene number
FE
5
10
-log10(p.value)
10.0
7.5
5.0
2.5

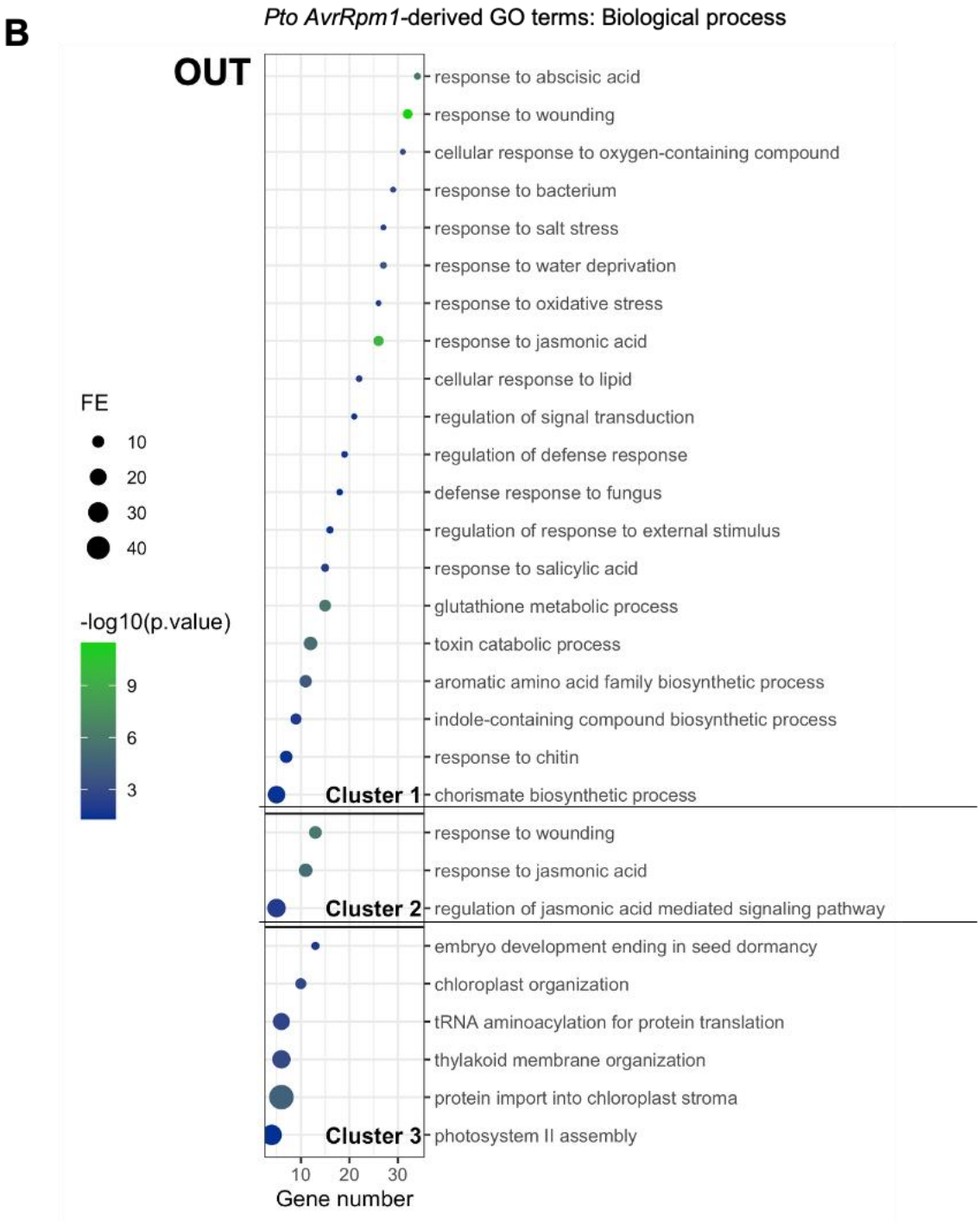

Figure S6. GO terms representing enriched biological processes derived from each cluster in *Pto AvrRpm1*-treated plants. GO term enrichment analysis was performed on those genes that had a membership score value (MSV) above or equal to 0.7 (see Materials and Methods). The most specific term from each family provided by PANTHER was plotted along with their corresponding gene number, fold enrichment (FE) and adj p value (Bonferroni Correction for

multiple testing) represented as log_{10}. Only GO Terms with a FE above 2 and adj p value below 0.05 were plotted. Enriched GO terms from cluster I (2,937 genes; MSV > 0.7 → 1069 genes), cluster II (4,183 genes; MSV > 0.7 → 2613 genes) and cluster III (6,428 genes; MSV > 0.7 → 4885 genes) at the IN area **(A)** in *Pto AvrRpm1*-treated plants were predominantly linked to processes related to immunity, protein turnover and photosynthesis, respectively. At the OUT area **(B)**, enriched GO terms from cluster I (1,552 genes; MS > 0.7 → 747 genes) and II (1,100 genes; MS > 0.7 → 184) suggest the importance of processes related to hormonal regulation in by-stander cells, whereas genes comprising cluster III (925 genes; MS > 0.7 → 181 genes) infer that photosynthesis and rearrangements in the chloroplast occur similarly compared to mock-treated samples at the OUT area

Figure S7

A

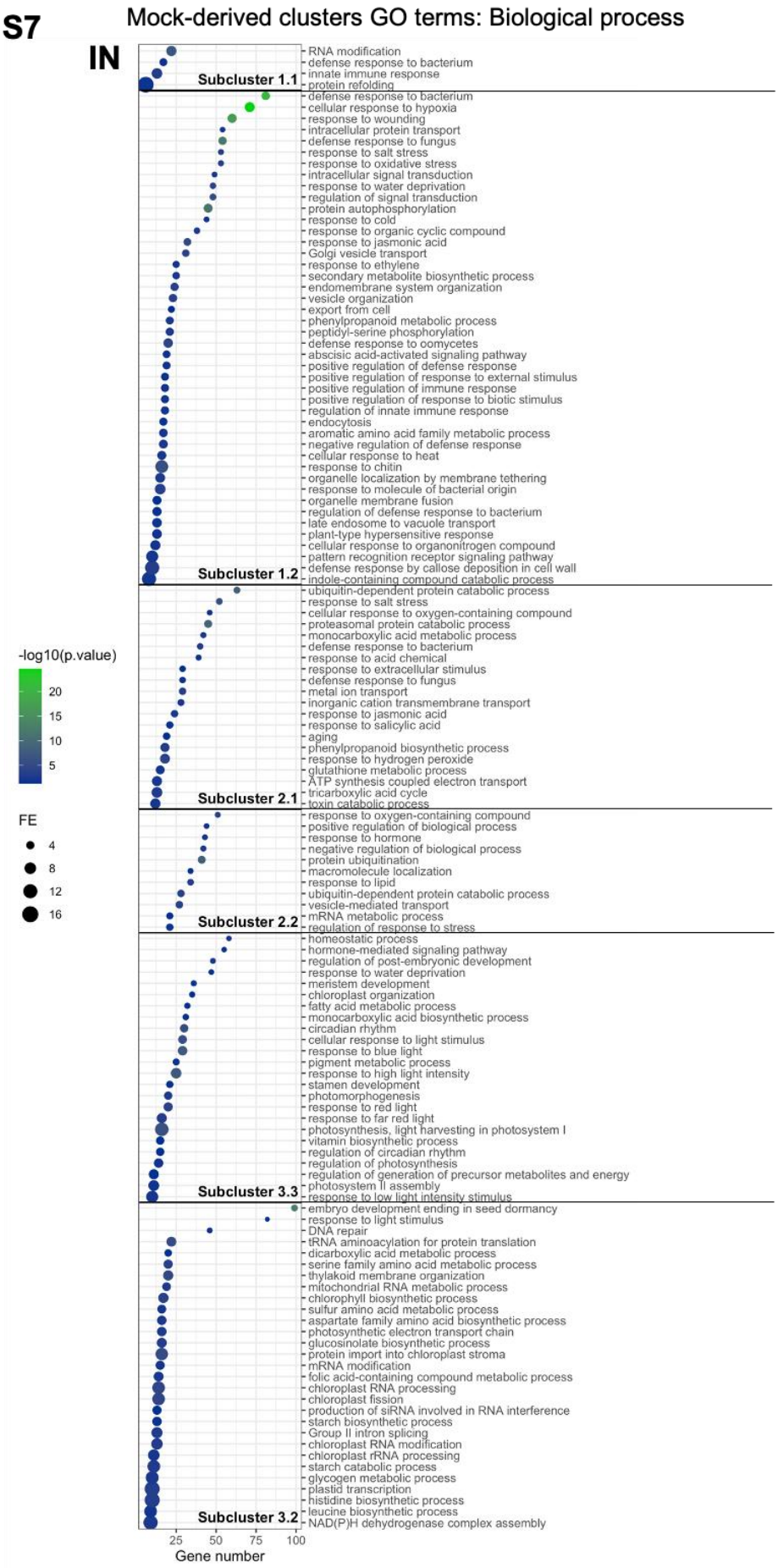
Mock-derived clusters GO terms: Biological process
IN
Subcluster 1.1
RNA modification
defense response to bacterium
innate immune response
protein refolding
Subcluster 1.2
defense response to bacterium
cellular response to hypoxia
response to wounding
intracellular protein transport
defense response to fungus
response to salt stress
response to oxidative stress
intracellular signal transduction
response to water deprivation
regulation of signal transduction
protein autophosphorylation
response to cold
response to organic cyclic compound
response to jasmonic acid
Golgi vesicle transport
response to ethylene
secondary metabolite biosynthetic process
endomembrane system organization
vesicle organization
export from cell
phenylpropanoid metabolic process
peptidyl-serine phosphorylation
defense response to oomycetes
abscisic acid-activated signaling pathway
positive regulation of defense response
positive regulation of response to external stimulus
positive regulation of immune response
positive regulation of response to biotic stimulus
regulation of innate immune response
endocytosis
aromatic amino acid family metabolic process
negative regulation of defense response
cellular response to heat
response to chitin
organelle localization by membrane tethering
response to molecule of bacterial origin
organelle membrane fusion
regulation of defense response to bacterium
late endosome to vacuole transport
plant-type hypersensitive response
cellular response to organonitrogen compound
pattern recognition receptor signaling pathway
defense response by callose deposition in cell wall
indole-containing compound catabolic process
Subcluster 2.1
ubiquitin-dependent protein catabolic process
response to salt stress
cellular response to oxygen-containing compound
proteasomal protein catabolic process
monocarboxylic acid metabolic process
defense response to bacterium
response to acid chemical
response to extracellular stimulus
defense response to fungus
metal ion transport
inorganic cation transmembrane transport
response to jasmonic acid
response to salicylic acid
aging
phenylpropanoid biosynthetic process
response to hydrogen peroxide
glutathione metabolic process
ATP synthesis coupled electron transport
tricarboxylic acid cycle
toxin catabolic process
Subcluster 2.2
response to oxygen-containing compound
positive regulation of biological process
response to hormone
negative regulation of biological process
protein ubiquitination
macromolecule localization
response to lipid
ubiquitin-dependent protein catabolic process
vesicle-mediated transport
mRNA metabolic process
regulation of response to stress
Subcluster 3.3
homeostatic process
hormone-mediated signaling pathway
regulation of post-embryonic development
response to water deprivation
meristem development
chloroplast organization
fatty acid metabolic process
monocarboxylic acid biosynthetic process
circadian rhythm
cellular response to light stimulus
response to blue light
pigment metabolic process
response to high light intensity
stamen development
photomorphogenesis
response to red light
response to far red light
photosynthesis, light harvesting in photosystem I
vitamin biosynthetic process
regulation of circadian rhythm
regulation of photosynthesis
regulation of generation of precursor metabolites and energy
photosystem II assembly
response to low light intensity stimulus
Subcluster 3.2
embryo development ending in seed dormancy
response to light stimulus
DNA repair
tRNA aminoacylation for protein translation
dicarboxylic acid metabolic process
serine family amino acid metabolic process
thylakoid membrane organization
mitochondrial RNA metabolic process
chlorophyll biosynthetic process
sulfur amino acid metabolic process
aspartate family amino acid biosynthetic process
photosynthetic electron transport chain
glucosinolate biosynthetic process
protein import into chloroplast stroma
mRNA modification
folic acid-containing compound metabolic process
chloroplast RNA processing
chloroplast fission
production of siRNA involved in RNA interference
starch biosynthetic process
Group II intron splicing
chloroplast RNA modification
chloroplast rRNA processing
starch catabolic process
glycogen metabolic process
plastid transcription
histidine biosynthetic process
leucine biosynthetic process
NAD(P)H dehydrogenase complex assembly
25
50
75
100
Gene number
-log10(p.value)
20
15
10
5
FE
4
8
12
16

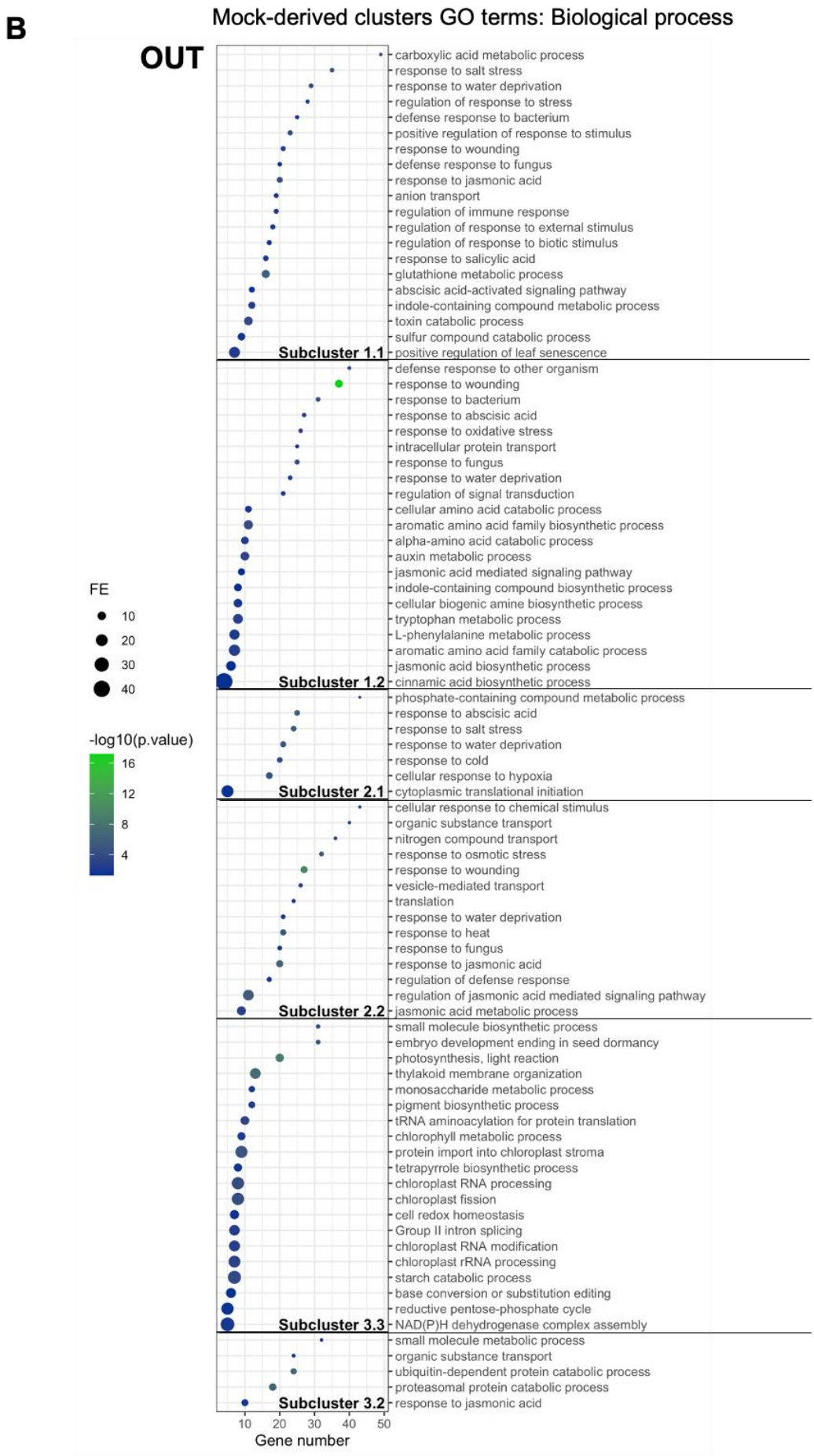
B
Mock-derived clusters GO terms: Biological process
OUT
carboxylic acid metabolic process
response to salt stress
response to water deprivation
regulation of response to stress
defense response to bacterium
positive regulation of response to stimulus
response to wounding
defense response to fungus
response to jasmonic acid
anion transport
regulation of immune response
regulation of response to external stimulus
regulation of response to biotic stimulus
response to salicylic acid
glutathione metabolic process
abscisic acid-activated signaling pathway
indole-containing compound metabolic process
toxin catabolic process
sulfur compound catabolic process
Subcluster 1.1
positive regulation of leaf senescence
defense response to other organism
response to wounding
response to bacterium
response to abscisic acid
response to oxidative stress
intracellular protein transport
response to fungus
response to water deprivation
regulation of signal transduction
cellular amino acid catabolic process
aromatic amino acid family biosynthetic process
alpha-amino acid catabolic process
auxin metabolic process
jasmonic acid mediated signaling pathway
indole-containing compound biosynthetic process
cellular biogenic amine biosynthetic process
tryptophan metabolic process
L-phenylalanine metabolic process
aromatic amino acid family catabolic process
jasmonic acid biosynthetic process
Subcluster 1.2
cinnamic acid biosynthetic process
phosphate-containing compound metabolic process
response to abscisic acid
response to salt stress
response to water deprivation
response to cold
cellular response to hypoxia
Subcluster 2.1
cytoplasmic translational initiation
cellular response to chemical stimulus
organic substance transport
nitrogen compound transport
response to osmotic stress
response to wounding
vesicle-mediated transport
translation
response to water deprivation
response to heat
response to fungus
response to jasmonic acid
regulation of defense response
regulation of jasmonic acid mediated signaling pathway
Subcluster 2.2
jasmonic acid metabolic process
small molecule biosynthetic process
embryo development ending in seed dormancy
photosynthesis, light reaction
thylakoid membrane organization
monosaccharide metabolic process
pigment biosynthetic process
tRNA aminoacylation for protein translation
chlorophyll metabolic process
protein import into chloroplast stroma
tetrapyrrole biosynthetic process
chloroplast RNA processing
chloroplast fission
cell redox homeostasis
Group II intron splicing
chloroplast RNA modification
chloroplast rRNA processing
starch catabolic process
base conversion or substitution editing
reductive pentose-phosphate cycle
Subcluster 3.3
NAD(P)H dehydrogenase complex assembly
small molecule metabolic process
organic substance transport
ubiquitin-dependent protein catabolic process
proteasomal protein catabolic process
Subcluster 3.2
response to jasmonic acid
10
20
30
40
50
Gene number
FE
10
20
30
40
-log10(p.value)
16
12
8
4

Figure S7. GO terms representing enriched biological processes derived from each sub-cluster in mock-treated plants at the IN and OUT areas. From each cluster belonging to mock-treated samples, GO term enrichment analysis was performed on those genes that had a membership score value (MSV) above or equal to 0.7 at the IN (a) and OUT areas (b). The most specific term from each family term provided by PANTHER was plotted along with their corresponding gene number, fold enrichment and adj p value (Bonferroni Correction for multiple testing) represented as $\log_{10}$. Only GO Terms with a fold enrichment above 2 and adj p value below 0.05 were plotted. **(A)** Sub-cluster 1.1 (638 genes; MSV >= 0.7 → 467 genes), sub-cluster 1.2 (2299 genes; MSV >= 0.7 → 1942 genes), sub-cluster 2.1 (2570 genes; MSV >= 0.7 → 1573 genes), sub-cluster 2.2 (1613 genes; MSV >= 0.7 → 649 genes), sub-cluster 3.1 (3172 genes; MSV >= 0.7 → 2391 genes), sub-cluster 3.2 (3256 genes; MSV >= 0.7 → 2557 genes). **(B)** Sub-cluster 1.1 (850 genes; MSV >= 0.7 → 319 genes), sub-cluster 1.2 (702 genes; MSV >= 0.7 → 183 genes), sub-cluster 2.1 (453 genes; MSV >= 0.7 → 286 genes), sub-cluster 2.2 (647 genes; MSV >= 0.7 → 389 genes), sub-cluster 3.1 (612 genes; MSV >= 0.7 → 555 genes), sub-cluster 3.2 (313 genes; MSV >= 0.7 → 257 genes).

Figure S8

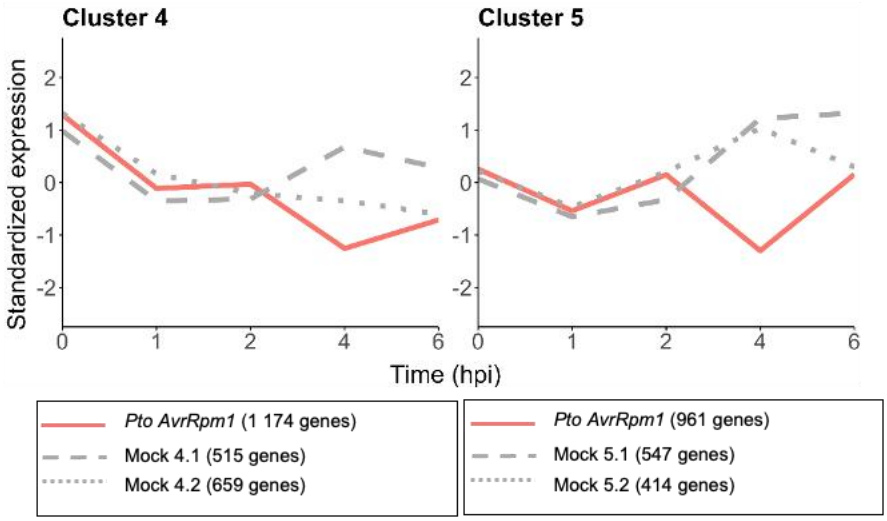

Figure S8. Clusters 4 (1,174 genes; MSV >= 0.7 → 57 genes) and 5 (961 genes; MSV >= 0.7 → 314 genes) from *Pto AvrRpm1*-treated plants at the OUT area share similar expression profiles and do not contain any relevant enriched GO terms associated with biological processes, possibly due to low gene number.

Figure S9

A

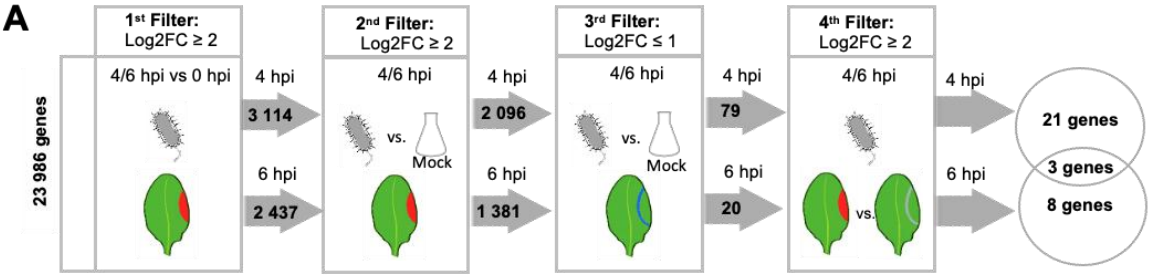

B

	Gene ID	1st Filter	2nd Filter	3rd Filter	4th Filter	Gene description
4 hpi	AT1G24095	4.03	2.49	0.77	2.36	Putative thiol-disulfide oxidoreductase DCC
	AT1G27720	3.51	3.01	0.94	2.55	Transcription initiation factor TFIID subunit 4 (TAF4)
	AT1G30270	2.59	3.07	0.67	2.54	CBL-interacting serine/threonine-protein kinase 23 (CIPK23)
	AT1G31880	3.00	3.27	0.84	2.56	DZC domain containing protein (NLM9)
	AT1G74810	3.70	3.09	0.90	2.51	Putative boron transporter 5 (BOR5)
	AT1G79710	3.50	2.94	0.85	2.11	Probable folate-biopterin transporter 3
	AT2G33120	2.74	2.71	0.86	2.13	Vesicle-associated membrane protein 722 (SAR1/VAMP722)
	AT2G39400	3.46	2.38	-1.08	3.61	Alpha/beta-Hydrolases superfamily protein
	AT3G04120	2.24	2.29	0.50	2.01	Glyceraldehyde-3-phosphate dehydrogenase (GAPC1)
	AT3G13782	3.38	2.95	0.83	2.85	Nucleosome assembly protein 1;4 (NAP 1;4)
	AT3G28850	2.72	2.16	0.79	2.14	Glutaredoxin family protein
	AT3G60680	2.03	2.87	0.70	2.05	DUF641 family protein
	AT4G18050	4.47	4.57	0.79	3.56	P-glycoprotein 9 (PGP9)
	AT4G24160	2.66	3.43	0.99	2.68	1-acylglycerol-3-phosphate O-acyltransferase
	AT4G30390	3.33	3.42	0.98	2.54	UDP-arabinopyranose mutase
	AT5G10820	3.55	2.01	0.72	2.05	Probable folate-biopterin transporter 6
	AT5G18480	2.86	2.54	0.94	2.04	Inositol phosphorylceramide glucuronosyltransferase1(IPUT1)
	AT5G20000	3.67	2.50	0.79	2.25	26S proteasome regulatory subunit 8 homolog B (RPT6B)
	AT2G36580	2.51	2.58	0.77	2.36	Pyruvate kinase
	AT5G37710	2.14	2.29	0.56	2.02	alpha/beta-Hydrolases superfamily protein
	AT5G54650	4.05	3.21	0.99	2.21	Formin-like protein 5 (FH5)
6 hpi	AT1G78380	3.88	3.45	0.96	3.88	Glutathione S-transferase U19 (GSTU19)
	AT3G02875	3.35	2.92	0.93	3.35	IAA-amino acid hydrolase (ILR1)
	AT3G06420	3.41	3.14	0.83	3.41	Autophagy-related protein 8h (ATG8H)
	AT3G17420	2.75	2.63	0.72	2.75	Probable receptor-like protein kinase (GPK1)
	AT5G05730	4.10	2.90	0.96	4.10	Anthranilate synthase alpha subunit 1 (ASA1)
	AT5G14730	3.47	3.17	-1.41	3.47	Unknown protein
	AT5G16910	2.26	2.83	0.96	2.26	Cellulose synthase-like protein D2 (CSLD2)
	AT5G17760	3.64	2.54	0.98	3.64	AAA-ATPase
4/6 hpi	AT5G20910	2.78	2.59	0.74	2.06	E3 ubiquitin-protein ligase (AIP2)
	AT2G31390	2.55	2.73	0.84	2.04	Probable fructokinase-1
	AT5G56350	3.20	2.55	0.79	2.22	Pyruvate kinase

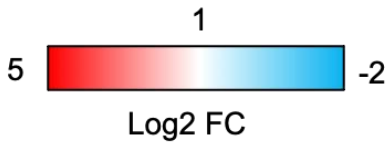

Figure S9. List of *in silico* HR indicators obtained after filtering at 4 and 6 hpi. **(A)** Briefly, we firstly selected genes that were upregulated (log2FC > 2) after *Pto AvrRpm1* infection at 4 or 6 hpi vs 0 hpi. From the genes that complied with this first filter, we selected those that were specifically upregulated in *Pto AvrRpm1*-infected vs mock-inoculated samples at 4 or 6 hpi (log2FC >2). From the genes that complied these criteria, we kept those with a log2FC <1 at the OUT area in *Pto AvrRpm1*-infected vs mock-inoculated samples at 4 or 6 hpi. Finally, from the genes that met those three criteria, we kept those that were differentially upregulated at the IN area compared to the OUT area in *Pto AvrRpm1*-infected plants. **(B)** Log_2FCs resulting from pairwise comparisons in the 1st, 2^{nd,} 3rd and 4th filters applied are indicated for each gene marker along with its corresponding gene description.

Figure S10

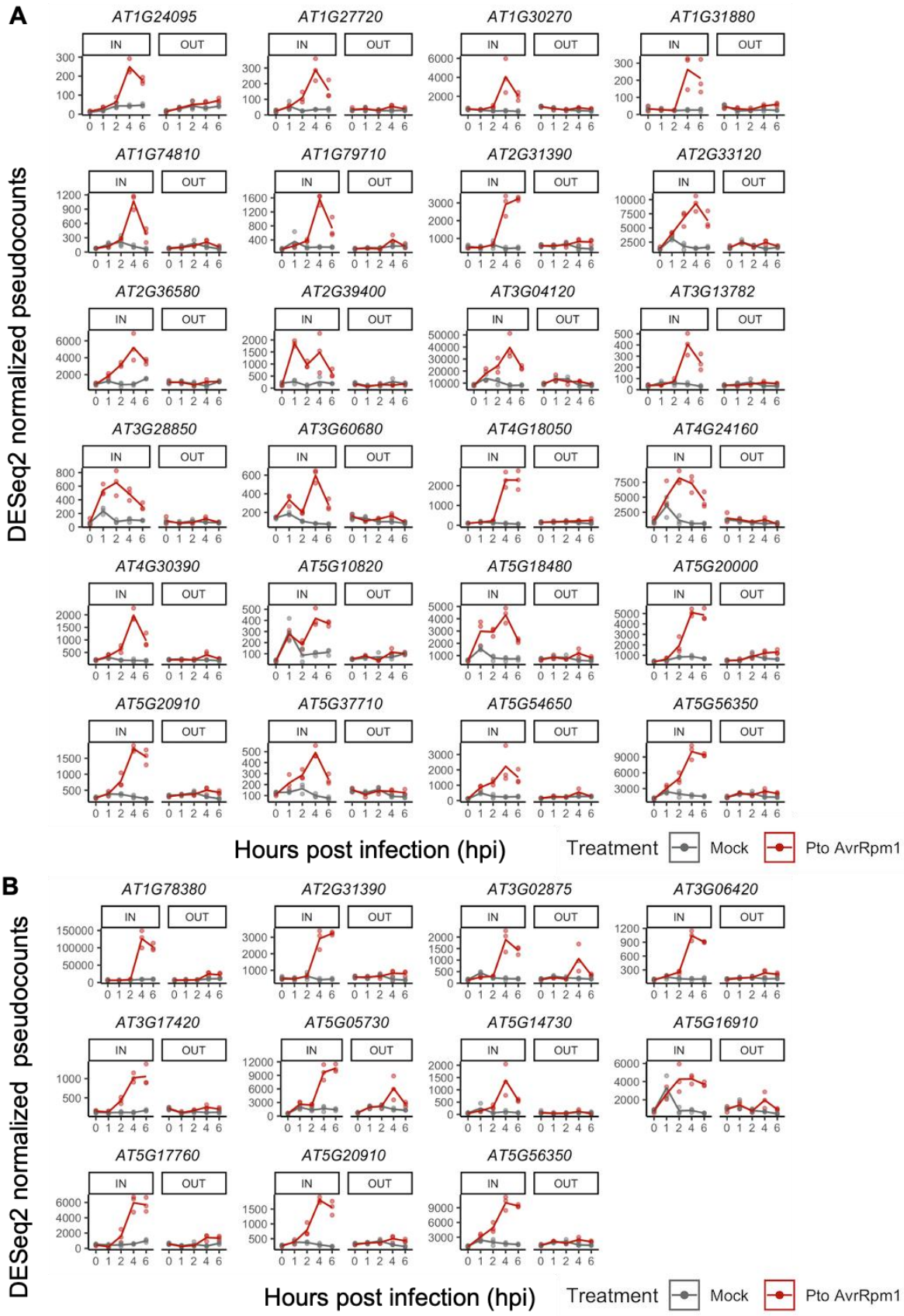
A
AT1G24095
AT1G27720
AT1G30270
AT1G31880
AT1G74810
AT1G79710
AT2G31390
AT2G33120
AT2G36580
AT2G39400
AT3G04120
AT3G13782
AT3G28850
AT3G60680
AT4G18050
AT4G24160
AT4G30390
AT5G10820
AT5G18480
AT5G20000
AT5G20910
AT5G37710
AT5G54650
AT5G56350
IN
OUT
DESeq2 normalized pseudocounts
Hours post infection (hpi)
Treatment
Mock
Pto AvrRpm1
B
AT1G78380
AT2G31390
AT3G02875
AT3G06420
AT3G17420
AT5G05730
AT5G14730
AT5G16910
AT5G17760
AT5G20910
AT5G56350
DESeq2 normalized pseudocounts
Hours post infection (hpi)
Treatment
Mock
Pto AvrRpm1

Figure S10. RNA-seq expression profiles of 4 **(A)** and 6 **(B)** hour candidate HR indicators at the IN and OUT areas of infection. Gene expression of genes from *Pto-AvrRpm1* or mock-infected plants is represented as DESeq2 pseudocounts.

Figure S11

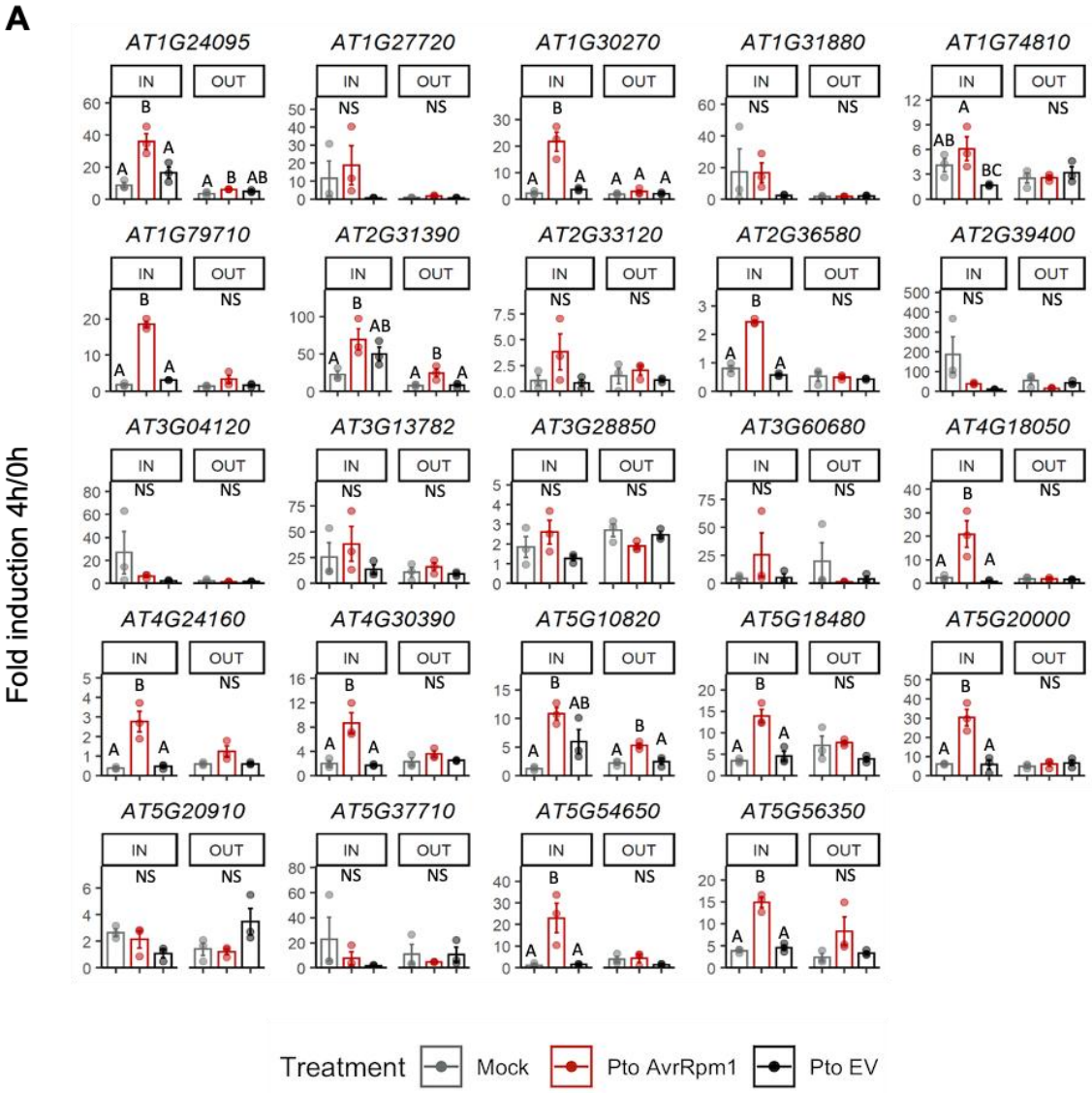
A
Fold induction 4h/0h
AT1G24095
AT1G27720
AT1G30270
AT1G31880
AT1G74810
AT1G79710
AT2G31390
AT2G33120
AT2G36580
AT2G39400
AT3G04120
AT3G13782
AT3G28850
AT3G60680
AT4G18050
AT4G24160
AT4G30390
AT5G10820
AT5G18480
AT5G20000
AT5G20910
AT5G37710
AT5G54650
AT5G56350
IN
OUT
Treatment
Mock
Pto AvrRpm1
Pto EV

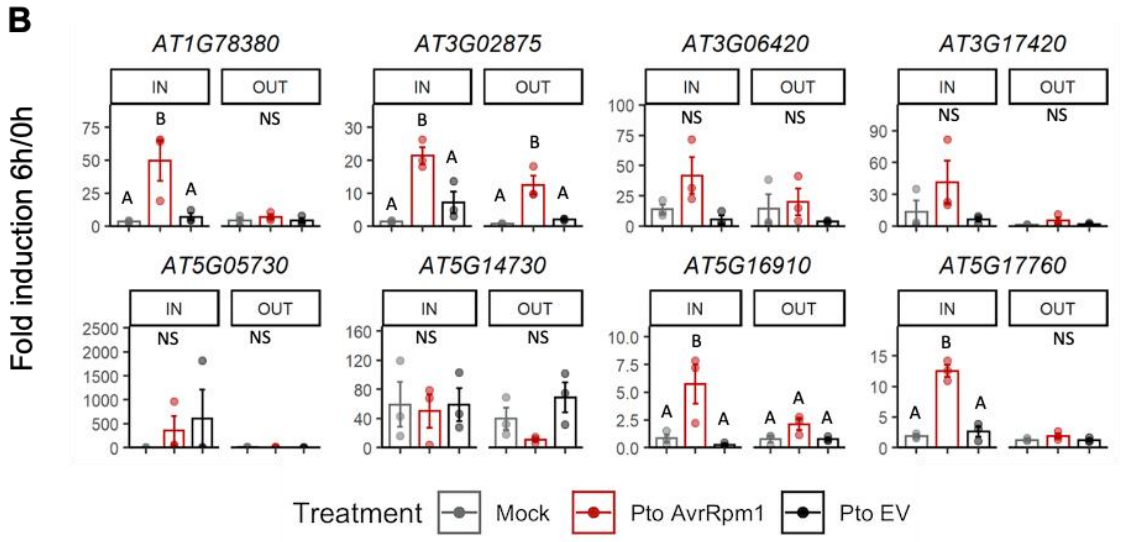
B
Fold induction 6h/0h
AT1G78380
AT3G02875
AT3G06420
AT3G17420
AT5G05730
AT5G14730
AT5G16910
AT5G17760
IN
OUT
Treatment
Mock
Pto AvrRpm1
Pto EV

Figure S11. RT-qPCR of 4- and 6-hour transcriptional HR indicators at IN and OUT areas upon treatment with either mock, *Pto AvrRpm1* or *Pto* DC3000 EV. Relative expression levels to the housekeeping gene *EIF4a* were represented as fold induction between 4 **(A)** or 6 **(B)** and 0 hpi. Error bars represent standard error of the mean from three independent experiments. Letters indicate statistically significant differences between treatments following one-way ANOVA with Tukey´s HSD test ($\alpha = 0.05$) performed independently at IN and OUT. NS (non-significant after one-way ANOVA). Exact p values are provided in **Table S5**.

Figure S12

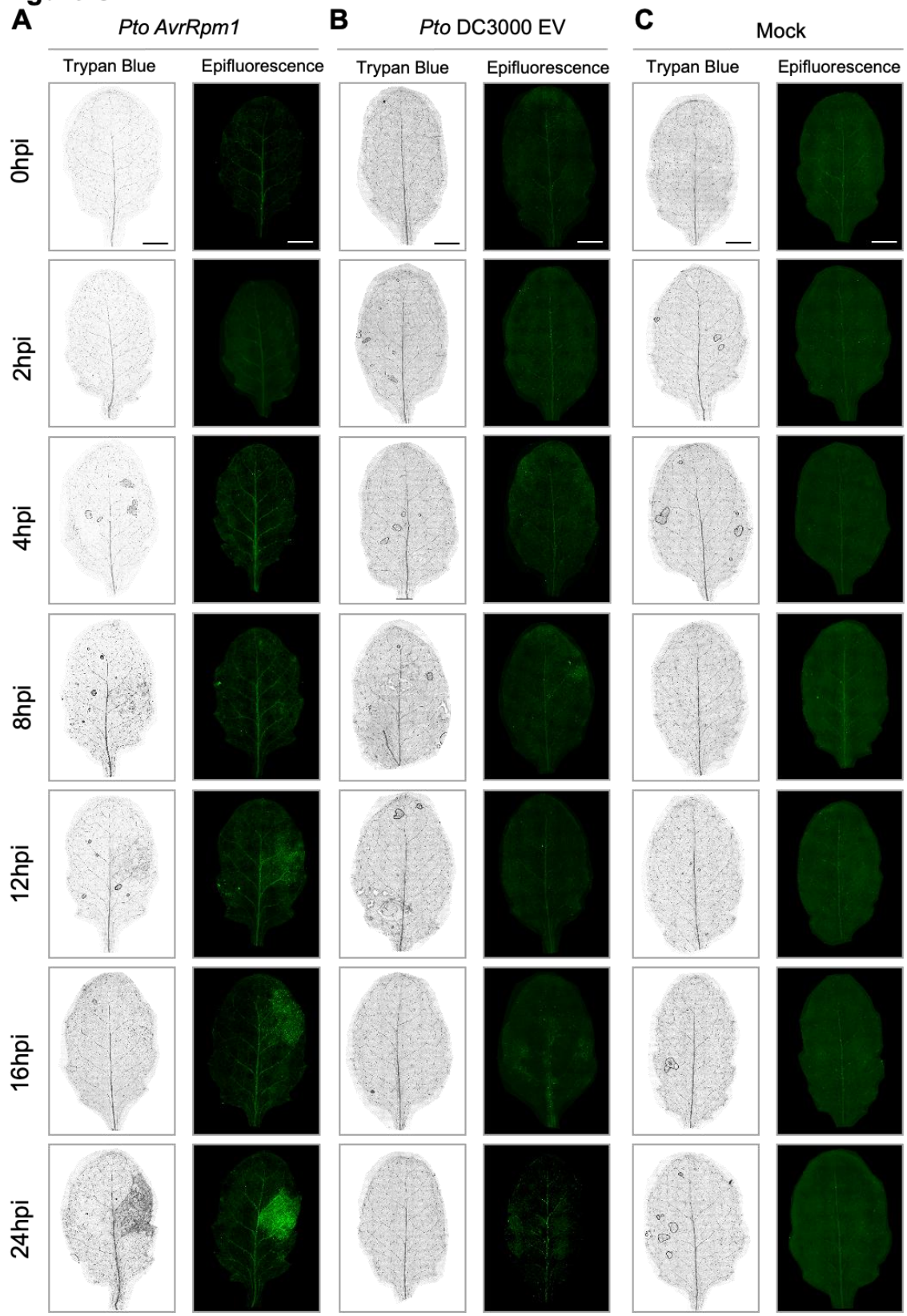
A
Pto AvrRpm1
B
Pto DC3000 EV
C
Mock
Trypan Blue
Epifluorescence
Trypan Blue
Epifluorescence
Trypan Blue
Epifluorescence
0hpi
2hpi
4hpi
8hpi
12hpi
16hpi
24hpi

Figure S12. Time course imaging of *pAT5G17760:NLS-3xGFP* Arabidopsis transgenic leaves infected with *Pto AvrRpm1* **(A)**, *Pto DC3000 EV* **(B)** or mock solution (10 mM $MgCl_2$) **(C)**. A small region of 4-week-old *pAT5G17760::NLS-3xGFP* leaves was syringe-infiltrated with *Pto* strains at $1*10^7$ colony-forming units (CFU)/ml ($O.D_{600}$ = 0.01). Fluorescent microscopy images were taken at 0, 2, 4, 8, 12, 16 and 24 hpi (right panels). Afterwards, leaves were subjected to trypan blue staining (left panels). Scale bar 3 mm.

Figure S13

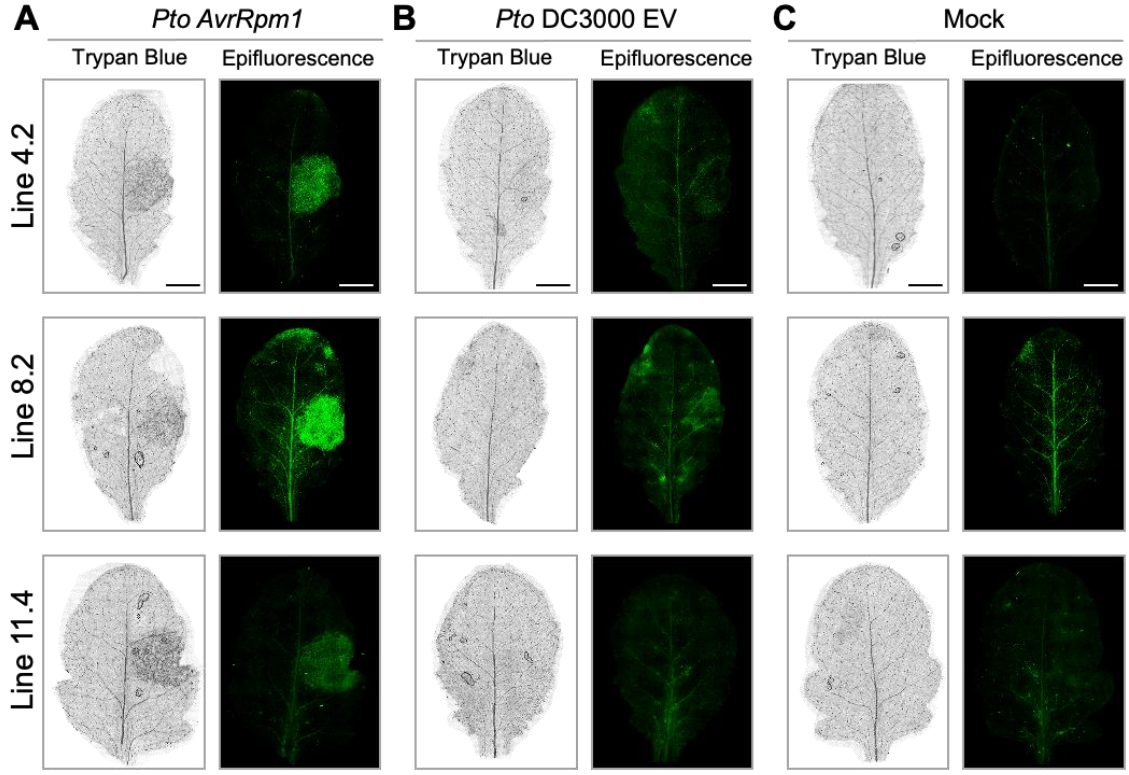

Figure S13. Activation of *pAT5G17760* in the syringe-infiltrated area occurred in several independent *pAT5G17760::*3xGFP transgenic lines. Leaves of Arabidopsis transgenics in the T2 generation were syringe infiltrated with *Pto AvrRpm1* **(A)**, *Pto DC3000* EV **(B)** at $1*10^7$ colony-forming units (CFU)/ml ($O.D_{600}$ = 0.01) and imaged at 16 hpi. Mock solution was used as a control **(C)**. Images in left panels are leaves stained with trypan blue whereas images in right panels are leaves under the epifluorescence microscope. Scale bars 3 mm.

Figure S14

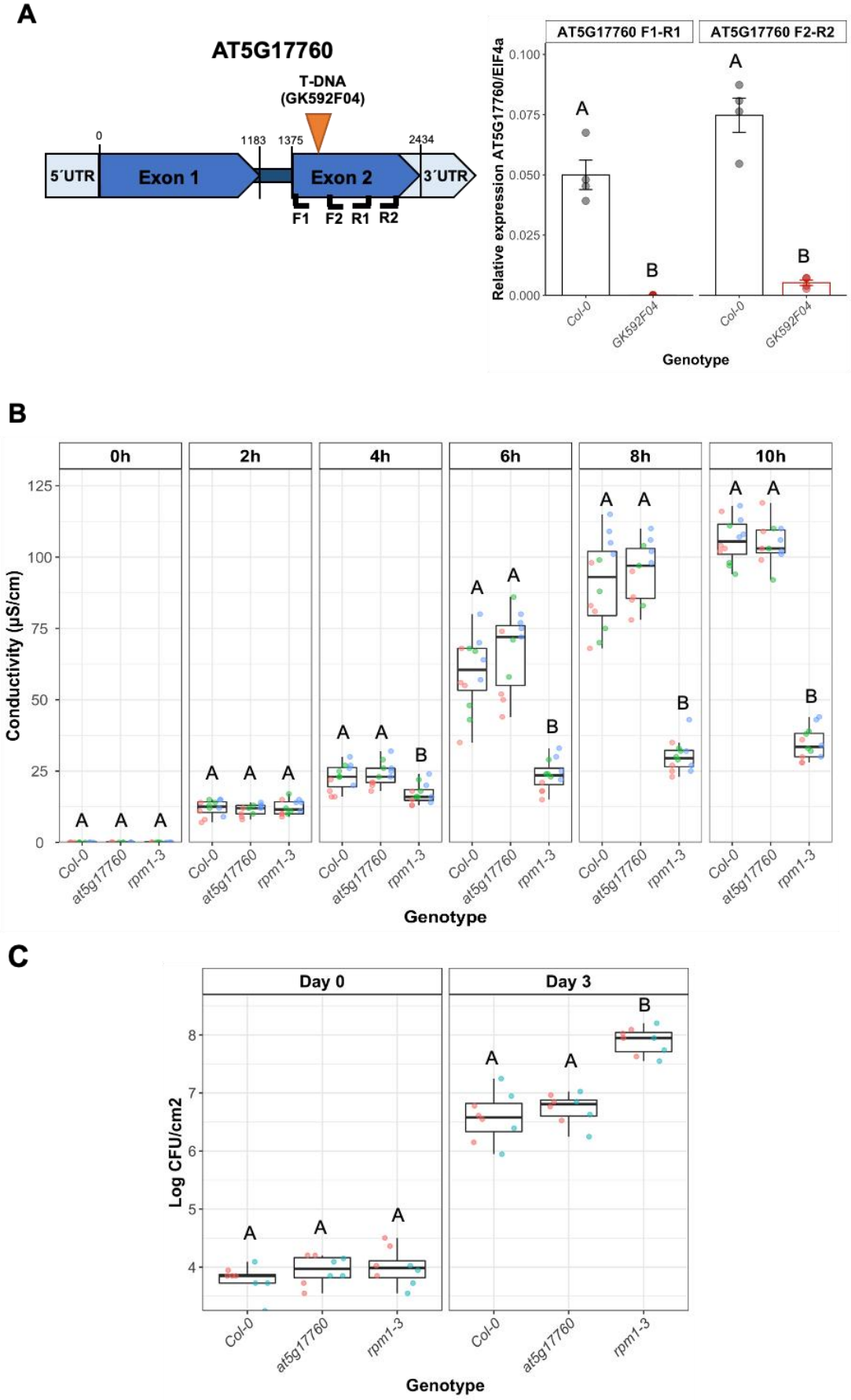
A
AT5G17760
T-DNA
(GK592F04)
0
1183
1375
2434
5´UTR
Exon 1
Exon 2
3´UTR
F1
F2
R1
R2
AT5G17760 F1-R1
AT5G17760 F2-R2
Relative expression AT5G17760/EIF4a
0.100
0.075
0.050
0.025
0.000
A
B
Col-0
GK592F04
Genotype
B
0h
2h
4h
6h
8h
10h
Conductivity (µS/cm)
125
100
75
50
25
0
Col-0
at5g17760
rpm1-3
Genotype
C
Day 0
Day 3
Log CFU/cm2
8
7
6
5
4
Col-0
at5g17760
rpm1-3
Genotype

Figure S14. Disease resistance and cell death triggered by avirulent Pto *AvrRpm1* strain is not compromised in Arabidopsis mutant lacking AT5G17760. (A) Scheme of AT517760 gene indicating the position of the T-DNA insertion in GK-59F04 mutant line (left panel) and RT-qPCR of two regions (F1-R1 and F2-R2) of exon 2 in Col-0 and GK-59F04 plants. RT-qPCR data is represented as relative expression levels of *AT5G17760* to the housekeeping gene *EIF4a* (right panel). Error bars represent standard error of the mean from four biological replicates. Letters indicate statistically significant differences between treatments following a Welch Two Sample t-test. Exact p values are provided in **Table S5**. **(B-C)** Four to 5 week-old Col-0, *at5g17760* and *rpm1-3* plants were syringe-infiltrated with *Pto* DC3000 *AvrRpm1* at $O.D_{600}$=0.05 for electrolyte leakage (b) and $O.D_{600}$=0.001 for bacterial growth assays **(C**)*, rpm1-3* mutant is used as a negative control since it is defective in the cognate NLR that recognizes the effector AvrRpm1. **(B)** Conductivity measurements of electrolyte leakage from dying cells were recorded at 0, 4, 6, 8 and 10 hpi. Dots represent data from 3 biological replicates (represented in different colors) consisting of 4 technical replicates each with 2 leaf discs measured per replicate. Letters indicate statistically significant differences between genotypes following one-way ANOVA with Tukey´s HSD test performed at each time point. Exact p values are provided in **Table S5**. **(C)** Bacterial growth at 0 and 3 days post-infection (dpi) was measured in Col-0, *at5g17760* and *rpm1-3*. Dots represent bacterial CFU (colony-forming units) per cm^2 from 2 biological replicates (represented in different colors) consisting of 4 technical replicates each with 2 leaf discs measured per replicate. Letters indicate statistically significant differences between genotypes following one-way ANOVA with Tukey´s HSD test performed at 0 and 3 days post infection. Exact p values are provided in **Table S5.**

Figure S15

A

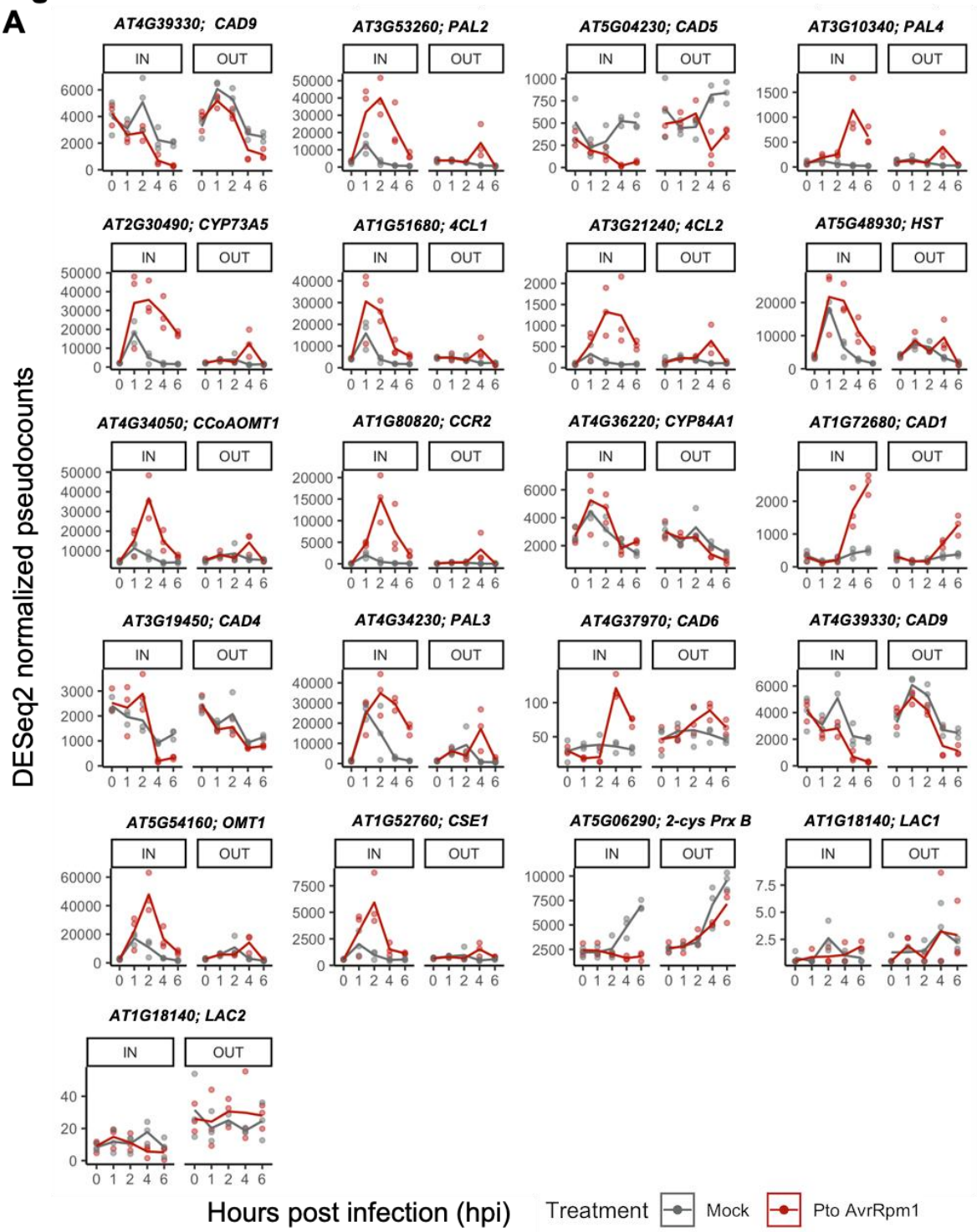
AT4G39330; CAD9
AT3G53260; PAL2
AT5G04230; CAD5
AT3G10340; PAL4
AT2G30490; CYP73A5
AT1G51680; 4CL1
AT3G21240; 4CL2
AT5G48930; HST
AT4G34050; CCoAOMT1
AT1G80820; CCR2
AT4G36220; CYP84A1
AT1G72680; CAD1
AT3G19450; CAD4
AT4G34230; PAL3
AT4G37970; CAD6
AT4G39330; CAD9
AT5G54160; OMT1
AT1G52760; CSE1
AT5G06290; 2-cys Prx B
AT1G18140; LAC1
AT1G18140; LAC2
IN
OUT
DESeq2 normalized pseudocounts
Hours post infection (hpi)
Treatment
Mock
Pto AvrRpm1

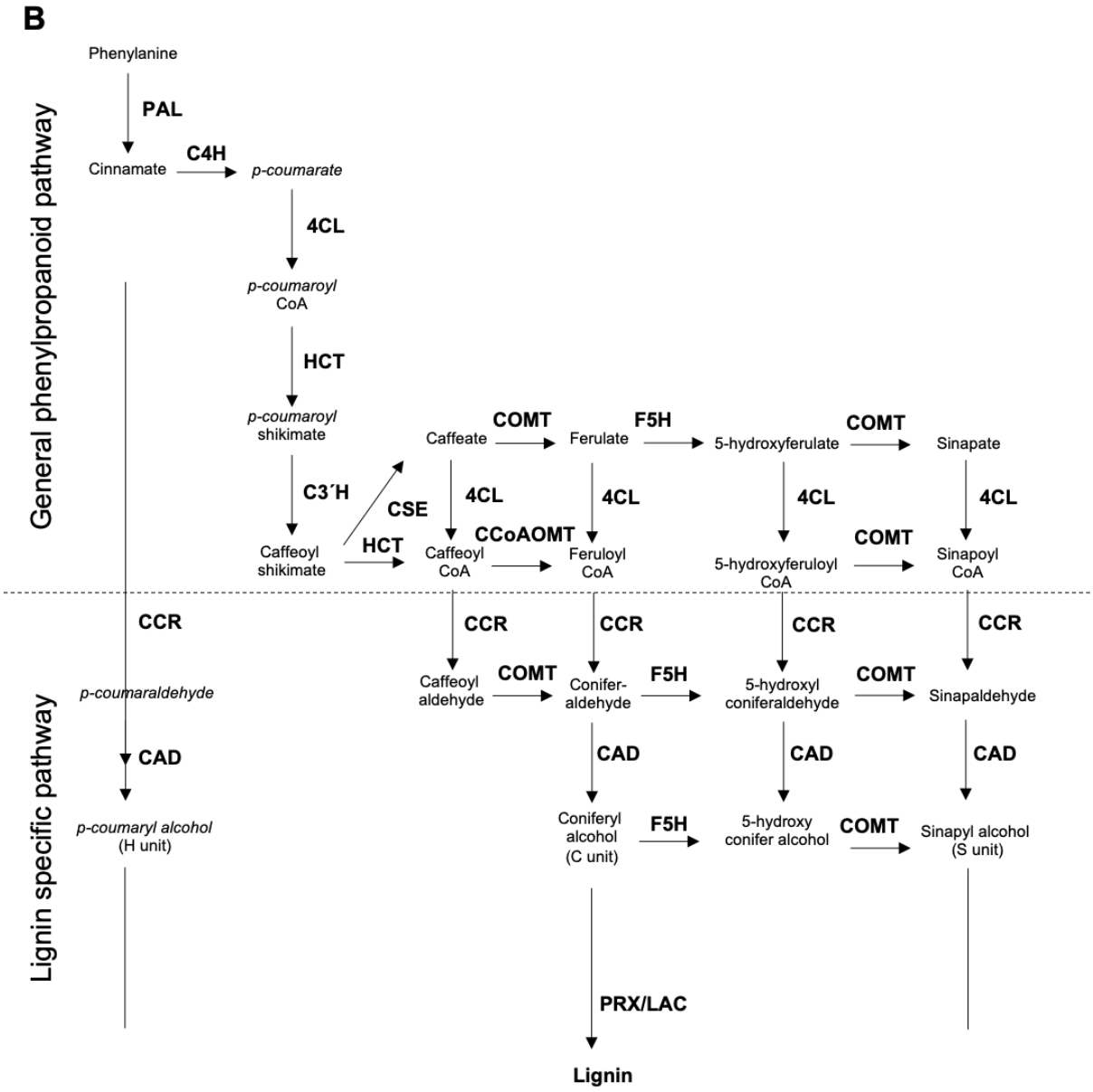

Figure S15. **RNA-seq expression profiles of genes involved in lignin biosynthesis.**

(A) Gene expression of genes from *Pto-AvrRpm1* or mock-infected plants is represented as DESeq2 pseudocounts. **(B)** Scheme of lignin biosynthesis in plants. Black arrow indicates the canonical lignin biosynthesis in plants. Bold font indicates enzymes involved in the different steps of the pathway. PAL, phenylalanine ammonia-lyase; C4H, cinnamate 4-hydroxylase; 4CL, 4-coumarate: CoA ligase; HCT, quinateshikimate *p*-hydroxycinnamoyltransferase;

C3′H, *p*-coumaroylshikimate 3′-hydroxylase; CCoAOMT, caffeoyl-CoA *O*-methyltransferase; CCR, cinnamoyl-CoAreductase; F5H, ferulate 5-hydroxylase; CAD, cinnamyl alcohol dehydrogenase; COMT, caffeic acid *O*-methyltransferase; CSE, caffeoyl shikimate esterase; PRX, peroxidase; LAC, laccase (Adapted from Meng Chie et al., 2018)

Figure S16

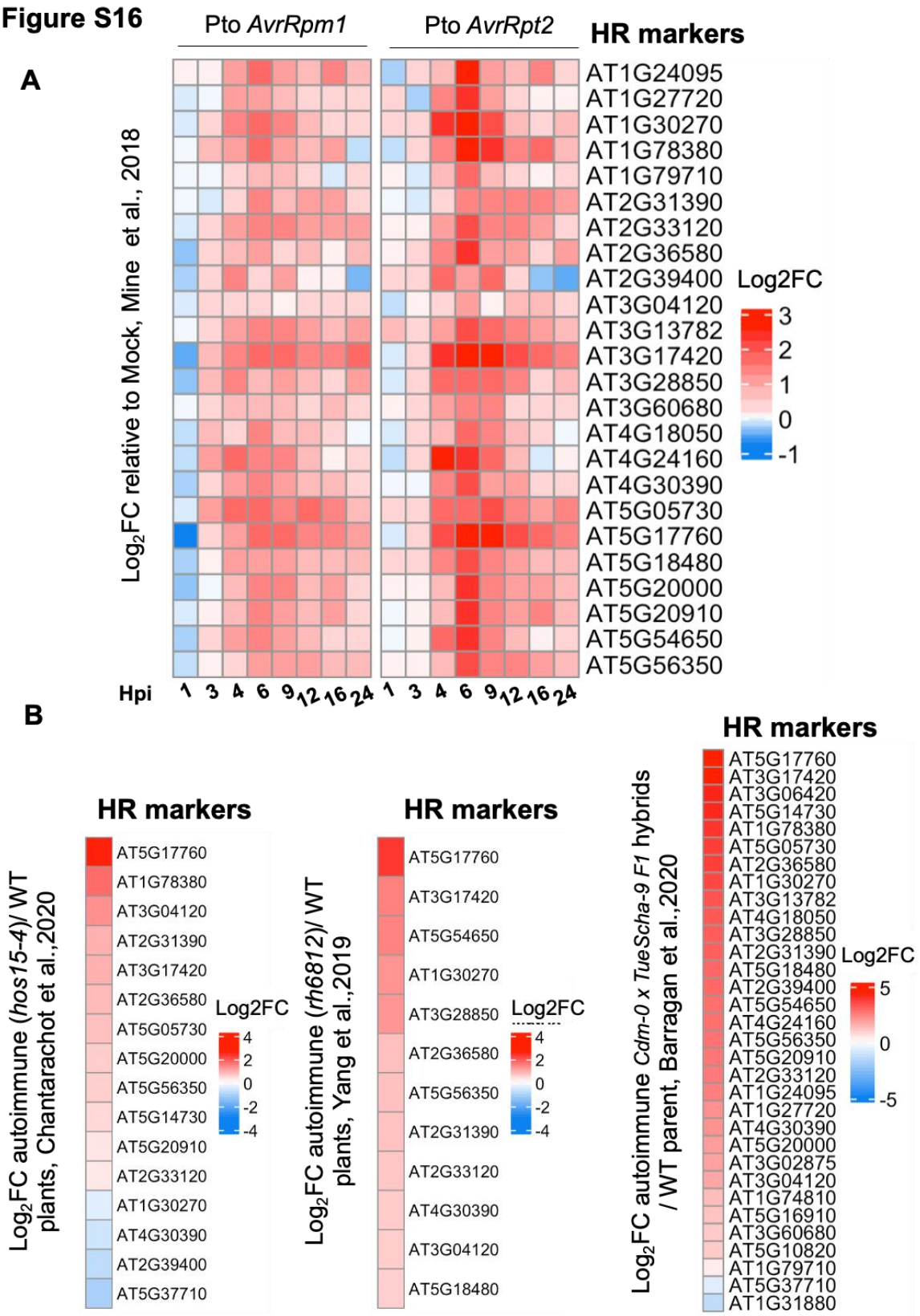
A
Pto AvrRpm1
Pto AvrRpt2
HR markers
Log2FC relative to Mock, Mine et al., 2018
AT1G24095
AT1G27720
AT1G30270
AT1G78380
AT1G79710
AT2G31390
AT2G33120
AT2G36580
AT2G39400
AT3G04120
AT3G13782
AT3G17420
AT3G28850
AT3G60680
AT4G18050
AT4G24160
AT4G30390
AT5G05730
AT5G17760
AT5G18480
AT5G20000
AT5G20910
AT5G54650
AT5G56350
Log2FC
3
2
1
0
-1
Hpi
1 3 4 6 9 12 16 24 1 3 4 6 9 12 16 24
B
HR markers
Log2FC autoimmune (hos15-4)/ WT plants, Chantarachot et al.,2020
AT5G17760
AT1G78380
AT3G04120
AT2G31390
AT3G17420
AT2G36580
AT5G05730
AT5G20000
AT5G56350
AT5G14730
AT5G20910
AT2G33120
AT1G30270
AT4G30390
AT2G39400
AT5G37710
Log2FC
4
2
0
-2
-4
HR markers
Log2FC autoimmune (rh6812)/ WT plants, Yang et al.,2019
AT5G17760
AT3G17420
AT5G54650
AT1G30270
AT3G28850
AT2G36580
AT5G56350
AT2G31390
AT2G33120
AT4G30390
AT3G04120
AT5G18480
Log2FC
4
2
0
-2
-4
HR markers
Log2FC autoimmune Cdm-0 x TueScha-9 F1 hybrids / WT parent, Barragan et al.,2020
AT5G17760
AT3G17420
AT3G06420
AT5G14730
AT1G78380
AT5G05730
AT2G36580
AT1G30270
AT3G13782
AT4G18050
AT3G28850
AT2G31390
AT5G18480
AT2G39400
AT5G54650
AT4G24160
AT5G56350
AT5G20910
AT2G33120
AT1G24095
AT1G27720
AT4G30390
AT5G20000
AT3G02875
AT3G04120
AT1G74810
AT5G16910
AT3G60680
AT5G10820
AT1G79710
AT5G37710
AT1G31880
Log2FC
5
0
-5

Figure S16. **Transcriptional regulation of HR markers found in this study compared to RNA-seq data sets from plants undergoing ETI and autoimmunity.** (A) HR markers found in this study were searched in Mine et al., 2018. In pairwise comparisons between infection with ETI-causing bacteria (Pto *AvrRpm1* and Pto *AvrRpt2*) and mock, only genes with high statistical confidence (q value ≤ 0,01) in at least one time point were plotted on a heatmap indicating Log_2FC for the different times tested in their study. (B) HR markers found in this study were searched in RNA-seq data sets of Arabidopsis *hos15-4* (Yang et al.,2019), *rh6812* autoimmune plants (Chantarachot et al., 2020) and *Cdm-0 x TueScha-9 F1* hybrids (Barragan et al., 2020). Genes with high statistical confidance in their data sets (FDR <0.05) were plotted on a heatmap indicating Log2FC between expression of WT (Col-0) and autoimmune plants.

Supplementary tables/dataset legends.

Table S1 (Associated to Figure 2A). List of differentially expressed genes upon *Pto AvrRpm1* infection at each time point and tissue area.

Table S2 (Associated to Figure S2). List of genes constituting each GO term in Figure S2. GO term enrichment analysis of upregulated and downregulated genes at either IN our OUT areas. Only those GO terms exhibiting an FDR < 0.05 after Bonferroni Correction for multiple testing and a fold enrichment above 2 are shown.

Table S3 (Associated to Figure 2B). List of genes that are upregulated upon *Pto AvrRpm1* at 4 and 6 hpi exclusively at IN, both at IN and OUT or exclusively at OUT.

Table S4 (Associated to Figure 2C). List of genes constituting each GO term in Figure 2C.GO term enrichment analysis of genes that are exclusively upregulated at either the IN or OUT area upon *Pto AvrRpm1* infection. Only those GO terms exhibiting an FDR < 0.05 after Bonferroni Correction for multiple testing and a fold enrichment above 2 are shown.

Table S5 (Associated to Figure 1C, Figure 4, Figure 5, Figure S11 and Figure S14). Tukey HSD p-values and Welch two sample t-test p-values obtained from statistical tests applied in the study.

Table S6 (Associated to Figure 3A). List of genes comprising each cluster derived from *Pto AvrRpm1* and mock-treated plants along with their corresponding MSV at IN.

Table S7 (Associated to Figure 3B). List of genes comprising each cluster derived from *Pto AvrRpm1* and mock-treated plants along with their corresponding MSV at OUT.

Table S8 (Associated to Figure S6A). List of genes constituting each GO term in Figure S6A. GO term enrichment analysis of genes from clusters of *Pto AvrRpm1*-inoculated plants at the IN area with a MSV of 0.7 or above. Only those GO terms exhibiting an FDR < 0.05 after Bonferroni Correction for multiple testing and a fold enrichment above 2 are shown.

Table S9 (Associated to Figure S6B). List of genes constituting each GO term in Figure S6B. GO term enrichment analysis of genes from clusters of *Pto AvrRpm1*-inoculated plants at the OUT area with a MSV of 0.7 or above. Only those GO terms exhibiting an FDR < 0.05 after Bonferroni Correction for multiple testing and a fold enrichment above 2 are shown.

Table S10 (Associated to Figure S7A). List of genes constituting each GO term in Figure S5. GO term enrichment analysis of genes from clusters of mock-inoculated plants at the IN area with a MSV of 0.7 or above. Only those GO terms exhibiting an FDR < 0.05 after Bonferroni Correction for multiple testing and a fold enrichment above 2 are shown.

Table S11 (Associated to Figure S7B). List of genes constituting each GO term in Figure S6. GO term enrichment analysis of genes from clusters of mock-inoculated plants at the OUT area with a MSV of 0.7 or above. Only those GO terms exhibiting an FDR < 0.05 after Bonferroni Correction for multiple testing and a fold enrichment above 2 are shown.

Table S12. Primers used in this study and primer concentration for RT-qPCRs.

Table S13. RT-qPCR results in numeric format along with Cp values of Targets and Cp value of Reference housekeeping gene.

CHAPTER 2

Lack of AtMC1 catalytic activity triggers autoimmunity dependent on NLR stability

(Pre-publication 4)

Lack of *At*MC1 catalytic activity triggers autoimmunity dependent on NLR stability

Jose Salguero-Linares[1], Laia Armengot[1,2], Joel Ayet[1], Nerea Ruiz-Solani[1], Svenja C. Saile[6], Marta Salas-Gómez[1], Jenna Krumbach[1], Fernando Navarrete[1], Farnusch Kaschani[3], Simon Stael[3], Frank Van Breusegem[4], Morten Petersen[4], Marc Valls[1,2], Farid El Kasmi[6] and Núria S. Coll[1,7*]

[1] *Centre for Research in Agricultural Genomics (CRAG), CSIC-IRTA-UAB-UB, Campus UAB, Bellaterra, Barcelona, 08193, Spain.*
[2] *Department of Genetics, Microbiology and Statistics, Universitat de Barcelona, 08028 Barcelona, Spain.*
[3] *Center of Medical Biotechnology (ZMB) University of Duisburg-Essen, Universitätsstr. 2 45141 Essen, Germany.*
[4] *Department of Plant Biotechnology and Bioinformatics, Ghent University, 9052 Ghent, Belgium. VIB-Gent Center for Plant Systems Biology, 9052 Ghent, Belgium.*
[5] *Department of Biology, University of Copenhagen, 2200 Copenhagen N, Denmark*
[6] *Center for Plant Molecular Biology, Eberhard Karls University of Tübingen, Tübingen, Germany*
[7] *Consejo Superior de Investigaciones Científicas (CSIC), 08001 Barcelona, Spain*

[*] Author for correspondence:
Nuria S. Coll. Centre for Research in Agricultural Genomics. 08193 Cerdanyola del Valles. Spain
e-mail: nuria.sanchez-coll@cragenomica.es

ABSTRACT

Plants utilize cell surface-localized pattern recognition receptors (PRRs) and intracellular nucleotide-binding leucine-rich repeat (NLR) receptors to detect non-self and elicit robust immune responses. During plant development and especially during aging, fine-tuning the homeostasis of these receptors is critical to prevent their hyperactivation. Here, we show that Arabidopsis plants lacking metacaspase 1 (*At*MC1) display autoimmunity dependent on immune signalling components downstream of NLR and PRR activation. Overexpression of catalytically inactive *At*MC1 in an *atmc1* background triggers severe autoimmunity partially dependent on the same immune signalling components. Although individual mutations in NLRs, PRRs or other immune-related components that interact with catalytically inactive *At*MC1 do not rescue the autoimmune phenotype, overexpression of SNIPER1, a master regulator of NLR homeostasis, fully attenuates the phenotype**,** inferring that a broad defect in NLR turnover may underlie the severe autoimmunity observed. As opposed to Wt *At*MC1 which exhibits a nucleocytoplasmic localization, catalytically inactive *At*MC1 localizes to puncta structures that are degraded through autophagy. We infer that the phenotypes observed in plants overexpressing catalytically inactive *At*MC1 may represent an additive phenotype to the relatively milder autoimmunity

observed in *atmc1* mutants. Altogether and considering previous evidence on the proteostatic functions of *At*MC1, we speculate that Wt *At*MC1 may either directly or indirectly control NLR protein levels as plants approach adulthood, thus preventing autoimmunity.

INTRODUCTION

Plants perceive pathogenic microbes by detecting conserved pathogen-associated molecular patterns (PAMPs) at the plasma membrane through pattern-recognition receptors (PRRs), triggering PAMP-triggered immunity (PTI) (Jones & Dangl, 2006). Successful pathogens deliver effector proteins to the plant cell that dampen PTI responses (Couto & Zipfel, 2016). Intracellular immune receptors of the nucleotide-binding leucine-rich repeat-type (NLRs) detect pathogen effectors either directly or indirectly unleashing a robust immune response termed effector-triggered immunity (ETI) that culminates in disease resistance (Jones & Dangl, 2006). Disease resistance is often, but not always, accompanied by a form of localized cell death at the pathogen ingress site termed hypersensitive response (HR) (Balint-Kurti, 2019). Accumulating evidence supports the notion that immune pathways activated by PRRs and NLRs mutually potentiate each other to activate strong defences against pathogens (Ngou et al., 2021; Tian et al., 2021; Yuan et al., 2021).

NLRs are functionally classified into sensor NLRs (sNLRs), involved in perceiving pathogen effectors or monitoring their activity, and helper NLRs (hNLRs), which amplify the immune signal downstream of effector recognition and are evolutionarily more conserved (Jubic et al., 2019). NLRs can be further classified based on their domain composition at the N-terminal end. While sNRLs can harbour either coil-coiled domain (CNLs) or a Toll/Interleukin 1-receptor domain (TNLs), hNLRs carry a RPW8 (RESISTANCE TO POWDERY MILDEW 8)-like CC domain (RNLs). Within hNLRs, two main gene families have been described in *Arabidopsis thaliana* (hereafter Arabidopsis) encoding ADR1 (ACTIVATED DISEASE RESISTANCE 1: ADR1, ADR1-L1 and ADR1-L2) and NRG1 (N-REQUIRED GENE 1: NRG1.1, NRG1.2 and NRG1.3) (Jubic et al., 2019). While certain activated CNLs oligomerize into pentameric resistosomes that perturb PM integrity acting as permeable Ca^{2+} channels on their own (Bi et al., 2021; Förderer et al., 2022; Wang et al., 2019), TNLs oligomerize into tetrameric resistosomes that hydrolyse nicotinamide adenine dinucleotide (NAD+) through their TIR domains (Martin et al., 2020; Wan et al., 2019). Chemical by-products of TIR enzymatic activity can directly bind to the two mutually exclusive heterodimers formed by the lipase-like proteins ENHANCED DISEASE STIMULATING 1-PHYTOALEXIN DEFICIENT 4 (EDS1-PAD4) and EDS1-SENESCENCE ASSOCIATED GENE 101 (EDS1-SAG101) (Huang et al., 2022; Jia et al., 2022). Allosteric changes caused by binding of these chemicals at the interfaces of the EDS1-PAD4 and EDS1-SAG101 heterodimers promote interactions with members of the ADR1 and NRG1 family, respectively (Huang et al., 2022; Jia et al., 2022). ADR1 and NRG1 also oligomerize into pentameric resistosomes that exert Ca^{2+} channel activity at the PM (Jacob et al., 2021). A genetically parallel pathway involving the synthesis of the phytohormone salicylic acid (SA) is required for transcriptional changes in defence-related genes during plant immunity (Cui et al., 2017; Mine et al., 2018). The SA pathway is dependent on the ISOCHORISMATE SYNTHASE 1

(ICS1 also known as SID2) enzyme and is bolstered by the EDS1-PAD4-ADR1 immune node via a mutually reinforcing feedback loop (**Figure 1**) (Cui et al., 2017; Sun et al., 2021). Recent reports demonstrated that certain PRRs, such as the receptor-like kinase SUPPRESSOR OF BIR1-1 (SOBIR1), links the surface-localized RECEPTOR-LIKE PROTEIN (RLP23), that recognizes PAMPs, to the EDS1-PAD4-ADR1 immune node. Hence, EDS-PAD4-ADR1 might serve as a convergence point for signalling cascades elicited by either NLRs or PRRs, in conferring plant immunity (**Figure 1**) (Pruitt et al., 2021).

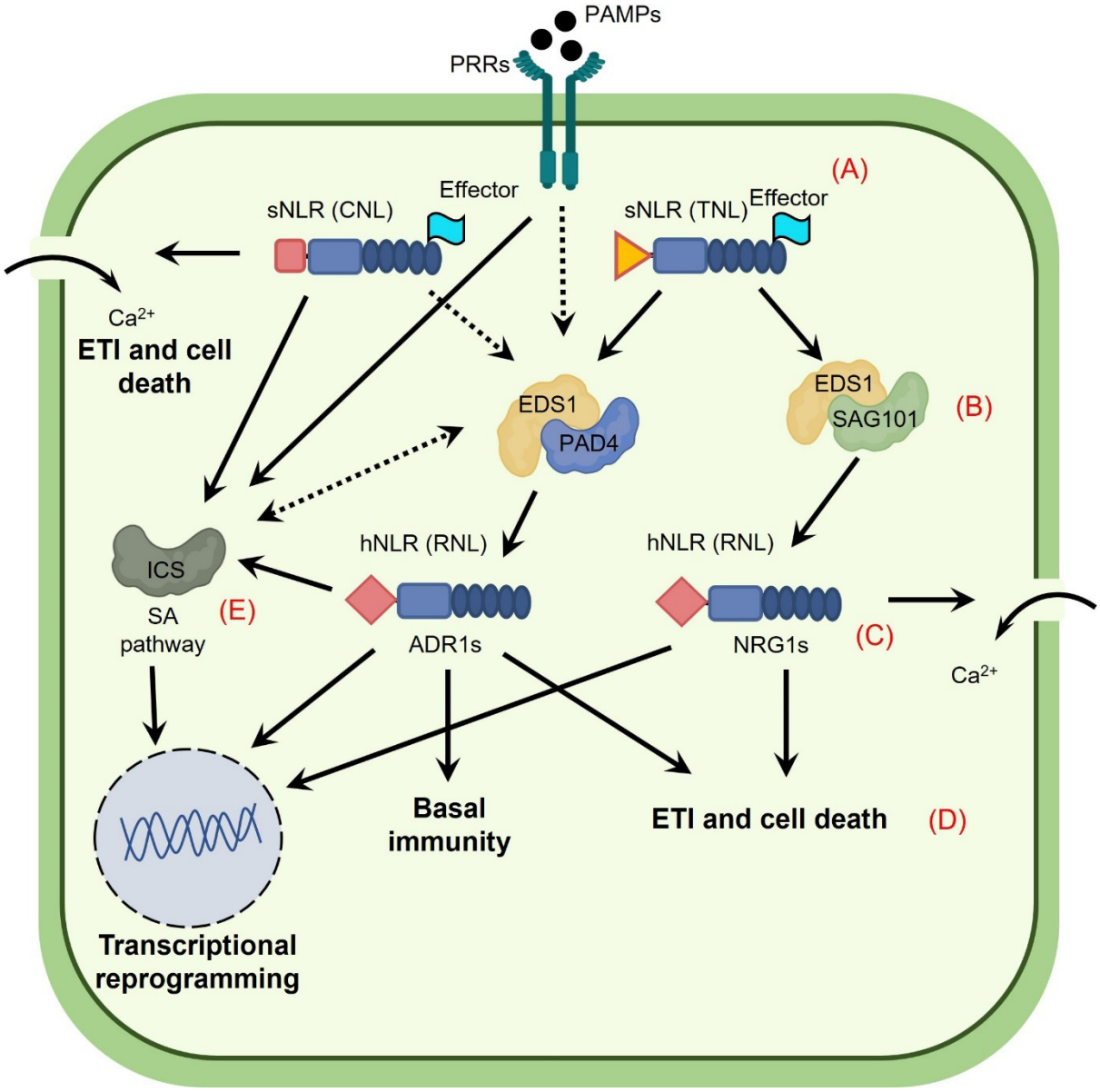

Figure 1: Schematic representation of immune signalling networks downstream of sNLR and PRR activation. (A) PRRs recognize molecular signatures from pathogens (PAMPs) at the cell surface whereas NLRs recognize pathogen effectors intracellularly. sNLRs are chiefly divided into CNLs and TNLs based on their domain composition at the N-terminal end or into sNLRs or hNLRs based on their function during the immune response. Upon effector perception TNLs oligomerize into tetrameric resistosomes acting as NADases and mediate signalling through either SAG101-EDS1 or PAD4-EDS1

heterodimers. CNLs can oligomerize into pentameric resistosomes upon effector perception independently of EDS1 acting as Ca^{2+} permeable channels. Certain CNLs, however, partially require (dashed line) EDS1-PAD4 for timely and effective ETI responses. Certain PRRs have also been shown to signal through EDS-PAD4 (dashed line) **(B)**. SAG101-EDS1 and PAD4-EDS1 heterodimers associate with either ADR1 or NRG1 hNLRs (RNLs), respectively **(C)**. Upon activation, RNLs oligomerize into pentameric resistosomes that can act as Ca^{2+} permeable channels inducing cell death and ETI. **(D)** While the EDS1-SAG101-NRG1 node is exclusively involved in ETI and cell death, the EDS1-PAD4-ADR1 node is also involved in basal immunity elicited by PRRs. **(E)** A genetically parallel pathway involving SA synthesis is required for transcriptional reprogramming of defence-related genes upon NLR and PRR activation. This pathway is dependent on the ICS enzyme and is bolstered by the EDS1-PAD1-ADR1 immune node via a mutually reinforcing feedback loop (dashed line).

Compared to mammals, higher plants encode a large number of NLRs and PRRs that upon pathogen recognition are transcriptionally upregulated to exert a robust immune response (Tian et al., 2021). At the post-translation level, NLR homeostasis is maintained by the ubiquitin-proteasome system (UPS). Plant genomes encode for an extensive number of E3 ubiquitin ligases (~1,500 genes) mediating diverse biological functions, including PRR and NLR turnover (Cheng et al., 2011; Gou et al., 2012; Liao et al., 2017; Lu et al., 2011; Mazzucotelli et al., 2006). Recently, the master E3 ligases, SNIPER1 and SNIPER2, have been shown to supress autoimmune phenotypes caused by hyperactive gain-of function NLR mutants by broadly regulating sNLR protein levels (Z. Wu et al., 2020). Since tight control of NLR and PRR homeostasis is of utter importance for plant fitness and for avoiding autoimmunity, parallel and possibly redundant mechanisms to regulate immune receptor homeostasis may exist.

Plant metacaspases are an ancient group of cysteine proteases found in plants, yeast and protozoa (Minina et al., 2017). They are structurally divided into Type I, which harbour an N-terminal prodomain, and Type IIs, which lack the prodomain but instead have a long linker region in between the p10 and p20 catalytic subunits. The Arabidopsis genome encodes for 9 metacaspases, three Type Is (*At*MC1-3) and six Type IIs (*At*MC4-*At*MC9) (Tsiatsiani et al., 2011). Metacaspases characterized so far have been involved in responses to stress, both biotic and abiotic (Coll et al., 2010; Escamez et al., 2016; Hander et al., 2019; He et al., 2008; Pitsili et al., 2022), though how they mechanistically work remains unknown for most of the functions described. In the context of plant immunity, the two type I metacaspases, *At*MC1 and *At*MC2, are known to antagonistically regulate HR triggered by avirulent pathogens in young plants (Coll et al., 2010). While *At*MC1 positively regulates HR in a catalytic dependent manner, *At*MC2 exerts its negative HR regulation despite the presence or absence of its catalytic cysteine (Coll et al., 2010). Importantly, this phenotype associated with HR regulation by *At*MC1 does not translate in enhanced pathogen growth or disease resistance in young plants (Coll et al., 2010). In adult plants, however, *At*MC1 has been shown to negatively regulate immunity as evidenced by decreased pathogen growth in plants lacking *At*MC1 (Wang et al., 2021).

In the context of proteostasis, our lab has recently shown that *At*MC1 acts as a disaggregase to mitigate proteotoxic stress (Ruiz-Solaní N. et al., 2023 unpublished: **Chapter 3**). Although proteotoxic stress has been mostly studied in the context of heat stress, it is plausible to think that upon pathogen-triggered

immune receptor activation proteotoxicity also occurs. In line with this, *At*MC1 has been shown to negatively regulate the protein accumulation of the auto-active hNLR mutant ADR1-L2 (D484V) and consequently, ADR1-L2 (D484V) autoimmunity is exacerbated when the *atmc1* mutant allele is introduced in ADR1-L2 (D484V) plants (Roberts et al., 2013). The maize *Zm*MC1 was also shown to negatively regulate immunity outputs triggered by auto-active sensor CNLs, though in this case causing re-localization of the NLRs tested to punctate dots without attenuating protein stability (Luan et al., 2021). The mechanistic basis of how *At*MC1 regulates the levels of NLRs in the context of immunity is lacking.

Herein we report that absence of *At*MC1 results in autoimmunity that is dependent on SA synthesis and immune signalling through the convergent node EDS1-PAD4. This phenotype is dramatically exacerbated by constitutive expression of a catalytically inactive *At*MC1 variant. The catalytically inactive variant localizes to puncta and co-immunoprecipitates with sNLRs, PRRs and other immune-related components. Since this phenotype is rescued by overexpressing the master regulator of sNLRs levels, SNIPER1, but not by mutating individual sNLRs or PRRs, we hypothesise that catalytically inactive *At*MC1 acts as platform where immune components are sequestered/trapped, thus interfering with their timely turnover. Based on this data, we infer that Wt *At*MC1 might participate in the proteostasis of immune components upstream of EDS1-PAD4 and SA synthesis, preventing immune hyperactivation as plants approach adulthood.

RESULTS

Absence of AtMC1 results in autoimmunity dependent on SA synthesis and signalling through the EDS1-PAD4 immune node.

We previously reported that the Arabidopsis transfer DNA (T-DNA) knockout mutant *atmc1* displays an early senescence phenotype when transferred from short day to long day photoperiod (Coll et al., 2014). When continuously grown under short day conditions, *atmc1* plants exhibited hallmarks of an autoimmune plant: age-dependent growth restriction (**Figure 2B and D**) and spontaneous cell death (**Figure 2C**). A full deletion CRISPR mutant of *AtMC1* (*atmc1-CR #1*) (**Figure 2A**), showed the same phenotypic features (**Figure 2B-E**). Interestingly, only *atmc1* mutants but no other type I metacaspase mutants, *atmc2* and *atmc3*, or a type II metacaspase mutant, *atmc4*, displayed autoimmunity (**Figure S1**).

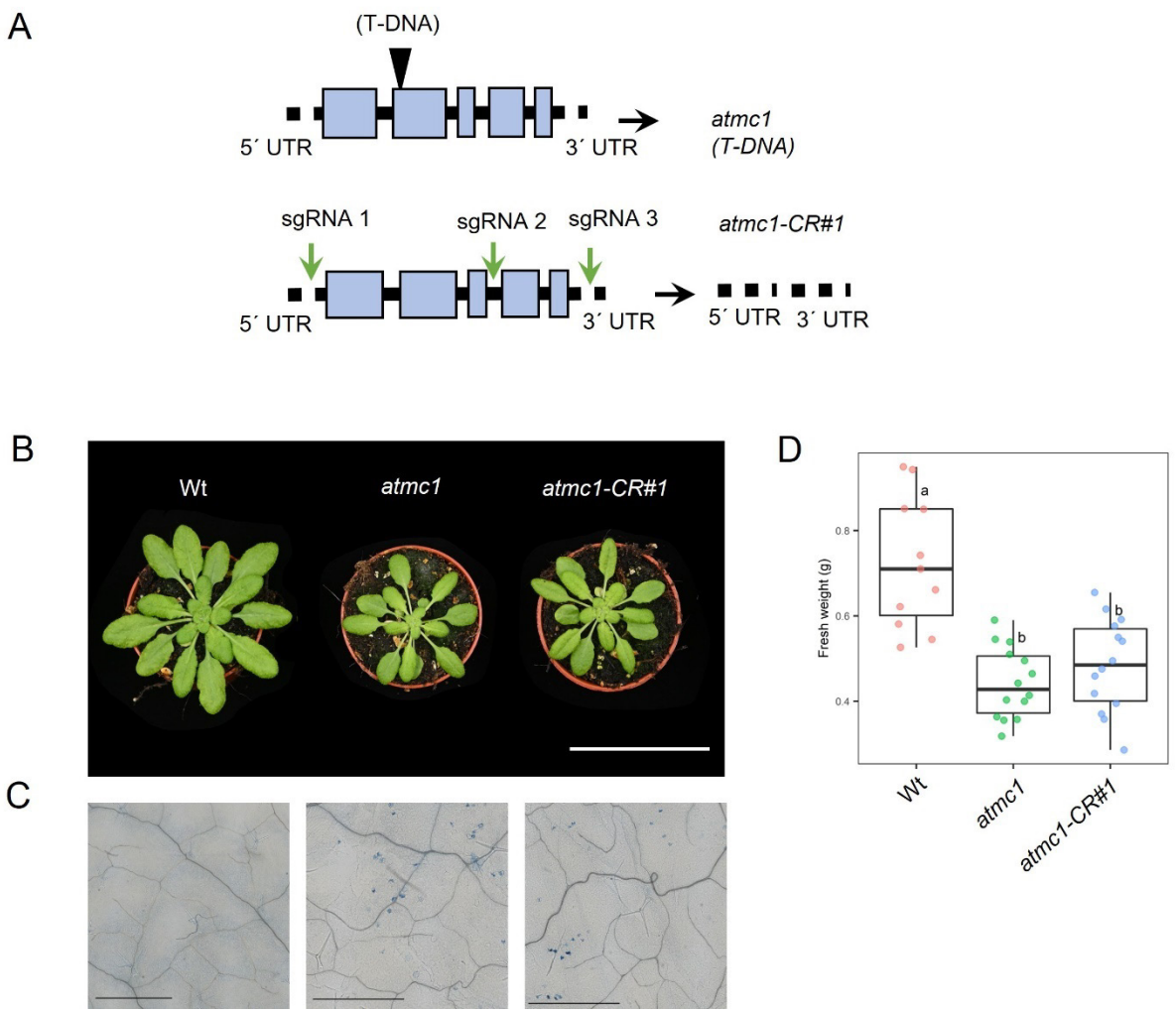

Figure 2. **Absence of *At*MC1 results in age-dependent growth defects and ectopic cell death. (A)** Scheme of the genomic DNA sequence of *AtMC1* in the *atmc1* (T-DNA) mutant and CRISPR deletion mutant (*atmc1-CR#1*). Blue rectangles represent exons whereas black ones represent introns. The triangle shows the insertion site of the T-DNA in *atmc1* mutant plants. Green arrows indicate the target site of single guide RNAs (sgRNAs) to create the CRISPR deletion. The resulting CRISPR mutant (*atmc1-CR#1*) carrying a full deletion from sgRNA 1 to sgRNA 3 is depicted. **(B)** Representative image of 40-day-old Wt, *atmc1* and *atmc1-CR#1* plants grown under short day conditions. Scale bar = 5.5 cm. **(C)** Trypan blue staining of an area belonging to the 6th true leaf of the plants shown in **B.** Scale bar = 0.5 mm. **(D)** Plant fresh weight of genotypes shown in B (n=12). Different letters indicate statistical difference in fresh weight between genotypes (one-way ANOVA followed by post hoc Tukey, p value < 0.05).

To explore the genetic contribution of core immune signalling components and SA synthesis in the autoimmune phenotype of *atmc1* plants, we individually introduced mutant alleles impaired in ETI signalling downstream of sensor NLRs (*eds1-12*, *pad4-1* and *nrg1 double*) and SA synthesis (*sid2-1*) into the *atmc1* mutant background. Interestingly, suppression of SA synthesis (*atmc1 sid2-1*) and

EDS1-PAD4-dependent immune signalling (*atmc1 eds1-12, atmc1 pad4-1*) restored Wt-like plant growth (**Figure 3A**), prevented spontaneous cell death (**Figure 3B**), and suppressed the PR1a protein accumulation (**Figure 3C**) observed in *atmc1* mutant plants. By contrast, introgression of the mutant alleles *nrg1.1 nrg1.2* which impair immunity through the hNLR gene family NRG1 neither restores Wt-like plant growth nor prevents spontaneous cell death and PR1a protein accumulation in *atmc1 nrg1.1 nrg1.2* plants (**Figure 3A-C**). Altogether, we conclude that autoimmunity in *atmc1* plants is dependent on SA synthesis and signalling through the EDS1-PAD4 immune node.

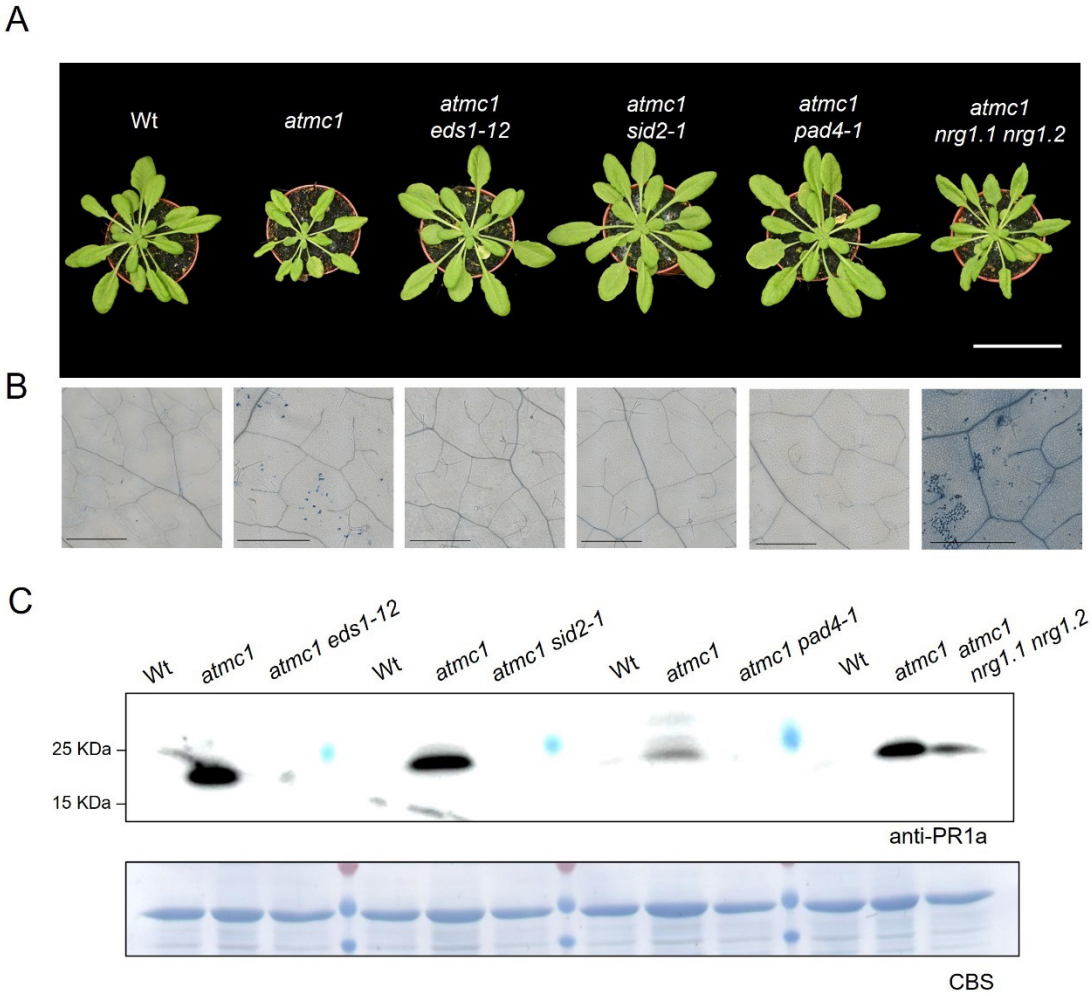

Figure 3. **Constitutive immune activation in *atmc1* plants is dependent on SA synthesis and immune signalling through EDS1-PAD4**. **(A)** Representative image of 40-day-old Wt, *atmc1, atmc1 eds1-12, atmc1 sid2-1, atmc1 pad4-1 and atmc1 nrg1.1 nrg1.2* grown under short day conditions. Scale bar = 5.5 cm. **(B)** Trypan blue staining of an area belonging to the 6th true leaf of the plants shown in **A.** Scale bar = 0.5 mm. **(C)** Total protein extracts from the plant genotypes shown in **A** were run on an SDS-PAGE gel and immuno-blotted against anti-PR1a. Comassie Blue Staining (CBS) of the immunoblotted membranes shows protein levels of Rubisco as s loading control.

Overexpression of a catalytically inactive variant of AtMC1 (AtMC1^{C220A}) in an atmc1 background triggers severe autoimmunity.

To ascertain whether the catalytic activity of *At*MC1 is important for the autoimmune phenotype observed in *atmc1* mutant plants, we created stable transgenics overexpressing either Wt *At*MC1 fused to a C-terminal GFP tag (*At*MC1–GFP) or *At*MC1–GFP with a Cys to Ala mutation that renders the protease catalytically inactive (*At*MC1^{C220A}) (**Figure 4A**) (Coll et al., 2010). While adult *atmc1 AtMC1–GFP* plants fully complemented the low fresh weight (**Figure 4B and E**), ectopic cell death (**Figure 4C**) and PR1a protein accumulation of *atmc1* plants (**Figure 4D**), complementation with the catalytically inactive variant (*atmc1 AtMC1*^{C220A}*–GFP*) not only failed to complement the *atmc1* phenotype but displayed more exacerbated hallmarks of autoimmunity compared to *atmc1* mutant plants: severe stunted growth and dwarfism, ubiquitous ectopic cell death activation and high protein levels of PR1a (**Figure 4B-E**)**.** The autoimmune phenotype occurred in more than two independent transgenic lines overexpressing *At*MC1^{C220A} (**Figure S2**). Independent transgenics expressing *AtMC1*–GFP driven by its native protomer visually rescued the autoimmune phenotype of *atmc1* mutant plants, whereas expression of catalytically inactive *At*MC1 driven by its native promoter phenocopied *atmc1* mutant plants (**Figure S3**). These results suggest that a certain threshold of *At*MC1^{C220A} is important to visualise the severe autoimmune phenotype. As expected, transgenic lines overexpressing catalytically inactive *At*MC2 in an *atmc2* mutant background (*atmc2 AtMC2*^{C258A}) did not display autoimmunity and grew as Wt and as *atmc2 AtMC2-GFP* plants (**Figure S4**), suggesting that this phenomenon is exclusive to overexpression of *At*MC1^{C220A}.

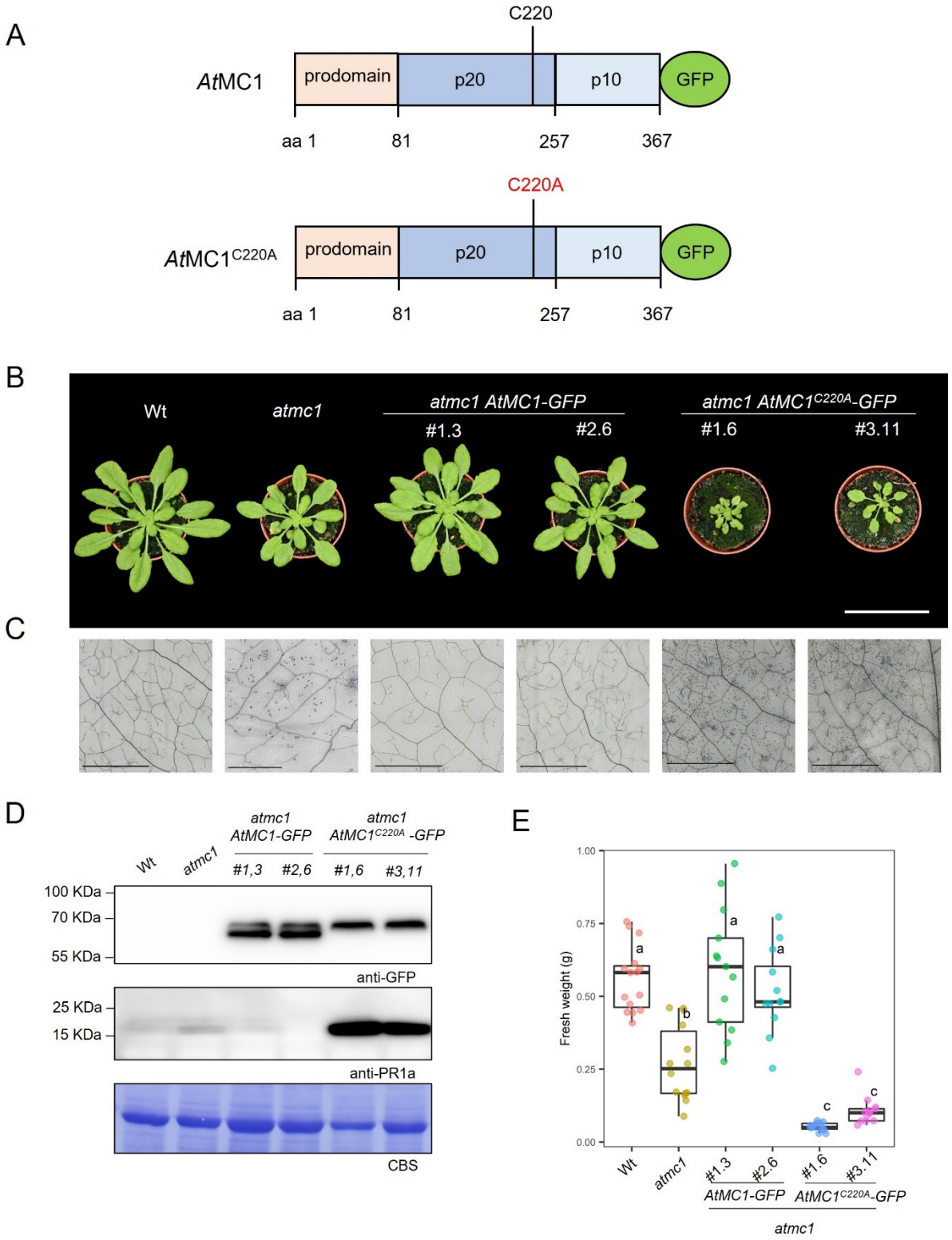

Figure 4. Overexpression of catalytically inactive *At*MC1 in an *atmc1* background leads to severe autoimmunity. (A) Scheme of *At*MC1 and catalytically inactive *At*MC1 (*At*MC1^{C220A}) proteins fused to GFP. The prodomain, p20 and p10 domains are indicated. The catalytic cysteine (C220) is also indicated. **(B)** Representative images of 40-day-old plants with the indicated genotypes grown under short day conditions. Two independent homozygous stable transgenics expressing either *AtMC1-GFP* (#1.3 and #2,6) or *AtMC1^{C220A}-GFP* (#1.6 and #3.11) under the control of a 35S constitutive promoter

from the Cauliflower Mosaic Virus in the *atmc1* mutant background are shown. Scale bar = 5.5 cm. **(C)** Trypan blue staining of an area belonging to the 6th true leaf of the plants shown in **B**. Scale bar = 0.5 mm. **(D)** Total protein extracts from the plants shown in **B** were run on an SDS-PAGE gel and immunoblotted against the indicated antisera. CBS of the immunoblotted membranes shows protein levels of Rubisco as a loading control. **(E)** Plant fresh weight of genotypes shown in A (n=12). Different letters indicate statistical difference in fresh weight between genotypes (one-way ANOVA followed by post hoc Tukey, p value < 0.05).

The N-terminal prodomain of *At*MC1 has been shown to negatively regulate its function (Asqui et al., 2018; Coll et al., 2010). To test whether the N-terminal prodomain was required for rescuing the autoimmune phenotype of *atmc1* plants or dispensable for the severe autoimmune phenotype in *atmc1 AtMC1*^{C220A}*–GFP* plants, we complemented *atmc1* plants with N-terminally truncated versions of *At*MC1 lacking the first 81 amino acids (**Figure 4A**), with either their catalytic site intact or mutated to alanine (*atmc1 ΔNAtMC1–GFP* or *atmc1 ΔNAtMC1* ^{C220A}*–GFP*). As evidenced by visual phenotypes and fresh weight quantifications, *atmc1 ΔNAtMC1–GFP* failed to rescue the *atmc1* phenotype to Wt levels (**Figure S5**). Interestingly, the N-terminal prodomain was required for the exacerbated autoimmune phenotype observed in *atmc1 AtMC1*^{C220A} plants (**Figure S5**).

*At*MC1^{C220A} is an inactive protease as evidenced by the lack of self-processing (single protein band) when detected in western blots compared to Wt AtMC1 (two protein bands) (**Figure 4D**). Accordingly, we asked whether the inability to be auto-processed at the junction between the N-terminal prodomain and p20 domain could explain the phenotype of plants expressing catalytically inactive *At*MC1. Given that most plant metacaspases (except *At*MC9) require Ca^{2+} binding to become active (Zhu et al., 2020), we generated transgenic plants overexpressing *At*MC1 with alanine substitutions within a conserved region of negatively charged residues in the p20 domain where Ca^{2+} binds and activates *At*MC1 (D173A, E174A and D176A: *At*MC1^{DED}) (35). Interestingly, although no auto-processing is observed by western blot in *At*MC1^{DED}–GFP extracts, *atmc1 AtMC1^{DED}–GFP* plants did not exhibit signs of severe autoimmunity and only partially restored the fresh weight defects of *atmc1* plants (**Figure S6A-C**). Similarly, overexpression of an *At*MC1 variant carrying a point mutation at the predicted Arg auto-processing site (*At*MC1^{R49A}) did not result in severe autoimmunity despite no auto-processing being observed (**Figure S6D-E**). Altogether, we conclude that catalytically inactive *At*MC1 triggers severe autoimmunity in a prodomain-dependent manner and that full length variants that are unable to be auto-processed (*At*MC1^{DED}–GFP or *At*MC1^{R49A}–GFP) do not trigger severe autoimmunity.

The autoimmune phenotype caused by catalytically inactive AtMC1 is almost fully dependent on SA synthesis and partially dependent on the EDS1-PAD4-ADR1 immune node.

Genetic studies support that the EDS1-PAD4-ADR1 node contributes to basal immune responses and ETI responses that slow pathogen proliferation upon activation of certain TNLs, PRRs or CNLs (Saile et al., 2020; Sun et al., 2021). By contrast, the EDS1-SAG101-NRG1 node is involved specifically in

TNL-mediated ETI and is strictly required for cell death initiated by certain TNLs (Saile et al., 2020; Sun et al., 2021). A genetically parallel SA pathway dependent on the ICS (SID2) enzyme is bolstered by PAD4-ADR1 via a mutually reinforcing feedback loop (Cui et al., 2017; Sun et al., 2021). We interrogated which of these components downstream of sNLRs or PRRs could be implicated in the autoimmune phenotype of *atmc1 AtMC1*^{C220A}*–GFP* plants. A deletion in EDS1 (*eds1-12*) partially rescued the fresh weight defects of *atmc1 AtMC1*^{C220A}*–GFP* plants (**Figure 5A and D**), though spontaneous cell death (**Figure 5B**) and PR1a accumulation still occurred (**Figure 5C**). Introducing a mutation in ICS1 (*sid2-1*), which impairs SA synthesis, considerably rescued fresh weight defects to the levels of *atmc1* mutant plants (**Figure 5D**), partially prevented spontaneous cell death (**Figure 5B**) and fully abolished PR1a protein accumulation (**Figure 5C**).

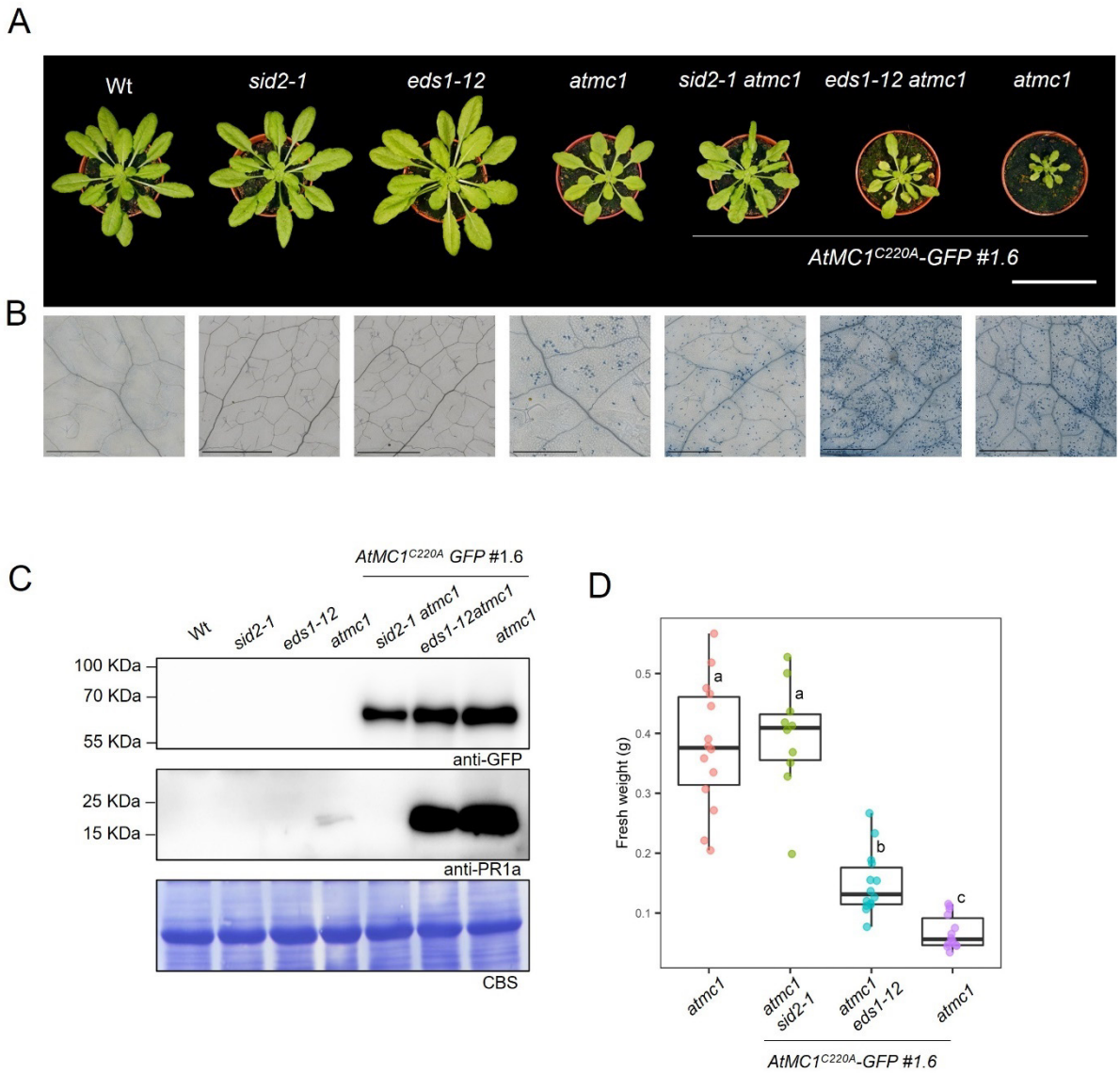

Figure 5. Autoimmunity caused by catalytically inactive *At*MC1 is dependent on SA synthesis and partially dependent on EDS1 signalling. (A) Representative images of 40-day-old plants with the indicated genotypes grown under short day conditions. Scale bar= 5.5 cm. **(B)** Trypan blue staining of an area belonging to the 6th true leaf of the plants shown in **A**. Scale bar = 0.5 mm. **(C)** Total protein

extracts from the plants shown in **A** were run on an SDS-PAGE gel and immuno-blotted against the indicated antisera. CBS of the immunoblotted membranes shows protein levels of Rubisco as a loading control. **(D)** Plant fresh weight of genotypes shown in **A** (n=12). Different letters indicate statistical difference in fresh weight between genotypes (one-way ANOVA followed by post hoc Tukey, p value < 0.05). Quantification of fresh weight from Wt*, sid2-1* and *eds1-12* were excluded from the fresh weight graph to better appreciate statistical differences between genotypes of interest.

Interestingly, mutating SAG101 (*sag101-1*) neither rescued the fresh weight defects (**Figure 6A and D**) nor prevented PR1a protein accumulation (**Figure 6C**). By contrast, mutating PAD1 (*pad4-1*) partially rescued the fresh weight defects phenocopying *eds1-12 atmc1 AtMC1*^{C220A}*–GFP* plants (**Figure 6A and D**). Finally, introducing a mutation in the NGR1 hNLR family (*nrg1.2 nrg1.2*) phenocopied *sag101-1 atmc1 AtMC1*^{C220A}*–GFP* plants (**Figure 7**), whereas introgression of the *helperless* genetic background (all helper NLRs mutated: *nrg1.1, nrg1.2, adr1, adr1-l1, adr1l-2;* **See Materials and Methods**) also partially rescued the fresh weight defects and PR1a protein accumulation phenocopying *pad4-1 atmc1 AtMC1*^{C220A}*–GFP* and eds*1-12 atmc1 AtMC1*^{C220A}*–GFP* plants (**Figure 7**). We conclude that the autoimmune phenotype caused by *At*MC1^{C220A}–GFP is partially dependent on the EDS1-PAD4-ADR1 immune node and almost fully dependent on SA synthesis, as the phenotype was rescued to *atmc1* mutant levels.

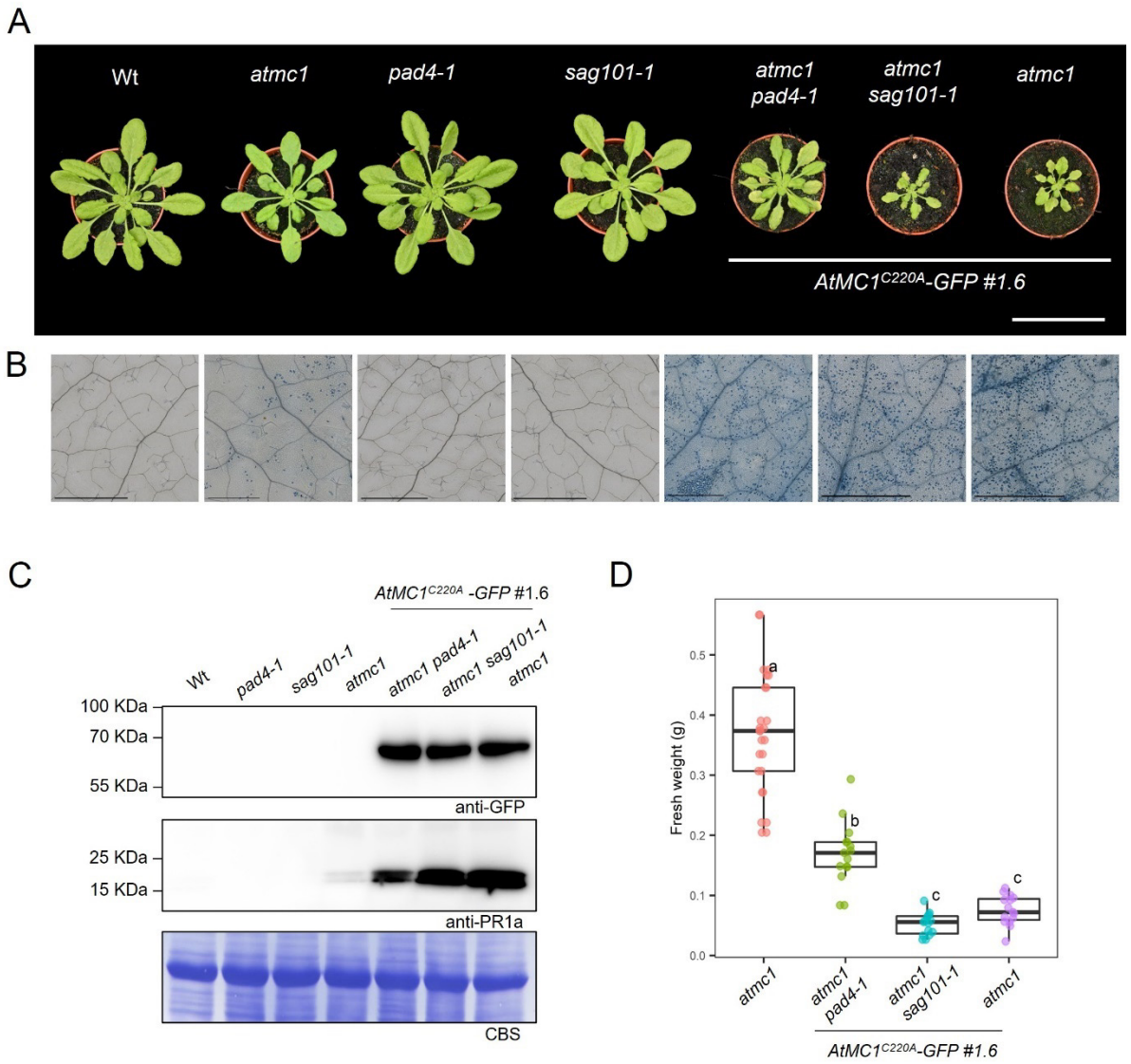

Figure 6. Autoimmunity caused by catalytically inactive *At*MC1 is partially dependent on PAD4 but not SAG101. (A) Representative images of 40-day-old plants with the indicated genotypes grown under short day conditions. Scale bar= 5.5 cm. **(B)** Trypan blue staining of an area belonging to the 6th true leaf of the plants shown in **A**. Scale bar = 0.5 mm. **(C)** Total protein extracts from the plants shown in **A** were run on an SDS-PAGE gel and immuno-blotted against the indicated antisera. CBS of the immunoblotted membranes shows protein levels of Rubisco as a loading control. **(D)** Plant fresh weight of genotypes shown in **A** (n=12). Different letters indicate statistical difference in fresh weight between genotypes (one-way ANOVA followed by post hoc Tukey, p value < 0.05). Quantification of fresh weight from Wt, *pad4-1* and *sag101-1* were excluded from the fresh weight graph to better appreciate statistical differences between genotypes of interest.

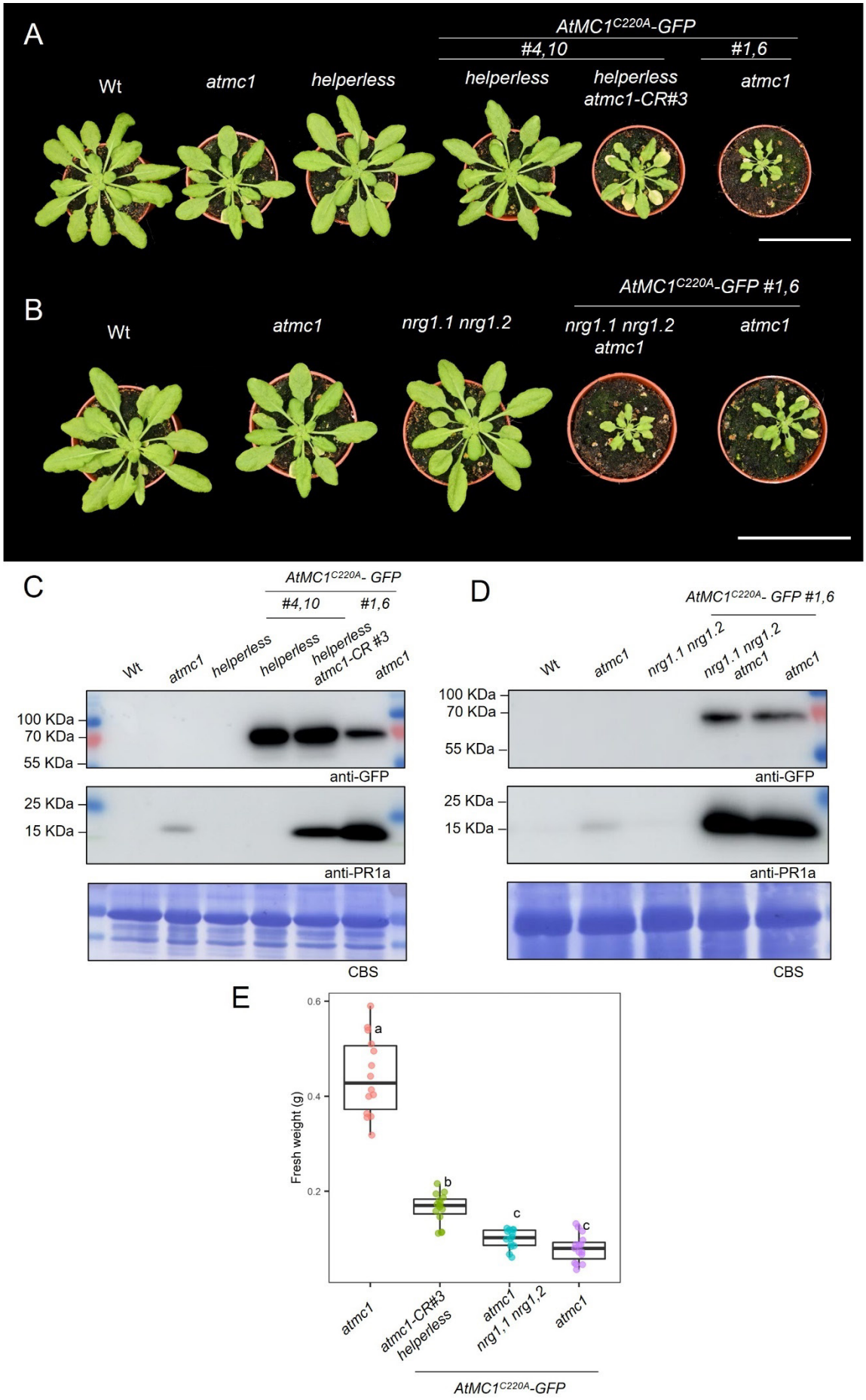
A
AtMC1C220A-GFP
#4,10
#1,6
Wt
atmc1
helperless
helperless
helperless atmc1-CR#3
atmc1
B
AtMC1C220A-GFP #1,6
Wt
atmc1
nrg1.1 nrg1.2
nrg1.1 nrg1.2 atmc1
atmc1
C
AtMC1C220A- GFP
#4,10
#1,6
Wt
atmc1
helperless
helperless
helperless atmc1-CR #3
atmc1
100 KDa
70 KDa
55 KDa
anti-GFP
25 KDa
15 KDa
anti-PR1a
CBS
D
AtMC1C220A- GFP #1,6
Wt
atmc1
nrg1.1 nrg1.2
nrg1.1 nrg1.2 atmc1
atmc1
100 KDa
70 KDa
55 KDa
anti-GFP
25 KDa
15 KDa
anti-PR1a
CBS
E
Fresh weight (g)
0.6
0.4
0.2
a
b
c
c
atmc1
atmc1-CR#3 helperless
atmc1 nrg1,1 nrg1,2
atmc1
AtMC1C220A-GFP

Figure 7. Autoimmunity caused by catalytically inactive *At*MC1 is partially dependent on the hNLR family ADR1 but not NRG1. (A-B) Representative images of 40-day-old plants with the indicated genotypes grown under short day conditions. Scale bar=5.5 cm. **(C-D)** Total protein extracts from the plant genotypes shown in **A-B** were run on an SDS-PAGE gel and immuno-blotted against the indicated antisera. CBS of the immunoblotted membranes shows protein levels of Rubisco as a loading control. **(E)** Plant fresh weight of genotypes shown in **A-B** (n=12). Different letters indicate statistical difference in fresh weight between genotypes (one-way ANOVA followed by post hoc Tukey, p value < 0.05). Quantification of fresh weight from Wt, *helperless, helperless/ AtMC1^{C220A}-GFP* and *nrg1.1 nrg1.2* were exluceded from the fresh weight graph to better appreciate statistical differences between genotypes of interest.

Wt *AtMC1 alleles supress the autoimmune phenotype caused by catalytically inactive AtMC1.*

To test whether overexpression of catalytically inactive *At*MC1 has a dominant effect over endogenous Wt *AtMC1* alleles, we crossed a Wt plant with an *atmc1 AtMC1*^{C220A}*–GFP* autoimmune plant and looked at the phenotype of Wt *AtMC1*^{C220A}*–GFP* in an F3 offspring. Interestingly, independent Wt *AtMC1*^{C220A}*–GFP* lines (#1,6 and #10,3) did not display autoimmunity features (**Figure 8**). To further substantiate our result, we generated a CRISPR *AtMC1* deletion mutant (*atmc1-CR#2*) in line Wt *AtMC1^{C220A}-GFP #10,3*, with single guide RNAs targeting the 5´ and 3´ untranslated region (UTRs) of the Wt *AtMC1* alleles (**Figure 2A**), thus not affecting the transgene which is in a coding sequence format. As expected, *atmc1-CR#2 AtMC1*^{C220A}*–GFP* plants displayed a similar autoimmune phenotype as *atmc1* (T-DNA) *AtMC1*^{C220A}*–GFP* plants (**Figure 8**). Altogether our data argues on the importance of gene dosage of Wt *AtMC1* alleles in supressing the phenotype caused by catalytically inactive *At*MC1 (**Figure 8**). Knowing that the autoimmune phenotype does not occur when catalytically inactive *At*MC1 is overexpressed in a Wt background and partial rescues are achieved when mutating the same signalling components (**Figure 3 and Figure 5,6,7**), we speculate that overexpression of catalytically inactive *At*MC1 may represents an additive phenotype to the autoimmunity observed in *atmc1* plants.

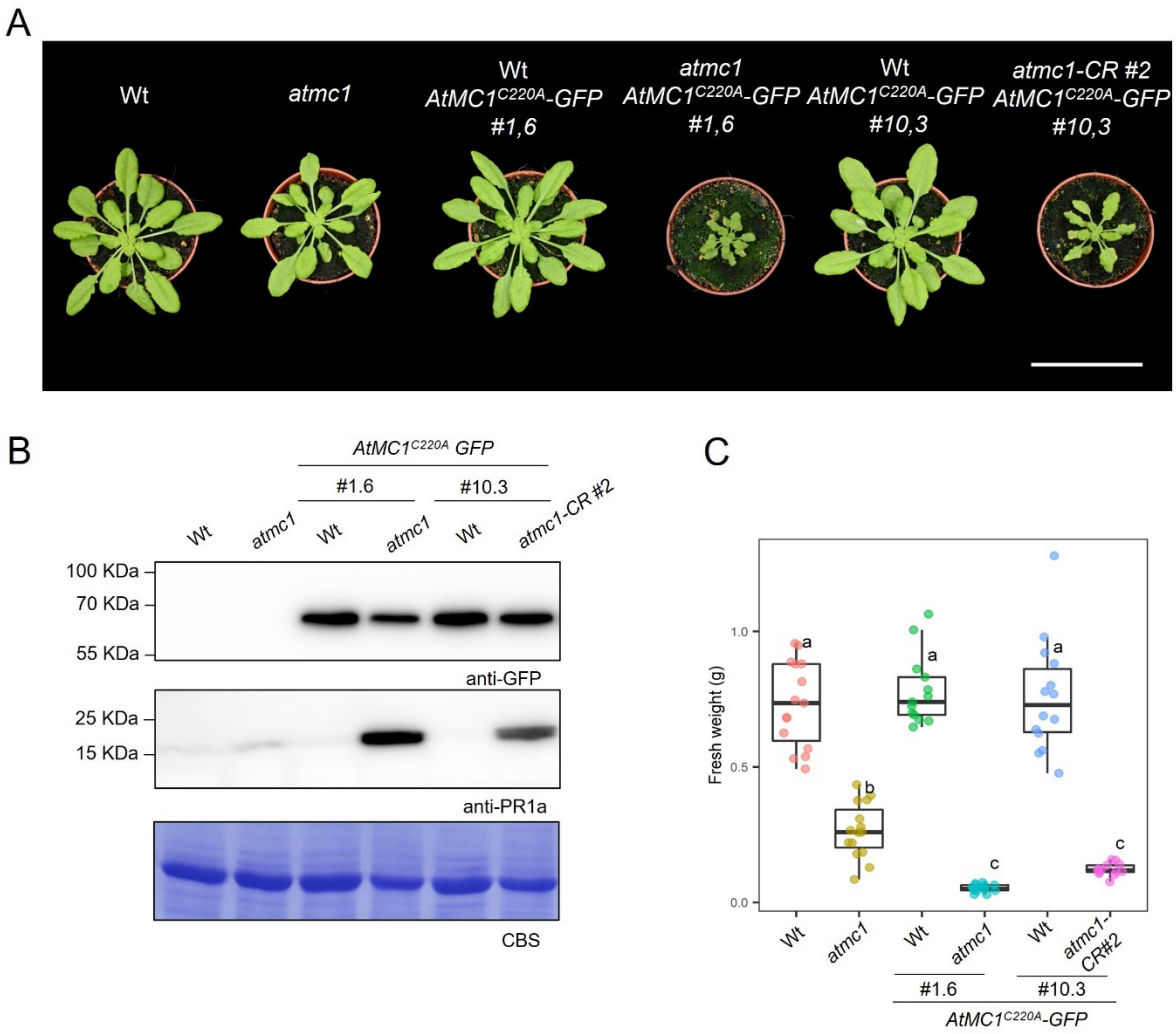

Figure 8. **Endogenous Wt *AtMC1* alleles supress the autoimmune phenotype caused by overexpression of catalytically inactive *At*MC1**. **(A)** Representative images of 40-day-old plants with the indicated genotypes grown under short day conditions. Scale bar= 5.5 cm. **(C)** Total protein extracts from the plant genotypes shown in **A** were run on an SDS-PAGE gel and immuno-blotted against the indicated antisera. CBS of the immunoblotted membranes shows protein levels of Rubisco as a loading control. **(D)** Plant fresh weight of genotypes shown in **A** (n=12). Different letters indicate statistical difference in fresh weight between genotypes (one-way ANOVA followed by post hoc Tukey, p value < 0.05).

Catalytically inactive AtMC1 forms protein complexes with immune related components involved in PTI and ETI.

To better understand the mechanism by which catalytically inactive *At*MC1 triggers autoimmunity, we performed immunoprecipitation followed by mass spectrometry (IP-MS). We pulled down *At*MC1^{C220A}–GFP from extracts of Wt *At*MC1^{C220A}–*GFP* plants in which no autoimmunity is visible *vs atmc1 AtMC1^{C220A}–GFP* plants in which plants display autoimmunity (**Figure 8 and Figure 9B**). IP from plant extracts expressing free GFP (Wt *35S::GFP*) were used as a negative control. Since catalytically inactive *At*MC1 localized to microsomal fractions (total membranes) and Wt *At*MC1 was mainly localized

in soluble fractions (cytosol) (**Figure 9A**), we conducted the IP-MS analysis in microsomal fractions. We reasoned that identifying interactors in this fraction could give us a better understanding of the underlying causes of autoimmunity.

Overall, a higher number of statistically significant ($log_2FC > 2$ FDR <0.05) peptides were identified when *At*MC1^{C220A}–GFP was pulled down from autoimmune plants (310 peptides) (*atmc1 AtMC1^{C220A}–GFP*) *vs* Wt-looking plants (215 peptides) (Wt *At*MC1^{C220A}–*GFP*) (**Figure 9B**). Gene Ontology (GO) searches revealed that interactors of *At*MC1^{C220A}–GFP in autoimmune plants are mainly involved in biological processes related to plant defence (**Figure S7**). GO terms such as “defence-response to bacterium”, “regulation of defence response”, “response to wounding” and “response to SA” exhibit the greatest statistical confidence among the GOs found (**Figure S7**).

Since it is estimated that a great proportion if not all, autoimmune phenotypes are either directly or indirectly NLR-dependent (Freh et al., 2022), we hypothesised that their hyperactivation through binding to catalytically inactive *At*MC1 could be the cause of the autoimmune phenotype. In our IP-MS data sets, we found one CNL and one TNL, RPS2 and SSI4 (AT5G41750), respectively, interacting at the microsomal fraction with catalytically inactive *At*MC1 specifically in the autoimmune plant *atmc1 AtMC1^{C220A}–GFP* (**Figure 9B-C**). Besides these NLRs, we also found interactors involved in PTI such as the PRR RECEPTOR-LIKE PROTEIN 42 (RLP42), and the receptor-like kinase, SOBIR1, which is required for the function of different PRRs of the RLP family (Liebrand et al., 2014). We also found the PM-localized NADPH oxidase, RBOHF, involved in active ROS production during HR and PTI, as an interactor (**Figure 9C**) (Torres et al., 2002). We tested interactions of all the selected proteins (**Figure 9C**) with either Wt or catalytically inactive versions of *At*MC1 by *in planta* co-immunoprecipitations (co-Ips) in *Nicotiana benthamiana* (*N. benthamiana*) (**Figure 10**). Both NLRs, RPS2-HA and SSI4-HA, interact with *At*MC1^{C220A}-GFP and to a lesser extent with Wt *At*MC1-GFP (**Figure 10A-B**). Similarly, 10xMyc-SOBIR1, 10xMyc-RLP42, and FLAG-RBOHF interact strongly with *At*MC1^{C220A}-GFP and to a lesser extent with Wt *At*MC1-GFP (**Figure 10C-E**). The interaction between SOBIR1 and *At*MC1 was tested in Arabidopsis by immunoprecipitating AtMC1^{C220A}-GFP in *atmc1 AtMC1^{C220A}–GFP* and Wt (Col-0)/*AtMC1^{C220A}–GFP* and probing with commercially available SOBIR1 antisera. Co-immunoprecipitation between AtMC1 and SOBIR1 occurred exclusively in the autoimmune plant *atmc1 AtMC1^{C220A}–GFP* but not in Wt *AtMC1^{C220A}–GFP* (**Figure 10F**).

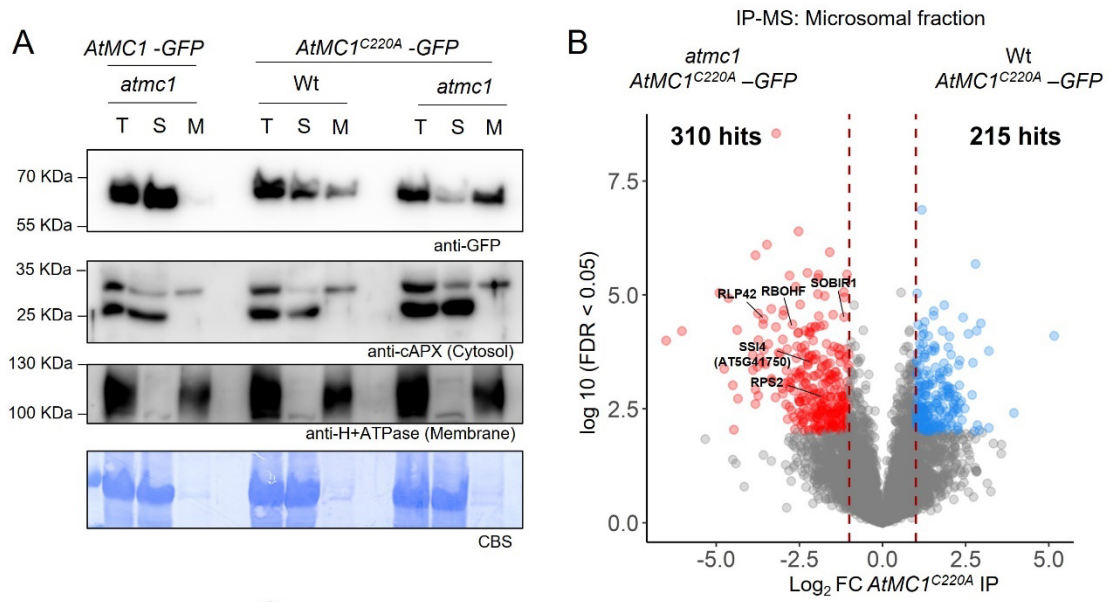

C

NLRs	PTI components
RPS2	SOBIR1
TIR-NLR (AT5G41750)	RLP42
	RBOHF

Figure 9. Catalytically inactive *At*MC1 is enriched in microsomes and form protein complexes with immune related components involved in PTI and ETI when expressed in an *atmc1* mutant background. (A) Fractionation assays from 40-day-old plant extracts with the indicated plant genotypes (transgene and genetic background indicated). Total (T), Soluble (S, cytoplasmic proteins) and Microsomal (M, total membranes) fractions were run on an SDS-PAGE gel and immunoblotted against the indicated antisera. Anti-cAPX and anti-H+ATPase were used as cytosol and membrane markers, respectively, to evaluate the success of fractionation. CBS of the immunoblotted membranes shows protein levels of Rubisco as a loading control. This experiment was repeated twice with similar results. **(B)** Volcano plot of normalized abundances (label free quantification (LFQ), log2 scale) for proteins that immunoprecipitated with *At*MC1^{C220A}–GFP when expressed in either an *atmc1* mutant background (red) or a Wt background (blue) (Student´s t-test p-value < 0.05 and $Log_2FC > 1$). The IP-MS analysis was performed on samples collected in four independent biological replicates. **(C)** NLRs, and immune components involved in PTI that immunoprecipitated with *At*MC1^{C220A}–GFP in *atmc1 AtMC1^{C220A}–GFP* autoimmune plants and that were selected for further studies.

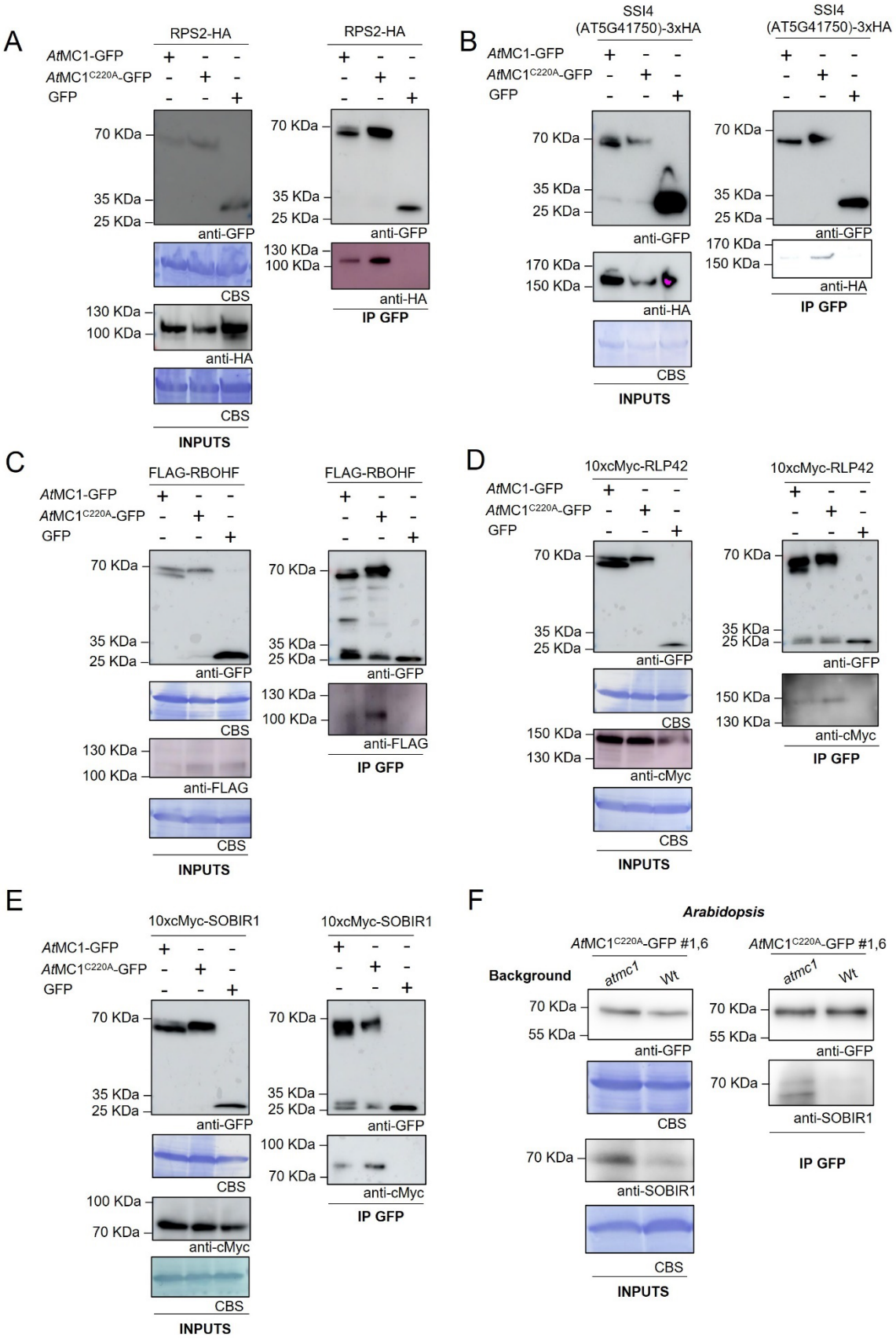
A
RPS2-HA
RPS2-HA
AtMC1-GFP
AtMC1C220A-GFP
GFP
70 KDa
35 KDa
25 KDa
anti-GFP
CBS
130 KDa
100 KDa
anti-HA
CBS
INPUTS
IP GFP
B
SSI4 (AT5G41750)-3xHA
170 KDa
150 KDa
C
FLAG-RBOHF
anti-FLAG
D
10xcMyc-RLP42
anti-cMyc
E
10xcMyc-SOBIR1
F
Arabidopsis
AtMC1C220A-GFP #1,6
Background
atmc1
Wt
55 KDa
anti-SOBIR1

Figure 10. Catalytically inactive *At*MC1 interacts *in planta* with NLRs, and immune components involved in PTI. **(A-E)** *At*MC1-GFP, *At*MC1^{C220A}-GFP or free GFP were transiently co-expressed with either RPS2-HA **(A)**, SSI4-3xHA **(B)**, FLAG-RBOHF **(C)**, 10xcMyc-RLP42 **(D)** or 10xcMyc SOBIR1 **(E)** in *N. benthamiana*. 3 days post-infiltration (dpi) plant extracts co-expressing the indicated constructs were immunoprecipitated with anti-GFP magnetic beads (IP GFP). Protein inputs from protein extracts before IP (INPUTS) and eluates from IPs were run on an SDS-PAGE and immunoblotted against the indicated antisera. CBS of the immunoblotted membranes shows protein levels of Rubisco as a loading control in the inputs. **(F)** IP of *At*MC1^{C220A}-GFP in extracts of Arabidopsis stable transgenics overexpressing *At*MC1^{C220A}-GFP either in an *atmc1* mutant or a Wt background. Inputs from extracts and eluates from the IP were run on an SDS-PAGE and immunoblotted against SOBIR1 (anti-SOBIR1). CBS of the immunoblotted membranes shows protein levels of Rubisco as a loading control in the inputs.

Based on these results, we formulated two different hypothesis that could explain the phenotypes observed in *atmc1* and *atmc1 AtMC1*^{C220A}*–GFP* plants: 1) *At*MC1 or its catalytic activity is guarded by (an) NLR(s). 2) *At*MC1 participates in the proteostasis of immune components and overexpression of catalytically inactive *At*MC1 binds and traps immune components (NLRs and components involved in PTI), thus preventing their otherwise correct turnover.

To test our first hypothesis, we carried out an NLR-targeted forward genetic screen to find suppressors of the severe autoimmune phenotype of *atmc1 AtMC1*^{C220A}*–GFP* plants. We independently transformed a previously described collection of dominant-negative (DN)-NLRs in *atmc1 AtMC1*^{C220A}*–GFP* plants (Lolle et al., 2017). DN-NLRs carry a mutation in a conserved P-loop region within the ATPase domain of the NLR which, by a yet unknown mechanism, can disrupt the function of Wt NLR alleles (Freh et al., 2022). This approach proved successful for the identification of two unrelated NLRs, DSC1 and DSC2, responsible for the autoimmune phenotype of *camta3* mutants (Freh et al., 2022; Lolle et al., 2017). Out of the 166 NLRs present in Arabidopsis Col-0 accession (Lee & Chae, 2020), we individually transformed 139 DN-NLRs into the autoimmune plant *atmc1 AtMC1*^{C220A}*–GFP* plants and screen for rescued plants in the T_1 generation (**Table S4).** Neither of these DN-NLR transformations yielded a rescued plant in T_1. Particularly, independent T_2 transgenics overexpressing *DN-RPS2* and *DN-SSI4 (AT5G41750)* did not rescue the autoimmune phenotype (**Figure S8A**). Moreover, a null mutation in RPS2 (*rps2-201c*) and the knockout mutations in RLP42 (*rlp42-2*) or RBOHF (*rbohf*) did not supress the autoimmune phenotype (**Figure S8B**). Recently, SOBIR1 complexes were shown to recruit the co-receptor BAK1 and connect RLP23 to PAD4-EDS1-ADR1 upon ligand (PAMP) binding to RLP23 (Pruitt et al., 2021). As shown in **Figure S8C,** introducing mutations in RLP23 (*rlp23-1*), SOBIR1 (*sobir1-12*) or the co-receptor BAK1 (*bak1-4*) did not result in rescues of the autoimmune phenotype. In light of these results, we hypothesised that instead of a single NLR or PTI component being aberrantly activated in *atmc1 AtMC1*^{C220A}*–GFP* plants, a broad hyperactivation of multiple NLRs or perhaps other immune components underlies the observed autoimmunity.

Overexpression of SNIPER1 rescues the autoimmune phenotype caused by catalytically inactive AtMC1.

Since no genetic rescues were achieved when individually introducing mutations in sNLRs (**Figure S8 and Table S4),** we explored whether a broad defect in sNLR homeostasis in plants expressing catalytically inactive *At*MC1 could account for the severe autoimmune phenotype observed. The E3 ubiquitin-ligase SNIPER1, is a master regulator that broadly controls sNLR levels (Z. Wu et al., 2020). SNIPER1 specifically binds to the nucleotide binding domain (NBD) of sensor TNLs and CNLs to mediate their turnover through the 26S proteasome. Accordingly, autoimmune mutants that are sNLR-dependent such as *snc1, chs1-2, chs2-1, and chs3-2D* are fully rescued by overexpression of SNIPER1 (Z. Wu et al., 2020). Interestingly, when SNIPER1 was overexpressed in the autoimmune background *atmc1 AtMC1*^{C220A}*–GFP*, independent transgenics (*atmc1 AtMC1*^{C220A}*–GFP x HA-SNIPER1*) exhibited an almost complete rescue in all phenotypic outputs tested: visual rescue, suppression of spontaneous cell death and low accumulation of PR1a that inversely correlated with expression of SNIPER1 (**Figure 11**). Based on this data we conclude that *atmc1 AtMC1*^{C220A}*–GFP* plants might suffer from defects in overall sNLR homeostasis and consequently the phenotype is attenuated when a master regulator of sNLR levels is overexpressed.

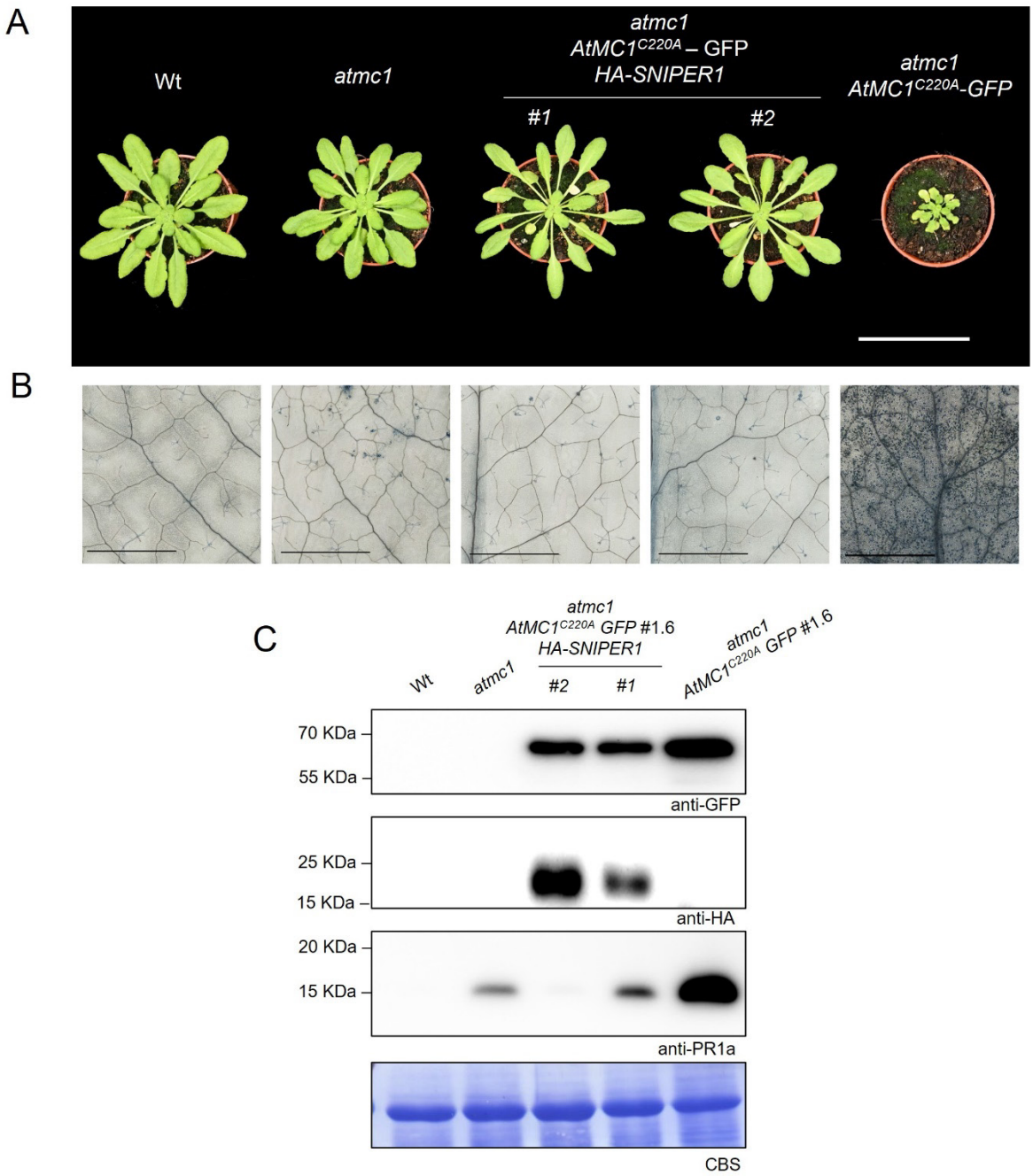

Figure 11. Overexpression of the E3 ubiquitin ligase SNIPER1 that broadly regulates homeostasis of sNLRs, rescues the autoimmune phenotype caused by catalytically inactive *At*MC1. (A) Representative images of 40-day-old plants with the indicated phenotypes grown under short day conditions. Two independent stable transgenics in the T_2 generation expressing HA-SNIPER1 (#1 and #2) under the control of a 35S constitutive promoter in the *atmc1 AtMC1^{C220A}-GFP* background are shown. Scale bar=5.5 cm. **(B)** Trypan blue staining of an area belonging to the 6th true leaf of the plants shown in **A**. Scale bar = 1.25 mm. **(C)** Total protein extracts from the plants shown in **A** were run on an SDS-PAGE gel and immuno-blotted against the indicated antisera. CBS of the immunoblotted membranes shows protein levels of Rubisco as a loading control.

Catalytically inactive AtMC1 localizes to puncta structures that colocalize with autophagosomes and are degraded through autophagy.

In biochemical assays, Wt *At*MC1-GFP was mainly enriched in total and soluble fractions, whereas *At*MC1^{C220A}-GFP is found in total and microsomal fractions (**Figure 9A**). Accordingly, when we probed their subcellular localization in leaf epidermal cells under the confocal microscope, we observed that while *At*MC1-GFP is mainly localized in the nucleus and cytoplasm, *At*MC1^{C220A} localized to puncta structures distributed all over the cell periphery **(Figure 12A)**. *At*MC1^{C220A} localization to puncta structures rarely occurred in Wt/*AtMC1*^{C220A}-GFP, further supporting the observation that the endogenous Wt *AtMC1* alleles supress the phenotype caused by the catalytically inactive variant (**Figure 12A and Figure 8).** Moreover, the N-terminal prodomain is required for the localization of the catalytically inactive *At*MC1 variant to the microsomal fraction and puncta structures (**Figure S9**).
To explore the identity of these puncta structures, we generated double transgenics stably expressing previously characterized cellular markers of early endosomes (EE) and late endosomes (LE), mCherry-RabA5d and mCherry-RabG3C, respectively, along with *At*MC1^{C220A}-GFP (*atmc1 AtMC1*^{C220A}*-GFP x mCherry-RabA5d* and *atmc1 AtMC1*^{C220A}*-GFP x mCherry-RabG3C*) (Geldner et al., 2009). Neither of these markers exhibited a clear colocalization with *At*MC1^{C220A}-GFP puncta (**Figure S10**). We then hypothesised whether these puncta are destined to the vacuole for degradation through autophagy, a membrane-trafficking pathway by which molecules of different nature are selected as cargo and engulfed in double membrane compartments known as autophagosomes (Slobodkin & Elazar, 2013). Interestingly, double transgenics expressing *AtMC1*^{C220A}*-GFP* along with the core autophagy receptor *ATG8a*, (*atmc1 AtMC1*^{C220A}*-GFP x mCherry-ATG8a*) exhibited partial colocalization upon treatment with the vacuolar ATPase inhibitor Concanamycin A (Conc A), which allows visualization of fluorescently labelled proteins in the vacuole (**Figure 12B**).

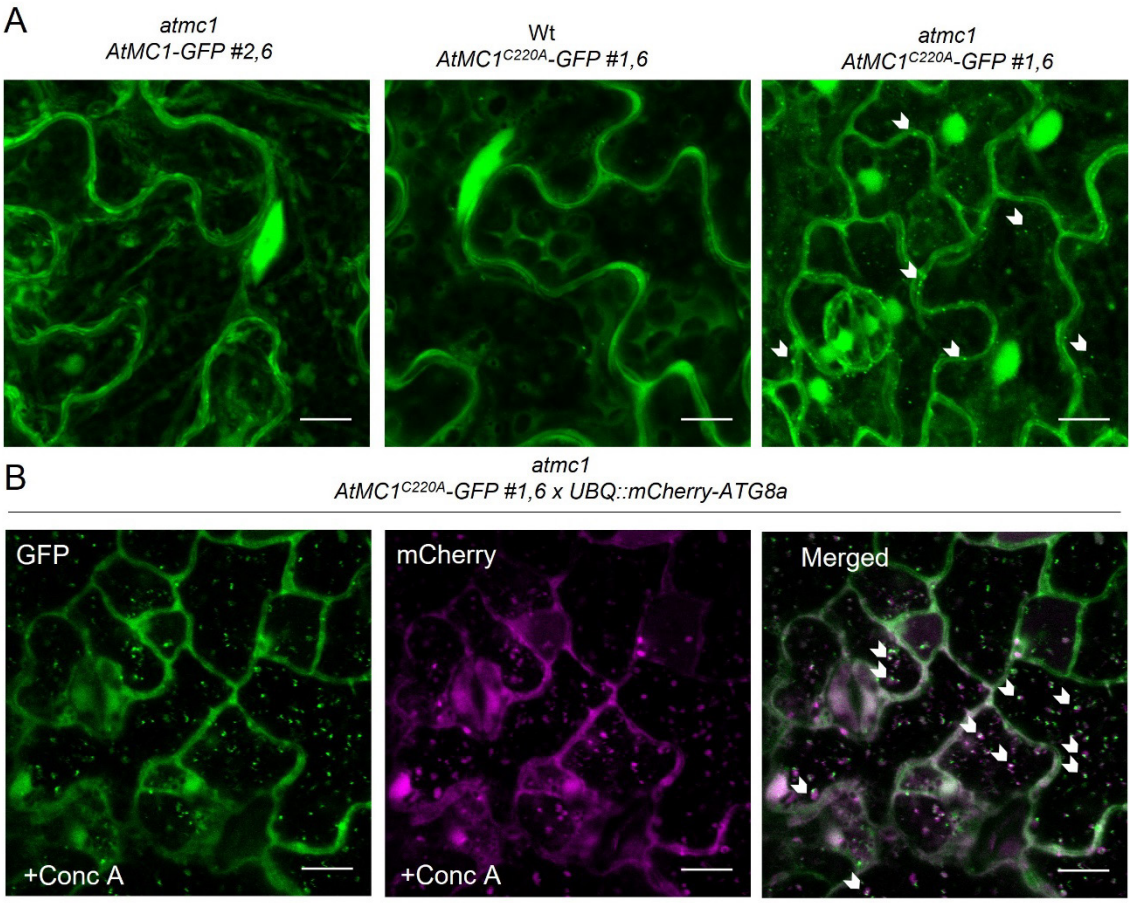

Figure 12. Catalytically inactive *At*MC1 but not Wt *At*MC1 localizes to puncta that partially localize to autophagosomes. (A) Representative confocal microscopy images from the leaf epidermis of 40-day-old plants grown under short day conditions with the indicated genotypes. Images represent a Z-stack of 18 images taken every 1 µm. Arrows indicate some of the puncta structures formed when *At*MC1^{C220A} is overexpressed in an *atmc1* mutant background. Scale bar = 10 µm. **(B)** Representative single-plane confocal microscopy images from the leaf epidermis of 40-day-old plants grown under short day conditions with the indicated genotypes. Double transgenics expressing *UBQ::mCherry-ATG8a* (T_2 generation) in the *atmc1 AtMC1^{C220A}-GFP* background were treated with 1 µM Concanamycin A (Conc A) to be able to visualize fluorescently labelled proteins inside the vacuole. Arrows in the merged image (GFP and RFP channel) indicate colocalization of ATG8a-labelled autophagosomes along with *At*MC1^{C220A} puncta structures. Scale bar = 10 µm.

To further substantiate our result, we independently introduced mutations in ATG2 (*atg2-1*) and ATG5 (*atg5-1*), which are core autophagy machinery proteins required for the biogenesis of autophagosomes (Leary et al., 2017), in the autoimmune genotype *atmc1 At*MC1^{C220A}-GFP. Accordingly, *atg2-1 atmc1 At*MC1^{C220A}-GFP and *atg5-1 atmc1 At*MC1^{C220A}-GFP plants exhibited a more severe autoimmune phenotype compared to *atmc1 At*MC1^{C220A}-GFP (**Figure 13A**). Moreover, these plants accumulated bigger and higher number of *At*MC1^{C220A}-GFP puncta compared to *atmc1 At*MC1^{C220A}-GFP plants (**Figure 13B**). Altogether our results suggest that *At*MC1^{C220A}-GFP complexes containing immune components are being degraded through autophagy, perhaps as an alternative turnover pathway, and

impairment of this recycling process further exacerbates the autoimmune phenotype displayed in *atmc1 At*MC1^{C220A}-GFP plants.

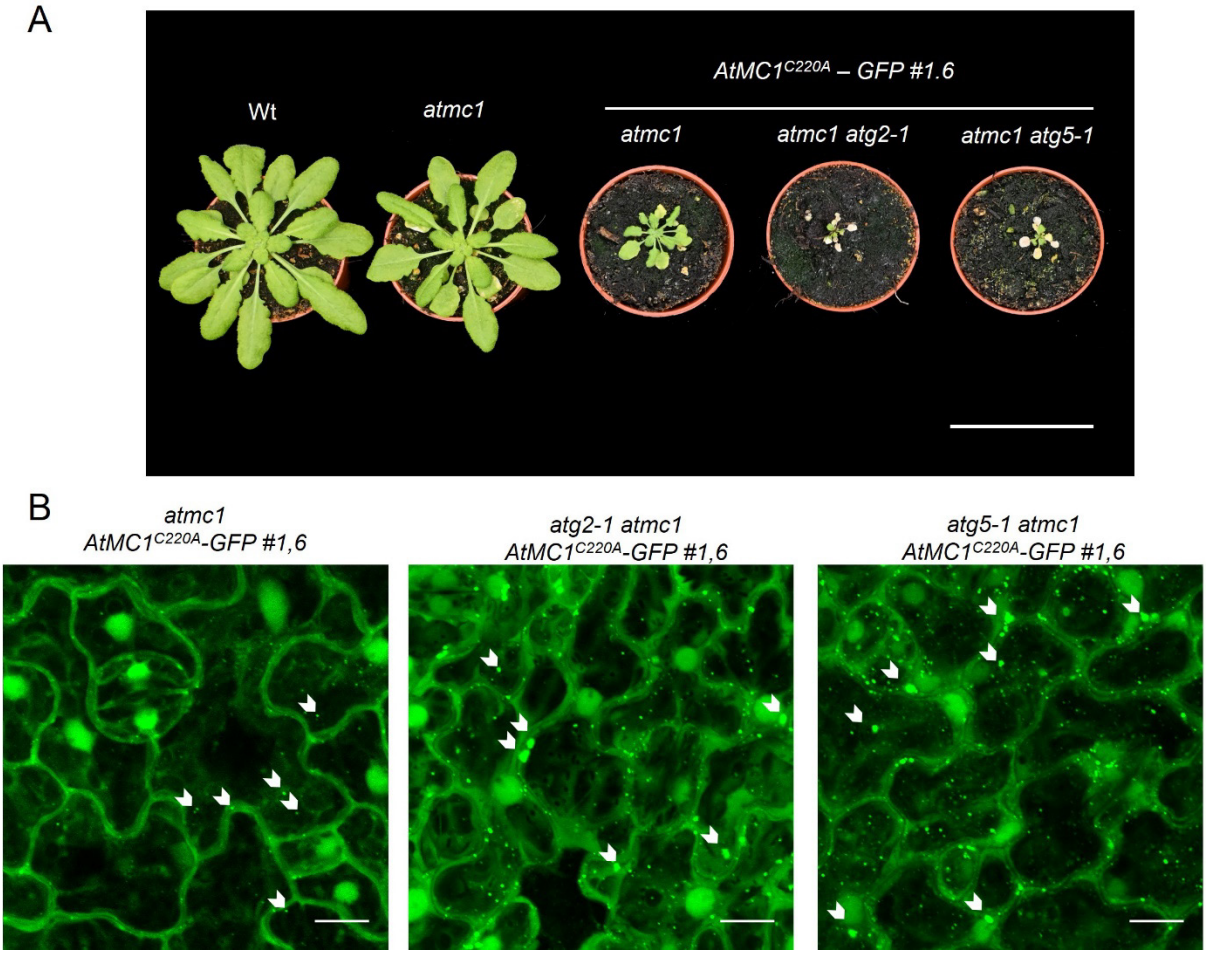

Figure 13. Introgression of the autophagy mutant alleles, *atg2-1,* and *atg5-1*, into *atmc1 AtMC1*^{C220A} plants further exacerbates the autoimmune phenotype and increases number and size of *At*MC1^{C220A} puncta structures. (A) Representative images of 40-day-old plants with the indicated phenotypes grown under short day conditions. **(B)** Representative confocal microscopy images from the leaf epidermis of plants shown in **A**. Images represent a Z-stack of 12 images taken every 1 µm. Arrows indicate puncta structures formed in the genotypes indicated. Scale bar = 10 µm.

DISCUSSION

Fine-tuning immune responses is of paramount importance for plant growth and fitness. Consequently, misregulation of immune receptor activation in the absence of pathogen attack leads to inappropriate and deleterious immune outputs, resulting in plant autoimmunity – a phenomenon in which spontaneous cell death, stunted growth, and sometimes plant lethality poses a serious disadvantage for plants (Freh et al., 2022). Hyperactivation of immune receptors during autoimmunity (particularly NLRs) may be caused by i) gain-of-function mutations in NLRs (Roberts et al., 2013; Zhang et al., 2003), ii) modifications or absence of NLR-monitored guardees including PTI components (Schulze et al., 2022; Y. Wu et al., 2020; Yang et al., 2022) or iii) aberrant regulation of NLRs at the transcriptional and

translational level (Freh et al., 2022; van Wersch et al., 2016; Z. Wu et al., 2020). Alternatively, unsuited interactions between NLR loci in heterozygous progeny derived from within-species ecotypes can lead to a class of autoimmunity known as hybrid incompatibility or hybrid necrosis (Bomblies & Weigel, 2007; Wan et al., 2021).

*At*MC1 and its homologue in maize *Zm*MC1 were previously shown to participate either in the regulation or subcellular re-localization of certain auto active NLRs, respectively (Luan et al., 2021; Roberts et al., 2013). In addition, our lab has recently demonstrated the dynamic recruitment of *At*MC1 to stress granules in proteotoxic stress conditions, inferring a proteostatic function of *At*MC1 in clearance of aberrant aggregates that are formed under these circumstances (Ruiz-Solina et al 2023., unpublished: **Chapter 3**).

Herein, we observed that mutant plants lacking *At*MC1 display hallmarks of autoimmunity as plants approach adulthood (**Figure 2B-D**). Thus, we explored the link between the previously reported homeostatic function of *At*MC1 and plant immunity. Interestingly, second-site mutations in key genes downstream of sNLR activation such as ICS1, EDS1 and PAD4, into the *atmc1* mutant background rescued the autoimmune phenotype, thus pointing towards contribution of sNLRs to the phenotype (**Figure 3**) (Cui et al., 2017). Whilst complementation with Wt *At*MC1 rescues the phenotype, overexpression of a catalytically inactive *At*MC1 variant (*At*MC1^{C220A}) in the *atmc1* mutant background results in severe autoimmunity (**Figure 4**). We made use of this C-terminally GFP-tagged knock-in variant as a tool to explore mechanisms that could infer the function of Wt *At*MC1 in plant immunity, and that would otherwise remain obscured when investigating the mild autoimmune phenotype of *atmc1* mutant plants.

Structural requirements for the autoimmune phenotype caused by catalytically inactive AtMC1.

Plant metacaspases are biochemically quite distinct to animal caspases, owing to their lack of aspartate specificity in their substrates and their preference for cleavage after Arg or Lys residues (Minina et al., 2020; Vercammen et al., 2007; Vercammen et al., 2004). However, metacaspases and caspases are often referred to as structural homologues as they share a common caspase-hemoglobinase fold at their catalytic domains (Minina et al., 2017). Strikingly, we observe remarkable similarities in the phenotypes derived from expression of catalytically inactive caspase 8 (CASP8 CA) in mammals (Fritsch et al., 2019; Newton et al., 2019) and overexpression of catalytically inactive *At*MC1 in plants. Wt CASP8 participates in apoptotic and necroptotic cell death (Orning & Lien, 2021) (**See Publication 1: INTRODUCTION**). Absence of CASP8 or loss of CASP8 catalytic activity results in embryonic lethality in mice (Fritsch et al., 2019; Newton et al., 2019). However, specific loss of CASP8 activity in mice epithelial cells induces intestinal inflammation as a result of aberrant activation of pyroptotic cell death (Fritsch et al., 2019). The authors showed a gene-dosage dependency in the phenotypes caused by inactive CASP8 and proposed that a distinct conformation in the protease compared to an active CASP8 may unmask the prodomain for interactions with components of the inflammasome (Fritsch et

al., 2019; Newton et al., 2019). In our study, we find remarkable similarities in the structural requirements for the phenotype caused by catalytically inactive *At*MC1 compared to inactive CASP8 in mice. Overexpression of catalytically inactive *At*MC1 in a Wt background does not lead to autoimmunity (**Figure 8**) in a similar way as Wt CASP8 alleles can supress the CASP8 CA-dependent inflammatory phenotypes in mice (Fritsch et al., 2019). Besides, the N-terminal prodomain of CASP8 is required to engage cells into pyroptosis through binding to ASC specks (Fritsch et al., 2019; Newton et al., 2019) (**See Publication 1: INTRODUCTION**). Similarly, Arabidopsis transgenics overexpressing a prodomainless catalytically inactive *At*MC1 variant do not display the autoimmune phenotype observed in plants overexpressing full-length catalytically inactive *At*MC1 (**Figure S5 and Figure 4**). Accordingly, this prodomainless variant is neither enriched in microsomal fractions nor localizes to puncta structures observed for full-length catalytically inactive *At*MC1 (**Figure 9A, Figure 12A and Figure S9**). We also showed that overexpression of non-cleavable *At*MC1 variants that carry point mutations either at the putative prodomain cleavage site (R49) or at the Ca^{2+} binding site does not result in severe autoimmunity (**Figure S6**) in a similar manner as non-cleavable mice CASP8 does not lead to inflammation (Tummers et al., 2020). Based on these similarities, it is tempting to speculate that although immune components and cell death pathways are not strictly conserved between plants and animals, structural conservation in the way these proteases fold may trigger similar phenotypic outputs. Therefore, inactive *At*MC1 might also favour a conformation in which the prodomain may serve as a docking site for protein-protein interactions that would otherwise not occur in an active *At*MC1 under basal conditions.

Catalytically inactive AtMC1 as a molecular platform for binding of immune-related protein complexes.

As opposed to Wt *At*MC1 that exhibits a diffuse nucleo-cytoplasmic localization and is mainly present in soluble fractions, catalytically inactive *At*MC1 localizes to puncta structures and is enriched in microsomal membrane fractions (**Figure 9A and Figure 12A**). Our proteomic analyses comparing interactors of catalytically inactive *At*MC1 when expressed in either an *atmc1* background (autoimmunity) or a Wt (no autoimmunity) background suggested that this variant interacts promiscuously with proteins involved in plant defence exclusively in plants exhibiting autoimmunity (**Figure 9B-C**). *In planta* co-immunoprecipitations (co-IPs) in *N. benthamiana* corroborated the ability of inactive *At*MC1 to bind sNLRs (RPS2 and SSI4 (AT5G41750)), PRRs (RLP42 and SOBIR1) or other immune-related components (RBOHF) (**Figure 10**). Absence of these interactors in the IP-MS experiment when plants express catalytically inactive *At*MC1 in a Wt background (Wt *AtMC1*^{C220A}*-GFP*) plants (**Figure 9B**), may imply that Wt *At*MC1 can compete for binding with defence-related interactors in these plants through more transient interactions, possibly participating in their homeostatic regulation or their re-localization to other cellular compartments, thus preventing inactive *At*MC1 from stabilizing NLRs, PRRs or other defence-related interactors.

Genetic requirements for the autoimmune phenotype caused by catalytically inactive AtMC1.

Introducing individual second-site mutations on these interactors or transgenesis of an almost-complete catalogue of Arabidopsis DN-NLRs (139 DN-NLRs or out 166 NLRs present in Arabidopsis) into the autoimmune background (*atmc1 At*MC1^{C220A}-GFP) did not result in a rescued phenotype (**Figure S8 and Table S4**). Therefore, we ruled out the possibility that *At*MC1 or perhaps its catalytic activity could be guarded by a single NLR. Interestingly, introducing mutations in EDS1, PAD4 or the ADR1 gene family partially rescued the severe autoimmune phenotype, whereas second-site mutations in SAG101 and the NRG1 gene family did not result in phenotypic differences compared to the autoimmune plant (**Figure 5, Figure 6, and Figure 7**). Suppression of SA synthesis, however, caused an almost complete rescue, abolishing PR1a protein accumulation and rescuing the fresh weight defects of autoimmune plants to the levels of *atmc1* mutants (**Figure 5**). Recent studies demonstrated that in Arabidopsis, ADR1s are required for full ETI triggered by all TNL tested and contribute, but are not strictly required, for ETI mediated by certain CNLs (Saile et al., 2020). NRG1s, on the other hand, are required for HR triggered by certain TNLs but do not have obvious functions during CNL-mediated HR and disease resistance (Castel et al., 2019; Saile et al., 2020) .Given that all autoimmune genotypes that are TNL-mediated are fully dependent on EDS1 (Rodriguez et al., 2016), our genetic data suggest that CNLs, which can be either fully or partially EDS1 independent, might also contribute to the phenotype of *atmc1 At*MC1^{C220A}-GFP plants **(Figure 5)**. We argue that the partial rescues observed when second-site mutations in EDS1, PAD4 and ADR1 are introduced (**Figure 5, Figure 6 and Figure 7**) might occur due to the interference with the SA-mediated feedback loop that goes into EDS1-PAD4-ADR1 to bolster ETI responses (Cui et al., 2017), therefore preventing amplification of the constitutive immune response taking place in autoimmune plants. Preventing SA synthesis by introducing mutations in ICS1 (*sid2-1*) almost completely rescued the phenotype but did not completely abolish cell death (**Figure 5**). Given that certain CNLs can act independently of SA synthesis and are Ca^{2+} permeable channels on their own (Bi et al., 2021; Lewis et al., 2010), it is tempting to speculate that autoimmunity in *atmc1 At*MC1^{C220A}-GFP plants could be due to hyperactivation of a combination of SA-independent and SA-dependent NLRs that require the feedback loop through EDS1-PAD4-ADR1 to amplify the immune response (Cui et al., 2017; Lewis et al., 2010; Saile et al., 2020). In agreement with this, overexpressing the E3 ubiquitin ligase SNIPER1, which is a master regulator of sNLRs (both CNLs and TNLs) but not hNLRs, in the autoimmune genetic background (*atmc1 AtMC1^{C220A}–GFP x HA-SNIPER1*) rescues the autoimmune phenotype (**Figure 11**).

Identity of AtMC1^{C220A} puncta structures and degradation through autophagy

Whilst Wt *At*MC1–GFP display a diffuse nucleocytoplasmic localization in leaf epidermal cells, catalytically inactive *At*MC1–GFP localizes to the nucleus, cytoplasm, and puncta structures **(Figure 12A).** Our data indicate that *At*MC1^{C220A}–GFP puncta may correspond to autophagosomes as i) we observed vacuolar targeting of *At*MC1^{C220A}–GFP puncta upon treatment with Conc A (**Figure 12B**) ii) we observed a partial colocalization with the core autophagy protein ATG8a (**Figure 12B**), while

endosomal localization was ruled out (**Figure S10**). The autophagosomal localization of *At*MC1^{C220A}–GFP puncta is in line with the fractionation assays in which catalytically inactive *At*MC1 localizes mainly to microsomal fractions (**Figure 9A**). Introgression of *atg2-1* and *atg5-1* mutant alleles into the autoimmune background (*atmc1 AtMC1^{C220A}-GFP*) further exacerbates the phenotype, implying that the inability to degrade *At*MC1^{C220A}–GFP puncta through autophagy has detrimental effects for the plant (**Figure 13**). These results are in line with the observation that *atmc1 atg18* double mutant plants also display an exacerbated early senescence phenotype compared to the one observed in *atmc1* mutant plants (Coll et al., 2014). One can hypothesise that defects in autophagy in *atmc1* mutant plants (*atmc1 atg18*) lead to further stabilization of immune-related components therefore accentuating its autoimmune phenotype. Given that autophagy has been recently shown to mediate degradation of aggregation-prone proteins or stress granules, and *At*MC1 is dynamically recruited therein upon proteotoxic stress (Jung et al., 2020; Munch et al., 2014) (Ruiz-Solaní N. et al., 2023 unpublished: **Chapter 3**), one can hypothesise that the observed *At*MC1^{C220A} puncta are indeed stress granules enriched with defence-related components (**Figure 9B-C and Figure 12A**). Ongoing experiments will determine whether these puncta structures colocalize with core stress granule markers.

A recent study reported that the master regulator of plant immunity NPR1, which act as a E3 ligase adaptor, promotes cell survival by targeting substrates for ubiquitination and degradation through formation of SA-induced NPR1 condensates (SINCs) (Zavaliev et al., 2020). SINCs are enriched with NLRs and ETI signalling components, and have been proposed to act as a hub in promoting cell survival upon stress (high SA concentration) (Zavaliev et al., 2020)**.** Although *At*MC1 is not present in SINCs based on proteomics data (Zavaliev et al., 2020), it is tempting to speculate that *At*MC1 recruits defence-related components in stress granules upon biotic stresses and thus, serves a pro-life function in the context of plant immunity in adult plants in parallel to SINCs. Localization of *At*MC1 to stress granules upon pathogen infection and whether they directly or indirectly regulate sNLRs levels or other defence components through direct cleavage or other degradation mechanisms remain to be determined. Finally, similarly to the function of SNIPER1 in broadly regulating sNLR homeostasis and in line with a plausible function of *At*MC1 in NLR homeostasis, it would be worth testing whether overexpression of *At*MC1 can supress phenotypes of previously characterized NLR-dependent autoimmune mutants.

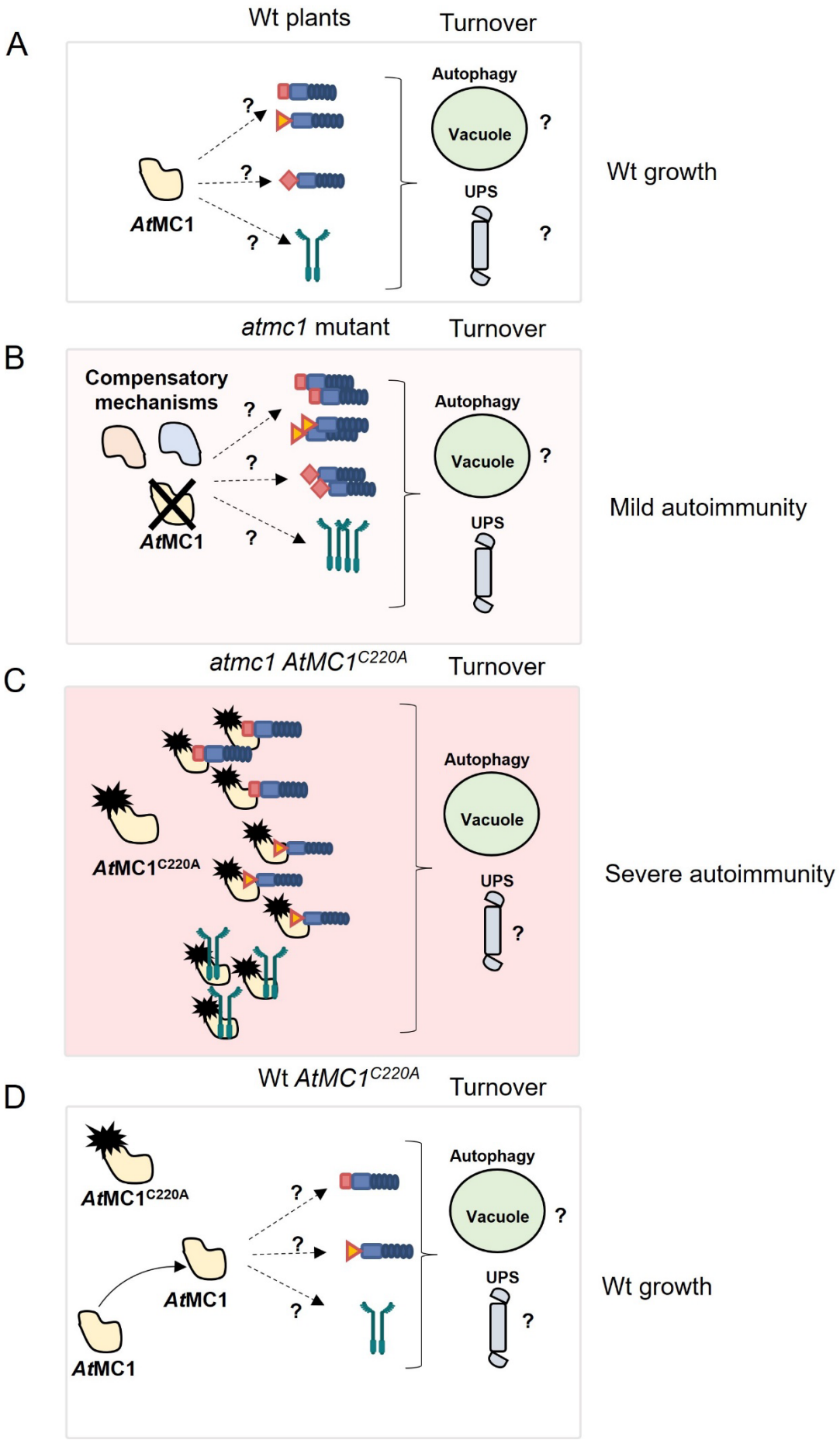
A
Wt plants
Turnover
Autophagy
Vacuole
UPS
AtMC1
Wt growth
B
atmc1 mutant
Turnover
Compensatory mechanisms
Autophagy
Vacuole
UPS
AtMC1
Mild autoimmunity
C
atmc1 AtMC1C220A
Turnover
Autophagy
Vacuole
UPS
AtMC1C220A
Severe autoimmunity
D
Wt AtMC1C220A
Turnover
Autophagy
Vacuole
UPS
AtMC1C220A
AtMC1
AtMC1
Wt growth

Figure 14. Hypothetical model for the function of *At*MC1 in the context of plant immunity in adult plants. (A) *At*MC1 may participate in the regulation and turnover of sNLR, hNLRs and/or PRRs together with other protein quality control systems such as the ubiquitin-proteasome system (UPS) or autophagy. **(B)** Plants lacking *At*MC1 exhibit mild autoimmunity since this regulation and turnover of immune components does not occur. Compensatory mechanisms may act redundantly to compensate for the loss of *At*MC1. **(C)** Plants that overexpress catalytically inactive *At*MC1 in an *atmc1* mutant background suffer from severe autoimmunity as this variant interacts promiscuously with immune components possibly stabilizing them and preventing their timely turnover. We speculate that when overexpressed, catalytically inactive *At*MC1 acts additively to the autoimmunity observed in *atmc1* plants. **(D)** Plants that overexpress catalytically inactive *At*MC1 in a Wt background do not exhibit autoimmunity as Wt *At*MC1 may outcompete *At*MC1^{C220A} for binding to immune components and regulate their turnover as in a Wt-like situation.

Final remarks

Based on the genetics of the autoimmune phenotype caused by catalytically inactive *At*MC1 and previous findings placing *At*MC1 as a negative regulator of an auto active hNLR variant (Roberts et al., 2013), we hypothesise that *At*MC1 might directly or indirectly participate in the regulation of NLR protein levels, genetically downstream of sNLRs. The relatively mild autoimmune phenotype exhibited by *atmc1* mutant plants (**Figure 2**), might indicate that defects occurring as a consequence of the mutation may be compensated by the many systems in place that exist in plants to ensure protein quality control (Llamas et al., 2022), potentially including redundant functions played by other metacaspases. Overexpression of a catalytically inactive *At*MC1 variant might exemplify a case in which immune components are trapped in otherwise very dynamic protein assemblies (Ruiz-Solaní et al., 2023 unpublished: **Chapter 3**). These aberrant puncta that remain in the cytoplasm as a result of defective turnover may directly underlie the observed autoimmune phenotype (**Figure 14 model**).

Investigating the molecular mechanisms underlying plant immune phenotypes can provide valuable knowledge about the systems in place to maintain NLR homeostasis. Since the field of plant immunity is gaining momentum with great advances in NLR bioengineering (Marchal et al., 2022), it is also worth considering the use of NLR regulators also as tools for engineering resistance.

MATERIALS AND METHODS

Plant materials and plant growth conditions

Arabidopsis thaliana Columbia-0 (Col-0) ecotype and Wt *Nicotiana benthamiana* were used for all experiments performed in this study. Arabidopsis mutants and transgenic lines are listed in **Table S1**. All seeds were sown directly in soil. To explore visual phenotypes and quantify fresh weight of mutants and transgenic lines, plants were grown in a controlled chamber with a short-day photoperiod of 8 h light and 16 h dark for 40 days under 65% relative humidity and 22 ºC. *N. benthamiana* plants were grown at a temperature ranging from 22-25 ºC and a relative humidity of 65% under a long-day photoperiod of 16 h light 8 h dark.

Plasmid construction and generation of Arabidopsis transgenics

All constructs and primers used in this study are listed in **Table S2** and **S3**, respectively. All plasmids were assembled using GreenGate cloning (Lampropoulos et al., 2013), except for *pro35S::SSI4 (AT5G41750)-3xHA* and the CRISPR destination vectors containing the RNA guides for *AtMC1* deletion. In the case of *pro35S::SSI4 (AT5G41750)-3xHA,* the genomic DNA sequence of *AtSSI4 (AT5G41750)* was introduced firstly into a pDONR207 by a BP reaction (Thermo Fisher Scientific) and subsequently introduced into a pGWB514 (Addgene #74856) binary destination vector by an LR reaction (Thermo Fisher Scientific). For the *AtMC1* deletion, 20 bp of the targeted sequences of *AtMC1* (5´UTR, intron 3 and 3´UTR) neighbouring a PAM sequence, tracrRNA sequence, U6 promoter, restriction enzyme sequence sites (BamHI/PstI/SalI) for cloning and attB overhangs were order as gBlocks® from IDT. The 3 gBlock sequences were introduced individually into different pDONR207 vectors by BP reactions. For the combination of the three gRNAs, pDONR207 vectors containing the guides were digested with restriction enzymes BamHI/PstI/SalI and ligated into a new pDONR207. Finally, the assembled gRNAs were transferred to the binary vector pDe-CAS9-DsRED (Morineau et al., 2017) by an LR reaction. For generation of *atmc1 #CR3 helperless/AtMC1^{C220A}-GFP #4.10*, we firstly introduced the transgene (*AtMC1^{C220A}-GFP #4.10*) into the *helperless* background (*adr1, adr1-l1, adr1-l2, nrg1.1 nrg1.2*) and subsequently we caused a CRIPSR deletion in the *AtMC1* endogenous Wt alleles. For generation of Arabidopsis transgenics, the *Agrobacterium tumefaciens* (ASE + pSOUP strain) floral dipping method was followed as previously described (Clough & Bent, 1998).

Protein extraction and western blotting

Five hundred milligrams of leaf material were mixed with extraction buffer (50 mM HEPES pH 7.5, 150 mM NaCl, 0.5% Nonidet P-40, 10% glycerol, 1 mM EDTA pH 8, 5 mM DTT and 1× cOmplete™ EDTA-free Protease Inhibitor Cocktail (Roche)) in a 5/1 volume/weight ratio and centrifuged for 10 min at 10,000 *xg* at 4 ºC. Supernatants were supplemented with 1X SDS-loading dye and boiled at 95 ºC before loading into an SDS-PAGE gel. Proteins were transferred to PVDF membranes (Roche) using the Trans-Blot Turbo Transfer System (Bio-Rad) following the manufacturer's instructions. Blotted membranes were blocked with 5% milk in Tris-buffered saline containing 0.01% Tween 20 (TBS-T) for an hour. Subsequently, membranes were incubated with antibodies at 4 °C overnight. Antibodies used for immunoblotting were as follows: α-GFP-HRP (1:5,000 Milteny Biotec), α-HA-HRP (1:5,000 Sigma), mouse α-cMyc (1:10,000, Sigma-Aldrich), rabbit α-FLAG (1:10,000, Sigma-Aldrich), α-PR1a (dilution 1:10,000, Agrisera), α-cAPXa (dilution 1:5,000, Agrisera), α-H+ATPase (dilution 1:5,000, Agrisera), α-SOBIR1 (dilution 1:1,000, Agrisera). To reveal membranes, we used the ECL Prime Western Blotting Detection Reagent (Cytiva). Image acquisition was carried out with an Amersham™ Image-Quant 800 luminescent imager (GE Healthcare Life Sciences).

Fractionation assays

Differential centrifugations were done to obtain total, soluble, and microsomal fractions from extracts of different plant genotypes. Briefly, 2 grams of aerial plant tissue from 40-day-old plants were homogenized in liquid nitrogen with mortar and pestle. Homogenization buffer (50 mM HEPES pH 7.5, 250 mM sucrose, 5 mM EDTA pH 8, cOmplete™ EDTA-free Protease Inhibitor Cocktail (Roche), 0.5% PVP-10 (Sigma) and 5 mM DTT) was added to the previously ground powder in a 5/1 volume/weight ratio. Subsequently, samples were left rotating in a rotator disc to reach complete homogenization for 15 minutes at 4 ºC. Extracts were filtered through two layers of miracloth (Merck Millipore) and subjected to a 15-minute centrifugation at 8,000 *xg*. The resulting supernatant (Total fraction, cytosolic and membrane proteins) was normalized by a Bradford Assay (BioRad) to ensure equal amount of protein was used before further fractionation. Adjusted extracts were centrifuged at 100,000 *xg* for 1 h at 4 ºC. The supernatant was designated at Soluble fraction (cytosolic proteins) and the resulting pellet dissolved in homogenization buffer without PVP-10 and supplemented with 1% Nonidet™ P40 (Sigma), was designated as Microsomal fraction (Total membranes). Total, soluble and microsomal fractions were supplemented with 1X SDS-loading dye and boiled at 65 ºC before loading into an SDS-PAGE gel.

Immunoprecipitation and mass spectrometry coupled to liquid chromatography (IP-MS)

Protein extraction to obtain Total and Microsomal protein fractions from aerial plant tissue of 40-day-old *atmc1 AtMC1*^{C220A}*–GFP*, Wt *AtMC1*^{C220A}*–GFP* and Wt *35S::GFP* plants was done as described in the fractionation assays section. Once fractions were obtained, extracts were incubated with anti-GFP magnetic beads (Miltenyi Biotec) for 2 hours at 4 ºC under constant rotation. Magnetic beads were immobilized on a magnetic separator (Miltenyi Biotec), washed 4 times with homogenization buffer and eluted with 1X elution buffer (4% SDS, 40 mM TCEP (Sigma), 160 mM CAM (Sigma) and 200 mM HEPES pH 7.5) previously boiled at 90 ºCe.

For mass spectrometry analysis, samples were processed on an Orbitrap Fusin Lumos instrument (Thermo) coupled to an Easy-nLC 1200 liquid chromatography (LC) system. A fused silica capillary (75 µm × 46 cm) was used as analytical column with an integrated PicoFrit emitter (CoAnn Tech). The analytical column was encased by a Sonation column oven (PRSO-V2) and attached to nanospray flex ion source (Thermo) at 50 ºC. The LC was equipped with two mobile phases: solvent A (0.1% (v/v) formic acid, FA, in water) and solvent B (0.1% FA in acetonitrile, ACN). All solvents were of UPLC grade (Sigma). Peptides were directly loaded onto the analytical column with a flow rate around 0.5 – 0.8 µL/min. Peptides were subsequently separated on the analytical column by running a 105 min gradient of solvent A and solvent B (start with 9% (v/v) B; gradient 9% to 35% B for 70 min; gradient 35% to 44% B for 15 min and 100% B for 20 min) at a flow rate of 250 nl/min. The mass spectrometer was set in the positive ion mode and operated using Xcalibur software (version 2.2 SP1.48). Precursor ion scanning was performed in the Orbitrap analyzer (FTMS; Fourier Transform Mass Spectrometry) in the scan

range of 200 or 400 m/z and at a resolution of 240000 with the internal lock mass option turned on (lock mass was 445.120025 m/z, polysiloxane).

Peptide and protein identification after IP-MS

RAW spectra were submitted to an Andromeda (Cox et al., 2011) search using MaxQuant (version 1.6.10.43) using the default settings label-free quantification (Cox et al., 2014). MS/MS spectra data were searched against the Uniprot reference proteome of Arabidopsis (UP000006548_3702). Further analysis and annotation of identified peptides was done in Perseus v1.5.5.3 (Tyanova et al., 2016). Only protein groups with at least three identified unique peptides were considered for further analysis. For quantification we combined related biological replicates to categorical groups and investigated only those proteins that were found in a minimum of one categorical group at least in 3 out of 4 biological replicas. Subsequently, peptides were visualized in Volcano plots comparing different categorical groups.

Transient expression in N. benthamiana

Proteins of interest were transiently expressed in Wt *N. benthamiana*. Briefly, leaves from 4-week-old plants were infiltrated with *Agrobacterium tumefaciencs* GV3101 using a 1 mL needleless syringe. The final OD_{600} of all bacterial suspension was adjusted in MMA agroinfiltration buffer (10 mM MES, 10 mM $MgCl_2$ and 150 µM acetosyringone at pH 5.6). Bacterial suspensions for all constructs were adjusted to an OD_{600} of 0.3. Tissue was harvested for sample processing 3 days post-infiltration.

Co-Immunoprecipitations (co-IPs)

For co-Ips, 400 mg of ground tissue were homogenized in IP homogenization buffer (50 mM HEPES pH 7.5, 150 mM NaCl, 1 mM EDTA pH 8, cOmplete™ EDTA-free Protease Inhibitor Cocktail (Roche), 0.5% PVP-10 (Sigma), 5 mM DTT and 0.5% Nonidet™ P40 (Sigma). Samples were left rotating in a rotator disc to reach complete homogenization for 15 minutes at 4 ºC. Extracts were filtered through two layers of Miracloth (Merck Millipore) and subjected to a 15-minute centrifugation at 10,000 *xg*. The resulting supernatant was normalized by a Bradford Assay (BioRad) and incubated with anti-GFP magnetic beads (Miltenyi Biotec) for 2 hours at 4 ºC under constant rotation. Magnetic beads were immobilized on a magnetic separator (Miltenyi Biotec), washed 4 times with IP homogenization buffer without PVP-10 and eluted with 1X SDS loading buffer (20 Mm Tris-HCl pH 7, 10% glycerol, 2% SDS, 0.1% Bromophenol blue and 100 mM DTT). Inputs (extracts before IP) diluted in 1X SDS loading buffer and IP samples were run on an SDS-PAGE gel to visualize proteins of interest through immuno-blotting.

Fresh weight experiments

For quantification of fresh weight, the aerial part of Arabidopsis plants grown for 40 days under short day conditions were cut through the stem and weigh in a precision scale (Mettler Toledo).

Confocal microscopy

Confocal imaging of proteins of interest was done using an Olympus FV1000 inverted confocal microscope with a x60/water objective. GFP signal was excited at 488 nm, whereas mRFP signal was excited at 543 nm. To visualize the vacuolar lumen, 1 µM Concanamycin A (Sigma) was syringe infiltrated with a needleless syringe. Imaging was performed 24 hours post-treatment. Information on whether images are single-plane or Z-stacks is indicated in figure legends.

Trypan blue staining

Ten Arabidopsis leaves per genotype were harvested in 50-ml Falcon tubes and incubated in 10 mL of a 1/3 dilution (trypan blue solution/ethanol) of trypan blue solution (100 mg Phenol solid, 100 mL lactic acid, 100 mL Glycerol and 100 mL water). Falcon tubes were submerged in boiling water for 10 minutes until leaves become completely blue. Subsequently, trypan blue solution was removed, and leaves were incubated with 10 mL of distaining solution (1 kg Chloral hydrate in 400 mL water) overnight on an orbital shaker. After removal of distaining solution, leaves were covered in 50% glycerol and photographed using a Leica DM6 epifluorescent microscope.

ACKNOWLEDGMENTS:

We would like to thank T. Nürnberger for *pro35S::10xMyc-AtRLP42* and *pro35S::10xMyc-AtSOBIR1* constructs, Z. Cipfel for the *pro35S::FLAG-AtRBOHF* construct and Y. Dagdas for the *proUBQ::mCherry-ATG8a* construct. We would like to thank Ignacio Rubio-Somoza for helpful comments and fruitful discussions on the project.

AUTHOR CONTRIBUTION

J.S-L. and N.S.C. conceived the study; J.S.-L., L.A. and N.S.C. designed experiments; J.S-L., L.A., N.R.-S., J.A., J.K., M.S-G., F.N., S.S.S., F.K. performed experiments. N.S.C, M.V., supervised the work. M.P., provided essential materials. J.S-L., L.A., J.A, N.R.-S., F.K. analyzed data. J.S-L. and N.S.C wrote the manuscript with comments from L.A.

DECLARATION OF INTEREST

The authors declare no competing interests.

SUPPLEMENTARY FIGURES

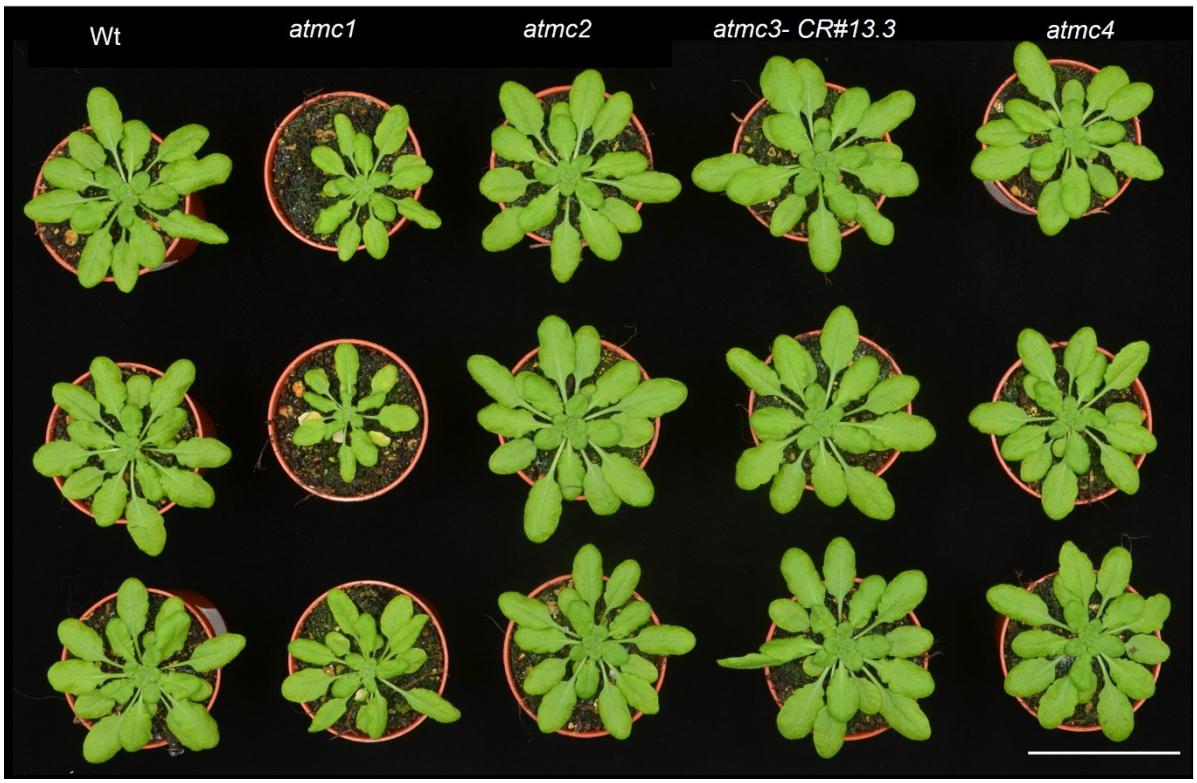

Figure S1. The autoimmune phenotype of *atmc1* mutant plants is specific to *At*MC1 and does not occur in other Type Is or a Type II metacaspase mutant. Representative images of 40-day-old Wt, *atmc1, atmc2* (T-DNA mutant), *atmc3-CR#13.3* (CRISPR mutant) and *atmc4* (T-DNA mutant) plants grown under short day conditions. Scale bar = 5.5 cm.

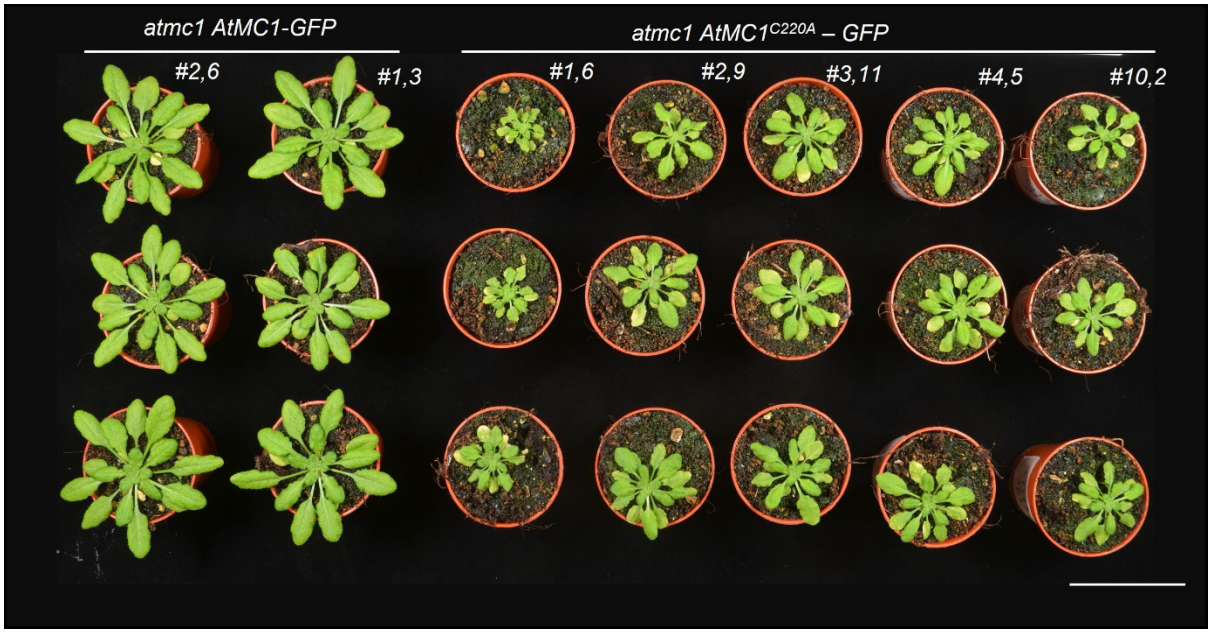

Figure S2. The autoimmune phenotype caused by catalytically inactive *At*MC1 occurs in independent transgenics. Representative images of 40-day-old *atmc1 AtMC1-GFP* and *atmc1 AtMC1^{C220A} – GFP* plants grown under short day conditions. 2 and 5 independent transgenics in

homozygosity for the transgene for *atmc1 AtMC1-GFP* and *atmc1 AtMC1*^{C220A}*–GFP* plants, respectively, are shown. Scale bar = 5.5 cm.

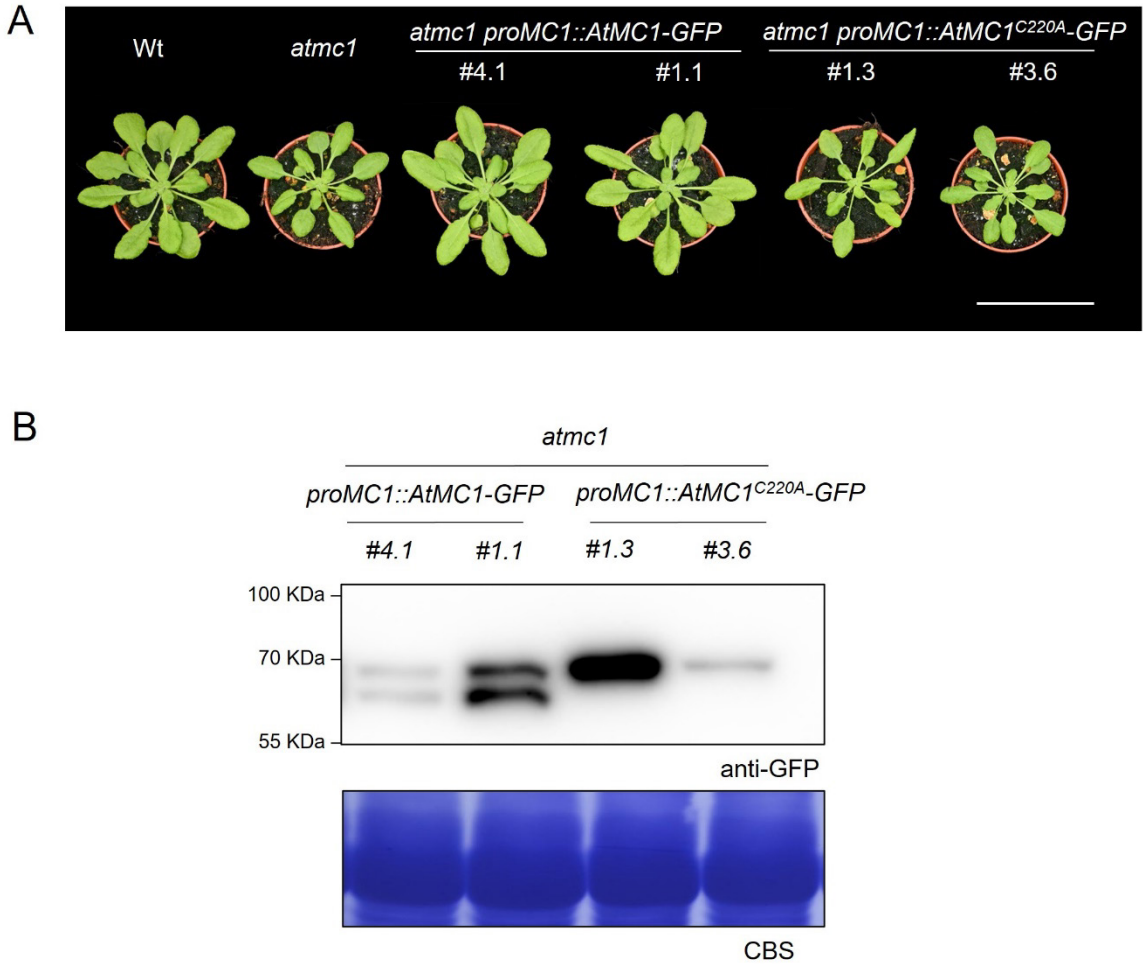

Figure S3. The autoimmune phenotype of *atmc1* mutant plants is fully rescued by expression of *At*MC1 but not by *At*MC1^{C220A} when the constructs are driven by the *AtMC1* native promoter. (A) Representative images of 40-day-old plants with the indicated genotypes grown under short day conditions. Two independent homozygous stable transgenics expressing either *AtMC1-GFP* (#4.1 and #1.1) or *AtMC1*^{C220A}*-GFP* (#1.3 and #3.6) under the control of the *AtMC1* native promoter in the *atmc1* mutant background are shown. Scale bar = 5.5 cm. **(B)** Total protein extracts from the plants shown in **A** were run on an SDS-PAGE gel and immuno-blotted against the indicated antisera. CBS of the immunoblotted membranes shows protein levels of Rubisco as a loading control.

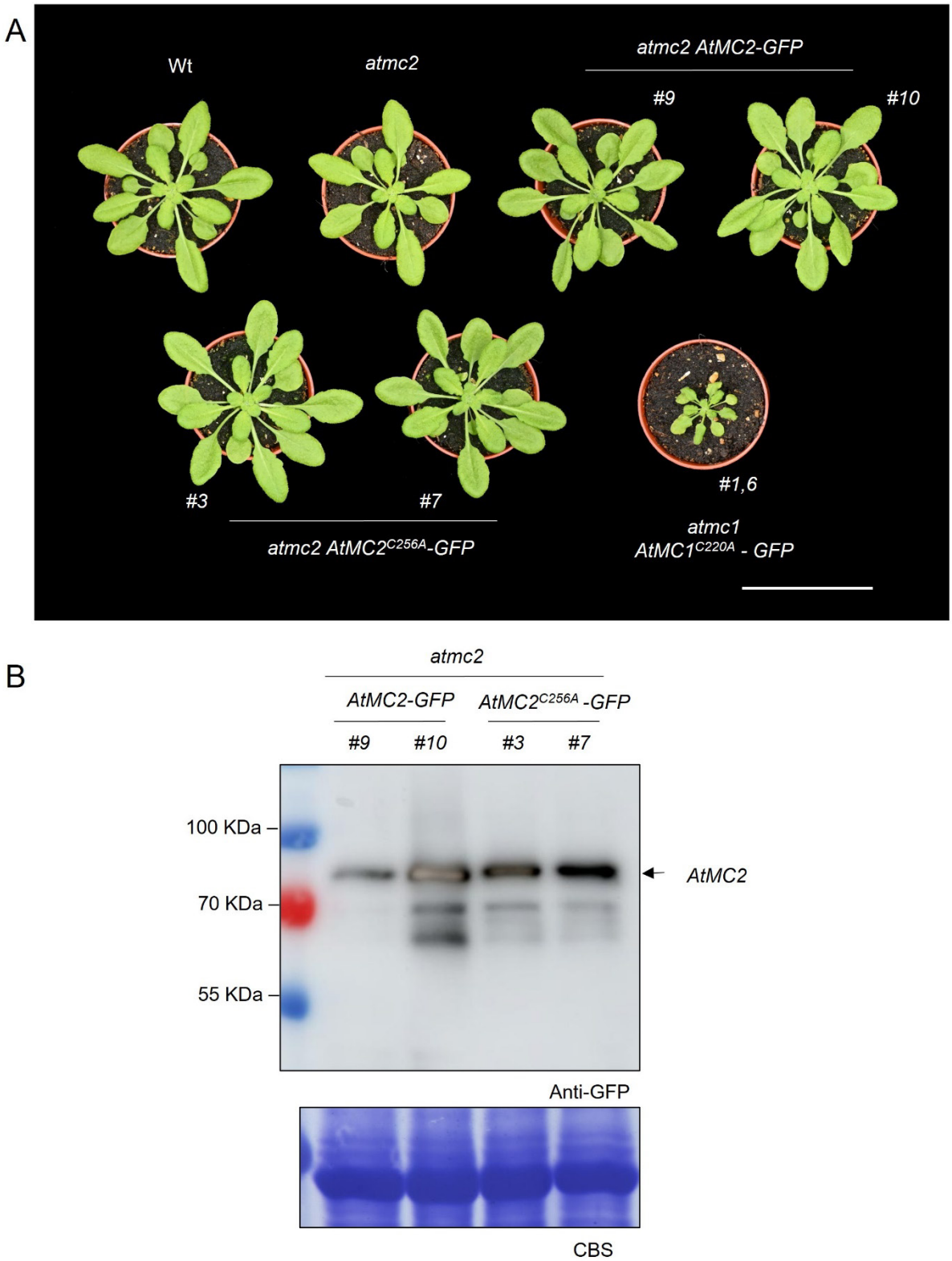

Figure S4. The autoimmune phenotype caused by catalytically inactive *At*MC1 does not occur when catalytically inactive *At*MC2 is overexpressed in an *atmc2* mutant background. (A) Representative images of 40-day-old plants with the indicated genotypes grown under short day conditions. Two independent stable transgenics in the T_2 generation expressing either *AtMC2-GFP* (#9

and #10) or *AtMC2*^{C256A}*-GFP* (#3 and #7) under the control of a 35S constitutive promoter in the *atmc2* mutant background are shown. Scale bar = 5.5 cm. **(B)** Total protein extracts from the plant genotypes shown in **A** were run on an SDS-PAGE gel and immuno-blotted against with the indicated antisera. CBS of the immunoblotted membranes shows protein levels of Rubisco as a loading control.

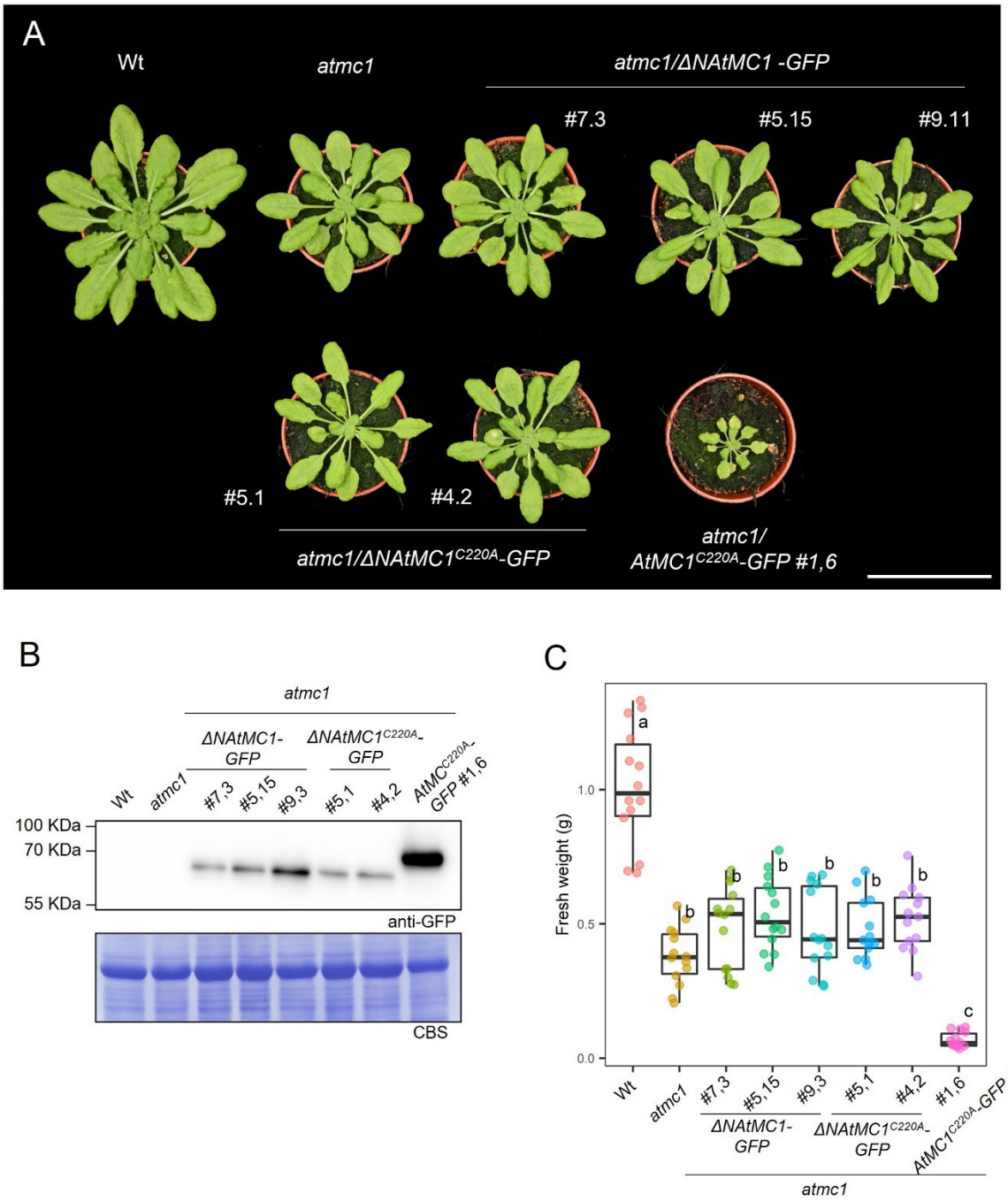

Figure S5. The N-terminal prodomain is required for the autoimmune phenotype caused by catalytically inactive *At*MC1. (A) Representative images of 40-day-old plants with the indicated genotypes grown under short day conditions. 3 and 2 independent homozygous stable transgenics expressing either prodomainless *At*MC1 (*ΔNAtMC1 -GFP* #7.3, #5.15 and 9.11) or prodomainless

*At*MC1 catalytically inactive (*ΔNAtMC1* ^{C220A}*-GFP* #5.1 and #4.2), respectively, under the control of a 35S constitutive promoter in the *atmc1* mutant background are shown. Scale bar = 5.5 cm. **(B)** Total protein extracts from the plant genotypes shown in **A** were run on an SDS-PAGE gel and immuno-blotted against the indicated antisera. CBS of the immunoblotted membranes shows protein levels of Rubisco as a loading control. **(C)** Plant fresh weight of genotypes shown in **A** (n=12). Different letters indicate statistical difference in fresh weight between genotypes (one-way ANOVA followed by post hoc Tukey, p value < 0.05).

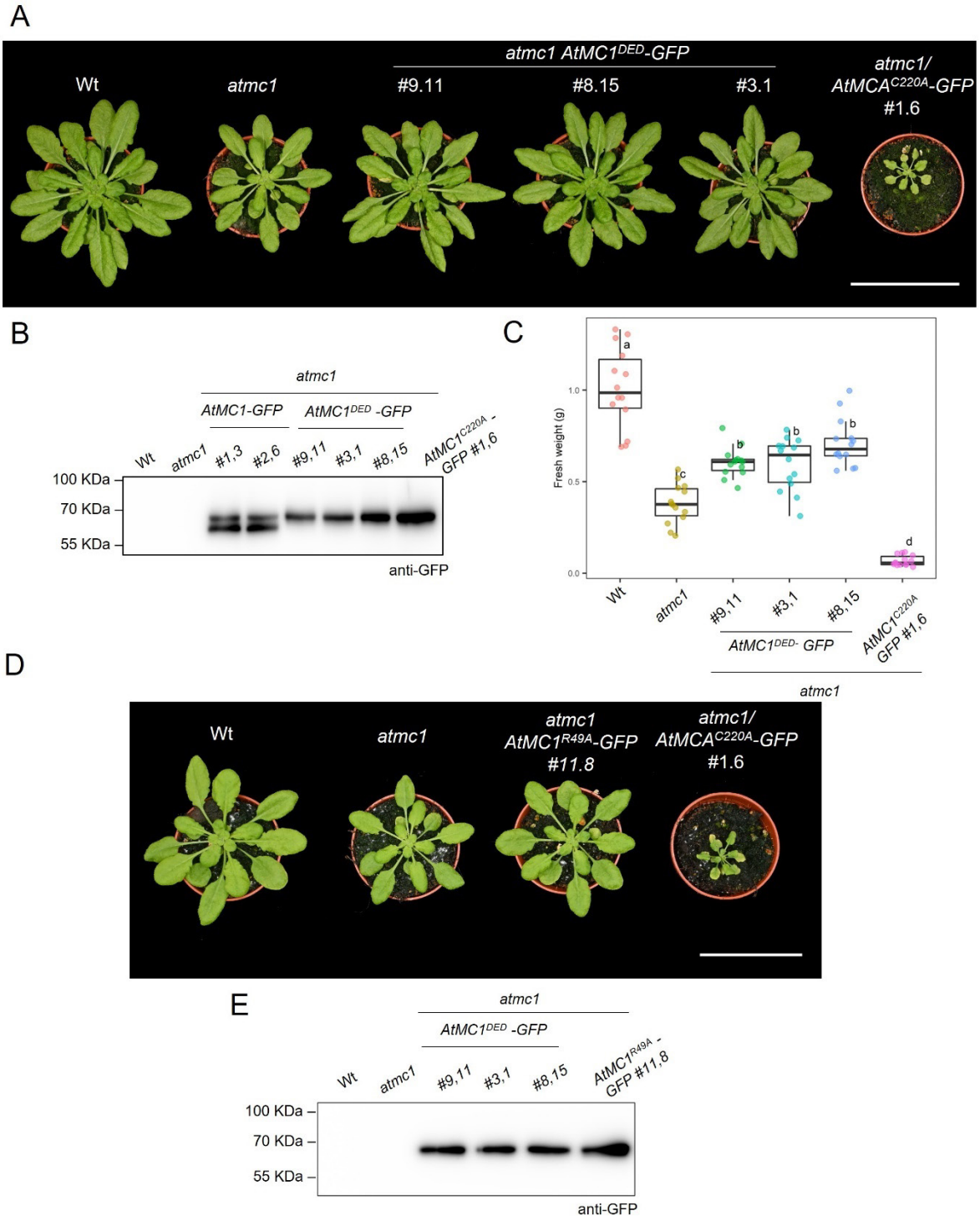

Figure S6. Non-autoprocessed *At*MC1 variants do not display autoimmunity. (A) Representative images of 40-day-old plants with the indicated genotypes grown under short day conditions. 3 independent homozygous stable transgenics expressing a Ca^{2+} insensitive variant (*At*MC1^{DED}-GFP #9.11, #8.15 and #3.1) from a 35S constitutive promoter in the *atmc1* mutant background are shown. Scale bar = 5.5 cm. **(B)** Total protein extracts from the plants shown in **A** were run on an SDS-PAGE gel and immuno-blotted against the indicated antisera. **(C)** Plant fresh weight of genotypes shown in A (n=12). Different letters indicate statistical difference in fresh weight between genotypes (one-way ANOVA followed by post hoc Tukey, p value < 0.05). **(D)** Representative images of 40-day-old plants with the indicated genotypes grown under short day conditions. One stable transgenic overexpressing a non-cleavable *At*MC1 variant (*At*MC1^{DED}-GFP #11.8) from a 35S constitutive promoter in the *atmc1* mutant background is shown. Scale bar = 5.5 cm. **(E)** Total protein extracts from *atmc1 AtMC1^{DED}-GFP* #9.11, #3.1 and #8.15 and *atmc1 AtMC1^{R49A}-GFP* #11.8 were run on an SDS-PAGE gel and immuno-blotted against the indicated antisera.

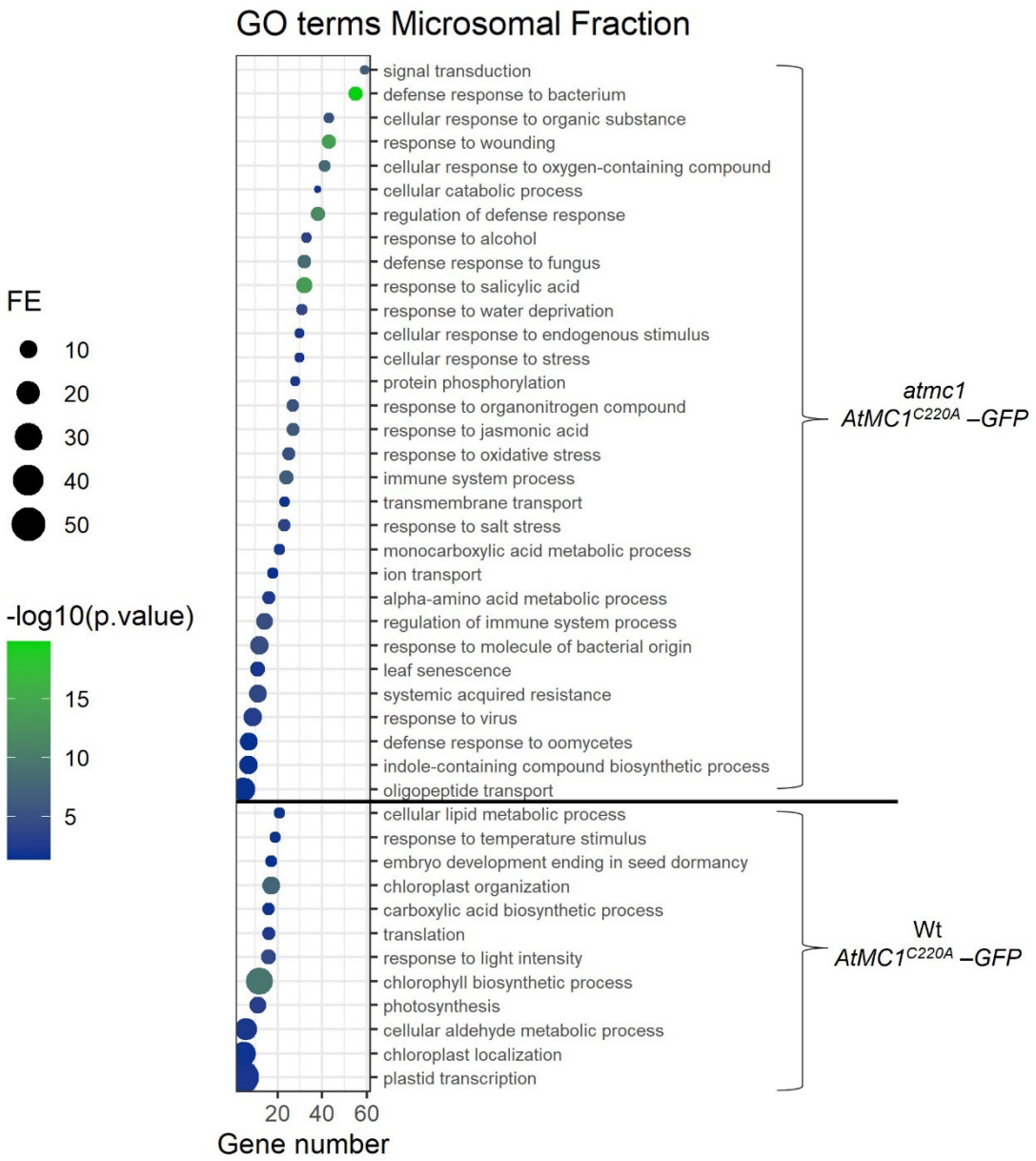

Figure S7. GO terms representing biological processes derived from significantly enriched peptides that co-immunoprecipitated with *At*MC1^{C220A}–GFP in extracts belonging to *atmc1*

***AtMC1^{C220A}–GFP* or Wt *AtMC1^{C220A}–GFP* plants.** The most specific term from each family term provided by PANTHER was plotted along with the corresponding gene number, fold enrichment (FE), and FDR (Bonferroni correction for multiple testing) represented as log10. Only GO terms with an FE above 2 and FDR below 0.05 were plotted.

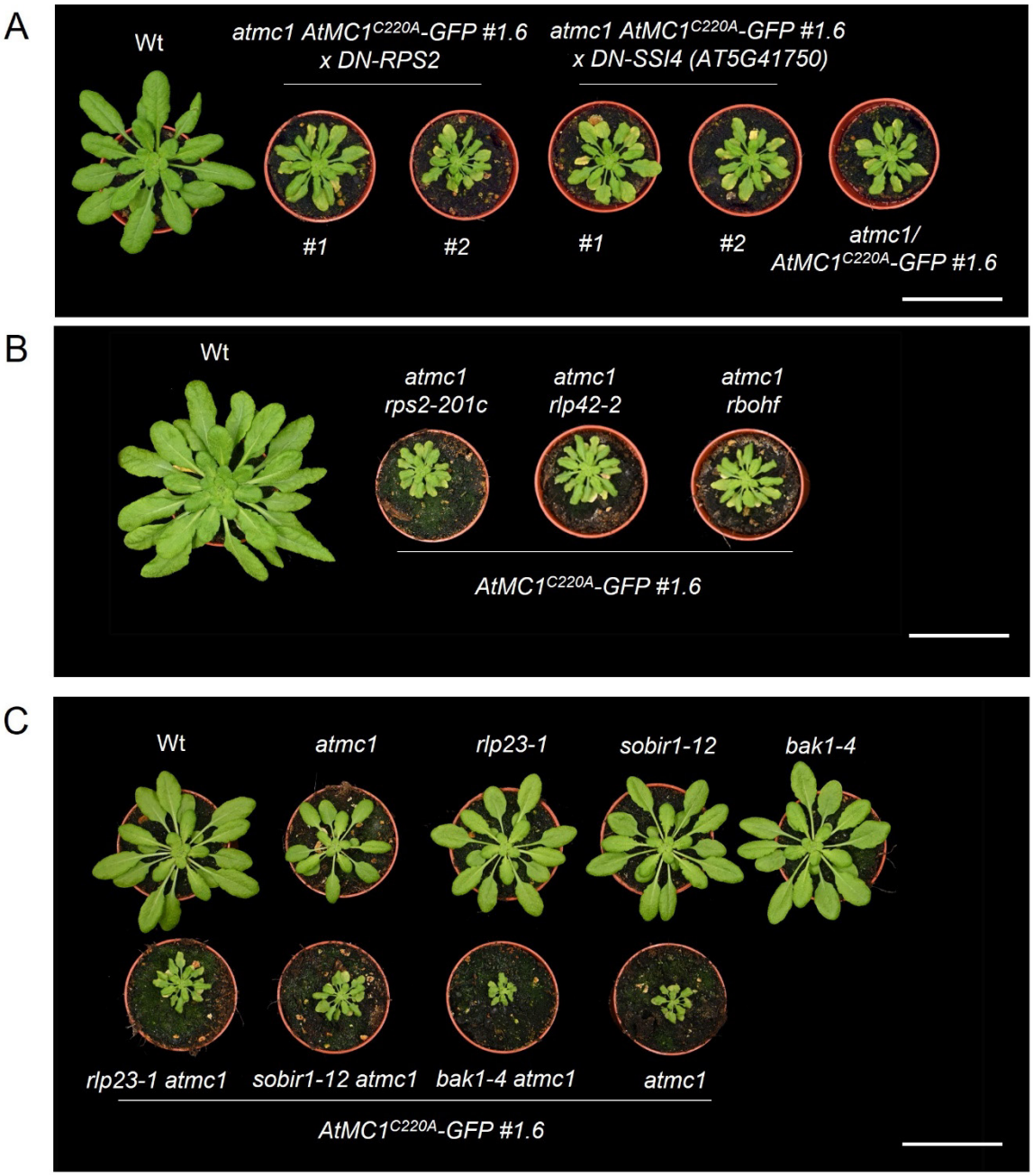

Figure S8. **Immune components that interact with catalytically inactive *At*MC1 are individually not required for the autoimmune phenotype caused by catalytically inactive *At*MC1. (A)** Representative images of 40-day-old plants with the indicated phenotypes grown under short day conditions. Two independent stable transgenics in the T_2 generation expressing either DN-RPS2 (*DN-RPS2* #1 and #2) or DN-SSI4 AT5G41750 (*DN-SSI4 AT5G41750* #1 and #2*)* under the control of a 35S constitutive promoter in the *atmc1 AtMC1^{C220A}-GFP* background are shown. Scale bar=5.5 cm. **(B)** Preliminary representative images of 50-day-old plants with the indicated phenotypes grown under

short day conditions. The *rps2-201c*, *rlp42-2* and *rbohf* mutant alleles were introgressed into the *atmc1 AtMC1^{C220A}-GFP* background by conventional crosses and pictures were taken in the F3 offspring. Scale bar= 5.5 cm. **(C)** Representative images of 40-day-old plants with the indicated phenotypes grown under short day conditions. The *rlp23-1*, *sobir1-12* and *bak1-4* mutant alleles were introgressed into the *atmc1/AtMC1^{C220A}-GFP* background by conventional crosses and pictures were taken in the F4 offspring. Scale bar= 5.5 cm.

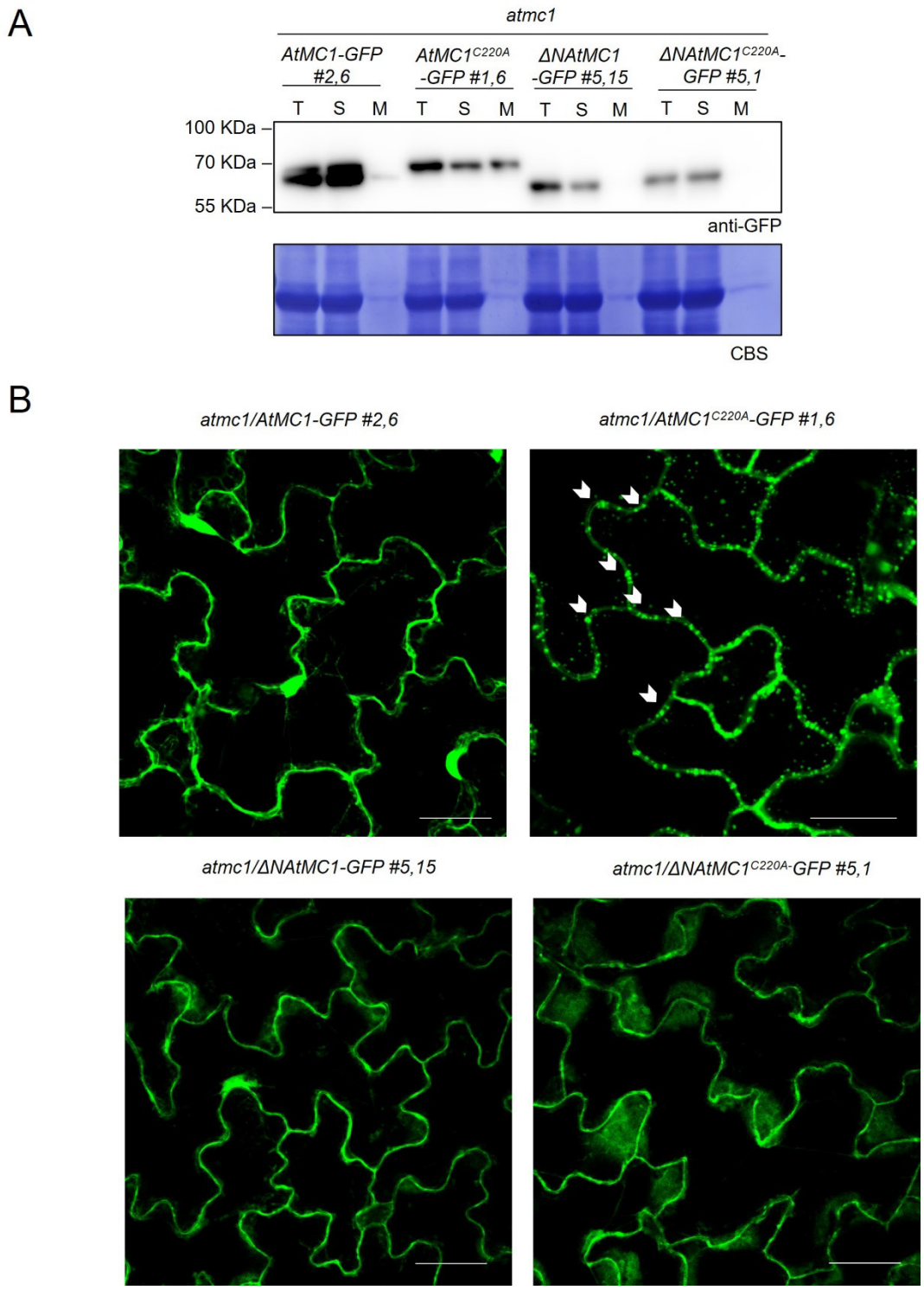

Figure S9. The N-terminal prodomain is required for microsomal and puncta localization in catalytically inactive *At*MC1. (A) Fractionation assays from plant extracts with the indicated plant genotypes (transgene and genetic background indicated). Total (T), Soluble (S, cytoplasmic proteins) and Microsomal (M, total membranes) fractions were run on an SDS-PAGE gel and immunoblotted against the indicated antisera. CBS of the immunoblotted membranes shows protein levels of Rubisco as a loading control. **(B)** Representative confocal microscopy images from the leaf epidermis of 40-day-old plants grown under short day conditions with the indicated genotypes. Images represent a Z-stack of 12 images taken every 1 µm. Arrows indicate some of the puncta structures formed when *At*MC1^{C220A} is expressed in an *atmc1* mutant background that are not present in Wt *At*MC1 expressing plants or prodomainless variants (*atmc1 ΔNAtMC1-GFP #5,15 and atmc1 ΔNAtMC1^{C220A}-GFP #5,1).* Scale bar = 10 µm.

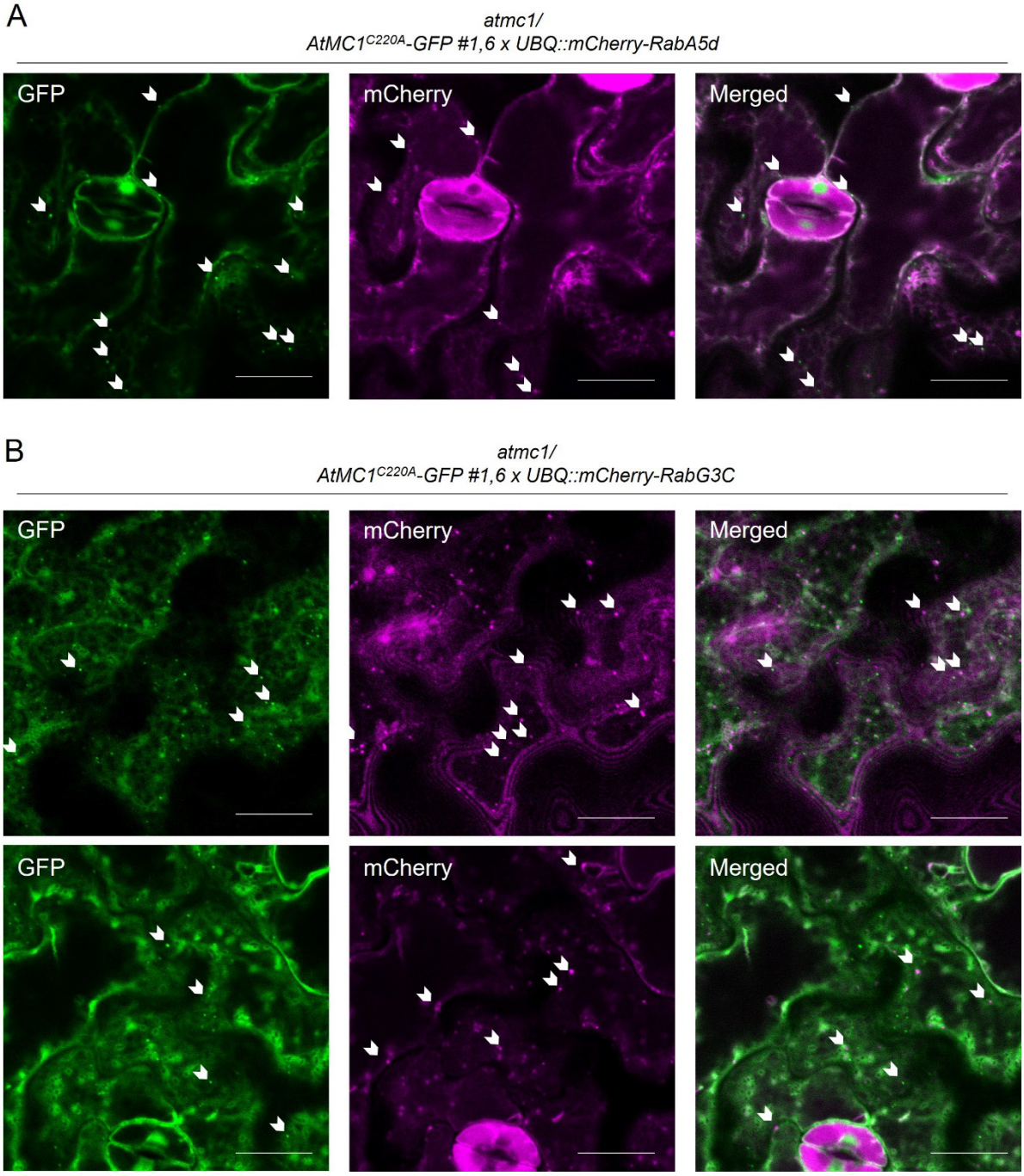

Figure S10. ***At*MC1^{C220A} puncta do not colocalize with early or late endosome markers, RabA5d and RabG3C, respectively. (A-B)** Representative single-plane confocal microscopy images from the leaf epidermis of 40-day-old plants grown under short day conditions with the indicated genotypes. Double transgenics expressing either an early endosome marker, mCherry-RabA5d (*UBQ::mCherry-RabA5d*) **(A)** or a late endosome marker, mCherry-RabG3C (*UBQ::mCherry-RabG3C*) **(B)** in the *atmc1 AtMC1*^{C220A}*-GFP* background were imaged. Arrows in GFP and RFP channel indicate some of the *At*MC1^{C220A} puncta structures and either early **(A)** or late endosomes **(B)**, respectively. Scale bar = 10 µm.

SUPPLEMENTARY INFORMATION

Table S1. Arabidopsis lines used in this study.

Table S2. Plasmids used in this study.

Table S3. Primers and synthetic sequences used in this study for genotyping and cloning.

Table S4. DN-NLRs carrying P-loop mutations transformed in the autoimmune background *atmc1 AtMC1*^{C220A}*–GFP*

Table S1: Arabidopsis seeds used in this study.

Arabidopsis seeds	Accession number	Source or reference
atmc1 (GABI-Kat: GK-096A10)	AT1G02170	(Coll et al., 2010)
atmc1-CR#1	AT1G02170	This study
atmc2 (SALK_009045)	AT4G25110	(Coll et al., 2010)
atmc3-CR#13.3	AT5G64240	(Pitsili et al., 2022)
atmc4 (SAIL_856_D0)	AT1G79340	(Watanabe & Lam, 2011)
eds1-12	AT3G48090	(Ordon et al., 2017)
sid2-1	AT1G74710	(Wildermuth et al., 2001)
pad4-1	AT3G52430	(Jirage et al., 1999)
sag101-1	AT5G14930	(Feys et al., 2005)
nrg1.1 nrg1.2	AT5G66900, AT5G66910	(Castel et al., 2019)

helperless (nrg1.1 nrg1.2, adr1, adr1-L1, adr1-L2)	AT5G66900, AT5G66910 AT1G33560, AT4G33300, AT5G04720	(Saile et al., 2020)
rps2-201-c	AT4G26090	(Kunkel et al., 1993)
rlp42-2	AT3G25020	(Wang et al., 2008)
rbohf	AT1G64060	(Torres et al., 2002)
bak1-4	AT4G33430	(Dressano et al., 2017)
rlp23-1	AT2G32680	(Wang et al., 2008)
sobir1-12	AT2G31880	(Gao et al., 2009)
atg2-1 (SALK_076727)	AT3G19190	(Thompson et al., 2005)
atg5-1 (SAIL_129B07)	AT5G17290	(Yoshimoto et al., 2009)
atmc1 eds1-12	AT1G02170, AT3G48090	This study
atmc1 sid2-1	AT1G02170, AT1G74710	This study
atmc1 pad4-1	AT1G02170, AT3G52430	This study
atmc1 nrg1.1 nrg1.2	AT1G02170, AT5G66900, AT5G66910	This study
atmc1 35S::AtMC1-GFP	AT1G02170	This study
atmc1 35S::AtMC1^{C220A}-GFP	AT1G02170	This study
atmc1 proMC1::AtMC1-GFP	AT1G02170	This study
atmc1 proMC1::AtMC1^{C220A}-GFP	AT1G02170	This study
Wt*; 35S::AtMC1^{C220A}-GFP*	AT1G02170	This study
atmc1-CR#2 35S::AtMC1^{C220A}-GFP	AT1G02170	This study
atmc1 35S::ΔNAtMC1 -GFP	AT1G02170	This study
atmc1 35S::ΔNAtMC1 ^{C220A} -GFP	AT1G02170	This study
atmc1 35S::AtMC1^{DEED}-GFP	AT1G02170	This study

atmc1 35S::AtMC1^{R49A}-GFP	AT1G02170	This study
atmc1 eds1-12 35S::AtMC1^{C220A}-GFP	AT1G02170, AT3G48090	This study
atmc1 sid2-1 35S::AtMC1^{C220A}-GFP	AT1G02170, AT1G74710	This study
atmc1 sag101-1 35S::AtMC1^{C220A}-GFP	AT1G02170, AT5G14930	This study
atmc1 pad4-1 35S::AtMC1^{C220A}-GFP	AT1G02170, AT3G52430	This study
atmc1 nrg1.1 nrg1.2 35S::AtMC1^{C220A}-GFP	AT1G02170, AT5G66900, AT5G66910	This study
atmc1-CR#2 helperless 35S::AtMC1^{C220A}-GFP	AT1G02170, AT5G66900, AT5G66910 AT1G33560, AT4G33300, AT5G04720	This study
atmc1 atg2-1 35S::AtMC1^{C220A}-GFP	AT1G02170, AT3G19190	This study
atmc1 atg5-1 35S::AtMC1^{C220A}-GFP	AT1G02170, AT5G17290	This study
atmc1 35S::HA-AtSNIPER x 35S::AtMC1^{C220A}-GFP	AT1G02170, AT1G14200	This study
atmc1 UBQ-mCherry-ATG8a x 35S::AtMC1^{C220A}-GFP	AT1G02170, AT4G21980	This study
atmc1 UBQ- mCherry-AtRabA5d x 35S::AtMC1^{C220A}-GFP	AT1G02170, AT2G31680	This study
atmc1 UBQ-mCherry-AtRabG3C x 35S::AtMC1^{C220A}-GFP	AT1G02170, AT3G16100	This study
atmc2 35S::AtMC2-GFP	AT4G25110	This study
atmc2 35S::AtMC2^{C256A}-GFP	AT4G25110	This study
atmc1 35S::DN-AtRPS2 x 35S::AtMC1^{C220A}-GFP	AT4G26090, AT1G02170	This study
atmc1 35S::DN-SSI4 (AT5G41750) x 35S::AtMC1^{C220A}-GFP	AT5G41750, AT1G02170	This study
atmc1 rps2-201c 35S::AtMC1^{C220A}-GFP	AT1G02170, AT4G26090	This study

atmc1 rlp42-2 35S::AtMC1^{C220A}-GFP	AT1G02170, AT3G25020	This study
atmc1 rbohf 35S::AtMC1^{C220A}-GFP	AT1G02170, AT1G64060	This study
atmc1 rlp23-1 35S::AtMC1^{C220A}-GFP	AT1G02170, AT2G32680	This study
atmc1 bak1-4 35S::AtMC1^{C220A}-GFP	AT1G02170, AT4G33430	This study
atmc1 sobir1-12 35S::AtMC1^{C220A}-GFP	AT1G02170, AT2G31880	This study

Table S2: Plasmids used in this study.

Name	Accesion number	Backbone	Source of Reference	Additional information
35S::AtMC1-GFP	AT1G02170	pZ003	This study	Hygromycin Resistance
35S::AtMC1^{C220A}-GFP	AT1G02170	pZ003	This study	Hygromycin Resistance
proMC1::AtMC1-GFP	AT1G02170	pZ003	This study	Hygromycin Resistance
proMC1::AtMC1^{C220A}-GFP	AT1G02170	pZ003	This study	Hygromycin Resistance
35S::ΔNAtMC1 -GFP	AT1G02170	pZ003	This study	Hygromycin Resistance
35S::ΔNAtMC1 ^{C220A} -GFP	AT1G02170	pZ003	This study	Hygromycin Resistance
35S::AtMC1^{DEED}-GFP	AT1G02170	pZ003	This study	Hygromycin Resistance
35S::AtMC1^{R49A}-GFP	AT1G02170	pZ003	This study	Hygromycin Resistance
35S::HA-AtSNIPER	AT1G14200	pZ003	This study	Fast Red selection
UBQ- mCherry-AtRabA5d	AT2G31680	pZ003	This study	BASTA Resistance
UBQ-mCherry-AtRabG3C	AT3G16100	pZ003	This study	BASTA Resistance
UBQ-mCherry-ATG8a	AT4G21980	pZ003	Gift from Yasin Dagdas´ lab	Fast Red selection
35S::AtMC2-GFP	AT4G25110	pZ003	This study	Hygromycin Resistance
35S::AtMC2^{C256A}-GFP	AT4G25110	pZ003	This study	Hygromycin Resistance
35S::DN-AtRPS2	AT4G26090	pUSER007	(Lolle et al., 2017)	BASTA Resistance
35S::DN-AtSSI4 (AT5G41750)	AT5G41750	pUSER007	(Lolle et al., 2017)	BASTA Resistance
35S::GFP	-	pZ003	This study	BASTA Resistance
pOCS::AtRPS2-HA	AT4G26090		Gift from Farid El Kasmi´s lab	BASTA Resistance
35S:: AtSSI4 (AT5G41750)-3xHA	AT5G41750	pGWB514	This study	Hygromycin Resistance

35S::10xcMyc-AtRLP42	AT3G25020	pGWB521	Gift from Thorsten Nürnberger´s lab	Hygromycin Resistance
35S::FLAG-RBOHF	AT1G64060	pBin19g	Gift from Cyril Zipfel´s lab	BASTA Resistance
35S::10xcMyc-AtSOBIR1	AT2G31880	pGWB521	Gift from Thorsten Nürnberger´s lab	Hygromycin Resistance

Table S3: Primers used in this study

Primer name	**Sequence**	**Purpose**
AtMC1 F3	GCGTCACCTTCTCATCAACA	Genotyping
AtMC1 R3	ACGGTACCACTATGGCAAGC	Genotyping
GABI LB (KIRK)	ATATTGACCATCATACTCATTGC	Genotyping
AtMC2 LP	TCCAAACTTCTGCAATGAAGG	Genotyping
AtMC2 RP	ATGACACCTGAAGTCCTGTGG	Genotyping
LBb1.3	ATTTTGCCGATTTCGGAAC	Genotyping
sid2-1 F	TGTCTGCAGTGAAGCTTTGG	Caps genotyping (MfeI)
sid2-1 R	CACAAACAGCTGGAGTTGGA	Caps genotyping (MfeI)
EDS1 959	AACTAGCATACAGAGGGGCA	Genotyping
EDS1 960	GCTGAGAGAAATCGAACCGG	Genotyping
EDS1 JG08	AAAGAAGACAACATTGATCTATATCTATTCTCTTTTC TT	Genotyping
PAD4 F	GCGATGCATCAGAAGAG	Caps genotyping BsmF1
PAD4 F	TTAGCCCAAAAGCAAGTATC	Caps genotyping BsmF1
SAG101 MW29	ATGCAAGGAGGTCAAGATCG	Genotyping
SAG101 MW43	TTGTGACTTACCATAACTCTCG	Genotyping
dSpm11	GGTGCAGCAAAACCCACACTTTTACTTC	Genotyping
NRG1 FEK_1070	GCATCTCCACCTCTTCACA	dCaps Genotyping (AvaII)
NRG1 FEK_1071	CTGAAGAAATGAACCCATGT	dCaps Genotyping (Ava II)
rps2-201-c F	GAATCTTAGAAAACTGAAGCATCTGG	dCaps Genotyping (RsaI)
rps2-201-c R	AGTTGTGAAGGCTGTGTAACGTCA	dCaps Genotyping (RsaI)
rlp42-2 LP	GTCCGAAGGGAAATCTCTTTG	Genotyping
rlp42-2 RP	TGGAGTGTTACTTGGATTGGC	Genotyping
rbohf F MAT 171F	CTTCCGATATCCTTCAACCAACTC	Genotyping
rbohf R MAT 212F	CGAAGAAGATCTGGAGACGAGA	Genotyping
sobir1-12 LP	GGAGCCATAGGAGGAACAATC	Genotyping
sobir1-12 RP	TGACATCTTTACTGTTCGGCC	Genotyping
atg5-1 F DH417	ATTCACTTCCTCCTGGTGAAG	Genotyping
atg5-1 R DH418	TTGTGCCTGCAGGATAAGCG	Genotyping
atg2-1 LP	GTGGGGCTCATAGCTTAGACC	Genotyping
atg2-1 RP	TCGAGTGATTCTGTGGTTTCC	Genotyping
AtMC1 pGB000 F	aacaGGTCTCaaacaATGTACCCGCCACCTCCCTCAA G	Cloning
AtMC1 pGB000 R	aacaGGTCTCtagccgaGAGTGAAAGGCTTTGCATAGA CATCGAATGTTTGG	**Cloning**
proAtMC1 pGA000 F	AACAGGTCTCAACCTGCTCGGATATCTGATTCTCCA TGT	**Cloning**

proAtMC1 pGA000 R	AACAGGTCTCTTGTTTATTATTCTCGGAAGGGAGGGAAT	**Cloning**
AtMC1^{C220A} F	CTCCATTCAATTATCGATGCTGCCCATAGTGGTACCGTTCTGG	**Cloning (Site-directed Mutagenesis)**
AtMC1^{C220A} R	CCAGAACGGTACCACTATGGGCAGCATCGATAATTGAATGGAG	**Cloning (Site-directed Mutagenesis)**
ΔNAtMC1 F	aacaGGTCTCaaacaATGTTCTCTCGCCACGAGCTCAAAGGCTG	**Cloning (Site-directed Mutagenesis)**
AtMC1^{DEED} F	GTCAAAGAAACTACAACGGTGCCGCCGTTGCCGGCTATGATGAAACACTCTG	**Cloning (Site-directed Mutagenesis)**
AtMC1^{DEED} R	CAGAGTGTTTCATCATAGCCGGCAACGGCGGCACCGTTGTAGTTTCTTTGAC	**Cloning (Site-directed Mutagenesis)**
AtMC1^{R49A} F	TACTCATATCGCCGACCCTGCTACCGCCCCTCCTCCGCA	**Cloning (Site-directed Mutagenesis)**
AtMC1^{R49A} R	GTTGCGGAGGAGGGGCGGTAGCAGGGTCGGCGATATGAG	**Cloning (Site-directed Mutagenesis)**
HA-SNIPER F	ATGTATCCGTATGATGTTCCGGATTATGCAATGTCTTCTGAGAATGATTTC	**Cloning**
HA-SNIPER pGB0000 F	aacaGGTCTCaaacaATGTATCCGTATGATGTTCCGGATTAT	**Cloning**
AtSNIPER pGB0000 R	aacaGGTCTCtagccTTAGTTTCTTCTGTCGCCGG	**Cloning**
AtRabA5d pGC0000 F	aacaGGTCTCaggctcaacaATGTCGTCCGATGACGAAGGAGGAG	**Cloning**
AtRabA5d pGC0000 R	aacaGGTCTCtctgaTCACGAGGAAGAACAGCAAGAGAAAC	**Cloning**
AtRabG3C pGC0000 F	aacaGGTCTCaggctcaacaATGGCTTCTCGGCGGCGAGT	**Cloning**
AtRabG3C pGB0000 R	aacaGGTCTCtctgaTTAGCATTCGCACCCAGTTGATCTTTGTTG	**Cloning**
AtMC2 pGB0000 F	aacaGGTCTCaaacaATGTTGTTGCTGGTGGACTGCT	**Cloning**
AtMC2 pGB0000 R	aacaGGTCTCtagccTAAAGAGAAGGGCTTCTCATATACAG	**Cloning**
AtMC2^{C256A} F	TGCCATCGTCGACGCTgcTCATAGTGGTACCGTCATGG	**Cloning (Site-directed Mutagenesis)**
AtMC2^{C256A} R	CCATGACGGTACCACTATGAgcAGCGTCGACGATGGCA	**Cloning (Site-directed Mutagenesis)**
AtSSI4 (AT5G41750) attB1	GGGGACAAGTTTgtacaaaaaagcaggctCCATGGCTTTGTCTTCTTCTTTGtc	**Cloning**
AtSSI4 (AT5G41750) attB2	GGGGACCACTTTGTACAAGaaagctgggtATGAGACTCCATGAGAATTCATC	**Cloning**

Table S4: DN-NLRs carrying P-loop mutations transformed in the autoimmune background *atmc1 AtMC1*^{C220A}*–GFP*. In green, TNLs and blue CNLs. The battery of DN negative NLRs was produced by Lolle and co-workers (Lolle et al., 2017). No rescues in T_1 were achieved after screening for suppression of the phenotype.

Accession number (TNLs)	Accession number (CNLs)
At1g17600	At1g12210
At1g17610	At1g12220
At1g27170	At1g12280
At1g31540	At1g12290
At1g56520	At1g52660
At1g56540	At5g63020
At1g63730	At4g33300
At1g69740	At1g53350
At1g63750	At1g63360
At1g63870	At1g33560
At1g64070	At5g43830
At1g65850	At5g43740
At1g66090	At3g14460
At1g69550	At3g14470
At1g72840	At4g14610
At1g72850	At5g04720
At1g72860	At5g05400
At1g72870	At5g35450
At1g72900	At5g45510
At1g72910	At1g15890
At1g72940	At3g46530
At1g72950	At5g66630
At2g16870	At5g66900
At2g17050	At5g66910
At3g04210	At3g07040
At3g04220	At4g27190
At3g44400	At4g27220
At3g44480	At1g58390
At3g44630	At1g58410
At3g44670	At1g58807
At3g51560	At1g58848
At3g51570	At1g59124
At4g09360	At1g59218
At4g09420	At1g59620
At4g12010	At1g17615
At4g16940	At1g61190
At4g16950	At1g63350
At4g16960	At1g63880

At4g19500	At3g15700
At4g19510	At3g46710
At4g19530	At3g46730
At4g23440	At4g14370
At5g11250	At4g19050
At5g17680	At4g26090
At5g17880	At5g47250
At5g17970	At5g47260
At5g18350	At5g47280
At5g18360	At5g56220
At5g18370	
At5g22690	
At5g36930	
At5g38340	
At5g38350	
At5g38850	
At5g40060	
At5g40090	
At5g40100	
At5g40910	
At5g40920	
At5g41540	
At5g41550	
At5g41740	
At5g41750	
At5g44510	
At5g45050	
At5g45060	
At5g45200	
At5g45230	
At5g45240	
At5g45260	
At5g46260	
At5g46270	
At5g46450	
At5g46470	
At5g46510	
At5g46520	
At5g48770	
At5g48780	
At5g49140	
At5g51630	
At5g58120	
At2g14080	
At4g36150	
At4g16890	

RPS4
At1g50180
At4g10780
at1g10920
At3g50950
At1g61180
At1g61310

REFERENCES:

Asqui, S. L., Vercammen, D., Serrano, I., Valls, M., Rivas, S., Van Breusegem, F., . . . Coll, N. S. (2018). AtSERPIN1 is an inhibitor of the metacaspase AtMC1-mediated cell death and autocatalytic processing in planta. *New Phytologist*, *218*(3), 1156-1166. https://doi.org/10.1111/nph.14446

Balint-Kurti, P. (2019). The plant hypersensitive response: concepts, control and consequences. *Molecular Plant Pathology*, *20*(8), 1163-1178. https://doi.org/10.1111/mpp.12821

Bi, G., Su, M., Li, N., Liang, Y., Dang, S., Xu, J., . . . Zhou, J.-M. (2021). The ZAR1 resistosome is a calcium-permeable channel triggering plant immune signaling. *Cell*, *184*(13), 3528-+. https://doi.org/10.1016/j.cell.2021.05.003

Bomblies, K., & Weigel, D. (2007). Hybrid necrosis: autoimmunity as a potential gene-flow barrier in plant species. *Nature Reviews Genetics*, *8*(5), 382-393. https://doi.org/10.1038/nrg2082

Castel, B., Ngou, P.-M., Cevik, V., Redkar, A., Kim, D.-S., Yang, Y., . . . Jones, J. D. G. (2019). Diverse NLR immune receptors activate defence via the RPW8-NLR NRG1 [Article]. *New Phytologist*, *222*(2), 966-980. https://doi.org/10.1111/nph.15659

Cheng, Y. T., Li, Y. Z., Huang, S. A., Huang, Y., Dong, X. N., Zhang, Y. L., & Li, X. (2011). Stability of plant immune-receptor resistance proteins is controlled by SKP1-CULLIN1-F-box (SCF)-mediated protein degradation. *Proceedings of the National Academy of Sciences of the United States of America*, *108*(35), 14694-14699. https://doi.org/10.1073/pnas.1105685108

Clough, S. J., & Bent, A. F. (1998). Floral dip: a simplified method for Agrobacterium-mediated transformation of Arabidopsis thaliana. *Plant Journal*, *16*(6), 735-743. https://doi.org/10.1046/j.1365-313x.1998.00343.x

Coll, N. S., Smidler, A., Puigvert, M., Popa, C., Valls, M., & Dangl, J. L. (2014). The plant metacaspase AtMC1 in pathogen-triggered programmed cell death and aging: functional linkage with autophagy. *Cell Death and Differentiation*, *21*(9), 1399-1408. https://doi.org/10.1038/cdd.2014.50

Coll, N. S., Vercammen, D., Smidler, A., Clover, C., Van Breusegem, F., Dangl, J. L., & Epple, P. (2010). Arabidopsis Type I Metacaspases Control Cell Death [Article]. *Science*, *330*(6009), 1393-1397. https://doi.org/10.1126/science.1194980

Couto, D., & Zipfel, C. (2016). Regulation of pattern recognition receptor signalling in plants. *Nature Reviews Immunology*, *16*(9), 537-552. https://doi.org/10.1038/nri.2016.77

Cox, J., Hein, M. Y., Luber, C. A., Paron, I., Nagaraj, N., & Mann, M. (2014). Accurate Proteome-wide Label-free Quantification by Delayed Normalization and Maximal Peptide Ratio Extraction, Termed MaxLFQ [Article]. *Molecular & Cellular Proteomics*, *13*(9), 2513-2526. https://doi.org/10.1074/mcp.M113.031591

Cox, J., Neuhauser, N., Michalski, A., Scheltema, R. A., Olsen, J. V., & Mann, M. (2011). Andromeda: A Peptide Search Engine Integrated into the MaxQuant Environment [Article]. *Journal of Proteome Research*, *10*(4), 1794-1805. https://doi.org/10.1021/pr101065j

Cui, H., Gobbato, E., Kracher, B., Qiu, J., Bautor, J., & Parker, J. E. (2017). A core function of EDS1 with PAD4 is to protect the salicylic acid defense sector in Arabidopsis immunity [Article]. *New Phytologist*, *213*(4), 1802-1817. https://doi.org/10.1111/nph.14302

Dressano, K., Ceciliato, P. H. O., Silva, A. L., Guerrero-Abad, J. C., Bergonci, T., Ortiz-Morea, F. A., . . . Moura, D. S. (2017). BAK1 is involved in AtRALF1-induced inhibition of root cell expansion [Article]. *Plos Genetics*, *13*(10), Article e1007053. https://doi.org/10.1371/journal.pgen.1007053

Escamez, S., Andre, D., Zhang, B., Bollhoner, B., Pesquet, E., & Tuominen, H. (2016). METACASPASE9 modulates autophagy to confine cell death to the target cells during Arabidopsis vascular xylem differentiation [Article]. *Biology Open*, *5*(2), 122-129. https://doi.org/10.1242/bio.015529

Feys, B. J., Wiermer, M., Bhat, R. A., Moisan, L. J., Medina-Escobar, N., Neu, C., . . . Parker, J. E. (2005). Arabidopsis SENESCENCE-ASSOCIATED GENE101 stabilizes and signals within an ENHANCED DISEASE SUSCEPTIBILITY1 complex in plant innate immunity [Article]. *Plant Cell*, *17*(9), 2601-2613. https://doi.org/10.1105/tpc.105.033910

Freh, M., Gao, J., Petersen, M., & Panstruga, R. (2022). Plant autoimmunity-fresh insights into an old phenomenon [Article]. *Plant Physiology*, *188*(3), 1419-1434. https://doi.org/10.1093/plphys/kiab590

Fritsch, M., Gunther, S. D., Schwarzer, R., Albert, M.-C., Schorn, F., Werthenbach, J. P., . . . Kashkar, H. (2019). Caspase-8 is the molecular switch for apoptosis, necroptosis and pyroptosis [Article]. *Nature*, *575*(7784), 683-+. https://doi.org/10.1038/s41586-019-1770-6

Förderer, A., Li, E., Lawson, A. W., Deng, Y. N., Sun, Y., Logemann, E., . . . Chai, J. (2022). A wheat resistosome defines common principles of immune receptor channels. *Nature*. https://doi.org/10.1038/s41586-022-05231-w

Gao, M., Wang, X., Wang, D., Xu, F., Ding, X., Zhang, Z., . . . Zhang, Y. (2009). Regulation of Cell Death and Innate Immunity by Two Receptor-like Kinases in Arabidopsis [Article]. *Cell Host & Microbe*, *6*(1), 34-44. https://doi.org/10.1016/j.chom.2009.05.019

Geldner, N., Denervaud-Tendon, V., Hyman, D. L., Mayer, U., Stierhof, Y.-D., & Chory, J. (2009). Rapid, combinatorial analysis of membrane compartments in intact plants with a multicolor marker set [Article]. *Plant Journal*, *59*(1), 169-178. https://doi.org/10.1111/j.1365-313X.2009.03851.x

Gou, M. Y., Shi, Z. Y., Zhu, Y., Bao, Z. L., Wang, G. Y., & Hua, J. (2012). The F-box protein CPR1/CPR30 negatively regulates R protein SNC1 accumulation. *Plant Journal*, *69*(3), 411-420. https://doi.org/10.1111/j.1365-313X.2011.04799.x

Hander, T., Fernandez-Fernandez, A. D., Kumpf, R. P., Willems, P., Schatowitz, H., Rombaut, D., . . . Stael, S. (2019). Damage on plants activates Ca2+-dependent metacaspases for release of immunomodulatory peptides [Article]. *Science*, *363*(6433), 1301-+, Article eaar7486. https://doi.org/10.1126/science.aar7486

He, R., Drury, G. E., Rotari, V. I., Gordon, A., Willer, M., Farzaneh, T., . . . Gallois, P. (2008). Metacaspase-8 modulates programmed cell death induced by ultraviolet light and H2O2 in Arabidopsis [Article]. *Journal of Biological Chemistry*, *283*(2), 774-783. https://doi.org/10.1074/jbc.M704185200

Huang, S., Jia, A., Song, W., Hessler, G., Meng, Y., Sun, Y., . . . Chai, J. (2022). Identification and receptor mechanism of TIR-catalyzed small molecules in plant immunity. *Science*, *377*(6605), 487-+, Article eabq3297. https://doi.org/10.1126/science.abq3297

Jacob, P., Kim, N. H., Wu, F., El Kasmr, F., Chi, Y., Walton, W. G., . . . Dangl, J. L. (2021). Plant "helper" immune receptors are Ca2+-permeable nonselective cation channels. *Science*, *373*(6553), 420-+. https://doi.org/10.1126/science.abg7917

Jia, A., Huang, S., Song, W., Wang, J., Meng, Y., Sun, Y., . . . Chai, J. (2022). TIR-catalyzed ADP-ribosylation reactions produce signaling molecules for plant immunity. *Science*, *377*(6605), 488-+, Article eabq8180. https://doi.org/10.1126/science.abq8180

Jirage, D., Tootle, T. L., Reuber, T. L., Frost, L. N., Feys, B. J., Parker, J. E., . . . Glazebrook, J. (1999). Arabidopsis thaliana PAD4 encodes a lipase-like gene that is important for salicylic acid signaling [Article]. *Proceedings of the National Academy of Sciences of the United States of America*, *96*(23), 13583-13588. https://doi.org/10.1073/pnas.96.23.13583

Jones, J. D. G., & Dangl, J. L. (2006). The plant immune system [Review]. *Nature*, *444*(7117), 323-329. https://doi.org/10.1038/nature05286

Jubic, L. M., Saile, S., Furzer, O. J., El Kasmi, F., & Dangl, J. L. (2019). Help wanted: helper NLRs and plant immune responses. *Current Opinion in Plant Biology*, *50*, 82-94. https://doi.org/10.1016/j.pbi.2019.03.013

Jung, H., Lee, H. N., Marshall, R. S., Lomax, A. W., Yoon, M. J., Kim, J., . . . Chung, T. (2020). Arabidopsis cargo receptor NBR1 mediates selective autophagy of defective proteins [Article]. *Journal of Experimental Botany*, *71*(1), 73-89. https://doi.org/10.1093/jxb/erz404

Kunkel, B. N., Bent, A. F., Dahlbeck, D., Innes, R. W., & Staskawicz, B. J. (1993). RPS2, AN ARABIDOPSIS DISEASE RESISTANCE LOCUS SPECIFYING RECOGNITION OF PSEUDOMONAS-SYRINGAE STRAINS EXPRESSING THE AVIRULENCE GENE AVRRPT2. *Plant Cell*, *5*(8), 865-875. https://doi.org/10.1105/tpc.5.8.865

Lampropoulos, A., Sutikovic, Z., Wenzl, C., Maegele, I., Lohmann, J. U., & Forner, J. (2013). GreenGate - A Novel, Versatile, and Efficient Cloning System for Plant Transgenesis. *Plos One*, *8*(12), Article e83043. https://doi.org/10.1371/journal.pone.0083043

Leary, A. Y., Sanguankiattichai, N., Duggan, C., Tumtas, Y., Pandey, P., Segretin, M. E., . . . Bozkurt, T. O. (2017). Modulation of plant autophagy during pathogen attack. *J Exp Bot*. https://doi.org/10.1093/jxb/erx425

Lee, R. R. Q., & Chae, E. (2020). Variation Patterns of NLR Clusters in Arabidopsis thaliana Genomes [Article]. *Plant Communications*, *1*(4), Article 100089. https://doi.org/10.1016/j.xplc.2020.100089

Lewis, J. D., Wu, R., Guttman, D. S., & Desveaux, D. (2010). Allele-Specific Virulence Attenuation of the Pseudomonas syringae HopZ1a Type III Effector via the Arabidopsis ZAR1 Resistance Protein [Article]. *Plos Genetics*, *6*(4), Article e1000894. https://doi.org/10.1371/journal.pgen.1000894

Liao, D. H., Cao, Y. R., Sun, X., Espinoza, C., Nguyen, C. T., Liang, Y., & Stacey, G. (2017). Arabidopsis E3 ubiquitin ligase PLANT U-BOX13 (PUB13) regulates chitin receptor LYSIN MOTIF

RECEPTOR KINASE5 (LYK5) protein abundance. *New Phytologist*, *214*(4), 1646-1656. https://doi.org/10.1111/nph.14472

Liebrand, T. W. H., van den Burg, H. A., & Joosten, M. H. A. J. (2014). Two for all: receptor-associated kinases SOBIR1 and BAK1 [Review]. *Trends in Plant Science*, *19*(2), 123-132. https://doi.org/10.1016/j.tplants.2013.10.003

Llamas, E., Koyuncu, S., Lee, H. J., Gutierrez-Garcia, R., Dunken, N., Charura, N., . . . Vilchez, D. (2022). Chloroplast protein import determines plant proteostasis and retrograde signaling. *bioRxiv*, 2022.2003.2019.484971. https://doi.org/10.1101/2022.03.19.484971

Lolle, S., Greeff, C., Petersen, K., Roux, M., Jensen, M. K., Bressendorff, S., . . . Petersen, M. (2017). Matching NLR Immune Receptors to Autoimmunity in camta3 Mutants Using Antimorphic NLR Alleles [Article]. *Cell Host & Microbe*, *21*(4), 518-+. https://doi.org/10.1016/j.chom.2017.03.005

Lu, D. P., Lin, W. W., Gao, X. Q., Wu, S. J., Cheng, C., Avila, J., . . . Shan, L. B. (2011). Direct Ubiquitination of Pattern Recognition Receptor FLS2 Attenuates Plant Innate Immunity. *Science*, *332*(6036), 1439-1442. https://doi.org/10.1126/science.1204903

Luan, Q.-L., Zhu, Y.-X., Ma, S., Sun, Y., Liu, X.-Y., Liu, M., . . . Wang, G.-F. (2021). Maize metacaspases modulate the defense response mediated by the NLR protein Rp1-D21 likely by affecting its subcellular localization [Article]. *Plant Journal*, *105*(1), 151-166. https://doi.org/10.1111/tpj.15047

Marchal, C., Pai, H., Kamoun, S., & Kourelis, J. (2022). Emerging principles in the design of bioengineered made-to-order plant immune receptors [; Review]. *Current opinion in plant biology*, *70*, 102311-102311. https://doi.org/10.1016/j.pbi.2022.102311

Martin, R., Qi, T., Zhang, H., Liu, F., King, M., Toth, C., . . . Staskawicz, B. J. (2020). Structure of the activated ROQ1 resistosome directly recognizing the pathogen effector XopQ. *Science*, *370*(6521), 1185-+, Article eabd9993. https://doi.org/10.1126/science.abd9993

Mazzucotelli, E., Belloni, S., Marone, D., De Leonardis, A. M., Guerra, D., Fonzo, N., . . . Mastrangelo, A. M. (2006). The E3 ubiquitin ligase gene family in plants: Regulation by degradation. *Current Genomics*, *7*(8), 509-522. https://doi.org/10.2174/138920206779315728

Mine, A., Seyfferth, C., Kracher, B., Berens, M. L., Becker, D., & Tsuda, K. (2018). The Defense Phytohormone Signaling Network Enables Rapid, High-Amplitude Transcriptional Reprogramming during Effector-Triggered Immunity. *Plant Cell*, *30*(6), 1199-1219. https://doi.org/10.1105/tpc.17.00970

Minina, E. A., Coll, N. S., Tuominen, H., & Bozhkov, P. V. (2017). Metacaspases versus caspases in development and cell fate regulation. *Cell Death and Differentiation*, *24*(8), 1314-1325. https://doi.org/10.1038/cdd.2017.18

Minina, E. A., Staal, J., Alvarez, V. E., Berges, J. A., Berman-Frank, I., Beyaert, R., . . . Bozhkov, P. V. (2020). Classification and Nomenclature of Metacaspases and Paracaspases: No More Confusion with Caspases [Letter]. *Molecular Cell*, *77*(5), 927-929. https://doi.org/10.1016/j.molcel.2019.12.020

Morineau, C., Bellec, Y., Tellier, F., Gissot, L., Kelemen, Z., Nogue, F., & Faure, J.-D. (2017). Selective gene dosage by CRISPR-Cas9 genome editing in hexaploid Camelina sativa [Article]. *Plant Biotechnology Journal*, *15*(6), 729-739. https://doi.org/10.1111/pbi.12671

Munch, D., Rodriguez, E., Bressendorff, S., Park, O. K., Hofius, D., & Petersen, M. (2014). Autophagy deficiency leads to accumulation of ubiquitinated proteins, ER stress, and cell death in Arabidopsis [Article]. *Autophagy*, *10*(9), 1579-1587. https://doi.org/10.4161/auto.29406

Newton, K., Wickliffe, K. E., Maltzman, A., Dugger, D. L., Reja, R., Zhang, Y., . . . Dixit, V. M. (2019). Activity of caspase-8 determines plasticity between cell death pathways [Article]. *Nature*, *575*(7784), 679-+. https://doi.org/10.1038/s41586-019-1752-8

Ngou, B. P. M., Ahn, H. K., Ding, P. T., & Jones, J. D. G. (2021). Mutual potentiation of plant immunity by cell-surface and intracellular receptors. *Nature*, *592*(7852), 110-+. https://doi.org/10.1038/s41586-021-03315-7

Ordon, J., Gantner, J., Kemna, J., Schwalgun, L., Reschke, M., Streubel, J., . . . Stuttmann, J. (2017). Generation of chromosomal deletions in dicotyledonous plants employing a user-friendly genome editing toolkit [Article]. *Plant Journal*, *89*(1), 155-168. https://doi.org/10.1111/tpj.13319

Orning, P., & Lien, E. (2021). Multiple roles of caspase-8 in cell death, inflammation, and innate immunity [Review]. *Journal of Leukocyte Biology*, *109*(1), 121-141. https://doi.org/10.1002/jlb.3mr0420-305r

Pitsili, E., Rodriguez-Trevino, R., Ruiz-Solani, N., Demir, F., Kastanaki, E., Dambire, C., . . . Coll, N. S. (2022). A phloem-localized Arabidopsis metacaspase (AtMC3) improves drought tolerance. *bioRxiv*, 2022.2011.2009.515759. https://doi.org/10.1101/2022.11.09.515759

Pruitt, R. N., Locci, F., Wanke, F., Zhang, L., Saile, S. C., Joe, A., . . . Nuernberger, T. (2021). The EDS1-PAD4-ADR1 node mediates Arabidopsis pattern-triggered immunity [Article]. *Nature*, *598*(7881), 495-+. https://doi.org/10.1038/s41586-021-03829-0

Roberts, M., Tang, S., Stallmann, A., Dangl, J. L., & Bonardi, V. (2013). Genetic Requirements for Signaling from an Autoactive Plant NB-LRR Intracellular Innate Immune Receptor [Article]. *Plos Genetics*, *9*(4), Article e1003465. https://doi.org/10.1371/journal.pgen.1003465

Rodriguez, E., El Ghoul, H., Mundy, J., & Petersen, M. (2016). Making sense of plant autoimmunity and "negative regulators' [Review]. *Febs Journal*, *283*(8), 1385-1391. https://doi.org/10.1111/febs.13613

Saile, S. C., Jacob, P., Castel, B., Jubic, L. M., Salas-Gonzales, I., Baecker, M., . . . El Kasmi, F. (2020). Two unequally redundant "helper" immune receptor families mediate Arabidopsis thaliana intracellular "sensor" immune receptor functions [Article]. *Plos Biology*, *18*(9), Article e3000783. https://doi.org/10.1371/journal.pbio.3000783

Schulze, S., Yu, L., Hua, C., Zhang, L., Kolb, D., Weber, H., . . . Kemmerling, B. (2022). The Arabidopsis TIR-NBS-LRR protein CSA1 guards BAK1-BIR3 homeostasis and mediates convergence of pattern- and effector-induced immune responses. *Cell host & microbe*, *30*(12), 1717-1731.e1716. https://doi.org/10.1016/j.chom.2022.11.001

Slobodkin, M. R., & Elazar, Z. (2013). The Atg8 family: multifunctional ubiquitin-like key regulators of autophagy. In J. D. Lane (Ed.), *Autophagy: Molecules and Mechanisms* (Vol. 55, pp. 51-64). Portland Press Ltd. https://doi.org/10.1042/bse0550051

Sun, X., Lapin, D., Feehan, J. M., Stolze, S. C., Kramer, K., Dongus, J. A., . . . Parker, J. E. (2021). Pathogen effector recognition-dependent association of NRG1 with EDS1 and SAG101 in TNL receptor immunity [Article]. *Nature Communications*, *12*(1), Article 3335. https://doi.org/10.1038/s41467-021-23614-x

Thompson, A. R., Doelling, J. H., Suttangkakul, A., & Vierstra, R. D. (2005). Autophagic nutrient recycling in Arabidopsis directed by the ATG8 and ATG12 conjugation pathways [Article]. *Plant Physiology*, *138*(4), 2097-2110. https://doi.org/10.1104/pp.105.060673

Tian, H., Wu, Z., Chen, S., Ao, K., Huang, W., Yaghmaiean, H., . . . Zhang, Y. (2021). Activation of TIR signalling boosts pattern-triggered immunity. *Nature*. https://doi.org/10.1038/s41586-021-03987-1

Torres, M. A., Dangl, J. L., & Jones, J. D. G. (2002). Arabidopsis gp91(phox) homologues AtrbohD and AtrbohF are required for accumulation of reactive oxygen intermediates in the plant defense response [Article]. *Proceedings of the National Academy of Sciences of the United States of America*, *99*(1), 517-522. https://doi.org/10.1073/pnas.012452499

Tsiatsiani, L., Van Breusegem, F., Gallois, P., Zavialov, A., Lam, E., & Bozhkov, P. V. (2011). Metacaspases. *Cell Death and Differentiation*, *18*(8), 1279-1288. https://doi.org/10.1038/cdd.2011.66

Tummers, B., Mari, L., Guy, C. S., Heckmann, B. L., Rodriguez, D. A., Ruhl, S., . . . Green, D. R. (2020). Caspase-8-Dependent Inflammatory Responses Are Controlled by Its Adaptor, FADD, and Necroptosis [Article]. *Immunity*, *52*(6), 994-+. https://doi.org/10.1016/j.immuni.2020.04.010

Tyanova, S., Temu, T., Sinitcyn, P., Carlson, A., Hein, M. Y., Geiger, T., . . . Cox, J. (2016). The Perseus computational platform for comprehensive analysis of (prote)omics data [Article]. *Nature Methods*, *13*(9), 731-740. https://doi.org/10.1038/nmeth.3901

van Wersch, R., Li, X., & Zhang, Y. (2016). Mighty Dwarfs: Arabidopsis Autoimmune Mutants and Their Usages in Genetic Dissection of Plant Immunity [Review]. *Frontiers in Plant Science*, *7*, Article 1717. https://doi.org/10.3389/fpls.2016.01717

Vercammen, D., Declercq, W., Vandenabeele, P., & Van Breusegem, F. (2007). Are metacaspases caspases? [Review]. *Journal of Cell Biology*, *179*(3), 375-380. https://doi.org/10.1083/jcb.200705193

Vercammen, D., van de Cotte, B., De Jaeger, G., Eeckhout, D., Casteels, P., Vandepoele, K., . . . Van Breusegem, F. (2004). Type II metacaspases Atmc4 and Atmc9 of Arabidopsis thaliana cleave substrates after arginine and lysine. *Journal of Biological Chemistry*, *279*(44), 45329-45336. https://doi.org/10.1074/jbc.M406329200

Wan, L., Essuman, K., Anderson, R. G., Sasaki, Y., Monteiro, F., Chung, E.-H., . . . Nishimura, M. T. (2019). TIR domains of plant immune receptors are NAD(+)-cleaving enzymes that promote cell death. *Science*, *365*(6455), 799-+. https://doi.org/10.1126/science.aax1771

Wan, W.-L., Kim, S.-T., Castel, B., Charoennit, N., & Chae, E. (2021). Genetics of autoimmunity in plants: an evolutionary genetics perspective [Review]. *New Phytologist*, *229*(3), 1215-1233. https://doi.org/10.1111/nph.16947

Wang, G., Ellendorff, U., Kemp, B., Mansfield, J. W., Forsyth, A., Mitchell, K., . . . Thomma, B. P. H. J. (2008). A genome-wide functional investigation into the roles of receptor-like proteins in Arabidopsis [Article]. *Plant Physiology*, *147*(2), 503-517. https://doi.org/10.1104/pp.108.119487

Wang, J., Hu, M., Wang, J., Qi, J., Han, Z., Wang, G., . . . Chai, J. (2019). Reconstitution and structure of a plant NLR resistosome conferring immunity. *Science*, *364*(6435), 44-+, Article eaav5870. https://doi.org/10.1126/science.aav5870

Wang, S., Xue, M., He, C., Shen, D., Jiang, C., Zhao, H., & Niu, D. (2021). AtMC1 Associates With LSM4 to Regulate Plant Immunity Through Modulating Pre-mRNA Splicing [Article]. *Molecular Plant-Microbe Interactions*, *34*(12), 1423-1432. https://doi.org/10.1094/mpmi-07-21-0197-r

Watanabe, N., & Lam, E. (2011). Arabidopsis metacaspase 2d is a positive mediator of cell death induced during biotic and abiotic stresses [Article]. *Plant Journal*, *66*(6), 969-982. https://doi.org/10.1111/j.1365-313X.2011.04554.x

Wildermuth, M. C., Dewdney, J., Wu, G., & Ausubel, F. M. (2001). Isochorismate synthase is required to synthesize salicylic acid for plant defence [Article]. *Nature*, *414*(6863), 562-565. https://doi.org/10.1038/35107108

Wu, Y., Gao, Y., Zhan, Y., Kui, H., Liu, H., Yan, L., . . . Li, J. (2020). Loss of the common immune coreceptor BAK1 leads to NLR-dependent cell death [Article]. *Proceedings of the National Academy of Sciences of the United States of America*, *117*(43), 27044-27053. https://doi.org/10.1073/pnas.1915339117

Wu, Z., Tong, M., Tian, L., Zhu, C., Liu, X., Zhang, Y., & Li, X. (2020). Plant E3 ligases SNIPER1 and SNIPER2 broadly regulate the homeostasis of sensor NLR immune receptors [Article]. *Embo Journal*, *39*(15), Article e104915. https://doi.org/10.15252/embj.2020104915

Yang, Y., Kim, N. H., Cevik, V., Jacob, P., Wan, L., Furzer, O. J., & Dangl, J. L. (2022). Allelic variation in the Arabidopsis TNL CHS3/CSA1 immune receptor pair reveals two functional cell-death regulatory modes. *Cell host & microbe*, *30*(12), 1701-1716.e1705. https://doi.org/10.1016/j.chom.2022.09.013

Yoshimoto, K., Jikumaru, Y., Kamiya, Y., Kusano, M., Consonni, C., Panstruga, R., . . . Shirasu, K. (2009). Autophagy Negatively Regulates Cell Death by Controlling NPR1-Dependent Salicylic Acid Signaling during Senescence and the Innate Immune Response in Arabidopsis [Article]. *Plant Cell*, *21*(9), 2914-2927. https://doi.org/10.1105/tpc.109.068635

Yuan, M. H., Jiang, Z. Y., Bi, G. Z., Nomura, K., Liu, M. H., Wang, Y. P., . . . Xin, X. F. (2021). Pattern-recognition receptors are required for NLR-mediated plant immunity. *Nature*, *592*(7852), 105-+. https://doi.org/10.1038/s41586-021-03316-6

Zavaliev, R., Mohan, R., Chen, T., & Dong, X. (2020). Formation of NPR1 Condensates Promotes Cell Survival during the Plant Immune Response [Article]. *Cell*, *182*(5), 1093-+. https://doi.org/10.1016/j.cell.2020.07.016

Zhang, Y. L., Goritschnig, S., Dong, X. N., & Li, X. (2003). A gain-of-function mutation in a plant disease resistance gene leads to constitutive activation of downstream signal transduction pathways in suppressor of npr1-1, constitutive 1 [Article]. *Plant Cell*, *15*(11), 2636-2646. https://doi.org/10.1105/tpc.015842

Zhu, P., Yu, X.-H., Wang, C., Zhang, Q., Liu, W., McSweeney, S., . . . Liu, Q. (2020). Structural basis for Ca2+-dependent activation of a plant metacaspase [Article]. *Nature Communications*, *11*(1), Article 2249. https://doi.org/10.1038/s41467-020-15830-8

CHAPTER 3

Arabidopsis metacaspase MC1 localizes in stress granules, clears protein aggregates, and delays senescence

(Pre-publication 5)

Arabidopsis metacaspase MC1 localizes in stress granules, clears protein aggregates and delays senescence

Short title: Proteostatic role of Arabidopsis metacaspase MC1

Nerea Ruiz-Solaní[1], Jose Salguero-Linares[1], Laia Armengot[1,2], Jaime Santos[3], Irantzu Pallarès[3], Katarina P. van Midden[4], Ujjal J. Phukkan[1,¥], Seda Koyuncu[5], Júlia Borràs-Bisa[1], Liang Li[1], Crina Popa[1], Frederik Eisele[6], Anna Maria Eisele-Bürger[6], Sandra Malgrem Hill[6], Emilio Gutiérrez-Beltrán[7,8], Thomas Nyström[6], Marc Valls[1,2], Ernesto Llamas[9], David Vilchez[5,10,11], Marina Klemenčič[4], Salvador Ventura[3], Nuria S. Coll[1,12,*]

[1] *Centre for Research in Agricultural Genomics (CRAG), CSIC-IRTA-UAB-UB, Campus UAB, 08193 Bellaterra, Spain*

[2] *Department of Genetics, Microbiology and Statistics, Universitat de Barcelona, 08028 Barcelona, Spain.*

[3] *Institut de Biotecnologia i de Biomedicina and Departament de Bioquímica i Biologia Molecular, Universitat Autònoma de Barcelona, Barcelona, Spain.*

[4] *Department of Chemistry and Biochemistry, Faculty of Chemistry and Chemical Technology, University of Ljubljana, Ljubljana, Slovenia.*

[5] *Cologne Excellence Cluster for Cellular Stress Responses in Aging-Associated Diseases (CECAD), University of Cologne, Cologne, Germany.*

[6] *Department of Microbiology and Immunology, The Sahlgrenska Academy at the University of Gothenburg, Gothenburg 41390, Sweden.*

[7] *Instituto de Bioquímica Vegetal y Fotosíntesis, Universidad de Sevilla and Consejo Superior de Investigaciones Científicas (CSIC), Seville, Spain.*

[8] *Departamento de Bioquímica Vegetal y Biología Molecular, Facultad de Biología, Universidad de Sevilla, Sevilla, Spain.*

[9] *Cluster of Excellence on Plant Sciences (CEPLAS), Institute for Plant Sciences, University of Cologne, D-50674 Cologne, Germany.*

[10] *Center for Molecular Medicine Cologne (CMMC), University of Cologne, Cologne, Germany.*

[11] *Faculty of Medicine, University Hospital Cologne, Cologne, Germany.*

[12] *Consejo Superior de Investigaciones Científicas (CSIC), 08001 Barcelona, Spain*

¥ School of Plant Sciences, University of Arizona, Tucson, AZ, United States

[*] Author for correspondence:
Nuria S. Coll. Centre for Research in Agricultural Genomics. 08193 Cerdanyola del Valles. Spain
e-mail: nuria.sanchez-coll@cragenomica.es

The author responsible for distribution of materials integral to the findings presented in this article in accordance with the policy described in the Instructions for Authors (https://academic.oup.com/plcell/pages/General-Instructions) is: Nuria S. Coll (nuria.sanchez-coll@cragenomica.es)

Abstract

Stress granules (SGs) are highly conserved cytoplasmic condensates that assemble in response to stress and contribute to maintaining protein homeostasis. These membraneless organelles are dynamic, dissassembling once the stress is no longer present. Persistence of SGs due to mutations or chronic stress has been often related to age-dependent protein-misfolding diseases in animals. Here, we find that the metacaspase MC1 is dynamically recruited into SGs upon proteotoxic stress in Arabidopsis. MC1 recruitment to SG and its release is mediated by two predicted disordered regions, the prodomain and the 360 loop. Importantly, we show that MC1 has the capacity to clear toxic protein aggregates *in vivo* and *in vitro*, acting as a disaggregase. Finally, we demonstrate that overexpressing MC1 delays senescence and this phenotype is dependent on the presence of the 360 loop and an intact catalytic domain. Together, our data indicate that MC1 regulates senescence through its recruitment into SGs and this function could potentially be linked to its remarkable protein aggregate-clearing activity.

Keywords: stress granules, biomolecular condensates, protein aggregates, metacaspases, heat stress, senescence

Introduction

To cope with stress, eukaryotic cells are equipped with multiple sophisticated mechanisms which ultimately confer robustness against various perturbations. As part of their stress responses, cells must readjust proteostasis (protein homeostasis), which is achieved through an arrest in protein synthesis and activation of protein quality control (PQC) mechanisms to prevent accumulation of misfolded proteins in the cytoplasm, potentially causing proteotoxicity (Alberti and Carra, 2018). The proteostatic capacity of cells declines with age, which may reduce their capacity to dispose of potentially harmful protein aggregates (Vilchez, Saez and Dillin, 2014; Hipp, Kasturi and Hartl, 2019). An important stress response mechanism in fungi, animals and plants is the formation of stress granules (SGs). SGs are biomolecular condensates specifically assembled in the cytosol under stress conditions with a highly dynamic behavior, containing a combination of mRNA and proteins -many of which have RNA binding ability (Jain *et al.*, 2016; Markmiller *et al.*, 2018; Youn *et al.*, 2019). These membraneless compartments were originally viewed as sites of accumulation and disposal of stalled mRNAs, but are currently emerging as major orchestrators of stress responses (Buchan and Parker, 2009; Maruri-López *et al.*, 2021).

Current models predict that SG formation is mediated by liquid-liquid phase separation (LLPS) promoted by multivalent molecules, such as proteins featuring low complexity regions (LCRs) / intrinsically disordered regions (IDRs) (Protter and Parker, 2016). Assembly and clearance of SGs is finely regulated, with initial formation of a dense core by LLPS followed by recruitment of peripheral proteins (Jain *et al.*, 2016; Markmiller *et al.*, 2018). Core components are proteins containing IDRs and RNA-binding domains together with proteins involved in translation, whereas the shell is composed of an array of mRNA, proteins and small molecules that vary depending on the species, cell type and developmental stage (Gonzalez-Garcia *et al.*, 2011; Jain *et al.*, 2016; Niewidok *et al.*, 2018; Kosmacz *et al.*, 2019; Guillén-Boixet *et al.*, 2020).

Compared to yeast and mammals, little is known about plant SGs, despite their important role in stress responses, including heat, hypoxia, salt and drought (Sorenson and Bailey-Serres, 2014; Yan *et al.*, 2014; Gutierrez-Beltran *et al.*, 2015; Marondedze *et al.*, 2020). Among these stress responses, heat is the best characterized so far, as it presents an archetypal form of acute stress resulting in proteotoxicity that must be handled by various mechanisms, including SG formation (Maruri-López *et al.*, 2021). SGs provide efficient regulatory platforms under stress conditions (Maruri-López *et al.*, 2021), serving as i) mRNA reorganization centers, wherein their fate is determined (re-initiation, decay, storage), ii) temporary protein storage centers, to protect them from unfolding and iii) enzyme recruitment centers, to facilitate rapid activation of certain metabolic pathways. Plant SG component catalogs and molecular markers have started to become available in recent years opening new avenues of research.

An essential property of SGs is their dynamism: to be functional, they must be inducible and reversible. In mammals, cumulative evidence links altered SG dynamics with pathologies featuring aberrant protein coalescence leading to aggregation (Baradaran-Heravi, Van Broeckhoven and van der Zee, 2020; Marcelo *et al.*, 2021). In several neurodegenerative diseases, mutations in LCRs/IDRs of certain proteins disrupts their biophysical properties, leading to enhanced LLPS and formation of pathological protein aggregates (Baradaran-Heravi, Van Broeckhoven and van der Zee, 2020). Pathological SGs undergo a liquid to solid transition and persist even after the stress has passed, acting as undissolvable protein traps. This is the case

of polyglutamine (PolyQ) pathologies, such as Huntington's disease, caused by abnormal PolyQ extensions, that make them more aggregation-prone (Sanchez *et al.*, 2021).

Plants may have evolved extremely efficient mechanisms to deal with toxic protein aggregation. It has been recently demonstrated that overexpression of synthetic extended polyQ proteins, that normally aggregate and cause cell death in animal models, do not cause deleterious defects in plants (Llamas *et al.*, 2022). In fact, plants overexpressing synthetic protein variants that constitutively aggregate, do not lead to major defects (Jung *et al.*, 2020; Llamas *et al.*, 2022). This may indicate that plants have evolved extremely efficient mechanisms to deal with protein aggregation. Selective autophagy has been previously involved in degradation of protein aggregates or aggrephagy during proteotoxic stress (Jung *et al.*, 2020). However, whether formation of these protein aggregates is related to molecular condensation including SG formation and dynamics has not been addressed.

Metacaspases are cystein proteases present in plants, yeast and protozoa (Uren *et al.*, 2000). Plant metacaspases are divided into Type I if they bear an N-terminal prodomain and Type II, if no prodomain is present but instead a long linker between the catalytic subunits exists (AG *et al.*, 2000; Klemenčič and Funk, 2019). Several metacaspases have been shown to play important roles in stress responses (Coll *et al.*, 2010; Hander *et al.*, 2019; Minina *et al.*, 2020; Luan *et al.*, 2021; Pitsili *et al.*, 2022), although in most cases the mode of action of these proteases remains obscure. The model plant *Arabidopsis thaliana* (hereafter Arabidopsis) encodes 9 metacaspases in its genome. MC1-3 (AtMC1-3/AtMCA-Ia-c) are Type I metacaspases, while MC4-9 (AtMC4-9/AtMCA-IIa-f) are Type II metacaspases (Minina *et al.*, 2020). We previously showed that plants lacking MC1 exhibit accelerated senescence and accumulate aggregated proteins, indicating a potential role of MC1 in proteostasis (Coll *et al.*, 2014). In addition, a portion of MC1 re-localizes to insoluble protein deposits under proteotoxic stress conditions. Data from our lab and others indicate that MC1 may help stabilizing various proteins (Roberts *et al.*, 2013; Wang *et al.*, 2021; Lema Asqui *et al.*, 2018). However, the specific mechanisms whereby MC1 contributes to protein stabilization and aggregate clearance remain unknown.

Here, we demonstrate that MC1 is dynamically recruited to SGs upon proteotoxic stress. This SG localization is mediated by a C-terminal intrinsically disordered region, the 360 loop. We show that MC1 participates in the clearance of pathological aggregates in evolutionarily distant organisms ranging from yeast and animals to plants. *In vitro*, recombinant MC1 alone acts as a highly efficient disaggregase. In plants, this function can be harnessed to delay senescence, as observed in MC1 overexpressing lines.

Results

MC1 dynamically localizes to cytoplasmic stress granules upon acute proteotoxic stress

To gain a deeper understanding into MC1 function, we generated transgenic lines expressing *MC1* tagged with a green fluorescent protein under the control of the *35S* promoter in the *mc1* mutant background (*mc1 Pro35S::MC1-GFP*) and evaluated its subcellular localization. Under basal conditions MC1 showed a diffuse pattern in both cytoplasm and nucleus (Fig. 1A). Heat stress treatment (39°C for 40 min; Gutierrez-Beltran *et al.*, 2015) resulted in rapid formation of dynamic cytoplasmic puncta that disappeared shortly after returning

the plants to non-stress conditions (Fig. 1A, B). The same heat-responsive re-localization pattern was observed when *MC1-GFP* was expressed under the control of its native promoter (Fig. S1A, B). To evaluate if such puncta correspond to stress granules we used cycloheximide, an inhibitor of translational elongation that prevents SG assembly and forces the disassembly of existing SGs (Weber *et al.*, 2008). Application of cycloheximide blocked the appearance of the observed heat stress-induced puncta (Fig. 1C, D), indicating that they may indeed correspond to SGs.

To further examine if MC1 co-localized with SGs we used the plant SG marker Translationally controlled tumour protein (TCTP), which locates into SGs specifically under HS conditions (Gutierrez-Beltran *et al.*, 2021). We observed that transgenic plants stably co-expressing *MC1-RFP* (*Pro35S::MC1*-RFP) and *GFP-TCTP* (*Pro35S::GFP-TCT*P) show cytoplasmic co-localization in SGs under heat stress conditions (Fig. 1E). Furthermore, MC1 immunoprecipitated with TCTP in transgenic plants subjected to HS (Fig. 1F). Similarly, MC1 co-localized with other well-known SG markers RBP47 and TSN2 (Lorković *et al.*, 2000; Gutierrez-Beltran *et al.*, 2021) in protoplasts from transgenic *MC1-GFP* lines transiently expressing *RFP-RBP47* or *RFP-TSN2* (Fig. S2A, B). Together, these data demonstrate that MC1 dynamically re-localizes to SGs upon heat treatment, disappearing upon stress removal.

The intrinsically disordered regions of MC1 are aggregation prone and confer insolubility in vitro

SGs are enriched in proteins containing predicted intrinsically disordered regions (IDRs) (Guillén-Boixet *et al.*, 2020; Gutierrez-Beltran *et al.*, 2021; Schmit, Feric and Dundr, 2021). IDRs have been proposed to act as one of the main driving forces of condensate assembly, although the exact mechanism by which this occurs remains to be fully elucidated (Posey, Holehouse and Pappu, 2018; Alberti, Gladfelter and Mittag, 2019). We used a combination of two predictive software (D^2P^2, https://d2p2.pro and DISOPRED3, http://bioinf.cs.ucl.uk/psipred; Oates *et al.*, 2013; Jones and Cozzetto, 2015) to pinpoint potential IDRs within MC1 amino acid sequence. Based on these predictions, MC1 encompasses 2 major IDRs (Fig. 2A), one at the N-terminal prodomain and another at a region of the predicted C-terminal p10 catalytic domain known as the 360 loop (van Midden, Peric and Klemenčič, 2021). Since aggregation propensity is also considered an intrinsic determinant of phase separation (Babinchak and Surewicz, 2020), we used AGGRESCAN3D (A3D) to predict the structural aggregation propensity of MC1 on top of its alphafold predicted structure (http://biocomp.chem.uw.edu.pl/A3D/; Zambrano *et al.*, 2015). Interestingly, MC1 displays strong aggregation propensity at the predicted IDRs (Fig. 2B). In particular, the 360 loop shows the longest stretch of amino acids with high aggregation propensity scores.

The 360 loop of MC1 is a highly hydrophobic sequence only present in plant Type I metacaspases (van Midden, Peric and Klemenčič, 2021). In fungi, protozoa and red algae, Type I metacaspases do not contain the 360 loop and interestingly, these proteins are soluble when full-length is produced recombinantly *in vitro* (McLuskey *et al.*, 2012; Wong, Yan and Shi, 2012). In contrast, previous efforts to produce recombinant plant Type I metacaspases proved unsuccessful due to the fact that their full-length versions are highly insoluble (van Midden *et al.*, 2021). Removal of the 360 loop and the prodomain was necessary to express soluble MC1 in *Escherichia coli* (Fig. 3A,B), similar to what was previously shown with the single Type I metacaspase of the green algae *Chlamydomonas reinhardtii* CrMCA-I (van Midden, Peric and Klemenčič, 2021). Removal of the 360 loop alone was not sufficient to solubilize MC1 (Fig. 3B). The soluble MC1 variant devoid of the

prodomain and the 360 loop carrying an N-terminal hexahistidine tag (6xHis) (referred to as recombinant MC1 or rMC1) was purified to homogeneity by nickel-affinity chromatography (Fig S3A) and further isolated by size-exclusion chromatography removing minor impurities (Figure 3C). Importantly, rMC1 was catalytically active as shown by its ability to cleave Arabidopsis SERPIN1, an inhibitor and previously reported *in planta* substrate of MC1 (Lema Asqui *et al.*, 2018) (Fig S4A). rMC1 behaved as a canonical Type I metacaspase, showing dependency on calcium ions at low millimolar concentrations (1-10 mM) and a neutral pH (pH 7) for maximum cleavage of the fluorogenic substrate Z-FR-AMC (Fig. S4B and C, respectively), similar to CrMCA-I (van Midden, Peric and Klemenčič, 2021). In agreement with the observed trypsin-like activity of metacaspases, rMC1 cleaved the trypsin substrate β-casein (rβ-casein) (Fig S4D) (Lee *et al.*, 2007). We also purified rMC1 carrying a point mutation in the catalytic cysteine (C220) to alanine (rMC1CA) (Figure S3B, C). Importantly, rMC1CA was unable to cleave SERPIN1 or rβ-casein (Fig S4A,D). Together, these data show that MC1 contains two distinct IDRs that are aggregation prone and confer high insolubility for protein overexpression and isolation *in vitro*. When removed, proteolytically active rMC1 can be expressed and isolated.

The IDRs of MC1 regulate its dynamic recruitment into SGs

To determine whether the prodomain and 360 loop IDRs of MC1 are important for its translocation into SGs, we generated transgenic plants stably expressing GFP-tagged truncated versions lacking the prodomain (ΔNMC1) or the 360 loop (MC1Δ360) under the control of the 35S promoter in the *mc1* mutant background (*mc1 Pro35S::ΔNMC1-GFP* and *mc1 Pro35S::MC1Δ360-GFP*). We also included transgenic plants carrying a full-length version of MC1 with the catalytic cysteine in position 220 mutated to an alanine, which renders the protease inactive (*mc1 ProMC1::MC1CA-GFP*)(Fig S4A,D) (Coll *et al.*, 2010; Lema Asqui *et al.*, 2018) to determine whether the catalytic activity of MC1 was required for its SG targeting. Under basal conditions, all MC1 versions showed a diffused cytoplasmic localization (Fig. 4A). Except for ΔNMC1, all other MC1 variants also localized in the nucleus (Fig. 4A). As shown above (Fig. 1), heat stress (39 ºC for 40 min) resulted in the rapid recruitment of MC1 into cytoplasmic SGs. This stress-triggered re-localization was not altered in the catalytically inactive or the prodomain-less version of MC1, which indicates that neither its proteolytic activity nor the prodomain are required for recruitment of MC1 into SGs (Fig. 4A, B). In contrast, removal of the 360 loop drastically reduced the localization of MC1 into SGs upon heat stress (Fig. 4A, B), indicating that the 360 loop is important for the correct recruitment of MC1 into SG during heat stress.

To address the association dynamics of MC1 with SGs, we used fluorescence recovery after photobleaching (FRAP) analysis. Previously described components of SGs show different modes of recruitment and association with SGs. For instance, TSN2 stably associates with the core of SGs and fluorescence fails to recover after photobleaching, while RBP47 is highly dynamic and exchanges rapidly between SGs and the cytosol, resulting in a rapid fluorescence recovery in FRAP experiments (Fig4C, D; Van Treeck and Parker, 2019; Gutierrez-Beltran *et al.*, 2015). MC1-GFP fluorescence partially recovered after photobleaching (Fig. 4C, D), displaying a faster recovery than TSN2 but slower than RBP47, which indicates an intermediate core/periphery behavior of the protein. Moreover, mutation of the catalytic site of MC1 (*MC1CA-GFP*) did not alter its recovery rate after photobleaching, indicating that MC1 catalytic activity is not required for its recruitment into SGs. However, mutating the IDRs of MC1 significantly altered the recovery capacity of the protein. On one hand, the few *MC1Δ360-GFP* -containing SGs showed a higher recovery rate, compared to WT, which suggests that the 360 loop is important for the stable association of MC1 with SGs. (Fig. 4C, D).

In contrast, *ΔNMC1-GFP*-containing SGs showed slower recovery rate, indicating a potential role of this IDR in the dynamic association of MC1 with SGs. This notion was further supported by evidence showing that *ΔNMC1-GFP*-containing SGs did not disappear in the recovery phase after HS, in contrast to WT plants (Fig S5A, B). Altogether, these results show that MC1 dynamically associates with the SGs with an intermediate behavior between core and shell proteins. The MC1 360 loop is required for its stable recruitment into SGs while the prodomain might be necessary for its disassembly from SGs.

MC1 can specifically degrade aggregated proteins

Sustained stress or certain pathological conditions lead to the formation of protein associations or aggregates that, in contrast to SGs, are non-regulated and non-dynamic, having detrimental consequences for the cell, tissue and even at the organismal level (Morimoto, 2008). Indeed, SGs may have an important role in the pathogenesis of proteotoxicity-derived conditions, although their exact function remains to be elucidated (Marcelo *et al.*, 2021). Because MC1 is recruited to SGs and we previously observed that *mc1* knock-out mutant plants have increased accumulation of aggregated proteins (Coll *et al.*, 2014), we sought to understand whether its function may be linked to clearance of protein aggregates under stressful/pathological conditions.

First, we investigated whether Arabidopsis plants lacking MC1 show defects in protein aggregate clearance and survival after proteotoxic stress. To monitor changes in protein aggregation we used filter trap analysis, a robust method to detect and quantify protein aggregates, in 5-day-old WT and *mc1* seedlings after heat stress. Seedlings were subjected to 90’ of a moderate heat shock at 37 ºC, followed by 90’ of recovery at 22 ºC and a severe heat shock at 45 ºC for 90’. Samples were collected after 1 day of recovery at 22 ºC, using non-stressed seedlings as control. We analyzed accumulation of aggregated forms of actin, Hsp90 and proteins containing polyQ stretches, all of them shown to aggregate in Arabidopsis after heat stress (Llamas *et al.*, 2022). Under basal conditions, protein aggregates (actin, Hsp90-tagged or poly-Q-containing proteins) are barely detectable both in wild-type (WT) and *mc1* mutants, as they can be efficiently cleared by PQC mechanisms (Fig. 5A, S6A-D). Stresses such as heat shock result in a sudden overaccumulation of misfolded proteins that often surpasses the PQC capacity of the cell and results in protein aggregation detectable by filter trap (Fig. 5A). Plants lacking MC1 accumulated higher quantities of aggregated proteins than WT after proteotoxic stress, indicating a reduced capacity to manage protein aggregation and proteotoxic stress in the mutant. These overaccumulation of protein aggregates in *mc1* mutants did not affect their thermotolerance (Fig. S6A), possibly owing to the fact that the experiment was performed on very young plants to avoid age as an additive effect and these may be extremely proficient at dealing with protein aggregation.

Second, we assessed the capacity of MC1 to disassemble pathological protein aggregates *in vitro*. We co-incubated equimolar concentrations of rMC1 with aggregates of human transthyretin (TTR). TTR is a homotetrameric thyroxine transport protein in which tetramer dissociation events lead to aggregation (Westermark *et al.*, 1990; Quintas *et al.*, 2001). Extracellular insoluble deposits of TTR in several human organs give rise to distinct progressive and fatal clinical syndromes known as transthyretin amyloidosis (Goren, Steinberg and Farboody, 1980; Hou, Aguilar and Small, 2007; Rapezzi *et al.*, 2010). Using turbidity measurements to monitor protein aggregation, we observed that rMC1 treatment caused a 90 % reduction of TTR aggregates (Fig. 5B). This protein aggregate clearance activity was dependent on MC1 catalytic activity,

as evidenced by the absence of disaggregation in the catalytically dead mutant rMC1CA. Indeed, a threefold higher turbidity signal was observed in the rMC1CA-treated samples suggesting that inactive MC1 becomes aggregated when TTR insoluble assemblies are present in the reaction. Visual inspection of TTR samples by transmission electron microscopy (TEM) (Fig 5C) confirmed the disaggregation activity of MC1. The need of catalytic activity for disaggregation is consistent with the observation that aggregated TTR becomes significantly degraded in presence of rMC1 (lane 3), as demonstrated by SDS-PAGE (Fig 5 D). Noteworthy, rMC1 acts as a specific disaggregase, clearing protein aggregates but not the functional form of proteins, since it is unable to degrade soluble TTR in its native tetrameric state (nTTR) (Fig 5D lane 3 and 4 respectively). The obtained data indicate that rMC1 targets and disassembles specifically the aggregated and pathogenic form of TTR. Notably, this disaggregase activity towards TTR aggregates was not observed in samples incubated with MC4 (Fig 5B, D). We confirmed the activity of the protease by its rapid autoprocessing in the presence of calcium (Fig 5D lane 10), as previously described (Zhu *et al.*, 2020).

Finally, we tested the capacity of MC1 to degrade protein aggregates *in vivo*. To this end we used two well-established model systems: i) human embryonic kidney (HEK) cells expressing a polyQ-expanded Huntingtin form (Q74) that causes aggregation and proteotoxicity used as a proxy for the neurodegenerative Huntington's disease (Jimenez-Sanchez *et al.*, 2015) and ii) yeast expressing a constitutively misfolded carboxypeptidase (ΔssCPY∗) that forms insoluble protein aggregates upon stress (Park *et al.*, 2007). Co-expression of full-length MC1 with Q74 fused to mCherry in HEK cells resulted in a reduction of protein aggregates in comparison to expression of Q74 fused to mCherry alone, as demonstrated by filter trap analysis using anti-mCherry antibody (Fig. 5E, Fig. S6E). In yeast, we expressed ΔssCPY∗ fused to the prototrophic marker Leu2 and a C-terminal myc tag (ΔssCL∗) in wild type (WT), a mutant lacking the single metacaspase *MCA1* in yeast (*ymca1Δ*) and *ymca1Δ* complemented with a WT copy of the Arabidopsis MC1. All strains grew normally on control media (Fig. S6A, left panel), while on selective media lacking leucine WT yeast had reduced growth capacity due to degradation of misfolded ΔssCL∗ by PQC systems (Fig. S7A, right panel and S7B). In contrast and as previously shown, *ymca1Δ* was not able to degrade ΔssCL∗ and therefore could grow normally on a leucine-selective media (Hill *et al.*, 2014). This phenotype could be fully complemented by AtMC1, that due to its ability to degrade ΔssCL∗ restored yeast WT growth levels (Fig. S7A, right panel and S7B). Altogether, these data demonstrate that MC1 can degrade protein aggregates *in vitro* and *in vivo* and a lack of MC1 leads to abnormal protein aggregate accumulation under proteotoxic stress.

MC1 delays senescence

Based on all the evidence presented above demonstrating the recruitment of MC1 into stress granules and its aggregate clearing function, we hypothesized that overproduction of the protein in plants may minimize the effects of proteotoxic stress occurring during plant aging and contribute to fitness. Previously, we reported that the lack of MC1 led to early senescence in Arabidopsis (Coll *et al.*, 2014). Here, we confirmed these results using a dark-induced senescence assay and tested the effects of stably overexpressing wild-type full-length MC1 and its mutant variants (*MC1, MC1CA, MC1Δ360*) in a *mc1* mutant background. Individual leaves from 3-week-old plants were covered with aluminum foil and 8 days later they were uncovered to evaluate senescence visually and by means of chlorophyll quantification and photosynthetic efficiency. In uncovered leaves (basal conditions), all lines showed similar total chlorophyll levels and photosynthetic efficiency (Fig. 6B, D). Leaf senescence resulted in a drop in chlorophyll levels and photosynthetic activity in WT plants. In

contrast, plants overexpressing *MC1* displayed a clear delay in senescence (Fig. 6A), accompanied by higher chlorophyll levels (Fig. 6C) and higher photosynthetic activity than WT (Fig. 6E). Importantly, the protease catalytic activity of MC1 was required for the observed anti-aging phenotype, demonstrated by the accelerated senescence of transgenic plants expressing MC1CA (Fig. 6A-C). The 360 loop was also required for the delayed senescence observed in plants overexpressing MC1, as the *mc1* mutants expressing MC1Δ360 behaved like WT (Fig. 6A-E).

Discussion

SGs are membraneless organelles formed by LLPS under stress conditions and act both as storage compartments and microreactors where signaling takes place (Alberti and Carra, 2018). Their functionality inside healthy cells is linked to their ability to assemble and disassemble dynamically in response to changing environments (*i.e.* assembling upon stress perception and disassembling when the causative stress subdues). SGs contain a high proportion of proteins bearing IDRs/LCRs, which together with RNA, drive formation of the condensate but at the same time are extremely misfolding-/aggregation-prone. Therefore, they are closely surveilled by the PQC machinery. Reduced proteostasic capacity derived from aging and/or mutations affecting the phase-separation behavior of these proteins lead to chronic activation of integrated stress responses. This will eventually surpass the PQC capacity of the cell, resulting in the accumulation of misfolded and aggregated proteins and leading to the formation of persistent SGs, which are linked to disease (Wolozin, 2012; Wang *et al.*, 2022).

Sessile organisms such as plants cannot flee from extreme and prolonged stress situations, such as heat or drought. Therefore, they must be equipped with extremely efficient PQC mechanisms to deal with massive protein misfolding and aggregation. In fact, proteins containing aggregation-prone polyQ proteins are enriched in plants, but no polyQ pathologies have been reported, in contrast to animals (Llamas *et al.*, 2022). In this context, it has been recently shown that the chloroplasts could act as important protein-degradation machines to maintain proteostasis of polyQ-containing proteins (Llamas *et al.*, 2022). Plants may also respond to proteotoxic stress by actively regulating protein solubility and phase behavior, similar to yeast that can tolerate high levels of insoluble proteins and form solid-like condensates (Franzmann and Alberti, 2019). Insoluble proteins within these condensates, including SGs, may have evolved to become stress sensors serving an adaptive function (Franzmann and Alberti, 2019).

MC1 as a SG component

In this work we focus on the characterization of MC1, an Arabidopsis Type I metacaspase. MC1 was previously shown to participate in immunogenic cell death and aging, although its mode of action remained obscure (Coll *et al.*, 2010, 2014). Aging caused re-mobilization of MC1 from the soluble fraction to insoluble protein aggregates. Further, absence of MC1 caused overaccumulation of insoluble protein aggregates in aging cells, potentially leading to the observed accelerated senescence phenotype in *mc1* mutant plants. Aging, with its overall loss of proteostatic capacity, unveils mutant phenotypes linked to PQC failure that remain hidden in young cells due to their very efficient control of protein misfolding/aggregation. Thus, to investigate the role of MC1 in acute proteotoxic stress in cells with full proteostatic capacity, we use a simple, well-characterized system such as heat stress on young seedlings, which are still devoid of persistent or aberrant condensates that accumulate as a result of aging (Gutierrez-Beltran *et al.*, 2015; Kosmacz *et al.*,

2018, 2019). We showed that upon heat stress, MC1 re-localizes into distinct cytoplasmic puncta that disappear during the recovery phase after stress removal (Figs. 1A, B and S1). These puncta correspond to SGs based on their dynamics (Figs. 1A, B and 4C), sensibility to cycloheximide (Figs. 1C, D) and co-localization/co-immunoprecipitation with SG markers *in planta* (Fig.1E-F, S2) (Kosmacz *et al.*, 2019; Gutierrez-Beltran *et al.*, 2021).

Phase-separation often drives the formation of SGs (Alberti and Carra, 2018; Maruri-López *et al.*, 2021; Allen and Strader, 2022). The main features of proteins that form membraneless compartments such as SGs through LLPS are i) presence of IDRs, ii) complex domain organization and iii) their marginal solubility in the cell (Alberti and Carra, 2018). MC1 is predicted to encompass two main IDR regions in its amino acid sequence, one coinciding with the N-terminal prodomain and the second near the C-terminus, known as the 360 loop (van Midden, Peric and Klemenčič, 2021) (Fig. 2A). Further, these two regions are predicted to be highly insoluble and aggregation prone, in particular the 360 loop (Fig. 2B). In agreement with this prediction, MC1 became soluble only when both the prodomain and the 360 loop were simultaneously removed (Fig. 3). Interestingly, the highly hydrophobic 360 loop is only present in plant Type I metacaspases (van Midden, Peric and Klemenčič, 2021). Type I metacaspases from protozoa and fungi do not possess this domain and accordingly, they are soluble *in vitro* and they can be readily purified without removal of any domain (Lee *et al.*, 2010; McLuskey *et al.*, 2012).

In this regard, our data show that the 360 loop mediates MC1 recruitment into SGs during heat stress, as demonstrated by the drastic reduction in MC1-containing SGs formed in the 360 loopless mutant (Fig. 4). In contrast, in mutants lacking the prodomain SGs are still formed upon heat stress. However, these granules are less dynamic, showing reduced recovery after photobleaching (Fig. 4). This may indicate that the prodomain is involved in SG clearance. Considering that the prodomain has been proposed to act as a negative regulator of Type I MCs activity, based on structural, as well as genetic data (Lee *et al.*, 2010; McLuskey *et al.*, 2012), it is then tempting to speculate that the prodomain contains certain amino acids or motifs that may mediate recognition and degradation of MC1 by granulostasis, which has been shown to involve chaperone-mediated PQC, autophagy or the ubiquitin-proteasome system (Alberti and Carra, 2018). Interestingly, maize MC1 has been shown to form puncta and co-localize with autophagosomes after heat stress when transiently expressed in *Nicotiana benthamiana* (Luan *et al.*, 2021), indicating that autophagy may be a possible degradation route for MC1-containing SGs as shown for other aggregation-prone proteins (Munch *et al.*, 2014; Jung *et al.*, 2020).

MC1 can specifically clear protein aggregates

From previous work in yeast (Lee *et al.*, 2010; Hill *et al.*, 2014) and plants (Coll *et al.*, 2014) it was unclear how MC1 contributes to aggregate clearance. Work with the yeast metacaspase yMCA1 showed that upon heat stress and aging, the protein re-localizes to PQC condensates known as JUNQ (juxtanuclear quality control compartment) and IPOD (insoluble protein deposit) (Hill *et al.*, 2014). In plants, we demonstrate here that MC1 is recruited to SGs upon heat stress, but what is its function and how is it connected to aggregate clearance? First, we showed that mutants lacking MC1 accumulated higher levels of aggregate-prone aggregated proteins, such as polyQ-containing, HSP90 or actin, than WT plants under basal condition, a phenotype exacerbated after applying heat stress (Fig. 5A). Second, MC1 exhibited a strong and

evolutionarily conserved capacity to degrade protein aggregates, as shown in various well-established systems *in vitro* (human protein) and *in vivo* (yeast and human cells) (Sant'Anna *et al.*, 2016; Koyuncu *et al.*, 2018; Llamas *et al.*, 2022) (Figs. 5, S5, S6). In particular, recombinant MC1 showed an extraordinary capacity to clear aggregated TTR, a pathological form of the protein that causes a diversity of life-threatening pathologies (Saelices *et al.*, 2015). MC1 proteolysis of TTR was prodomain- and 360 loop-independent, but dependent on its catalytic activity. In fact, mutation of the catalytic cysteine in MC1 resulted in increased insolubility and self-aggregation of the protein, indicating a marked change in its biophysical properties.

MC1 proteolytic activity was specifically directed towards aggregated forms of the protein, since monomeric TTR was not processed by MC1 (Fig. 5D). The protein aggregate-targeted behavior of MC1 could potentially be due to its slow kinetics. MC1 is an active protease, as shown by its ability to self-cleave and cleave its inhibitor Serpin *in vivo* (Lema Asqui *et al.*, 2018) and *in vitro* (Fig. S4A). Here we show that in addition to that, recombinant MC1 can cleave metacaspase-specific synthetic substrates *in vitro* in the presence of calcium and neutral pH (Fig. S4B, C). However, compared to Arabidopsis Type II metacaspases, MC1 displays slower and/or less efficient protease activity towards typical metacaspase substrates (Vercammen *et al.*, 2004; Hander *et al.*, 2019; Zhu *et al.*, 2020). We hypothesize that precisely this slower kinetics may favor its disaggregase activity, rather than a quicker protein processing activity that could cleave monomeric forms of TTR. Notwithstanding, this newly discovered function of MC1 may inspire further research on protein disaggregases as an avenue for therapeutic intervention in age-related protein-misfolding diseases.

Anti-aging role of MC1: physiological implications of the role of MC1 in protein aggregate clearance

In previous work we showed that plants lacking MC1 displayed accelerated senescence, which has been confirmed here using a different senescence-inducing system (Fig. 6A, Coll *et al.*, 2014). Beyond that, here we present data demonstrating that overexpression of MC1 delays leaf senescence (Fig. 6A). The onset of senescence triggers the formation of cytoplasmic MC1-containing puncta that could also correspond to SGs (Fig. S6). Mutation of the conserved MC1 catalytic cysteine or removal of the 360 loop abolishes the observed senescence delay caused by overexpression of the protein. This indicates that MC1 proteolytic activity as well as its recruitment into SGs may be involved in this anti-aging function of the protein. This pro-life function of MC1 is evolutionarily conserved, as overexpression of yeast *MC1* can also extend replicative lifespan, a function partly dependent on the presence of an intact catalytic cysteine and attributed to a role in protein aggregate management as part of PQC (Hill *et al.*, 2014).

An interesting question is why altering the levels of MC1 in knock-out mutants or overexpressing lines did not result in an obvious phenotypic effect compared to WT in response to heat (Fig. S6), such as the one observed during senescence. A plausible explanation coming from the animal field is that young individuals/tissues/cells, have multiple and very active misfolded protein clearance mechanisms, which can efficiently manage proteotoxicity ensued from stress situations, such as heat stress, even in the presence of mutations affecting PQC. In contrast, old individuals/tissues/cells experience a global decrease in proteostasis, uncovering the effect of mutations affecting PQC, which is the causative ground of many age-associated protein-misfolding diseases that have a late onset in life (Alberti and Hyman, 2021).

All considered, a plausible hypothesis is the following (Fig. 7): i) proteotoxic stress, such as heat stress, triggers the formation of SGs; ii) MC1 is recruited to SGs via the 360 loop; iii) once there, MC1 participates in protein clearance via its proteolytic activity to help dissolving the granules. In favor of this hypothesis, removal of the catalytic cysteine of MC1 does not affect recruitment into SGs, but it alters aggregate clearance.

Materials and Methods

Materials used and growth conditions

All experiments were performed using *Arabidopsis thaliana* Columbia-0 (Col-0) ecotype. Lines used for this work are listed in Table S1. The single mutant *mc1* has been previously described (GK-096A10; Coll *et al.*, 2010). All seeds were surface-sterilized with 35% NaClO for 5 min and washed five times for 5 min with sterile dH_2O. Sterile seeds were sown in solid ½ Murashige and Skoog (MS) medium with vitamins and stratified 48 h at 4 °C. Plants were grown vertically under long day (LD) conditions (16-h light/8-h dark) at 22 ºC. For dark-induced senescence studies, one-week-old seedlings were transferred into soil and grown for an additional 2 weeks under LD conditions.

The following transgenic lines in *mc1* background were used for SG visualization and dark-senescence studies: *Pro35S::MC1-GFP*, *ProMC1::MC1C220A-GFP*, *Pro35S::ΔNMC1-GFP*, *Pro35S::MC1Δ360loop-GFP, ProMC1::MC1-GFP* and *ProMC1::MC1C220A-GFP* (Table S1). Additionally, transgenic *Col-0* lines expressing *Pro35S::GFP-TCTP* (Gutierrez-Beltran *et al.*, 2021) or both *Pro35S::GFP-TCTP* and *Pro35S::MC1-RFP* were used for SG colocalization experiments.

Plasmid construction

All constructs and primers used in this study are described in Tables S2 and S3, respectively. To generate *Pro35S::MC1-GFP*, *Pro35S::MC1-RFP*, *Pro35S::ΔNMC1-GFP*, *Pro35S::MC1Δ360loop-GFP*, *ProMC1:MC1-GFP*, *ProMC1:MC1C220A-GFP* constructs, the coding sequence and native promoter (approximately 1kb) of Arabidopsis *MC1* (*AT1G02170*) were amplified from Col-0 cDNA and genomic DNA, respectively. Plasmids were assembled through GreenGate cloning (Lampropoulos *et al.*, 2013). To generate *Pro35S::RFP-RBP47* and *Pro35S::RFP-TSN2,* the coding sequence of RBP47 and ADH2 were amplified from *Col-0* cDNA and cloned into pGWB655 following the Gateway strategy (Karimi, Inzé and Depicker, 2002).

For purification of recombinant MC1 (rMC1), the MC1 coding sequence lacking the 360 loop and with or without the prodomain (MC1Δ360 or ΔNMC1Δ360/rMC1) (Fig. 2) were synthesized (Twist Bioscience) with codon optimization for expression in *Escherichia coli*. Synthetic sequences contained NdeI and XhoI restriction sites at the 5´and 3´ends of the sequence, respectively. Both synthetic genes and destination vector pET28 b(+) were cut with NdeI and XhoI and subsequently ligated so that an N-terminal 6xHis tag precedes the start site of the MC1 variants. QuickChange Site-Directed Mutagenesis (Agilent Technologies) was used to cause point mutations in the catalytic site of rMC1.

To complement the yeast metacaspase mutant strain *ymca1Δ* with Arabidopsis MC1 (AT1G02170), we constructed a gene replacement cassette by PCR-directed homologous recombination (Gardner and Jaspersen, 2014). The cassette consisted of three fragments: 1) yeast 5'flanked with N-acetyltransferase

(NAT) resistance gene and a GPD (glyceraldehyde-3-phosphate dehydrogenase) constitutive promoter, 2) Arabidopsis *MC1* gene fused to a C-terminal HA tag, 3) 3' flanking of the yeast *yMCA1* gene. These three fragments were PCR-amplified and fused into the final recombinant DNA by using the double-joint PCR method as previously described (Yu *et al.*, 2004). The resulting DNA product (*NATNT2:pGPD::AtMC1-HA*) was transformed into *the ymca1Δ* mutant strain KanMX4.

Protoplasts and plant transformation

Arabidopsis protoplasts were obtained as previously described (Truskina *et al.*, 2020). In short, leaves from three-week-old plants were collected and digested in an enzyme solution (1% cellulose R10, 0.25% macerozyme R10, 0.4 M mannitol, 10 mM $CaCl_2$, 20 mM KCl, 0.1% BSA, 20 mM MES at pH 5.7) for 1 or 2 hours. Protoplasts were collected through a 70-micron strainer, washed twice with ice-cold W5 solution (154 mM NaCl, 125 mM $CaCl_2$, 5 mM KCl, 5 mM glucose, 2 mM MES at pH 5.7) and incubated on ice for 30 min. The protoplasts were then resuspended in MMG solution (0.4 M mannitol, 15 mM MgCl2, 4 mM MES at pH 5.7) at a final concentration of 2,5 x 10^5 cells per ml. To transform the protoplasts, 30 µg of the appropriate plasmid were mixed with 200 µl of protoplast solution. Immediately, 210 µl of PEG solution (40% PEG 4000, 0.2 M mannitol, 0.1 M $CaCl_2$) was added and the protoplasts were incubated for 5 min at room temperature and then washed twice in W5 solution. The protoplasts were resuspended in 500 µl of the W5 solution and incubated for 24 h in 16 h light/8 h dark growth chamber. Before imaging, the protoplasts were incubated at 39 ºC for 40 minutes in a hot air incubator.

Arabidopsis plants were transformed as described previously through the *Agrobacterium tumefaciens*-mediated floral-dip method (Clough and Bent, 1998) .

HEK293T cells transfection and protein extraction

The *MC1* (*AT1G02170*) gene was codon-optimized for expression in animal cells and synthetized (Twist Bioscience). To generate *ProCMV::GFP-MC1*, the synthetic gene was cloned in the pDEST-CMV-N-GFP vector by Gateway technology (Addgene). *ProCMV::mRFP-Q74* (Balaji *et al.*, 2022)*, ProCMV::GFP-MC1* and *ProCMV::GFP* (Llamas *et al.*, 2022) were used for transfection of HEK cells (CRL-1573) (Table S5) following the protocol described in (Llamas *et al.*, 2022). After 72 h of incubation, cells were lysed in non-denaturing native lysis (300 mM NaCl, 100 mM Hepes pH 7.4, 2 mM EDTA, 2% Triton X-100) supplemented with 1X plant protease inhibitor (Merck), scraped from the tissue culture plates, and homogenized through a syringe needle (27G). Samples were centrifuged at 10,000 x g for 10 min at 4 °C and supernatant was collected. Protein concentration was determined with the Pierce BCA Protein Assay Kit (Thermo Fisher).

Yeast strains and spot dilution assays

Yeast media preparation and molecular biology techniques were carried out using standard methods (Lázaro-Silva *et al.*, 2015). All experiments were done using the genetic background of *Saccharomyces cerevisiae* strain BY4741 (Table S4). To test the capacity of each yeast strain to remove misfolded proteins, yeast cells were transformed with the plasmid pFE15 encoding the fusion construct ΔssCL∗myc (Table S2, Eisele and Wolf, 2008). Growth phenotypes were assessed with spot dilution assays. Ten-fold serial dilutions were made, ranging from undiluted to a 10^4 dilution. Five µl of each dilution were spotted onto the corresponding selective media (-ura or -ura -leu plates) and plates were incubated for at least 3 days before images were taken.

Microscopy analysis

Microscopy images were acquired with an Olympus FV1000 inverted confocal microscope with a x60/water objective. For detection of fluorescent signals, GFP was excited at 488nm and mRFP at 543nm.

Root meristem cells from 5-day-old seedlings vertically grown under long day (LD) conditions (16-h light/8-h dark) at 22 ºC were used to determine protein subcellular localization. For heat stress treatment, 5-day-old seedlings were transferred to a hot air incubator at 39 ºC and incubated for 40 min. For CHX treatment, 5-day-old seedlings were incubated in ½ MS liquid medium with 200 ng/µl CHX for 30 min. The number of granules were quantified with ImageJ.

Fluorescence recovery after photobleaching (FRAP)

The assay was performed as described previously (Moschou *et al.*, 2013). Five-day-old seedlings grown vertically in LD conditions were incubated for 40 min at 39 ºC in a hot air incubator. During analyses, the Olympus FV1000 software was set up for the acquisition of two pre-bleach images, one bleach scan and 30 post-bleach scans. A region of 2 µm of diameter was bleached using a laser intensity of 100% at 488nm. Prebleach and post-bleach scans were at the minimum possible laser power. A zoom factor of 5 was used.

Analyses of fluorescence intensities during FRAP were performed in the bleached regions. One region of interest outside of the bleached area was also measured to serve as the background. The background values were subtracted from the fluorescence recovery values, and the resulting values were normalized by the first post-bleach time point. Initial signal recovery (%) = 100 × (Ifinal,post-bleach - Iinitial,post-bleach)/(Iprebleach - Iinitial,post-bleach), where I is the normalized signal intensity (relative to the background intensity).

Protein purification

E. coli OverExpress C41 (DE3) Chemically Competent Cells from BioCat GmbH (Heidelberg, Germany) or *E.coli* BL21 strain containing the pBB542 vector (de Marco *et al.*, 2007) were transformed with expression plasmids and grown in either autoinduction media or LB, respectively. Cells were grown first at 37 ºC with continuous shaking until OD_{600} reached 0.6 and then transferred to 25 ºC for overnight growth. In the case of expression in *E. coli* Chaperone Competent Cells BL21, Isopropyl β-D-1-thiogalactopyranoside (IPTG) at 1 mM concentration was added to 400 ml cell cultures when transferred to 25 ºC to induce protein expression. The pellet from overnight cultures was resuspended in 20 mM HEPES, pH 7.5, 500 mM NaCl and sonicated on ice. A centrifugation of lysates at 25,000 x g for 20 min was performed to remove cell debris and insoluble proteins. Soluble lysate was filtered through 0.45 µM sterile filters and loaded into a 5 mL nickel ion HisTrap purification column (Cytiva, Marlborough, MA, USA). Washes of the columns were performed with 20 mM HEPES, pH 7.5, 500 mM NaCl and 20 mM imidazole. Elution of proteins was performed by increasing imidazole concentrations up to 250 mM. The cleanest elutions were concentrated using Amicon filters and loaded onto a Superdex 75 size-exclusion chromatography column (GE Healthcare Life Sciences, Chicago, IL, USA) connected to an AKTA FPLC system. The Superdex 75 column was equilibrated in 20 mM HEPES, pH 7.5, 500 mM NaCl. A flow rate of 0.75 ml per minute was used to separate proteins. Samples belonging to the most prominent peaks were kept and loaded onto an SDS-PAGE gel to verify the purity of the samples. MC4 was provided by F. van Breusegem and it is described in Vercammen *et al.*, 2004.

Enzymatic activity assays

Protease activity was measured by quantification of the fluorescence intensity released from the AMC (7-amino-4-methylcoumarin) group of the fluorogenic substrate Z-FR-AMC (PeptaNova, Sandhausen, Germany) at 383 nm and 455 nm excitation and emission wavelengths, respectively, in a Tecan Infinite M200 Microplate Reader System (Männedorf, Switzerland). All proteolytic assays were performed in 20 mM HEPES (pH 7.0) containing 150 mM NaCl, varying $CaCl_2$ concentrations and 5 mM DTT. For estimation of pH optima, buffers containing 100 mM acetate (pH 4–pH 5.5), 100 mM MES (pH 6–pH 6.5), 100 mM HEPES (pH 7.0–pH 8.0), 100 mM Tris (pH 8.5–pH 9) and 100 mM CAPS (pH 9.5–pH 11) were used. 0.2 µg of recombinant protease was used and the concentration of fluorogenic substrates was 5 µM.

Preparation of TTR aggregates

TTR was expressed and purified following previously described procedures (Pinheiro *et al.*, 2021). Briefly, TTR aggregation was induced by mixing 7 µM of purified TTR with an equal volume of 400 mM sodium acetate, 200 mM KCl, pH 4.4, obtaining a final TTR concentration of 3.5 µM. Samples were incubated for 72 h at 37 ºC in quiescent conditions. Aggregated samples were centrifuged at 20,000 x g for 1 h to recover the insoluble material that was subsequently resuspended in 20 mM HEPES 150 mM, NaCl pH 7.5 to a concentration of 100 µM.

***In vitro* disaggregation assay**

End-point disaggregation reactions were performed by coincubating TTR aggregates at a concentration of 7 µM with 0.25 mg mL-1 of protease at 37 ºC in presence of 5 mM DTT and 5 mM $CaCl_2$. Protease disaggregation was monitored using sample turbidity, SDS-PAGE and transmission electron microscopy.

Turbidity assay

Sample turbidity was monitored as an indicator of the amount of aggregated material using synchronous light scattering. The spectra were recorded in a JASCO Spectrofluorometer FP-8200 with an excitation wavelength of 360 nm, and emission range from 340 to 380 nm. Excitation and emission bandwidth were set to 5 nm. The light scattered at 360 nm was used as a measure of turbidity.

Protein extraction and immunoblotting

Five hundred milligrams of leaf material were mixed with 2 ml of extraction buffer (50 Mm HEPES pH 7.3, 150 mM NaCl, 0.5% Nonidet P-40, 10% glycerol, 1 mM EDTA pH 8, 5 mM DTT, 1% PVPP and 1× Protease inhibitor cocktail (Sigma, P599)) and centrifuged for 10 min at 14,000 x g at 4 ºC. 5× Laemmli sample buffer was added to 100 µl supernatant and boiled for 5 min. Equal amounts of supernatant were loaded on 12% SDS-PAGE gels. Antibodies used for immunoblotting were as follows: α-GFP-HRP (1:5,000 Milteny Biotec), α-RFP-HRP (1:5,000 Abcam), α-myc (1:10,000, Sigma-Aldrich, α-actin (dilution 1:5,000, Agrisera), α-Hsp90-1 (1:2,000 Abcam) and α-polyQ (1:1,000 Merck).

Filter trap assay

Protein extracts were obtained with native lysis buffer (300 mM NaCl, 100 mM HEPES pH 7.4, 2 mM EDTA, 2% Triton X-100) supplemented with EDTA-free protease inhibitor cocktail. When processing plant protein

extracts 1X plant protease inhibitor (Merck) was added to native lysis buffer. In experiments with HEK cells, cells were homogenized by passing 7 times through syringe needle (27 G). Cellular debris was removed by several centrifugation steps at 8,000 x g for 10 min at 4 °C. Supernatant was recollected and protein concentration determined with the Pierce BCA Protein Assay Kit (Thermo Fisher). A cellulose acetate membrane filter (GE Healthcare Life Sciences) was placed in a slot blot apparatus (Bio-Rad) coupled to a vacuum system. The membrane was equilibrated with 3 washes with equilibration buffer (native buffer supplemented with 0.5% SDS). Approximately 150 µg of protein extract was supplemented with SDS at a final concentration of 0.5% and loaded and filtered through the membrane. Then, the membrane was washed three times with 0.2% SDS. The membrane was blocked in 3% BSA in TBST for 30 min followed by 3 washes with TBST. The membrane was incubated with indicated antibody and then washed 3 times for 5 min and incubate with secondary antibodies in TBST 3% BSA for 30 min. The membrane was developed using an Odissey DLx (Licor). Extracts were also analyzed by SDS-PAGE and western blotting to determine loading controls.

Heat treatments

Thermotolerance assays were performed using 5-day-old seedlings. Seedlings were grown at 22 °C for 5 days, put in a hot-air incubator set at 37 ºC for 90 min, put in a growth chamber set at 37 ºC for 90 min, incubated at 45 ºC for 90 min and allowed to recover at 22 ºC for 8 days. The percentages of seedlings in different phenotypic classes were calculated based on results from three biological replicates. In each biological replicate, at least 50 seedlings were used for each genotype.

Dark-induced senescence assay

Leaves number 5 and 6 of three-week-old plants grown in LD conditions were covered with aluminium foil for 8 days (Li *et al.*, 2016). Control plants kept without covered leaves were grown in parallel.

Chlorophyll analysis

Covered and uncovered leaves from 3 different plants were snap-frozen in liquid nitrogen and ground with TissueLyser II (QIAGEN). A 50 mg aliquot of crushed leaf material was mixed with 1.5 ml of 80% pre-chilled acetone and thoroughly mixed for 5 min. Samples were centrifuged at 20,000 g for 1 min and the supernatant was transferred to spectrophotometer cuvettes. Chlorophyll was then quantified at 663nm and 646nm with a spectrophotometer UV-2600, Shimadzu) as previously described (Lichtenthaler and Wellburn, 1983).

PAM fluorometric measurements

After 30 min of dark adaptation, the kinetics of chlorophyll fluorescence in whole rosettes were monitored by measuring F0 in the dark and Fm with initial saturation pulse using Imaging PAM M-series, MAXI version device (Walz). Fv/Fm and Fv´/Fm´ (PSII efficiency) ratio for the maximum quantum efficiency upon dark and light conditions was calculated according to the manufacturer's instructions.

Bioinformatic analyses

Intrinsically disordered regions of MC1 were predicted using the D2P2 database (D^2P^2, http://d2p2.pro/, Oates *et al.*, 2013) and DISOPRED3 (http://bioinf.cs.ucl.uk/psipred, Jones and Cozzetto, 2015). LLPS predisposition was evaluated using the PSPredictor tool (http://www.pkumdl.cn:8000/PSPredictor/, Chu *et al.*, 2022)

Analysis of the aggregation propensity of MC1 amino acids was performed with Aggrescan3D (http://biocomp.chem.uw.edu.pl/A3D/; Zambrano *et al.*, 2015) using as input file the Alphafold2 (https://alphafold.ebi.ac.uk/, Jumper *et al.*, 2021) predicted MC1 structure.

Statistical analysis

All quantification analyses and statistical tests were performed with R software. T-test was used to compare the significance of differences between two experimental groups. For comparing the significance of differences between multiple experimental groups, one-way ANOVA was performed as indicated in each experiment. Different letters show statistically significant differences between samples.

Accession Numbers

Sequence data for the genes described in this study can be found in the TAIR database (https://www.arabidopsis.org) and NCBI under the following accession numbers: *MC1* (*AT1G02170*), *RBP47* (*AT3G19130*), *TCTP* (*AT3G16640*) and *yMCA1* (*Q08601*).

Supplemental Data files

Table S1. Arabidopsis lines used in this study.

Table S2. List of plasmids used in this study.

Table S3. List of primers and synthetic sequences used in this study for genotyping and cloning.

Table S4. Yeast strains used in this study.

Table S5. Other materials used in this study.

Table S6. Table for statistical analysis

Figure S1. MC1-GFP expressed under the control of its own promoter re-localizes to cytoplasmic condensates upon heat stress.

Figure S2. MC1 co-localizes with stress granule markers in protoplasts upon heat stress.

Figure S3. Production and purification of recombinant MC1 in *Escherichia coli* cells.

Figure S4. rMC1 is a proteolytically active enzyme and behaves as a canonical Type I metacaspase.

Figure S5. The MC1 prodomain contributes to SG clearance.

Figure S6. *mc1* knock-out mutants do not display thermotolerance or total protein accumulation differences compared to WT.

Figure S7. MC1 participates in the clearance of terminally misfolded proteins.

Figure S8. Dark-induced senescence results in the formation of MC1-containing cytoplasmic condensates.

Acknowledgements

Thanks to F. van Breusegem for providing MC4 recombinant protein and I. Rubio-Somoza for providing us with plasmids pGGD-RBCSt (D-F) and pGGD-UBQt (D-F) and the members of the Microscopy Services of the UAB for their assistance. Research at CRAG was supported by grants PID2019-108595RB-I00 funded by MCIN/AEI/10.13039/501100011033 and AGL2016-78002-R funded by MCIN/AEI/10.13039/501100011033 and by ‘‘ERDF A way of making Europe’’ (to N.S.C. and M.V.); fellowship BES-2017-080210 funded by MCIN/AEI/10.13039/501100011033 and by ‘‘ESF Investing in your future’’ (to J.S.-L.); FPU19/03778 funded by MU (o Ministerio de Universidades) (to N.R.-S.); by the ‘‘Severo Ochoa Programme for Centres of Excellence in R&D’’ (SEV-2015-0533 and CEX2019-000902-S funded by

MCIN/AEI/10.13039/501100011033); by the grant PID2020-119737GA-I00 funded by the Ministerio de Ciencia e Innovacion (MCIN/AEI/10.13039/501100011033) (to E.G.-B); by the Spanish Ministry of Science and Innovation (MICINN) grant PID2019-105017RB-I00 (to S.V.), by ICREA, ICREA-Academia 2020 (to S.V); by the MICINN fellowship (FPU17/01157) (to J.S.); and by the CERCA Programme/Generalitat de Catalunya. L.A. is supported by a Maria Zambrano postdoctoral fellowship by de Ministerio de Universidades and the European Union - NextGenerationEU. This work was also funded by the Deutsche Forschungsgemeinschaft (DFG) Germany's Excellence Strategy (CECAD, EXC 2030-390661388 to D.V. and CEPAS EXC-2048/1–390686111 to E.L.) and the Else Kröner-Fresenius-Stiftung (2021-EKSE.95) (to D.V.). We also acknowledge support from COST Actions PROTEOSTASIS (BM1307) and ProteoCure (CA20113), supported by COST (European Cooperation in Science and Technology) (N.R.-S., U.P., L.L. and N.S.C. We acknowledge support of the publication fee by the CSIC Open Access Publication Support Initiative through its Unit of Information Resources for Research (URICI).

Author contribution

N.R.-S. and N.S.C. conceived the study; N.R.-S., J.S.-L., L.A. and N.S.C. designed experiments; N.R.-S., J.S.-L., L.A., I.P., J.S., K.P.v.M., U.J.P., S.K., J.B.-B., L.L., C.P., F.E., A.M.B.-E., E.L. and S.M.H. performed the experiments, E.G.-B. provided essential material; N.R.-S., J.S.-L., L.A., I.P., J.S. and K.P.v.M., analyzed the data; T.N., M.V., D.V., M.K., S.V. and N.S.C. supervised the work; N.R.-S. and N.S.C. wrote the manuscript with comments from J.S.-L., L.A., I. P., K.P.v.M., U.J.P., S.K., F.E., E.G.-B., M.V., E.L., D.V., S.V. All authors reviewed the manuscript.

Declaration of Interests

The authors declare no competing interests.

References

Alberti, S. and Carra, S. (2018) 'Quality Control of Membraneless Organelles', *Journal of Molecular Biology*, 430(23), pp. 4711–4729. Available at: https://doi.org/10.1016/j.jmb.2018.05.013.

Alberti, S., Gladfelter, A. and Mittag, T. (2019) 'Considerations and Challenges in Studying Liquid-Liquid Phase Separation and Biomolecular Condensates', *Cell*, 176(3), pp. 419–434. Available at: https://doi.org/10.1016/j.cell.2018.12.035.

Alberti, S. and Hyman, A.A. (2021) 'Biomolecular condensates at the nexus of cellular stress, protein aggregation disease and ageing', *Nature Reviews Molecular Cell Biology*, 22(3), pp. 196–213. Available at: https://doi.org/10.1038/s41580-020-00326-6.

Allen, J.R. and Strader, L.C. (2022) 'Beating the heat: Phase separation in plant stress granules', *Developmental Cell*, 57(5), pp. 563–565. Available at: https://doi.org/10.1016/J.DEVCEL.2022.02.012.

Babinchak, W.M. and Surewicz, W.K. (2020) 'Liquid-Liquid Phase Separation and Its Mechanistic Role in Pathological Protein Aggregation', *Journal of molecular biology*, 432(7), pp. 1910–1925. Available at: https://doi.org/10.1016/J.JMB.2020.03.004.

Balaji, V. *et al.* (2022) 'A dimer-monomer switch controls CHIP-dependent substrate ubiquitylation and processing', *Molecular cell*, 82(17), pp. 3239-3254.e11. Available at:

https://doi.org/10.1016/J.MOLCEL.2022.08.003.

Baradaran-Heravi, Y., Van Broeckhoven, C. and van der Zee, J. (2020) 'Stress granule mediated protein aggregation and underlying gene defects in the FTD-ALS spectrum', *Neurobiology of disease*, 134. Available at: https://doi.org/10.1016/J.NBD.2019.104639.

Buchan, J.R. and Parker, R. (2009) 'Eukaryotic stress granules: the ins and outs of translation', *Molecular cell*, 36(6), pp. 932–941. Available at: https://doi.org/10.1016/J.MOLCEL.2009.11.020.

Chu, X. *et al.* (2022) 'Prediction of liquid–liquid phase separating proteins using machine learning', *BMC Bioinformatics*, 23(1), pp. 1–13. Available at: https://doi.org/10.1186/S12859-022-04599-W/FIGURES/5.

Clough, S.J. and Bent, A.F. (1998) 'Floral dip: a simplified method for Agrobacterium-mediated transformation of Arabidopsis thaliana', *The Plant journal : for cell and molecular biology*, 16(6), pp. 735–743. Available at: https://doi.org/10.1046/J.1365-313X.1998.00343.X.

Coll, N.S. *et al.* (2010) 'Arabidopsis type I metacaspases control cell death', *Science*, 330(6009), pp. 1393–1397. Available at: https://doi.org/10.1126/SCIENCE.1194980/SUPPL_FILE/COLL.SOM.PDF.

Coll, N.S. *et al.* (2014) 'The plant metacaspase AtMC1 in pathogen-triggered programmed cell death and aging: functional linkage with autophagy', *Cell Death and Differentiation*, 21(9), p. 1399. Available at: https://doi.org/10.1038/CDD.2014.50.

Eisele, F. and Wolf, D.H. (2008) 'Degradation of misfolded protein in the cytoplasm is mediated by the ubiquitin ligase Ubr1', *FEBS letters*, 582(30), pp. 4143–4146. Available at: https://doi.org/10.1016/J.FEBSLET.2008.11.015.

Franzmann, T.M. and Alberti, S. (2019) 'Protein Phase Separation as a Stress Survival Strategy', *Cold Spring Harbor perspectives in biology*, 11(6). Available at: https://doi.org/10.1101/CSHPERSPECT.A034058.

Gardner, J.M. and Jaspersen, S.L. (2014) 'Manipulating the yeast genome: deletion, mutation, and tagging by PCR', *Methods in molecular biology (Clifton, N.J.)*, 1205, pp. 45–78. Available at: https://doi.org/10.1007/978-1-4939-1363-3_5.

Gonzalez-Garcia, M.-P. *et al.* (2011) 'Brassinosteroids control meristem size by promoting cell cycle progression in Arabidopsis roots', *Development*, 138(5), pp. 849–859. Available at: https://doi.org/10.1242/dev.057331.

Goren, H., Steinberg, M.C. and Farboody, G.H. (1980) 'Familial oculoleptomeningeal amyloidosis', *Brain : a journal of neurology*, 103(3), pp. 473–495. Available at: https://doi.org/10.1093/BRAIN/103.3.473.

Guillén-Boixet, J. *et al.* (2020) 'RNA-Induced Conformational Switching and Clustering of G3BP Drive Stress Granule Assembly by Condensation', *Cell*, 181(2), pp. 346-361.e17. Available at: https://doi.org/10.1016/J.CELL.2020.03.049/ATTACHMENT/4A66A2D6-41BF-46CF-BE60-045CAC185392/MMC2.ZIP.

Gutierrez-Beltran, E. *et al.* (2015) 'Tudor Staphylococcal Nuclease Links Formation of Stress Granules and Processing Bodies with mRNA Catabolism in Arabidopsis', *The Plant Cell*, 27(3), pp. 926–943. Available at: https://doi.org/10.1105/TPC.114.134494.

Gutierrez-Beltran, E. *et al.* (2021) ' Tudor staphylococcal nuclease is a docking platform for stress granule components and is essential for SnRK1 activation in Arabidopsis ', *The EMBO Journal*, 40(17), pp. 1–21. Available at: https://doi.org/10.15252/embj.2020105043.

Hander, T. *et al.* (2019) 'Damage on plants activates Ca2+-dependent metacaspases for release of

immunomodulatory peptides', *Science (New York, N.Y.)*, 363(6433). Available at: https://doi.org/10.1126/SCIENCE.AAR7486.

Hill, S.M. *et al.* (2014) 'Life-span extension by a metacaspase in the yeast Saccharomyces cerevisiae', *Science*, 344(6190), pp. 1389–1392. Available at: https://doi.org/10.1126/science.1252634.

Hipp, M.S., Kasturi, P. and Hartl, F.U. (2019) 'The proteostasis network and its decline in ageing', *Nature reviews. Molecular cell biology*, 20(7), pp. 421–435. Available at: https://doi.org/10.1038/S41580-019-0101-Y.

Hou, X., Aguilar, M.I. and Small, D.H. (2007) 'Transthyretin and familial amyloidotic polyneuropathy', *The FEBS Journal*, 274(7), pp. 1637–1650. Available at: https://doi.org/10.1111/J.1742-4658.2007.05712.X.

Jain, S. *et al.* (2016) 'ATPase-Modulated Stress Granules Contain a Diverse Proteome and Substructure', *Cell*, 164(3), pp. 487–498. Available at: https://doi.org/10.1016/J.CELL.2015.12.038.

Jimenez-Sanchez, M. *et al.* (2015) 'siRNA screen identifies QPCT as a druggable target for Huntington's disease.', *Nature Chemical Biology*, 11(5), pp. 347–354. Available at: https://doi.org/10.1038/NCHEMBIO.1790.

Jones, D.T. and Cozzetto, D. (2015) 'DISOPRED3: precise disordered region predictions with annotated protein-binding activity', *Bioinformatics*, 31(6), p. 857. Available at: https://doi.org/10.1093/BIOINFORMATICS/BTU744.

Jumper, J. *et al.* (2021) 'Highly accurate protein structure prediction with AlphaFold', *Nature 2021 596:7873*, 596(7873), pp. 583–589. Available at: https://doi.org/10.1038/s41586-021-03819-2.

Jung, H. *et al.* (2020) 'Arabidopsis cargo receptor NBR1 mediates selective autophagy of defective proteins', *Journal of Experimental Botany*, 71(1), pp. 73–89. Available at: https://doi.org/10.1093/JXB/ERZ404.

Karimi, M., Inzé, D. and Depicker, A. (2002) 'GATEWAY vectors for Agrobacterium-mediated plant transformation', *Trends in plant science*, 7(5), pp. 193–195. Available at: https://doi.org/10.1016/S1360-1385(02)02251-3.

Klemenčič, M. and Funk, C. (2019) 'Evolution and structural diversity of metacaspases', *Journal of experimental botany*, 70(7), pp. 2039–2047. Available at: https://doi.org/10.1093/JXB/ERZ082.

Kosmacz, M. *et al.* (2018) 'Interaction of 2',3'-cAMP with Rbp47b Plays a Role in Stress Granule Formation', *Plant physiology*, 177(1), pp. 411–421. Available at: https://doi.org/10.1104/pp.18.00285.

Kosmacz, M. *et al.* (2019) 'Protein and metabolite composition of Arabidopsis stress granules', *New Phytologist*, 222(3), pp. 1420–1433. Available at: https://doi.org/10.1111/NPH.15690.

Koyuncu, S. *et al.* (2018) 'The ubiquitin ligase UBR5 suppresses proteostasis collapse in pluripotent stem cells from Huntington's disease patients', *Nature Communications*, 9(1). Available at: https://doi.org/10.1038/S41467-018-05320-3.

Lampropoulos, A. *et al.* (2013) 'GreenGate - A Novel, Versatile, and Efficient Cloning System for Plant Transgenesis', *PLoS ONE*, 8(12), p. 83043. Available at: https://doi.org/10.1371/JOURNAL.PONE.0083043.

Lázaro-Silva, D.N. *et al.* (2015) 'The Use of DNA Extraction for Molecular Biology and Biotechnology Training: A Practical and Alternative Approach', *Creative Education*, 6(8), pp. 762–772. Available at: https://doi.org/10.4236/CE.2015.68079.

Lee, N. *et al.* (2007) 'Characterization of Metacaspases with Trypsin-Like Activity and Their Putative Role in Programmed Cell Death in the Protozoan Parasite Leishmania', *Eukaryotic Cell*, 6(10), p. 1745.

Available at: https://doi.org/10.1128/EC.00123-07.

Lee, R.E.C. *et al.* (2010) 'Metacaspase Yca1 is required for clearance of insoluble protein aggregates', *Proceedings of the National Academy of Sciences of the United States of America*, 107(30), pp. 13348–13353. Available at: https://doi.org/10.1073/PNAS.1006610107/SUPPL_FILE/PNAS.201006610SI.PDF.

Lema Asqui, S. *et al.* (2018) 'AtSERPIN1 is an inhibitor of the metacaspase AtMC1-mediated cell death and autocatalytic processing in planta', *The New phytologist*, 218(3), pp. 1156–1166. Available at: https://doi.org/10.1111/NPH.14446.

Li, L. *et al.* (2016) 'Characterization of a novel β-barrel protein (AtOM47) from the mitochondrial outer membrane of Arabidopsis thaliana', *Journal of experimental botany*, 67(21), pp. 6061–6075. Available at: https://doi.org/10.1093/JXB/ERW366.

Lichtenthaler, H.K. and Wellburn, A.R. (1983) 'Determinations of total carotenoids and chlorophylls a and b of leaf extracts in different solvents', *Biochemical Society Transactions*, 11(5), pp. 591–592. Available at: https://doi.org/10.1042/BST0110591.

Llamas, E. *et al.* (2022) 'Chloroplast protein import determines plant proteostasis and retrograde signaling', *bioRxiv*, p. 2022.03.19.484971. Available at: https://www.biorxiv.org/content/10.1101/2022.03.19.484971v1%0Ahttps://www.biorxiv.org/content/10.1101/2022.03.19.484971v1.abstract.

Lorković, Z.J. *et al.* (2000) 'RBP45 and RBP47, two oligouridylate-specific hnRNP-like proteins interacting with poly(A)+ RNA in nuclei of plant cells', *RNA (New York, N.Y.)*, 6(11), pp. 1610–1624. Available at: https://doi.org/10.1017/S1355838200001163.

Luan, Q.L. *et al.* (2021) 'Maize metacaspases modulate the defense response mediated by the NLR protein Rp1-D21 likely by affecting its subcellular localization', *Plant Journal*, 105(1), pp. 151–166. Available at: https://doi.org/10.1111/tpj.15047.

Marcelo, A. *et al.* (2021) 'Stress granules, RNA-binding proteins and polyglutamine diseases: too much aggregation?', *Cell Death & Disease 2021 12:6*, 12(6), pp. 1–17. Available at: https://doi.org/10.1038/s41419-021-03873-8.

de Marco, A. *et al.* (2007) 'Chaperone-based procedure to increase yields of soluble recombinant proteins produced in E. coli', *BMC Biotechnology*, 7, p. 32. Available at: https://doi.org/10.1186/1472-6750-7-32.

Markmiller, S. *et al.* (2018) 'Context-Dependent and Disease-Specific Diversity in Protein Interactions within Stress Granules', *Cell*, 172(3), pp. 590-604.e13. Available at: https://doi.org/10.1016/J.CELL.2017.12.032.

Marondedze, C. *et al.* (2020) 'Drought Stress Causes Specific Changes to the Spliceosome and Stress Granule Components', *Frontiers in Molecular Biosciences*, 6, p. 163. Available at: https://doi.org/10.3389/FMOLB.2019.00163/BIBTEX.

Maruri-López, I. *et al.* (2021) 'Plant Stress Granules: Trends and Beyond', *Frontiers in Plant Science*, 12(August), pp. 1–16. Available at: https://doi.org/10.3389/fpls.2021.722643.

McLuskey, K. *et al.* (2012) 'Crystal structure of a Trypanosoma brucei metacaspase', *Proceedings of the National Academy of Sciences of the United States of America*, 109(19), pp. 7469–7474. Available at: https://doi.org/10.1073/PNAS.1200885109.

van Midden, K.P., Peric, T. and Klemenčič, M. (2021) 'Plant type I metacaspases are proteolytically active

proteases despite their hydrophobic nature', *FEBS Letters*, 595(17), pp. 2237–2247. Available at: https://doi.org/10.1002/1873-3468.14165.

Minina, E.A. *et al.* (2020) 'Classification and Nomenclature of Metacaspases and Paracaspases: No More Confusion with Caspases', *Molecular cell*, 77(5), pp. 927–929. Available at: https://doi.org/10.1016/J.MOLCEL.2019.12.020.

Morimoto, R.I. (2008) 'Proteotoxic stress and inducible chaperone networks in neurodegenerative disease and aging', *Genes & development*, 22(11), pp. 1427–1438. Available at: https://doi.org/10.1101/GAD.1657108.

Moschou, P.N. *et al.* (2013) 'The Caspase-Related Protease Separase (EXTRA SPINDLE POLES) Regulates Cell Polarity and Cytokinesis in Arabidopsis', *The Plant Cell*, 25(6), p. 2171. Available at: https://doi.org/10.1105/TPC.113.113043.

Munch, D. *et al.* (2014) 'Autophagy deficiency leads to accumulation of ubiquitinated proteins, ER stress, and cell death in Arabidopsis', *Autophagy*, 10(9), pp. 1579–1587. Available at: https://doi.org/10.4161/AUTO.29406.

Niewidok, B. *et al.* (2018) 'Single-molecule imaging reveals dynamic biphasic partition of RNA-binding proteins in stress granules', *The Journal of cell biology*, 217(4), pp. 1303–1318. Available at: https://doi.org/10.1083/JCB.201709007.

Oates, M.E. *et al.* (2013) 'D^2P^2: database of disordered protein predictions', *Nucleic acids research*, 41(Database issue). Available at: https://doi.org/10.1093/NAR/GKS1226.

Park, S.H. *et al.* (2007) 'The cytoplasmic Hsp70 chaperone machinery subjects misfolded and endoplasmic reticulum import-incompetent proteins to degradation via the ubiquitin-proteasome system', *Molecular Biology of the Cell*, 18(1), pp. 153–165. Available at: https://doi.org/10.1091/MBC.E06-04-0338/ASSET/IMAGES/LARGE/ZMK0010779040010.JPEG.

Pinheiro, F. *et al.* (2021) 'Tolcapone, a potent aggregation inhibitor for the treatment of familial leptomeningeal amyloidosis', *The FEBS Journal*, 288(1), pp. 310–324. Available at: https://doi.org/10.1111/FEBS.15339.

Pitsili, E. *et al.* (2022) 'A phloem-localized Arabidopsis metacaspase (AtMC3) improves drought tolerance', *bioRxiv*, p. 2022.11.09.515759. Available at: https://doi.org/10.1101/2022.11.09.515759.

Posey, A.E., Holehouse, A.S. and Pappu, R. V. (2018) 'Phase Separation of Intrinsically Disordered Proteins', *Methods in Enzymology*, 611, pp. 1–30. Available at: https://doi.org/10.1016/BS.MIE.2018.09.035.

Protter, D.S.W. and Parker, R. (2016) 'Principles and Properties of Stress granules', *Trends in cell biology*, 26(9), p. 668. Available at: https://doi.org/10.1016/J.TCB.2016.05.004.

Quintas, A. *et al.* (2001) 'Tetramer dissociation and monomer partial unfolding precedes protofibril formation in amyloidogenic transthyretin variants', *The Journal of biological chemistry*, 276(29), pp. 27207–27213. Available at: https://doi.org/10.1074/JBC.M101024200.

Rapezzi, C. *et al.* (2010) 'Transthyretin-related amyloidoses and the heart: a clinical overview', *Nature reviews. Cardiology*, 7(7), pp. 398–408. Available at: https://doi.org/10.1038/NRCARDIO.2010.67.

Roberts, M. *et al.* (2013) 'Genetic requirements for signaling from an autoactive plant NB-LRR intracellular innate immune receptor', *PLoS genetics*, 9(4). Available at: https://doi.org/10.1371/JOURNAL.PGEN.1003465.

Saelices, L. *et al.* (2015) 'Uncovering the Mechanism of Aggregation of Human Transthyretin', *The Journal of Biological Chemistry*, 290(48), p. 28932. Available at: https://doi.org/10.1074/JBC.M115.659912.

Sanchez, I.I. *et al.* (2021) 'Huntington's disease mice and human brain tissue exhibit increased G3BP1 granules and TDP43 mislocalization', *The Journal of clinical investigation*, 131(12). Available at: https://doi.org/10.1172/JCI140723.

Sant'Anna, R. *et al.* (2016) 'Repositioning tolcapone as a potent inhibitor of transthyretin amyloidogenesis and associated cellular toxicity', *Nature communications*, 7. Available at: https://doi.org/10.1038/NCOMMS10787.

Schmit, J.D., Feric, M. and Dundr, M. (2021) 'How Hierarchical Interactions Make Membraneless Organelles Tick Like Clockwork', *Trends in Biochemical Sciences*, 46(7), pp. 525–534. Available at: https://doi.org/10.1016/j.tibs.2020.12.011.

Sorenson, R. and Bailey-Serres, J. (2014) 'Selective mRNA sequestration by OLIGOURIDYLATEBINDING PROTEIN 1 contributes to translational control during hypoxia in Arabidopsis', *Proceedings of the National Academy of Sciences of the United States of America*, 111(6), pp. 2373–2378. Available at: https://doi.org/10.1073/PNAS.1314851111/SUPPL_FILE/SM04.MP4.

Van Treeck, B. and Parker, R. (2019) 'Principles of Stress Granules Revealed by Imaging Approaches', *Cold Spring Harbor Perspectives in Biology*, 11(2). Available at: https://doi.org/10.1101/CSHPERSPECT.A033068.

Truskina, J. *et al.* (2020) 'A network of transcriptional repressors modulates auxin responses', *Nature 2020 589:7840*, 589(7840), pp. 116–119. Available at: https://doi.org/10.1038/s41586-020-2940-2.

Uren, A. *et al.* (2000) 'Identification of paracaspases and metacaspases: two ancient families of caspase-like proteins, one of which plays a key role in MALT lymphoma', *Molecular cell*, 6(4), pp. 961–967. Available at: https://doi.org/10.1016/S1097-2765(00)00094-0.

Vercammen, D. *et al.* (2004) 'Type II metacaspases Atmc4 and Atmc9 of Arabidopsis thaliana cleave substrates after arginine and lysine', *The Journal of biological chemistry*, 279(44), pp. 45329–45336. Available at: https://doi.org/10.1074/JBC.M406329200.

Vilchez, D., Saez, I. and Dillin, A. (2014) 'The role of protein clearance mechanisms in organismal ageing and age-related diseases', *Nature Communications 2014 5:1*, 5(1), pp. 1–13. Available at: https://doi.org/10.1038/ncomms6659.

Wang, J. *et al.* (2022) 'Pathophysiology of stress granules: An emerging link to diseases (Review)', *International Journal of Molecular Medicine*, 49(4). Available at: https://doi.org/10.3892/IJMM.2022.5099.

Wang, S. *et al.* (2021) 'AtMC1 Associates With LSM4 to Regulate Plant Immunity Through Modulating Pre-mRNA Splicing', *Molecular plant-microbe interactions : MPMI*, 34(12), pp. 1423–1432. Available at: https://doi.org/10.1094/MPMI-07-21-0197-R.

Weber, C., Nover, L. and Fauth, M. (2008) 'Plant stress granules and mRNA processing bodies are distinct from heat stress granules', *The Plant journal : for cell and molecular biology*, 56(4), pp. 517–530. Available at: https://doi.org/10.1111/J.1365-313X.2008.03623.X.

Westermark, P. *et al.* (1990) 'Fibril in senile systemic amyloidosis is derived from normal transthyretin.', *Proceedings of the National Academy of Sciences*, 87(7), pp. 2843–2845. Available at: https://doi.org/10.1073/PNAS.87.7.2843.

Wolozin, B. (2012) 'Regulated protein aggregation: stress granules and neurodegeneration', *Molecular neurodegeneration*, 7(1). Available at: https://doi.org/10.1186/1750-1326-7-56.

Wong, A.H.H., Yan, C. and Shi, Y. (2012) 'Crystal Structure of the Yeast Metacaspase Yca1', *The Journal of*

Biological Chemistry, 287(35), p. 29251. Available at: https://doi.org/10.1074/JBC.M112.381806.

Yan, C. *et al.* (2014) 'Tudor-SN, a component of stress granules, regulates growth under salt stress by modulating GA20ox3 mRNA levels in Arabidopsis', *Journal of experimental botany*, 65(20), pp. 5933–5944. Available at: https://doi.org/10.1093/JXB/ERU334.

Youn, J.Y. *et al.* (2019) 'Properties of Stress Granule and P-Body Proteomes', *Molecular cell*, 76(2), pp. 286–294. Available at: https://doi.org/10.1016/J.MOLCEL.2019.09.014.

Yu, J.H. *et al.* (2004) 'Double-joint PCR: a PCR-based molecular tool for gene manipulations in filamentous fungi', *Fungal genetics and biology : FG & B*, 41(11), pp. 973–981. Available at: https://doi.org/10.1016/J.FGB.2004.08.001.

Zambrano, R. *et al.* (2015) 'AGGRESCAN3D (A3D): server for prediction of aggregation properties of protein structures', *Nucleic Acids Research*, 43(W1), pp. W306–W313. Available at: https://doi.org/10.1093/NAR/GKV359.

Zhu, P. *et al.* (2020) 'Structural basis for Ca2+-dependent activation of a plant metacaspase', *Nature communications*, 11(1). Available at: https://doi.org/10.1038/S41467-020-15830-8.

MAIN FIGURES

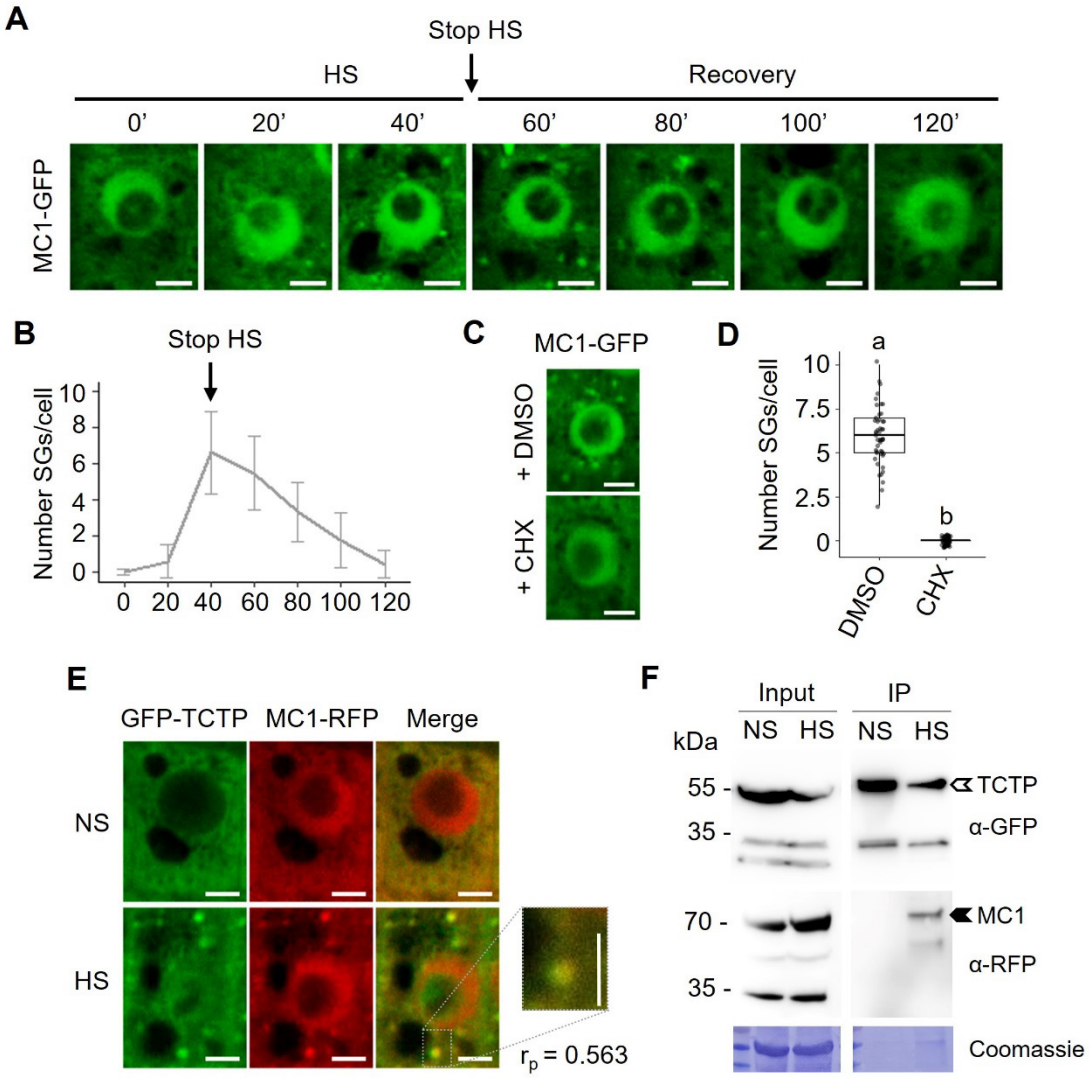

Figure 1. MC1 is recruited to stress granules (SGs) upon heat stress.

A. Five-day-old *mc1* Arabidopsis seedlings expressing *Pro35S::MC1-GFP* were heat-stressed at 39 ºC for 40 min (heat shock, HS), followed by incubation at 22 ºC for up to 120 min (Recovery). Images of root tips were taken at indicated time points. Bars = 5 µm.

B. Kinetics of the assembly and disassembly of MC1 cytoplasmic foci. Graph shows means ± sd of three independent experiments, each including 5 seedlings. Eight to 10 cells for each seedling were analyzed for SG quantification. "Stop HS" corresponds to the time point when plants were transferred from 39 °C to 22 ºC.

C. Treatment with cycloheximide (CHX) inhibits the formation of MC1 foci in root tip cells. For CHX treatment, five-day-old seedlings expressing *Pro35S::MC1-GFP* were incubated with 200 ng/µl CHX for 30 min at 22 °C before HS. Images show localization of MC1-GFP in heat-stressed (39 °C for 40 min) root tip cells of 5-day-old seedlings previously treated with CHX or DMSO (control).

D. Quantification of MC1-GFP foci in the experiment shown in C. Upper and lower box boundaries represent the first and third quantiles, respectively; horizontal lines mark the median and whiskers mark the highest and lowest values. Three independent experiments, each containing at least five individual measurements, were performed. Means with different letters are significantly different at $P < 0.05$ (one-way ANOVA).

E. Co-localization of GFP-TCTP (green) with MC1-RFP (red) in heat-stressed (39°C for 40 min) root tip cells of 5-day-old seedlings expressing both *Pro35S::GFP-TCTP* and *Pro35S::MC1-RFP*. Inset show enlarged boxed areas. Pearson coefficient (r_P) of co-localization of GFP-TCTP and MC1-RFP represents the mean of five replicate measurements from three independent experiments. Scale bars = 5 µm.

F. Immunoprecipitation (IP) of GFP-TCTP and MC1-RFP in protein extracts prepared from leaves of 3-week-old transgenic Arabidopsis seedlings expressing both *Pro35S::GFP-TCTP* and *Pro35S::MC1-RFP*. Samples were kept in control (NS) conditions or heat-stressed (HS, 39°C for 40 min). Input and IP fractions were analyzed by immunoblotting using α-GFP or α-RFP.

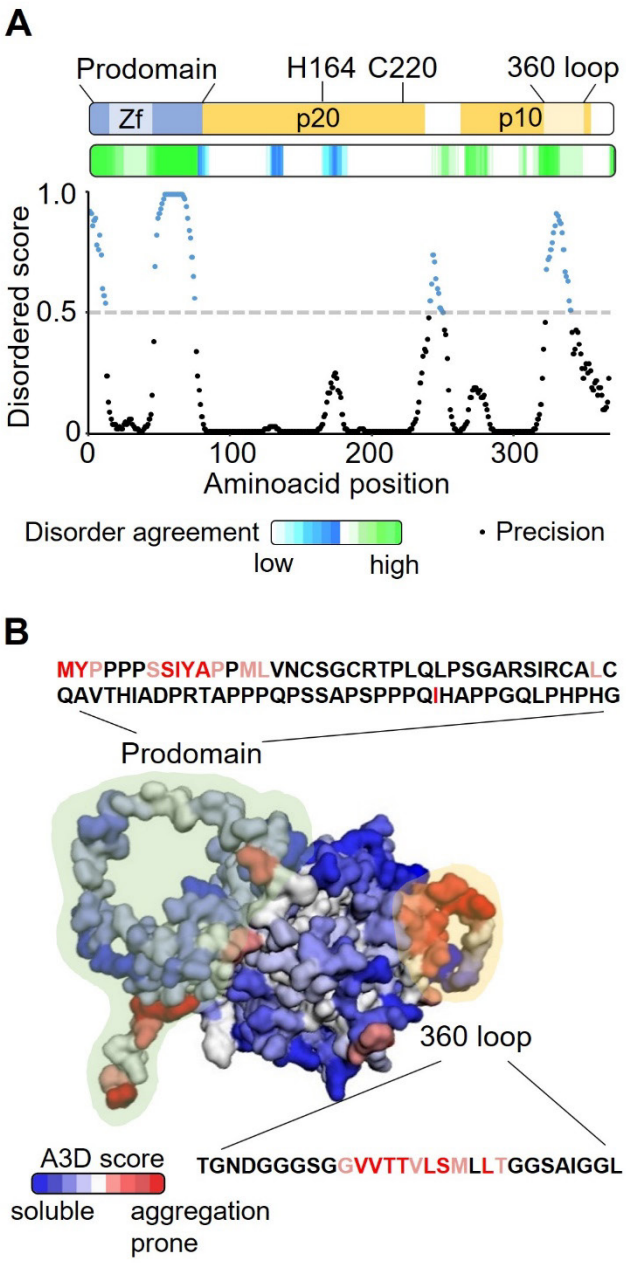

Figure 2. MC1 contains intrinsically disordered and aggregation-prone regions.

A. Prediction of intrinsically disordered regions of MC1. Top, scheme of MC1 protein structure. Zf: LSD1-Zinc finger domain within the prodomain (amino acids 1-77); H164 and C220 correspond to the amino acids of the catalytic dyad within the large p20 catalytic subunit; 360 loop (amino acids 318-346): hydrophobic loop within the small p10 catalytic subunit. Middle and Bottom, prediction of the disordered regions by D^2P^2 (https://d2p2.pro) and DISOPRED3 (http://bioinf.cs.ucl.ac.uk/psipred), respectively. Blue precision dots, show disordered scores higher than 0.5 and black precision dots disordered scores lower than 0.5.

B. Aggrescan 3D structure of MC1. The prodomain is highlighted in light green and the 360 loop in light yellow. The amino acid sequences are of the prodomain and 360 loop are shown and the amino acids with high A3D scores (agreggation-prone) are highlighted in red colors.

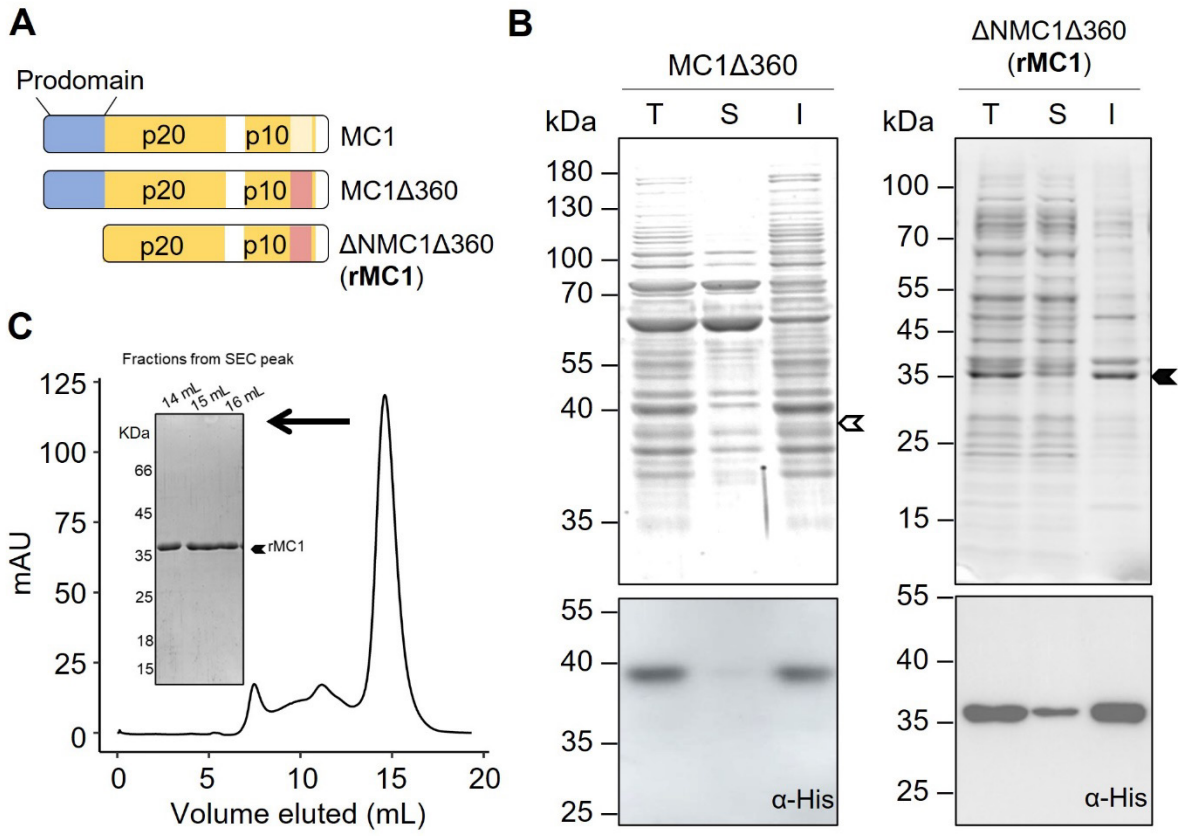

Figure 3. The prodomain and the 360 loop confer insolubility to MC1.

A. Schematic representation of MC1 full length, MC1Δ360 (without 360 loop) and ΔNMC1Δ360 (without prodomain and 360 loop) domain architecture. The region highlighted in red denotes absence of 360 loop (Δ360).

B. SDS-PAGE coomassie-stained gels (upper panels) and western blot analysis (lower panels) of lysates from total, soluble or insoluble fractions of *E. coli* cells expressing either MC1Δ360 or ΔNMC1Δ360 (rMC1) carrying an N-terminal 6xHis tag. Arrow denotes expected molecular weight of each of the two MC1 variants.

C. Size-exclusion chromatography of concentrated eluates obtained by nickel affinity chromatography (Fig. S3A). The inlet shows an SDS-PAGE Coomassie-stained gel of fractions 14ml to 16 mL of the eluted volume from a Superdex 75 column.

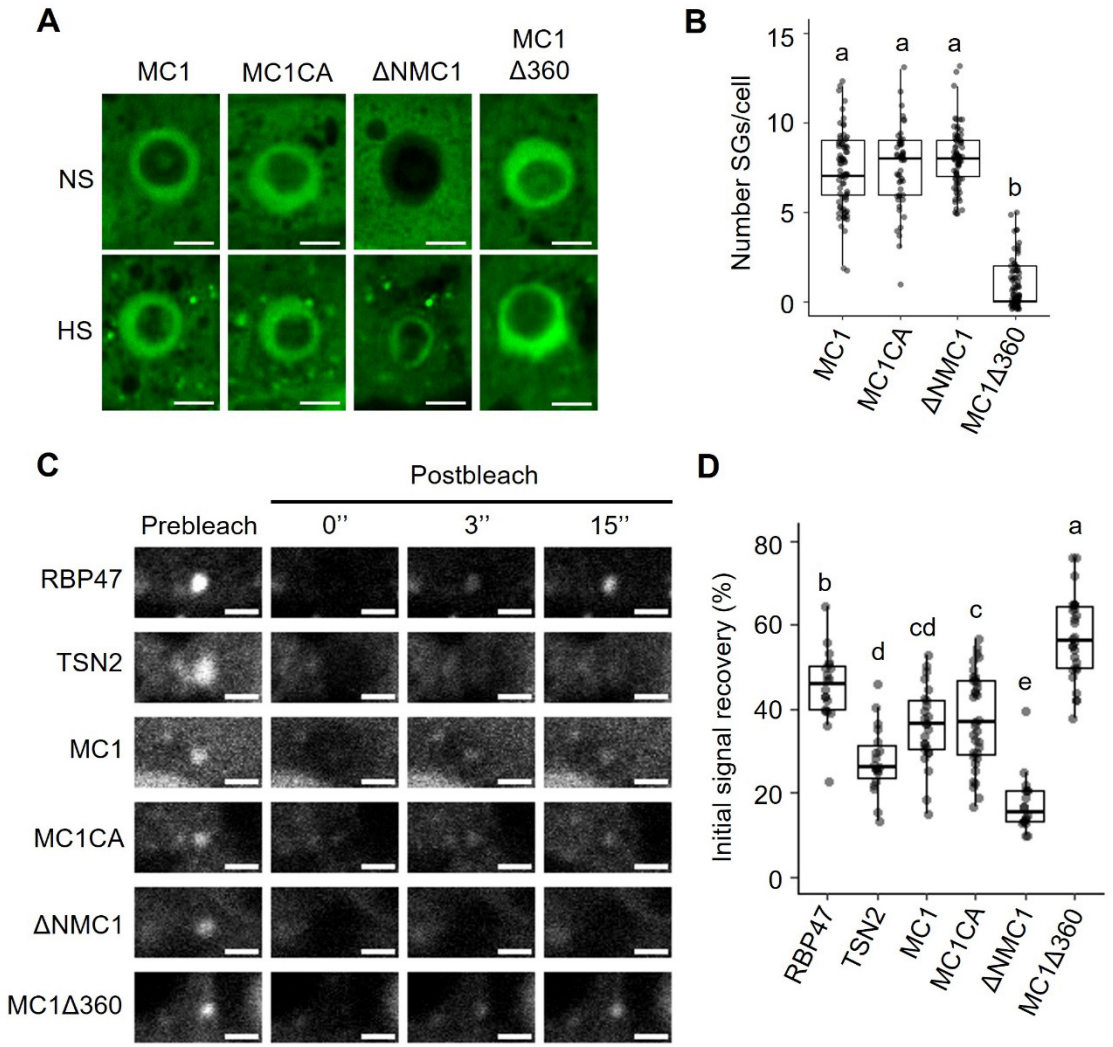

Figure 4. The 360 loop and the prodomain of MC1 are involved, respectively, in recruitment to and clearance from SGs.

A. Five-day-old *mc1* seedlings expressing *Pro35S::MC1-GFP, Pro35S::MC1C220A-GFP*, *Pro35S::ΔNMC1-GFP* or *Pro35S::MC1Δ360loop-GFP* were heat-stressed at 39ºC for 40 min. Images of root tips show seedlings in basal (NS) and stress conditions (HS). Bars = 5 µm.

B. Quantification of condensates in the experiment shown in A.

C. Selected time frames (prebleach and 0, 3, and 15 seconds after bleaching) from FRAP analysis of GFP-Rbp47, TSN2-GFP, MC1-GFP, MC1C220A-GFP, ΔNMC1-GFP and MC1Δ360loop-GFP foci formed upon heat stress (40 min at 39°C) in root tip cells of seedlings expressing *Pro35S::GFP*-Rbp47, *ProTSN2::TSN2*-GFP, *Pro35S::MC1-GFP*, *Pro35S::MC1C220A-GFP*, *Pro35S::ΔNMC1-GFP* or *Pro35S::MC1Δ360loop-GFP*, respectively. Bars = 2µm.

D. Initial signal recovery (%) of the experiment shown in C.

In B and D, upper and lower box boundaries represent the first and third quantiles, respectively; horizontal lines mark the median and whiskers mark the highest and lowest values. Three independent experiments, each containing at least five individual measurements, were performed. Means with different letters are significantly different at $P < 0.05$ (one-way ANOVA).

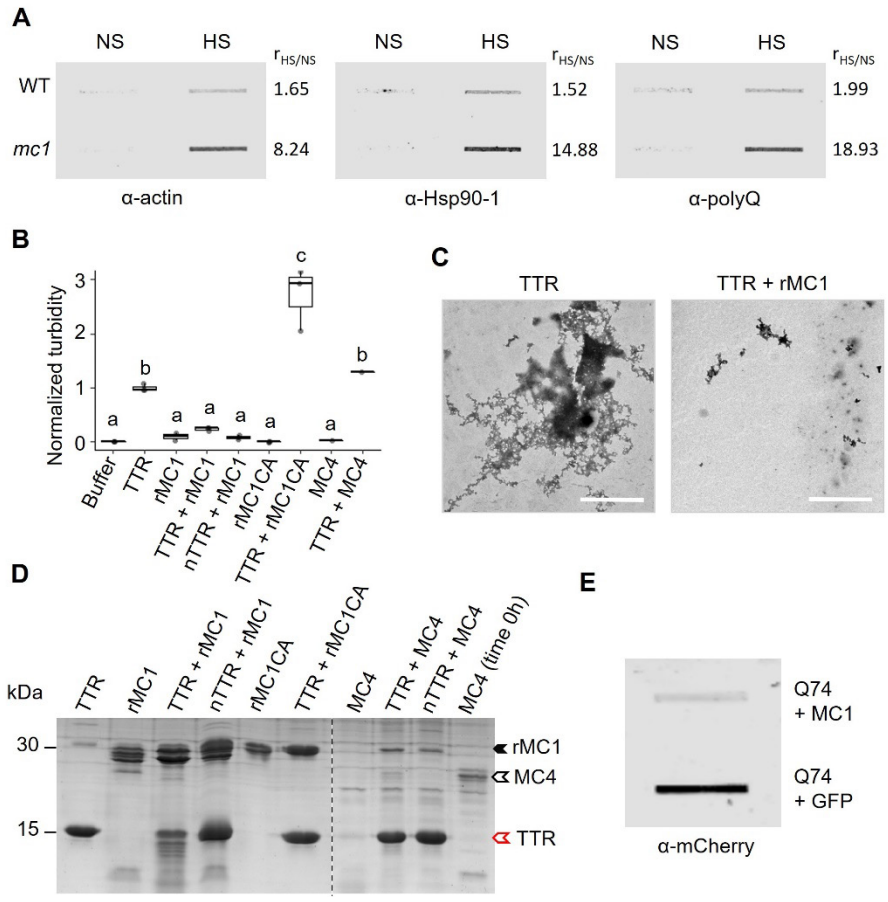

Figure 5. MC1 can specifically clear protein aggregates *in vitro* and *in vivo* and the lack of MC1 results in protein aggregate accumulation.

A. Filter trap analysis of protein extracts from five-day-old *Arabidopsis mc1* or WT seedlings in control conditions (NS) or subjected to a severe heat stress (HS, 90 min at 37 ºC, 90 min at 22 ºC and 90 min at 45 ºC). SDS resistant aggregates were detected using antibodies against actin, HSP90-1 or polyQ proteins. $r_{HS/NS}$ represents the ratio between HS and NS protein levels. Signal intensity of the bands was quantified using Image J. Two independent experiments were performed with similar results.

B. Turbidity assays of end-point disaggregation reactions using light scattering at 360 nm. rMC1 or the catalytic inactive form rMC1C220A (rMC1CA) were co-incubated with TTR aggregates or native tetrameric TTR for 24 hours at 37ºC. Recombinant MC1 proteins and TTR aggregates, incubated for the same period were also measured as controls. Data represents three individual measurements. Upper and lower box boundaries represent the first and third quantiles, respectively; horizontal lines mark the median and whiskers mark the highest and lowest values. Means with different letters are significantly different at $P < 0.05$ (one-way ANOVA).

C. Electron microscopy images of end-point disaggregation reactions of TTR aggregates incubated with or without purified rMC1 for 24 hours at 37 ºC.

D. SDS-PAGE analysis of the end-point samples shown in panel C.

E. Filter trap analysis showing mRFP-Q74 aggregation levels in HEK293 cells. HEK293 cells were transfected with mRFP-Q74 and GFP-MC1 or mRFP-Q74 and GFP as a control. mCherry antibody was used to detect Q74 SDS-resistant aggregates.

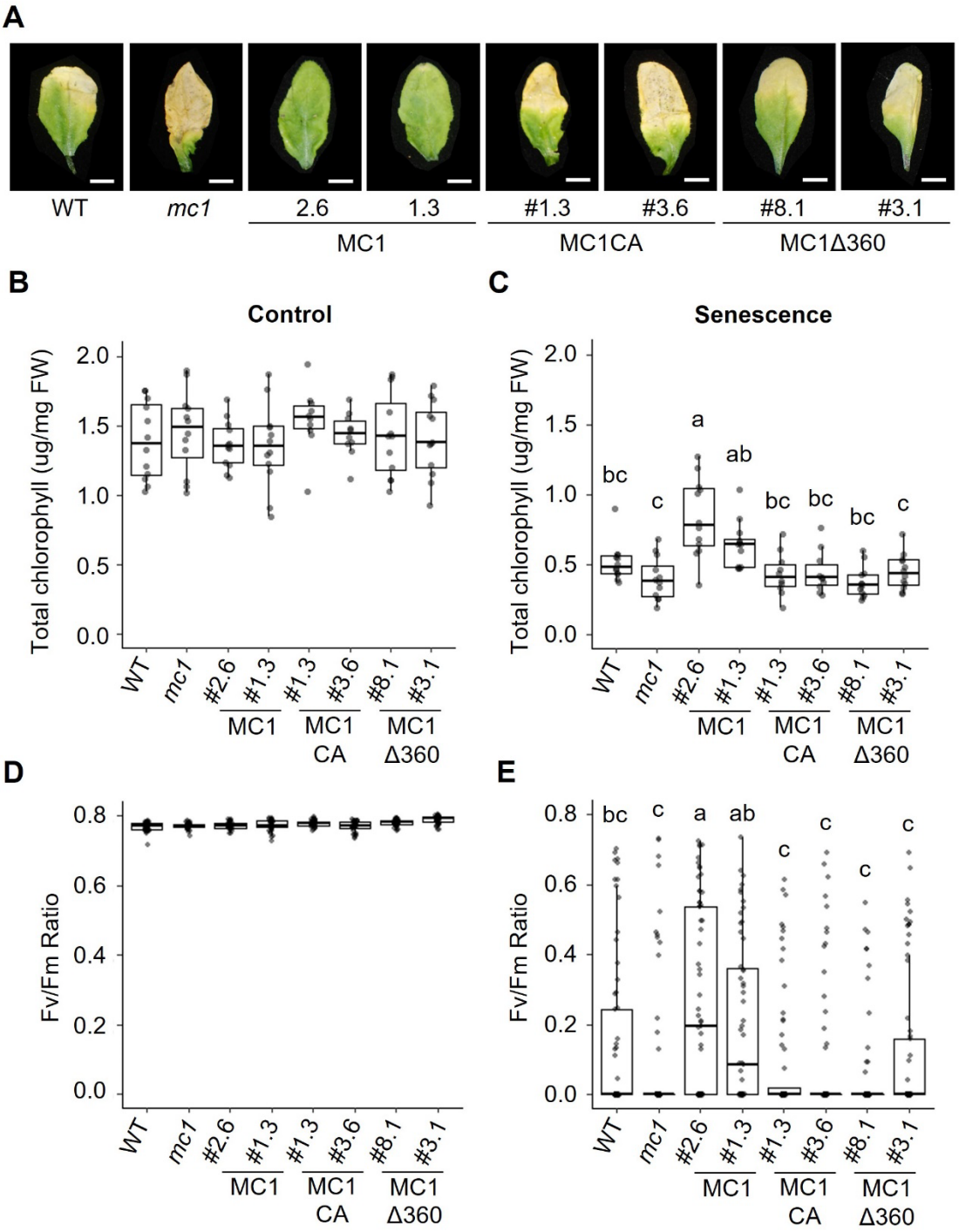

Figure 6. Overexpression of MC1 delays dark-induced senescence.

A. Representative leaf images of Arabidopsis wild type, *atmc1* mutants and *Pro35S::MC1-GFP atmc1*, *ProMC1::MC1C220A-GFP atmc1* and *Pro35S::MC1Δ360loop-GFP atmc1* grown for three

weeks under controlled groWTh conditions (16 h light/8 h dark photoperiod) and covered for 8 days to induce senescence. For each plant, only leaves 5 and 6 were either dark acclimated or used as controls. Bars = 0.5 cm.

B. and C) Total chlorophyll concentration (ug/mg FW) of uncovered (Control, B) or covered (Senescence, C) leaves of three-week-old *Arabidopsis* wild type, *atmc1* mutants and *Pro35S::MC1-GFP atmc1*, *ProMC1::MC1C220A-GFP atmc1* and *Pro35S::MC1Δ360loop-GFP atmc1.* Means with different letters are significantly different at $P < 0.05$ (one-way ANOVA).

D and E) PSII maximum efficiency (Fv/Fm) quantifications capacity of uncovered (Control, D) or covered (Senescence, E) leaves of three-week-old Arabidopsis wild type, *atmc1* mutants and *Pro35S::MC1-GFP atmc1*, *ProMC1::MC1C220A-GFP atmc1* and *Pro35S::MC1Δ360loop-GFP atmc1.* Means with different letters are significantly different at $P < 0.05$ (Krustal-Wallis test).

In B, C, D and E, upper and lower box boundaries represent the first and third quantiles, respectively; horizontal lines mark the median and whiskers mark the highest and lowest values. Four independent experiments, each containing at least ten leaves for each phenotype, were performed.

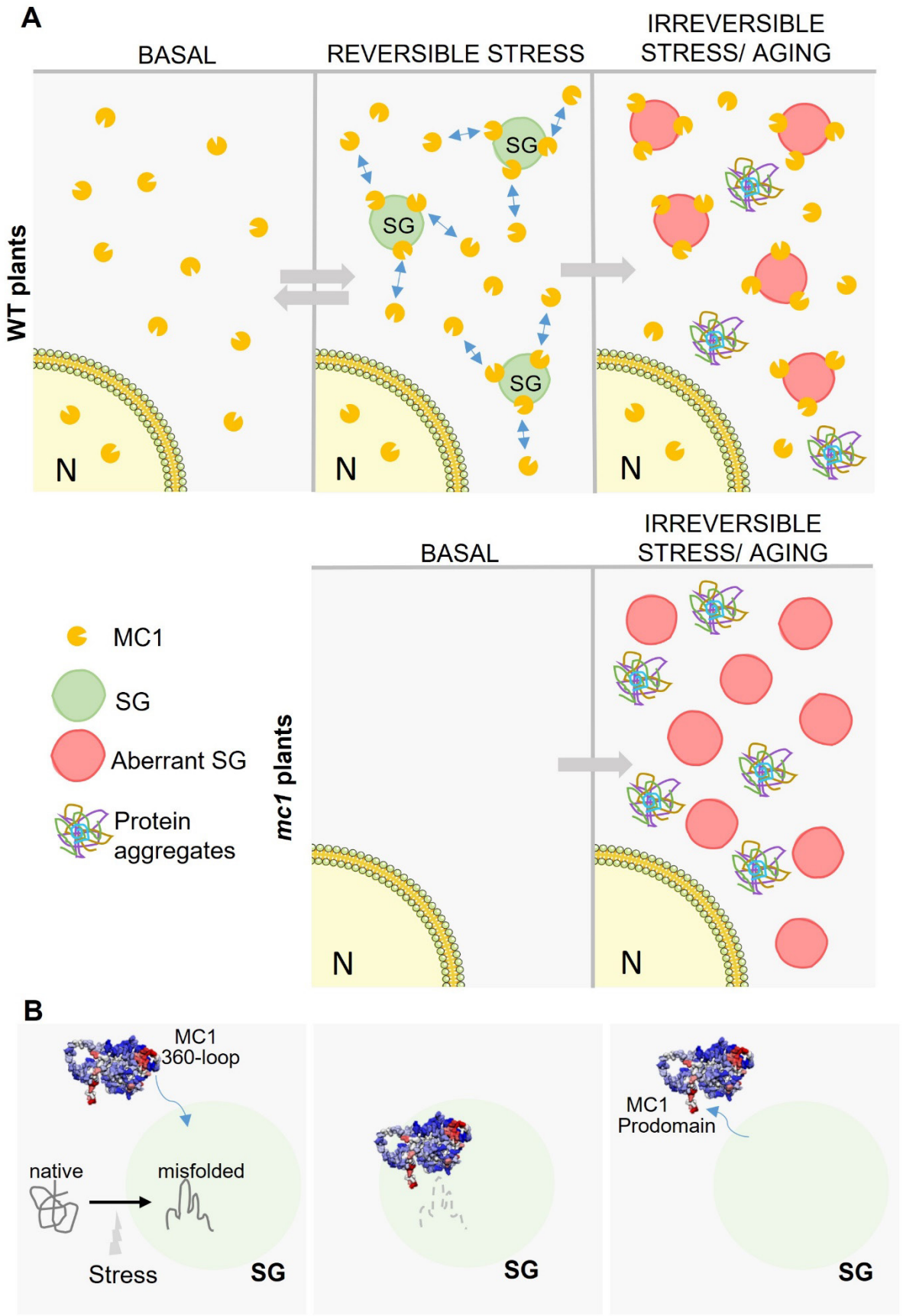
A
BASAL
REVERSIBLE STRESS
IRREVERSIBLE STRESS/ AGING
WT plants
SG
SG
SG
N
N
N
BASAL
IRREVERSIBLE STRESS/ AGING
MC1
SG
Aberrant SG
Protein aggregates
mc1 plants
N
N
B
MC1 360-loop
native
misfolded
Stress
SG
SG
MC1 Prodomain
SG

Figure 7. Working model on the role of MC1 in stress granules

A. Upper panel (WT plants): Under basal conditions, no SGs are detectable and MC1 presents a diffuse nucleo-cytoplasmic localization pattern. Upon perception of an acute, reversible stress, MC1 is recruited to SGs where it hypothetically clears misfolded/aggregated proteins. Under chronic or irreversible stress, the proteostatic capacity of the cell is surpassed and toxic protein aggregates that cannot be cleared start accumulating in the cytoplasm. Lower panel (*mc1* mutant plants): Plants devoid of MC1 cannot cope as WT with proteotoxic stress. Any stress may result in accumulation of protein aggregates that over time manifest as the observed accelerated senescence phenotype.

B. MC1 is recruited to SGs via its 360 loop. Once in SGs it clears aggregated proteins via its disaggregase activity. Release of MC1 from stress granules is dependent on the prodomain.

SUPPLEMENTARY FIGURES

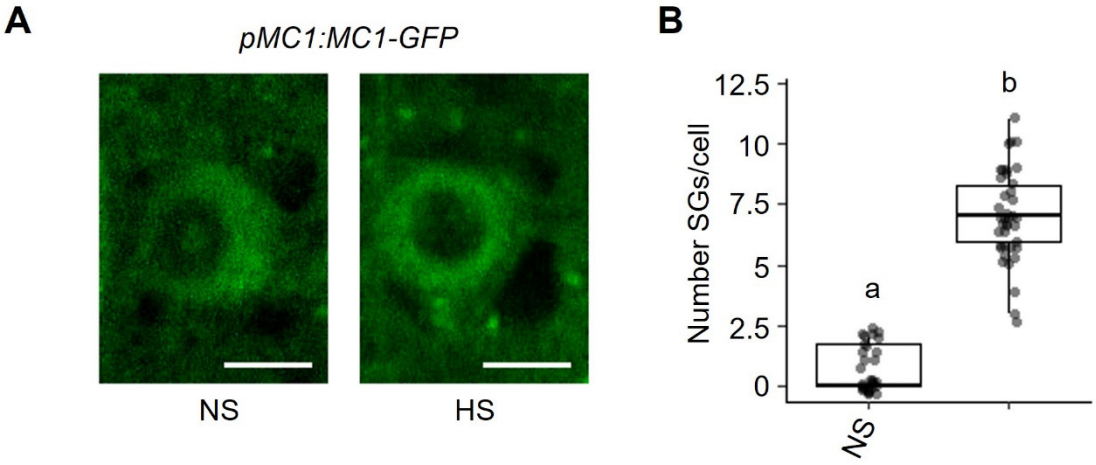

Figure S1. MC1-GFP expressed under the control of its own promoter re-localizes to cytoplasmic condensates upon heat stress.

A) Five-day-old Arabidopsis *mc1* mutant seedlings expressing *ProMC1::MC1-GFP* were heat-stressed at 39ºC for 40 min. Images of root tips were taken before (NS) and after being subjected to heat stress (HS) Bars = 5 µm.

B) Quantification of MC1-GFP foci in the experiment shown in A). Upper and lower box boundaries represent the first and third quantiles, respectively; horizontal lines mark the median and whiskers mark the highest and lowest values. Three independent experiments, each containing five individual measurements, were performed. Means with different letters are significantly different at $P < 0.05$ (T-test).

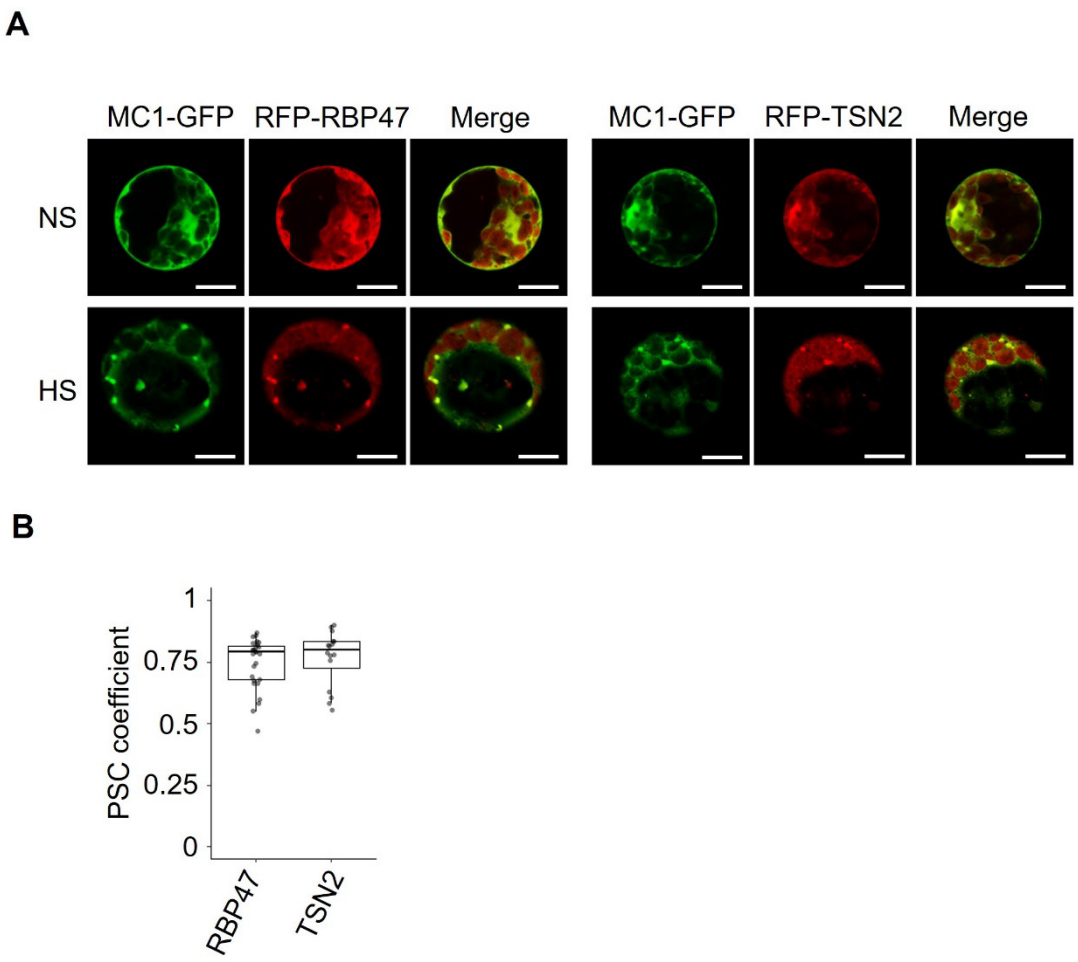

Supplementary Figure 2. MC1 co-localizes with stress granule markers in protoplasts upon heat stress.

A) Co-localization analysis using leaf protoplasts of 3-week-old *mc1 Pro35S::MC1-GFP* Arabidopsis plants transiently co-expressing *Pro35S::RFP-RBP47* or *Pro35S::RFP-TSN2.* Images were taken in control (NS) conditions or after heat-stressing (HS) the protoplasts.

B) Pearson coefficient of co-localization of RFP-RBP47 or RFP-TSN2 and MC1-RFP. Upper and lower box boundaries represent the first and third quantiles, respectively; horizontal lines mark the median and whiskers mark the highest and lowest values. Three independent experiments, each containing at least five individual measurements, were performed.

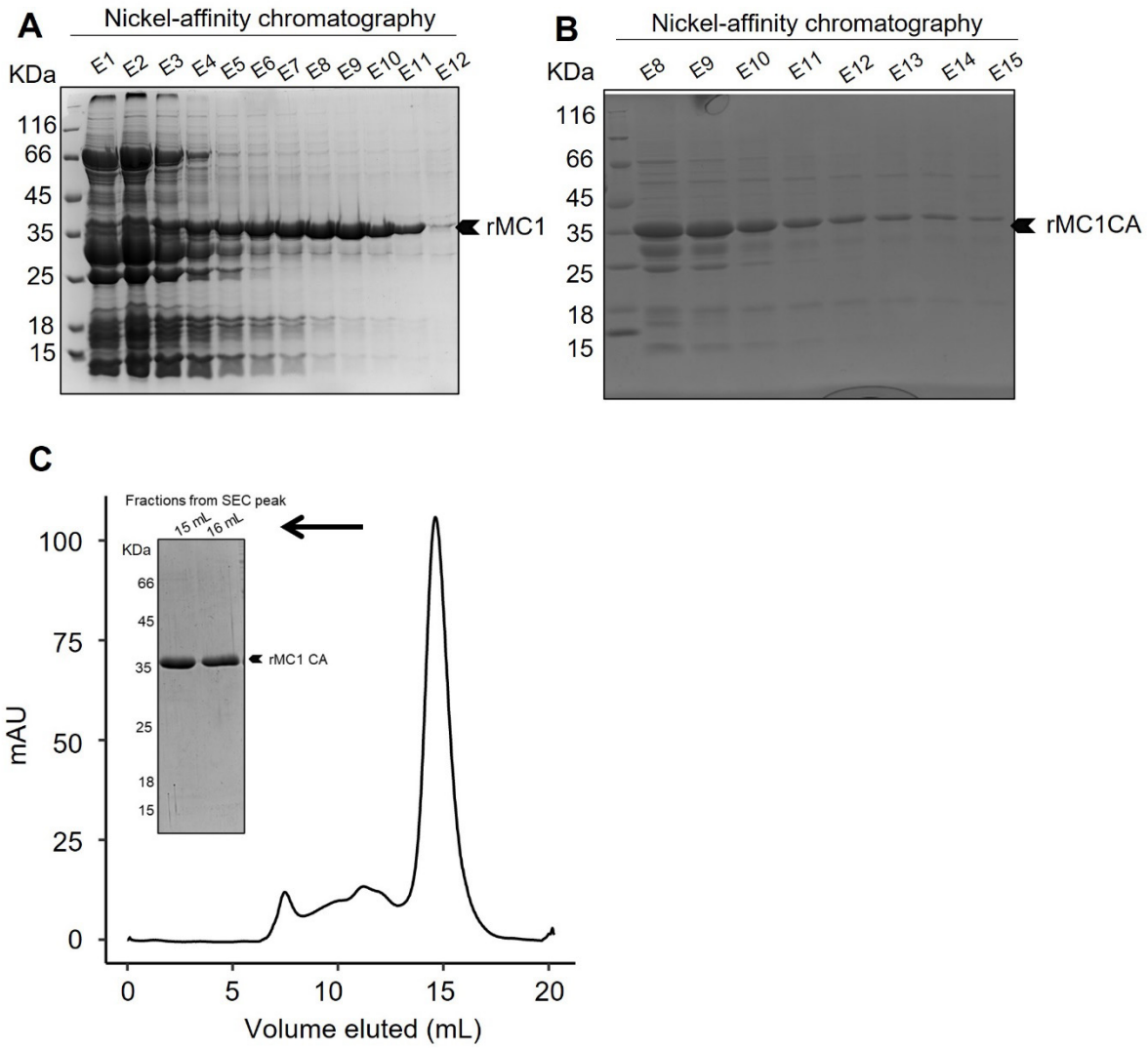

Supplementary Figure 3. Production and purification of recombinant MC1 in *Escherichia coli* cells.

A and B) SDS-PAGE Coomassie-stained gels of eluted fractions after nickel-affinity chromatography of *Escherichia coli* soluble lysates expressing either rMC1 (A) or rMC1CA (B). Arrow indicates expected molecular weight of rMC1.

C) Size-exclusion chromatography (SEC) from concentrated eluates shown in B. The inlet shows an SDS-PAGE Coomassie-stained gel of fractions 15 ml and 16 mL of the eluted volume from a Superdex 75 column.

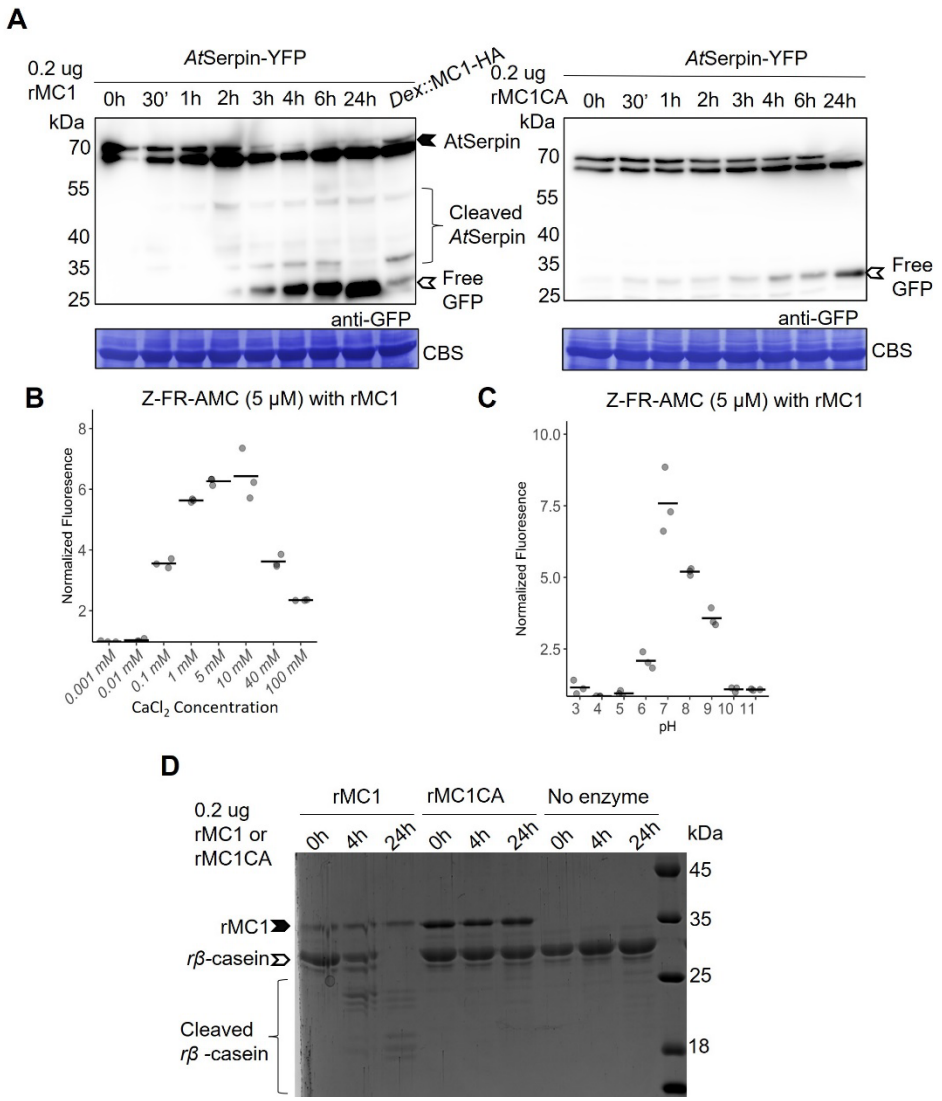

Supplementary Figure 4. rMC1 is a proteolytically active enzyme and behaves as a canonical type I metacaspase

A) Western blot analysis of *Nicotiana benthamiana* protein extracts transiently expressing Serpin-YFP incubated with either 0.2 µg rMC1 or 0.2 µg rMC1CA for the indicated times (hours) at room temperature. Extracts from *N. benthamiana* plants co-expressing *At*Serpin-YFP and MC1 fused to HA (Dexamethasone::MC1-HA) were included in the experiment as a positive control for Serpin1 cleavage (Lema Asqui *et al*., 2018). Coomassie blue staining of immunoblotted membranes (CBS) are shown as loading controls.

B-C) Activity of the fluorogenic substrate (Z-FR-AMC; 5 µM) when incubated with 0.2 µg of rMC1 under different concentrations of $CaCl_2$ (C) or different pH in 5 mM $CaCl_2$ (D).

D) SDS-PAGE Coomassie-stained gel of 2 µg *rβ*–casein incubated with 200 µg of either rMC1 or rMC1CA for 0, 4 or 24 h.

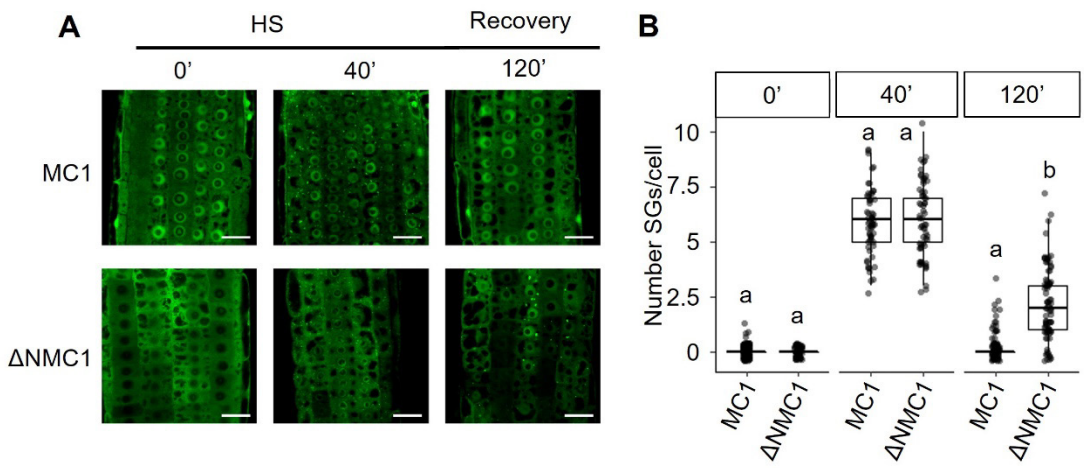

Figure S5. The MC1 prodomain contributes to SG clearance

A) Five-day-old *mc1* Arabidopsis seedlings stably expressing *Pro35S::MC1-GFP* or *Pro35S::ΔNMC1-GFP* were heat-stressed at 39ºC for 40 min (heat shock, HS), followed by incubation at 22ºC for up to 120 min (Recovery). Images of root tips were taken at indicated time points. Bars = 20 µm.

B) Quantification of MC1-GFP foci in the experiment shown in C. Upper and lower box boundaries represent the first and third quantiles, respectively; horizontal lines mark the median and whiskers mark the highest and lowest values. Three independent experiments, each containing at least five individual measurements, were performed. Means with different letters are significantly different at $P < 0.05$ (T-test in each time point).

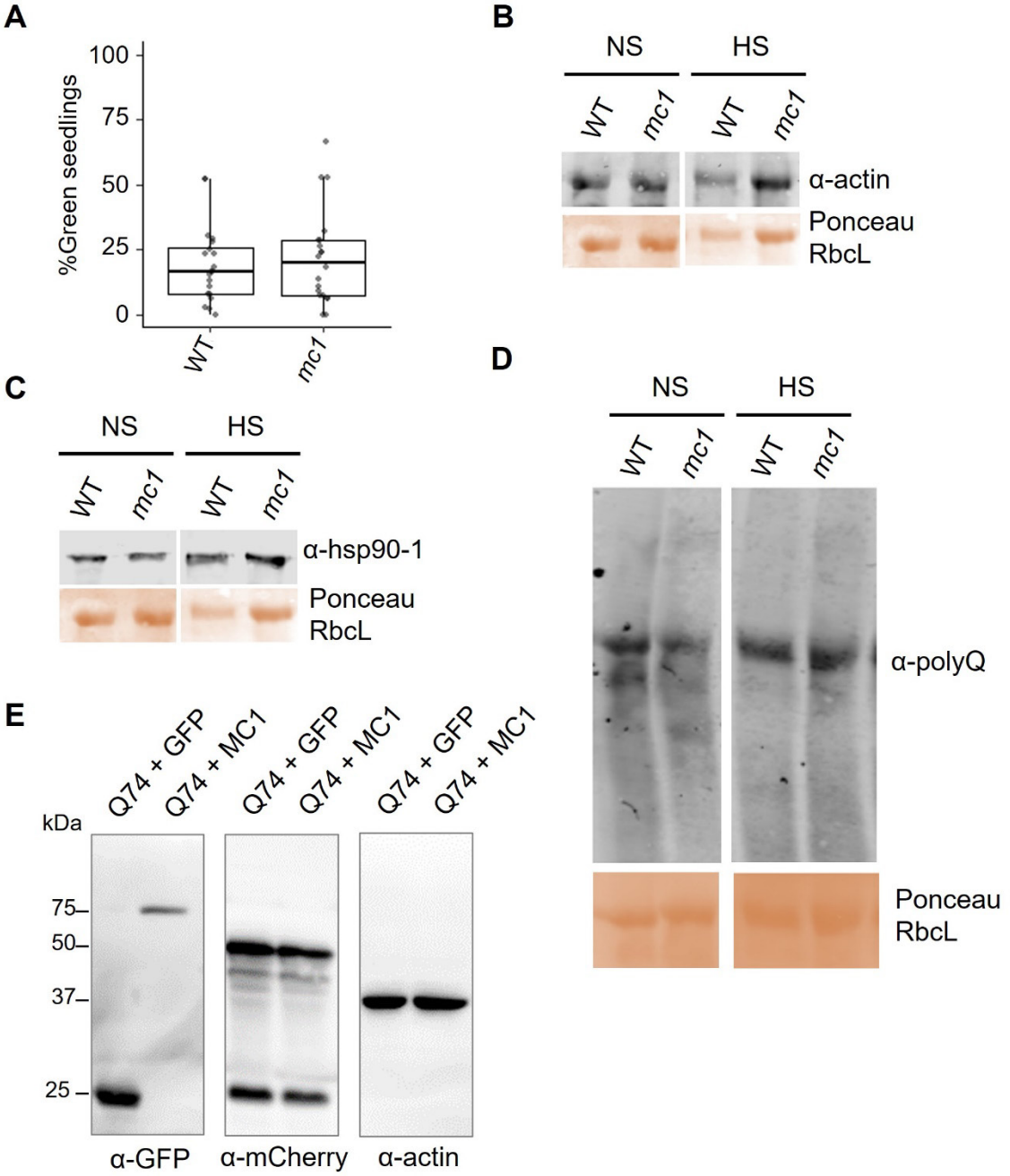

Figure S6. *mc1* knock-out mutants do not display thermotolerance or total protein accumulation differences compared to WT.

A) Five-day-old WT or *mc1* Arabidopsis seedlings were subjected to heat stress (HS, 90 min at 37ºC, 90 min at 22ºC and 90 min at 45ºC) followed by incubation at 22ºC for 7 days. Data represents the percentage of green seedlings. Upper and lower box boundaries represent the first and third quantiles, respectively; horizontal lines mark the median and whiskers mark the highest and lowest values. Ten independent experiments were performed. Means with different letters are significantly different at $P < 0.05$ (one-way ANOVA).

B, C and D) SDS-PAGE of protein extracts from five-day-old *Arabidopsis mc1* or WT seedlings in control conditions (NS) or subjected to a severe heat stress (HS, 90 min at 37ºC, 90 min at 22ºC and

90 min at 45ºC). SDS resistant aggregates were detected using antibodies against Actin (B), HSP90-1 (C) or polyQ proteins (D).

E) SDS-PAGE of protein extracts from HEK293 cells were transfected with mRFP-Q74 and GFP-MC1 or mRFP-Q74 and GFP as a control. GFP antibody was used to detect GFP-MC1 and control GFP, while mCherry antibody was used to detect Q74 SDS-resistant aggregates. α-actin was used as a loading control.

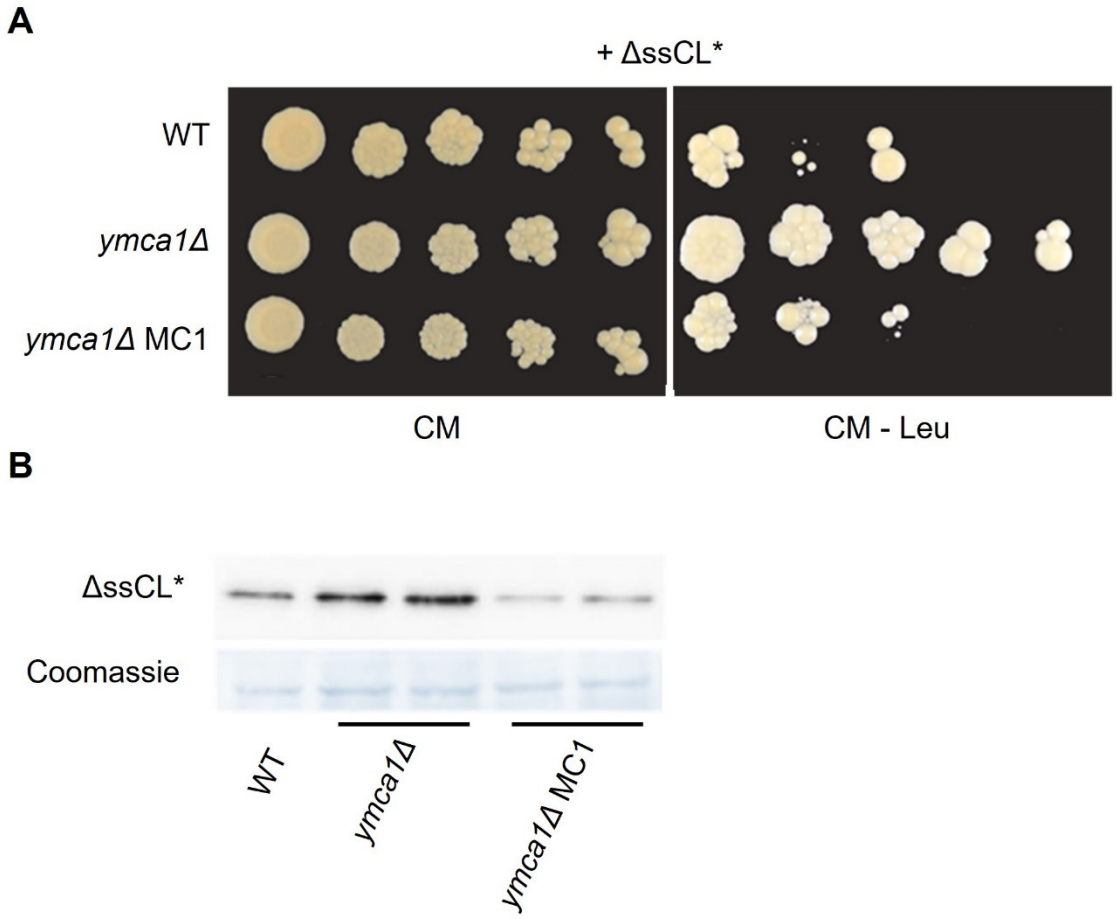

Figure S7. MC1 participates in the clearance of terminally misfolded proteins in yeast.

A) Serial dilutions of wild type (WT), *ymca1Δ* mutant and *ymca1Δ* MC1-complemented cells expressing ΔssCL* were spotted on indicated media and incubated for 3 days at 30ºC. Enhanced growth on plates lacking leucine (CM –Leu) indicates stabilization of ΔssCL*, whereas reduced growth indicates increased degradation. Three independent experiments were performed.

B) SDS-PAGE of ΔssCL* levels of the strains shown in A. α-myc was used to detect ΔssCL*.

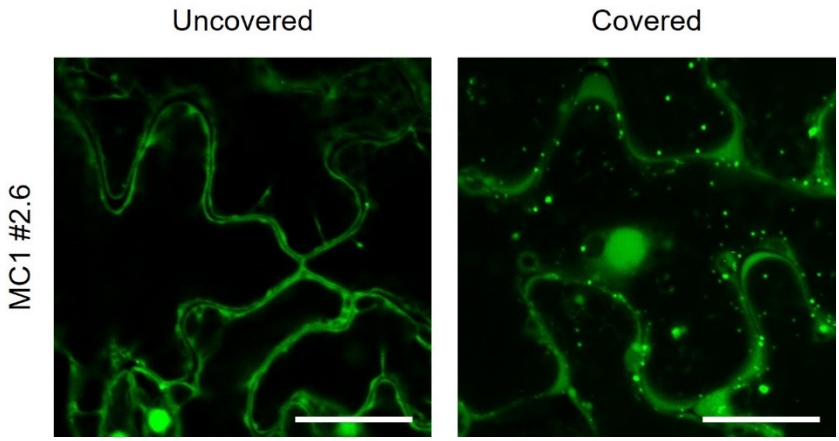

Figure S8. Dark-induced senescence results in the formation of MC1-containing cytoplasmic condensates.

Representative confocal microscopy images of leaves of Arabidopsis *Pro35S::MC1-GFP atmc1* 3-week-old plants grown for three weeks under controlled growth conditions (16h light/8h dark photoperiod) and covered for 4 days to induce senescence. Z-stacks with 10 slides (0.5 µm width) were performed. Bars = 20 µm.

Supplemental Data Set S1. List of *A. thaliana* lines, yeast strains, plasmids, primers and synthetic sequences used in this study.

Table S1: Arabidopsis lines used in this study

Arabidopsis thaliana seeds	**Accession number**	**Source or reference**
mc1 mutant GABI-Kat (GK-096A10)	AT1G02170	Coll *et al.,* 2010
mc1; Pro35S::MC1-GFP	AT1G02170	This study
mc1; Pro35S::MC1C220A-GFP	AT1G02170	This study
mc1; Pro35S::ΔNMC1-GFP	AT1G02170	This study
mc1; Pro35S::MC1Δ360loop-GFP	AT1G02170	This study
Col-0; Pro35S::GFP-TCTP	AT3G16640	Gutierrez *et al.,* 2021
Col-0; Pro35S::MC1-RFP Pro35S::GFP-TCTP	AT1G02170 (MC1), AT3G16640 (TCTP)	This study

Table S2: List of plasmids used in this study

Name	**Expression system**	**Backbone**	**Additional information**	**Source or reference**
Pro35S::MC1-GFP	*A.thaliana* *N.benthamiana*	pGGZ003	Hygromycin resistance	This study
Pro35S::MC1C220A-GFP	*A.thaliana*	pGGZ003	Hygromycin resistance	This study
Pro35S::MC1Δ360-GFP	*A.thaliana*	pGGZ003	Hygromycin resistance	This study
Pro35S::ΔNMC1-GFP	*A.thaliana*	pGGZ003	Hygromycin resistance	This study
ProMC1::MC1-GFP	*A.thaliana*	pGGZ003	Hygromycin resistance	This study
ProMC1::MC1C220A-GFP	*A.thaliana*	pGGZ003	Hygromycin resistance	This study
Pro35S::MC1-RFP	*A.thaliana*	pGGZ003	AlliYFP seed coat selection	This study
Pro35S::RFP-RBP47	*N.benthamiana*	pGWB655	BASTA resistance	This study
Pro35S::RFP-ADH2	*N.benthamiana*	pGWB655	BASTA resistance	This study

ProT7::6xHIS-ΔN MC1 Δ360 (rMC1)	*E. coli*	pET28 b(+)	Kanamycin resistance	This study
ProT7::6xHIS-ΔN MC1 Δ360 ^{C220A} (rMC1CA)	*E. coli*	pET28 b(+)	Kanamycin resistance	This study
ProCMV::mRFP-Q74	*HEK293T*	*pDEST-CMV-N-GFP*	Ampicillin resistance	Llamas *et al*., 2022
ProCMV::GFP	*HEK293T*	*pDEST-CMV-N-GFP*	Ampicillin resistance	Llamas *et al*., 2022
ProCMV::GFP-MC1	*HEK293T*	*pDEST-CMV-N-GFP*	Ampicillin resistance	This study
ProGPD::MC1-HA	*S. cerevisiae*	pRS415	Hygromycin resitance	This study
ProPRC1::ΔssCPY-LEU2-myc*	*S. cerevisiae*	pFE15	Hygromycin resitance	Eisele & Wolf, 2008

Table S3: List of primers and synthetic sequences used in this study for genotyping and cloning

Name	**Sequence**	**Additional information**	**Source or reference**
MC1 F3	GCGTCACCTTCTCATCAACA	For genotyping	Coll *et al.,* 2010
MC1 R3	ACGGTACCACTATGGCAAGC	For genotyping	Coll *et al.,* 2010
F-pMC1 (GG A000)	AACAGGTCTCAACCTGCTCGGATATCTGATTCTCCATGT	For cloning	This study
R-pMC1 (GG A000)	AACAGGTCTCTTGTTTATTATTCTCGGAAGGGAGGGAAT	For cloning	This study
F- MC1 (GG B000)	AACAGGTCTCAAACAATGTACCCGCCACCTCCCTCAAG	For cloning	This study
R- MC1 (GG B000)	AACAGGTCTCTAGCCGAGAGTGAAAGGCTTTGCATAGACATCGAATGTTTGG	For cloning	This study
F-MC1 C220A	CTCCATTCAATTATCGATGCTGCCCATAGTGGTACCGTTCTGG	Mutagenesis	This study

R-MC1 C220A	CCAGAACGGTACCACTATGGGCAGCATCGATAATTGAATGGAG	Mutagenesis	This study
F- ΔN MC1 (GG B000)	AACAGGTCTCAAACAATGTTCTCTCGCCACGAGCTCAAAGGCTG	For cloning	This study
F- MC1 Δ360	CTATGCGCACCACAATAAGGAATAGACAGGAGCCTCAACTGAC	Mutagenesis	This study
R -MC1 Δ360	GTCAGTTGAGGCTCCTGTCTATTCCTTATTGTGGTGCGCATAG	Mutagenesis	This study
F-GFP (GG C000)	AACAGGTCTCAAACAATGGTGAGCAAGGGCGAGG	For cloning	This study
R-GFP (GG C000)	AACAGGTCTCTAGCCTCACTTGTACAGCTCGTCCATGCC	For cloning	This study
F-mRFP (GG C000)	AACAGGTCTCAGGCTCAACAATGGCCTCCTCCGAGGACGTCATCA	For cloning	This study
F-mRFP (GG C000)	AACAGGTCTCTCTGATTAGGCGCCGGTGGAGTGGCGG	For cloning	This study
F-MC1 C220A E.c	ATCCAGGACCGTTCCAGAGTGGGCCGCATCGATAATAGAATGCAG	Mutagenesis	This study
R-MC1 C220A E.c	CTGCATTCTATTATCGATGCGGCCCACTCTGGAACGGTCCTGGAT	Mutagenesis	This study
ΔN MC1 Δ360 E.c	ATGGGTCGCAAACGTGCGGTCATTTGTGGAATTAGCTACCGTTTTAGCCGCCATGAGCTGAAAGGATGCATCAACGATGCAAAGTGCATGCGCCATCTGCTGATCAACAAGTTTAAGTTTTCGCCGGATTCAATCCTGATGCTGACGGAGGAGGAAACAGATCCATATCGTATTCCGACTAAACAAAACATGCGTATGGCATTGTATTGGCTGGTGCAGGGATGTACTGCCGGCGATAGCCTTGTTTTTCATTATAGCGGTCACGGTTCGCGCCAGCGCAACTACAACGGCGATGAAGTAGACGGCTATGATGAGACGCTTTGTCCGCTCGATTTTGAAACGCAAGGGATGATCGTAGATGATGAGATCAACGCCACGATTGTGCGCCCGCTGCCACATGGCGTGAAACTGCATTCTATTATCGATG	Synthetic sequence	Twist Bioscience

	CGTGTCACTCTGGAACGGTCCTGGATCTGC CGTTTCTGTGTCGCATGAACCGTGCCGGTC AGTATGTGTGGGAAGATCACCGTCCGCGCA GTGGATTATGGAAAGGTACCGCTGGTGGGG AAGCCATCTCTATTTCCGGTTGTGATGATGA CCAGACGAGCGCGGATACCTCTGCGTTGTC CAAAATTACCAGCACGGGGGCCATGACTTTT TGTTTTATCCAGGCCATTGAACGCAGCGCCC AAGGAACTACCTACGGGAGCTTACTGAACTC CATGCGTACTACTATTCGCAATCGTCAGGAA CCGCAGCTGACCGCGTGCCAAACCTTTGAT GTTTATGCCAAACCGTTTACCTTA		
HsMC1	ATGTATCCTCCTCCACCGTCCTCTATATACG CTCCCCCTATGCTCGTGAACTGTTCTGGATG CCGCACCCCTTTACAGCTGCCTAGCGGCGC CCGGAGTATCAGATGTGCCTTGTGTCAGGC TGTCACTCATATTGCCGACCCTAGAACGGCA CCTCCTCCTCAGCCTAGCTCCGCTCCAAGT CCACCTCCTCAGATACACGCTCCTCCAGGG CAATTACCACATCCCCACGGCCGGAAACGA GCTGTCATCTGTGGAATCTCTTATAGATTCA GTAGACATGAGTTGAAAGGCTGTATTAATGA TGCCAAATGCATGCGGCACTTACTGATCAAT AAGTTCAAGTTTAGTCCCGATAGCATTCTGA TGCTGACTGAAGAGGAAACAGATCCCTACC GCATCCCAACTAAACAAAACATGCGTATGGC ACTGTATTGGCTGGTGCAGGGTTGCACGGC TGGCGACTCTCTGGTCTTTCATTACAGTGGT CACGGCAGCAGGCAGCGCAACTATAATGGG GATGAAGTGGACGGTTACGACGAAACCCTG TGTCCACTTGATTTTGAGACCCAGGGCATGA TAGTGGACGACGAGATTAATGCCACCATTGT CCGGCCCTTGCCTCACGGTGTGAAGCTGCA CAGCATCATCGATGCATGTCACAGTGGAACA	Synthetic sequence	Twist Bioscience

	GTGCTCGATCTCCCCTTCCTCTGCCGCATGA ATAGAGCTGGCCAGTACGTCTGGGAAGATC ATCGTCCCAGGTCTGGCTTGTGGAAGGGAA CAGCCGGCGGTGAGGCAATCTCAATCAGCG GCTGCGACGACGACCAGACCTCCGCTGACA CCTCCGCCCTGTCCAAGATTACCTCAACTGG CGCTATGACCTTTTGCTTTATACAAGCCATA GAGCGATCAGCGCAAGGTACCACCTATGGG AGCCTGCTCAACAGCATGAGGACCACAATTA GAAACACAGGTAATGATGGTGGTGGAAGCG GGGGGGTTGTCACGACCGTCCTTAGCATGT TGCTGACCGGAGGATCCGCTATCGGGGGG CTGCGACAGGAGCCCCAGTTAACCGCATGC CAGACATTCGATGTTTACGCAAAGCCATTCA CTCTG		
attB1	GGGGACAAGTTTGTACAAAAAAGCAGGCT	For Gateway cloning	This study
attB2	GGGGACCACTTTGTACAAGAAAGCTGGGT	For Gateway cloning	This study
HsMC1 attB1	GGGGACAAGTTTGTACAAAAAAGCAGGCTT CATGTATCCTCCTCCACCGTC	For Gateway cloning	This study
HsMC1 attB2	GGGGACCACTTTGTACAAGAAAGCTGGGTC CTACAGAGTGAATGGCTTTGCG	For Gateway cloning	This study
RBP47 CDS attb1	AAAAAGCAGGCTCCATGGCAGACGTCAAGA TTCA	For Gateway cloning	This study
RBP47 CDS attb2	AGAAAGCTGGGTATCAGCTAACTTGTTGCTG AT	For Gateway cloning	This study
TCTP CDS attb1	AAAAAGCAGGCTCCATGTTGGTGTACCAAGA TCT	For Gateway cloning	This study
TCTP CDS attb2	AGAAAGCTGGGTATCAGCACTTGACCTCCTT CA	For Gateway cloning	This study

Table S4. Yeast strains used in this study

Strain name	Genotype	Background	Source or reference
WT	*MATa his3Δ1 leu2Δ0 met15Δ0 ura3Δ0*	BY4741	Open Biosystems, ThermoFisher Scientific, USA
Saccharomyces cerevisiae ymca1Δ	*MATa Scmca1Δ::kanMX4 his3Δ1 leu2Δ0 met15Δ0 ura3Δ0*	BY4741	Lee, Puente *et al.,* 2008
Saccharomyces cerevisiae ymca1Δ ProGPD::AtMC1-HA	*MATa his3Δ1 leu2Δ0 met15Δ0 ura3Δ0 pGDP-natNT2-AtMC1-HA*	BY4741	This study

Table S5. Other materials used in this study

Name	Accession number	Source or reference
Human Embrionic Kidney (HEK) 293T cells	CRL-1573	Llamas *et al*., 2022

Table S6. Table for statistical analysis

FIGURE 4B: ONE-WAY ANOVA, Tukey HSD				
	diff	**lwr**	**upr**	**p adj**
MC1CA-MC1	0.1847586	-0.6527327	1.022250	0.9408954
ΔNMC1-MC1	0.6368631	-0.1169524	1.390679	0.1303408
MC1Δ360-MC1	-6.2993589	-7.0508006	-5.547917	0.0000000
ΔNMC1-MC1CA	0.4521045	-0.3831952	1.287404	0.5011418
MC1CA -MC1CA	-6.4841175	-7.3172756	-5.650959	0.0000000
MC1Δ360- ΔNMC1	-6.9362220	-7.6852204	-6.187224	0.0000000
FIGURE 4D: ONE-WAY ANOVA, Tukey HSD				
	diff	**lwr**	**upr**	**p adj**
TSN2-RBP47	-17.620401	-26.3450673	-8.89573463	0.0000005
MC1-RBP47	-9.451622	-17.6217633	-1.28148035	0.0133386
MC1CA -RBP47	-7.693737	-15.3275346	-0.05993924	0.0470299
ΔNMC1-RBP47	-27.892557	-36.7406336	-19.04448057	0.0000000
MC1CA -RBP47	11.578085	3.6048438	19.55132709	0.0006743
MC1-TSN2	8.168779	-0.1199482	16.45750651	0.0558948
MC1CA -TSN2	9.926664	2.1660805	17.68724757	0.0041692
ΔNMC1-TSN2	-10.272156	-19.2298482	-1.31446403	0.0146114
MC1CA -TSN2	29.198486	21.1037738	37.29319900	0.0000000
MC1CA -MC1	1.757885	-5.3735992	8.88936900	0.9801845
ΔNMC1-MC1	-18.440935	-26.8594658	-10.02240473	0.0000000
MC1CA -MC1	21.029707	13.5359911	28.52342335	0.0000000
ΔNMC1- MC1CA	-20.198820	-28.0978905	-12.29974981	0.0000000
MC1CA - MC1CA	19.271822	12.3667926	26.17685218	0.0000000
MC1CA - ΔNMC1	39.470643	31.2430653	47.69821977	0.0000000
FIGURE 5B: ONE-WAY ANOVA, Tukey HSD				
	diff	**lwr**	**upr**	**p adj**
TTR-Buffer	0.99999985	0.307527282	1.692472418	0.003173252
MC1-Buffer	0.095235373	-0.678972494	0.869443241	0.999909575
MC1+TTR-Buffer	0.234657017	-0.457815551	0.927129585	0.931167923

MC1+native-Buffer	0.082478327	-0.609994241	0.774950895	0.999929007
CA-Buffer	0.0001611	-0.692311468	0.692633668	1
CA+TTR-Buffer	2.707581317	2.015108749	3.400053885	6.21E-08
MC4-Buffer	0.018671783	-0.960632314	0.997975881	1
MC4+TTR-Buffer	1.294898983	0.315594886	2.274203081	0.006682605
MC1-TTR	-0.904764477	-1.678972344	-0.130556609	0.017413195
MC1+TTR-TTR	-0.765342833	-1.457815401	-0.072870265	0.025919823
MC1+native-TTR	-0.917521523	-1.609994091	-0.225048955	0.006570919
CA-TTR	-0.99983875	-1.692311318	-0.307366182	0.003177715
CA+TTR-TTR	1.707581467	1.015108899	2.400054035	1.44E-05
MC4-TTR	-0.981328067	-1.960632164	-0.002023969	0.049363499
MC4+TTR-TTR	0.294899133	-0.684404964	1.274203231	0.963054408
MC1+TTR-MC1	0.139421643	-0.634786224	0.913629511	0.998565393
MC1+native-MC1	-0.012757047	-0.786964914	0.761450821	1
CA-MC1	-0.095074273	-0.86928214	0.679133594	0.999910714
CA+TTR-MC1	2.612345943	1.838138076	3.386553811	3.78E-07
MC4-MC1	-0.07656359	-1.115272442	0.962145262	0.999998225
MC4+TTR-MC1	1.19966361	0.160954758	2.238372462	0.018973008
MC1+native-MC1+TTR	-0.15217869	-0.844651258	0.540293878	0.994499964
CA-MC1+TTR	-0.234495916	-0.926968484	0.457976652	0.931405021
CA+TTR-MC1+TTR	2.4729243	1.780451732	3.165396868	1.91E-07
MC4-MC1+TTR	-0.215985233	-1.195289331	0.763318864	0.994370193
MC4+TTR-MC1+TTR	1.060241967	0.080937869	2.039546064	0.029861547
CA-MC1+native	-0.082317226	-0.774789794	0.610155342	0.999930043
CA+TTR-MC1+native	2.62510299	1.932630422	3.317575558	9.14E-08
MC4-MC1+native	-0.063806543	-1.043110641	0.915497554	0.999999324
MC4+TTR-MC1+native	1.212420657	0.233116559	2.191724754	0.0112768

CA+TTR-CA	2.707420216	2.014947648	3.399892784	6.21E-08
MC4-CA	0.018510683	-0.960793414	0.99781478	1
MC4+TTR-CA	1.294737883	0.315433786	2.27404198	0.0066894
MC4-CA+TTR	-2.688909533	-3.668213631	-1.709605436	4.24E-06
MC4+TTR-CA+TTR	-1.412682333	-2.391986431	-0.433378236	0.00320337
MC4+TTR-MC4	1.2762272	0.076829529	2.475624871	0.033547271
FIGURE 6C: KRUSTAL WALLIS				
Pairwise comparisons using Wilcoxon rank sum test with continuity correction, p adj:				
WT-*mc1*	0.22395			
WT-2.6	0.02740			
WT-1.3	0.14359			
WT-360 2.3	0.29024			
WT-360 2.8	0.36185			
WT-CA 1.3	0.20895			
WT-CA 3.6	0.65577			
mc1-2.6	0.00096			
mc1-1.3	0.00267			
mc1-360 2.3	0.81264			
mc1-360 2.8	0.79654			
mc1-CA 1.3	0.99373			
mc1-CA 3.6	0.46142			
2.6-1.3	0.49421			
2.6-360 2.3	0.00074			
2.6-360 2.8	0.00163			
2.6-CA 1.3	0.00074			
2.6-CA 3.6	0.00267			
1.3-360 2.3	0.00267			
1.3-360 2.8	0.00675			
1.3-CA 1.3	0.00267			

1.3-CA 3.6	0.02740			
360 2.3-360 2.8	0.95224			
360 2.3-CA 1.3	0.79654			
360 2.3-CA 3.6	0.58939			
360 2.8-CA 1.3	0.79654			
360 2.8-CA 3.6	0.65577			
CA 1.3-CA 3.6	0.41108			
FIGURE 6E: ONE-WAY ANOVA, Tukey HSD				
	diFF	**lwr**	**upr**	**p adj**
atmc1-WT	-0.116667835	-0.328554127	0.095218457	0.679729944
2.6-WT	0.314132458	0.102246166	0.52601875	0.000369658
1.3-WT	0.123455733	-0.088430559	0.335342025	0.614336753
1.3CA-WT	-0.085531119	-0.307759336	0.136697099	0.930793292
3.6CA-WT	-0.073868079	-0.296096296	0.148360139	0.967933077
2.3-WT	-0.142505947	-0.354392239	0.069380345	0.429332484
2.8-WT	-0.070808052	-0.282694344	0.14107824	0.966983128
2.6-atmc1	0.430800293	0.218914001	0.642686585	3.30E-07
1.3-atmc1	0.240123568	0.028237276	0.452009859	0.015253904
1.3CA-atmc1	0.031136716	-0.191091502	0.253364934	0.999853947
3.6CA-atmc1	0.042799756	-0.179428462	0.265027974	0.998810912
2.3-atmc1	-0.025838112	-0.237724404	0.186048179	0.99994274
2.8-atmc1	0.045859782	-0.166026509	0.257746074	0.997494748
1.3-2.6	-0.190676725	-0.402563017	0.021209567	0.109512059
1.3CA-2.6	-0.399663577	-0.621891794	-0.177435359	7.46E-06
3.6CA-2.6	-0.388000537	-0.610228754	-0.165772319	1.47E-05
2.3-2.6	-0.456638405	-0.668524697	-0.244752113	6.22E-08
2.8-2.6	-0.38494051	-0.596826802	-0.173054218	5.88E-06
1.3CA-1.3	-0.208986851	-0.431215069	0.013241366	0.080702827
3.6CA-1.3	-0.197323811	-0.419552029	0.024904406	0.119452916

2.3-1.3	-0.26596168	-0.477847972	-0.054075388	0.004550834
2.8-1.3	-0.194263785	-0.406150077	0.017622507	0.096596645
3.6CA-1.3CA	0.01166304	-0.220446763	0.243772843	0.999999873
2.3-1.3CA	-0.056974829	-0.279203046	0.165253389	0.99285322
2.8-1.3CA	0.014723066	-0.207505151	0.236951284	0.999999134
2.3-3.6CA	-0.068637869	-0.290866086	0.153590349	0.978690749
2.8-3.6CA	0.003060026	-0.219168191	0.225288244	1
2.8-2.3	0.071697895	-0.140188397	0.283584187	0.964664384

4. CONCLUSIONS

From the objectives of this PhD, the following conclusions can be drawn:

Robust transcriptional indicators of immune cell death revealed by spatiotemporal transcriptome analysis

1. There are unique and time-dependent differences in the repertoire of differentially expressed genes, expression profiles and biological processes derived from tissue undergoing HR and that of its surroundings.

2. Robust transcriptional indicators can be used to define cells that are destined to die upon infection, potentially serving as tools to perform high-throughput techniques to study HR at a single cell level in future studies.

Lack of *At*MC1 catalytic activity triggers autoimmunity dependent on NLR stability

3. Absence of *At*MC1 results in autoimmunity dependent on immune signalling components downstream of sensor NLR activation (EDS1-PAD4).

4. Overexpression of catalytically inactive *At*MC1 in an *atmc1 mutant* background triggers severe autoimmunity partially dependent on the EDS1-PAD4-ADR1 immune node

5. This variant interacts promiscuously with immune components possibly stabilizing them and preventing their timely turnover.

6. While individual mutations in NLRs, PRRs or other immune-related components that interact with catalytically inactive *At*MC1 do not rescue the autoimmune phenotype, overexpression of SNIPER1, a master regulator of NLR homeostasis, fully rescues the phenotype.

7. Catalytically inactive *At*MC1 localizes to puncta that are destined to the vacuole for degradation through autophagy, potentially as a turnover pathway to dispose accumulated immune components.

8. Based on the phenotypes and molecular events observed in plants overexpressing catalytically inactive *At*MC1, we infer that Wt *At*MC1 might participate in NLR homeostasis and therefore its absence, together with the decline in proteostasis/PQC during aging results in autoimmunity.

Arabidopsis metacaspase MC1 localizes in stress granules, clears protein aggregates, and delays senescence.

9. Upon proteotoxic stress (heat stress), *At*MC1 is dynamically recruited to cytoplasmic condensates, known as stress granules (SGs), that contribute to maintaining protein homeostasis.

10. *At*MC1 can be expressed and isolated recombinantly when two aggregation-prone disordered regions (the prodomain and the 360-loop located in the p10 domain) are removed.

11. *At*MC1 exhibits an extremely efficient aggregate-clearing activity (disaggregase activity) both *in vitro* and *in vivo* in distantly related organisms.

12. Owing to its evolutionarily conserved capacity to clear protein aggregates, *At*MC1 could be a potential candidate for therapeutic intervention in human diseases caused by pathological protein assemblies.

13. In plants, this remarkable aggregate-clearing activity may underlie the delay in plant senescence caused by *At*MC1 overexpression.

ANNEX

Detection and quantification of the hypersensitive response cell death in Arabidopsis thaliana

(Publication 6)

Chapter 16

Detection and Quantification of the Hypersensitive Response Cell Death in *Arabidopsis thaliana*

Jose Salguero-Linares, Saul Lema-Asqui, Marta Salas-Gómez, Andrea Froilán-Soares, and Núria S. Coll

Abstract

In plants, the hypersensitive response (HR) is a programmed cell death modality that occurs upon recognition of harmful non-self. It occurs at the site of pathogen infection, thus preventing pathogens to live off plant tissue and proliferate. Shedding light on the molecular constituents underlying this process requires robust and quantitative methods that can determine whether plants lacking functional genes are defective in HR execution compared to wild-type controls. In this chapter, we provide two quantitative protocols in which we measure cell death from *Arabidopsis thaliana* leaves infected with avirulent HR-causing bacterial strains. Firstly, we use trypan blue staining to quantify the stained area of leaves upon bacterial infection using a personalized macro in the Image J (Fiji) software. Alternately, we incorporate an electrolyte leakage protocol in order to measure HR caused by different avirulent bacterial strains at different bacterial titers. We encourage users to perform a combination of both methods when assessing HR in different plant genotypes.

Key words *Arabidopsis thaliana*, Hypersensitive response, *Pseudomonas syringae* pv *tomato* DC3000, Trypan Blue Staining, Cell death quantification by Image J, Electrolyte leakage

1 Introduction

As a means of restricting pathogen growth, plants deploy a tightly regulated form of immune cell death at the attempted pathogen ingress site, traditionally known as the hypersensitive response (HR) [1, 2]. Upon recognition of harmful non-self, host intracellular immune receptors of the nucleotide-binding leucine rich repeat (NLR) type recognize pathogen effector molecules triggering an amplified immune response named effector-triggered immunity (ETI), which usually culminates in HR cell death [3]. When plant cells undergo HR as a consequence of pathogenic infection, the following hallmarks are generally displayed: cytoplasmic

Marina Klemenčič et al. (eds.), *Plant Proteases and Plant Cell Death: Methods and Protocols*,
Methods in Molecular Biology, vol. 2447, https://doi.org/10.1007/978-1-0716-2079-3_16,

shrinkage, mitochondrial swelling, chromatin condensation, chloroplast and plasma membrane disruption, and vacuolization [4, 5].

A thorough understanding of the molecular players and mechanisms regulating HR-cell death is still lacking. With the advent of the genomic era, numerous HR regulators have been reported [6]. Consequently, robust methods for quantitative analysis of HR cell death are of utter importance to effectively evaluate whether mutations in certain genes render a plant unable to execute HR.

Trypan blue staining of infected plant tissue has been extensively used as a qualitative method for visualization of dead cells [7–9]. Since live cells possess intact membranes, the Trypan Blue dye is excluded from the cells, whereas in dead cells the dye transverse the plasma membrane as a consequence of the loss of its integrity [10]. Hence, dead cells are stained and appear in a distinctive blue color when imaged under a microscope. Subsequently, stained cells can be quantified in order to precisely determine whether differences exist between distinct plant genotypes in terms of HR cell death.

Loss of plasma membrane integrity in dying cells also results in the release of electrolytes to the extracellular milieu. The degree of electrolyte leakage from dying cells can also be used as a readout of the extent to which cell death is taking place in the infected tissue [11]. Currently available conductivity meters allow measurements of electrolyte leakage in relatively small volumes (2 mL), which facilitate accurate and rapid quantification of a larger number of samples.

On the one hand, we provide a detailed method for the quick and automated quantification of cell death using trypan blue staining. For this, we use *Arabidopsis thaliana* plants (Arabidopsis) belonging to the Columbia-0 ecotype (Col-0) inoculated with the HR-causing bacterial strain *Pseudomonas syringae* pv. *tomato* DC3000 carrying the effector *avrRpm1* (*Pto* DC3000 *avrRpm1*) using the syringe-infiltration method. In Col-0 HR is triggered upon recognition of avrRpm1 by the NLR receptor RPM1 [12]. Upon trypan blue staining of leaves at different time points after infection, we quantify stained cells in the infiltrated leaves using the image processing package Fiji (built upon the ImageJ2 free software) [13], using a newly developed macro that allows automated quantification of the stained area.

On the other hand, we describe a robust method for quantification of electrolyte leakage of dying cells from Arabidopsis Col-0 leaves infiltrated with both *Pto* DC3000 (*avrRpm1*) and *Pto* DC3000 (*avrRpt2*) using different bacterial titers adapted from a previously described protocol [11]. avrRpt2 also causes HR in Col-0, as this effector is recognized by the NLR RPS2 [14]. As a negative control for our experiments, we use the Arabidopsis Col-0 *rpm1–3* and *rps2* mutants, which do not display HR triggered by

Pto DC3000 (*avrRpm1*) and *Pto* DC3000 (*avrRpt2*), respectively, since they are defective in the cognate NLRs RPM1 and RPS2 [12, 14].

2 Materials

2.1 Plant Material and Growth Conditions

1. *Arabidopsis* thaliana Col-0 seeds from the following phenotypes: wild-type, *rpm1–3* (N68739) and *rps2* (N6196) from the Nottingham Arabidopsis Stock Centre (NASC) based in the University of Nottingham, UK (*see* **Note 1**).
2. Soil mix: 5 parts peat soil + 2 parts vermiculite + 1 part perlite.
3. A growth chamber with controlled temperature (22 °C), photoperiod (9 h light, 15 h dark), humidity (70% relative humidity) and white LED light intensity of 150 μmol/m^2/s.
4. Small size plastic pots.
5. Flat polypropene trays.

2.2 Bacterial Strains, Preparation of Inoculum and Infection

1. *Pseudomonas syringae pv tomato (Pto)* DC3000 (*avrRpm1*) and *Pto* DC3000 (*avrRpt2*) avirulent strains (*see* **Note 2**).
2. Solid King's Broth medium (KB medium): For 500 mL: 10 g peptone from meat, 0.75 g K_2HPO_4, 0.75 g $MgSO_4 \bullet 7H_2O$, 5 ml glycerol, 7.5 g bacteriological agar, and Milli Q sterilized water.
3. Antibiotics for selection of avirulent *Pto* DC3000 strains (*see* **Note 3**).
4. Microwave.
5. Water bath with adjustable temperature.
6. Resuspension buffer: Autoclaved 10 mM magnesium chloride ($MgCl_2$).
7. 50 and 15-mL centrifuge tubes.
8. Petri dishes.
9. Polystyrene disposable cuvettes.
10. 1 mL Needleless syringes.
11. Spectrophotometer.
12. Laminar flow hood.
13. Plastic wrapping paper/plastic dome.
14. Marker pen (black).

2.3 Trypan Blue Staining and Microscopy Slide Preparation

1. Stock of trypan blue staining solution: 100 mg phenol (solid), 100 mL lactic acid, 100 mL glycerol, 100 mL Milli Q sterilized water.
2. Trypan blue staining working solution: 1 part trypan blue staining solution +3 parts 96% ethanol.

3. Destaining solution: 1 kg chloral hydrate dissolved in 400 mL Milli Q sterilized water.
4. Magnetic stirrer with adjustable temperature.
5. Grid cloth mesh.
6. Tilt shaker.
7. Fume hood.
8. Slide preparation: 50% glycerol, fine painting brush, microscopy glass slides, and coverslips.
9. Optivisor lenses 3.5×.
10. Clear glue.
11. Microdissection microscope.

2.4 Electrolyte Leakage

1. Scissors.
2. Cork borer.
3. Forceps.
4. Milli Q sterilized water.
5. Sterile 12-well plate.
6. LAQUAtwin EC-11 Conductivity meter (HORIBA Advanced Techno Co., Ltd).

2.5 Quantification of Cell Death by Trypan Blue Staining and Electrolyte Leakage

1. Image J (Fiji) software for trypan blue staining quantification [13].
2. R software for graph plotting of conductivity measurements and statistical analysis.

3 Methods

3.1 Sowing of Arabidopsis Seeds and Plant Growth

1. Fill small plastic pots with soil peat, vermiculite, and perlite mix ($5/1/_{1/2}$). Compress the mix without exerting too much pressure into the pot, place the pots on a middle size flat polypropene tray, and wet the mixture to field capacity with tap water.
2. Sow 4–5 seeds in each pot. Fill 6–8 pots per genotype for electrolyte leakage experiments and 8 pots per genotype for a time course of infected leaves (2 plants per time point) stained with trypan blue staining (*see* **Note 4**).
3. Randomize the previously labeled pots on the tray.
4. Cover the tray with plastic wrapping paper or a plastic dome in order to maintain humidity required for germination.
5. Stratify the seeds by placing the tray on a cold room/refrigerator at 4 °C for 2 days.

6. Transfer the tray to a growth chamber with a photoperiod of short-day conditions: 9 h light/15 h dark (*see* **Note 5**), 22 °C, 70% relative humidity, and light intensity of 150 μmol/m^2/s.
7. Remove the plastic wrapping paper or dome after 3 days and let the seedlings grow for 5–6 more days.
8. With the help of thin forceps, remove unwanted seedlings from each pot and leave only one seedling growing.
9. Water plants two to three times per week without overwatering to avoid stress on the plants.
10. On the second to third week of growth, use a marker pen to mark leaf eighth of the Arabidopsis plant, which will be the one infected (*see* **Note 6**).
11. Four- to five-week-old plants grown in these conditions are ideal for bacterial infection by syringe infiltration.

3.2 Preparation of Bacterial Inoculum and Syringe Infiltration

3.2.1 Growth of Bacteria in KB Medium Plates

1. Sterilize a laminar flow cabin by cleaning surfaces with 70% ethanol and switch on the UV light for 5 min.
2. Prepare the KB medium and add appropriate antibiotics for selection of avirulent bacterial strains.
3. Pour 25 mL of KB + antibiotics into each plate.
4. Three days before infecting Arabidopsis, streak avirulent bacteria from a −80 °C glycerol stock with a sterile tip. Place the plate on a still 28 °C incubator. Bacteria will grow after 2 days of incubation.
5. One day before infecting Arabidopsis, collect all bacteria grown on the initial plate and re-streak them on the surface of a new KB plate using a sterile inoculating loop.

3.2.2 Preparation of Bacterial Inoculum

1. On the day of the infection, add 10 mL of autoclaved 10 mM Mg_2Cl inside the plate and wait 10 min in order for the bacteria to detach from the surface of the plate.
2. Re-suspend bacteria with the help of a 10 mL Pasteur pipette by gently pipetting up and down in order to detach as much bacteria as possible from the plate.
3. Take 1 mL of bacteria from the plate and mix it with 9 mL of 10 mM $MgCl_2$ in a 15 mL tube.
4. Make a 1:10 dilution in 10 mM $MgCl_2$ and measure bacterial optical density at 600 nm (OD_{600}) using a spectrophotometer. Calculate the volume needed from undiluted bacteria in the previous step and dilute it in 10 mM $MgCl_2$ in order to reach the OD_{600} desired for infection (*see* **Note 7**).

3.3 Trypan Blue Staining

1. Label the time point after infection at which each plant leaf will be collected on each pot.

2. Pressure infiltrate the eighth leaf of Arabidopsis plant with avirulent bacteria using a needleless syringe (*see* **Note 8**).
3. After infiltration, gently dry the excess of liquid on the surface of the leaf and collect the leaves corresponding to each time point by cutting through the petiole with the aid of small scissors.
4. Place the leaves in a 50 mL tube containing 15 mL of trypan blue staining working solution. Always work in a fume hood when handling trypan blue staining solution and destaining solution.
5. Pour boiling water into a plastic box and submerge the sealed tubes inside the water for 5 min or until the leaves turn blue.
6. Pour the trypan working solution along with the leaves onto a sieve and transfer the leaves carefully with tweezers to a new 50 mL tube containing 20 mL of destaining solution (*see* **Note 9**). From this step onward, the leaves will stay in the same tube in order to avoid damage caused by transferring leaves from one tube to another.
7. Let the tubes rotate on a tilt shaker at 80 rpm for 1 h.
8. Use a mesh grid in order to sieve and discard the destaining solution and replace it with fresh 20 mL destaining solution (*see* **Note 10**). Let the 50 mL tubes rotate overnight.
9. The following day, sieve the destaining solution using a new mesh grid and add 20 mL of 50% glycerol. Leaves can be stored for prolonged periods in this solution.

3.4 Mounting Microscopy Slides

1. Pour the 20 mL of 50% glycerol containing eight leaves into a petri dish.
2. With the aid of a fine painting brush, gently transfer a single leave onto a microscopy glass slide.
3. Place 500 μL of 50% glycerol on top of the glass slide.
4. Gently expand the leaf on the surface of the glass slide with fine touches using a paint brush (*see* **Note 11**).
5. Once the leaf is correctly expanded on the glass slide, place a coverslip on top of the leaf by gently dropping the coverslip from the top of the leaf to the bottom. Try to avoid bubbles forming in between the leaf and the coverslip (*see* **Note 12**).
6. Gently brush clear glue at the edges of the coverslip so that it adheres to the glass slide and coverslips do not detach.

3.5 Microscopy Imaging

1. Image individual leaves with a microdissection microscope at 5× magnification. Always use the same settings for all samples.

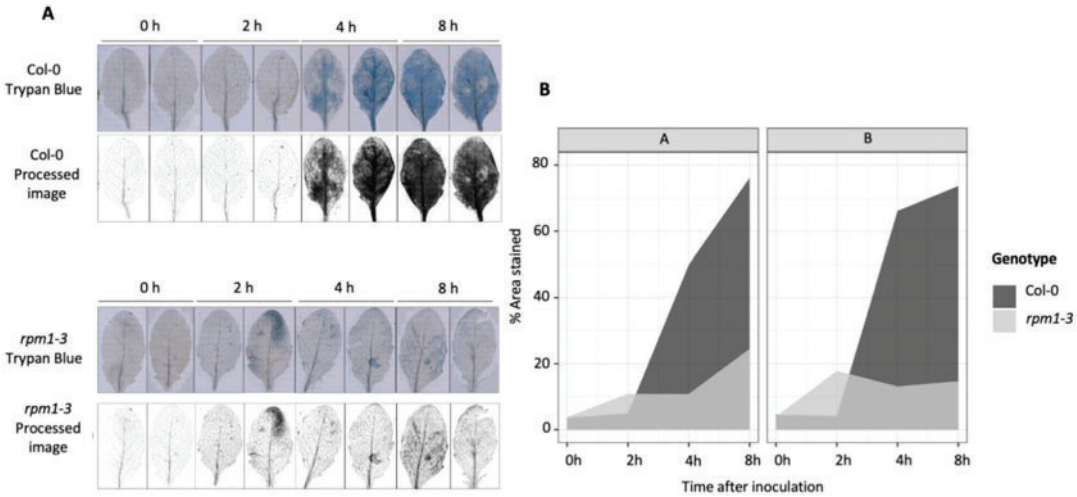

Fig. 1 Quantification of trypan blue stained area of Arabidopsis leaves infected with an HR-causing avirulent bacterial strain. (**a**) Four- to five-week-old Arabidopsis leaves of either Col-0 or *rpm1–3* were syringe-infiltrated with *Pto* DC3000 (*avrRpm1*) at 2.5×10^7 CFUs/O.D_{600} = 0.05. Two independent leaves were stained in trypan blue at different time points after infiltration (0, 2, 4 and 8 h) and subsequently imaged under the microscope. (**b**) Image J software was used for quantification of stained area which is represented as a percentage (*see* **Note 12**)

3.6 Quantification of Cell Death Using Image J

1. Open the image files obtained in the microscope using the Fiji software (Image J distribution).
2. Install the cell death quantification macro (*see* **Note 13**).
3. Select process image for cell death macro and follow the instructions for quantification.
4. Plot the percentage of stained leaf as a function of time (Fig. 1).

3.7 Electrolyte Leakage Assay

1. Pressure infiltrate the seventh and eighth leaf of an Arabidopsis plant with avirulent bacteria. Four plants per genotype are required for the experiment.
2. After infiltration, gently dry the excess of liquid on the surface of the leaf.
3. Collect the leaves by cutting through the petiole with the aid of small scissors.
4. Place the infiltrated leaves on top of a flat surface and punch out discs (one disc per leaf) using a cork-borer (size 4, diameter = 7.5 mm) (*see* **Note 14**).
5. Immediately after punching out leaf discs, place two leaf discs from a single plant into one well of a 12-well plate containing 2 mL Milli Q sterilized water.

6. Use as many 12-well plates as required depending on the number of genotypes included in the experiment.
7. Cover the plate with the lid and place it on a tilt shaker at 90 rpm for 1 h (*see* **Note 15**).
8. In the meantime, perform a one-point calibration of the LAQUAtwin EC-11 Conductivity meter (HORIBA Advanced Techno Co., Ltd) using the conductivity standard solution to 1.41 mS/cm.
9. Replace the 2 mL water from the wells with new 2 mL Milli Q sterilized water. Once the water is replaced, a time series of measurements of water conductivity start (*see* **Note 16**).
10. Record water conductivity by pipetting 100 μL of water per well into the conductivity meter. Ions released from dying cells during the course of HR correlate with the conductivity of the solution. The unit used to measure conductivity is microSiemens per centimeter (μS/cm) where cm denotes the distance between the two electrodes sensors of the conductivity meter.
11. Return the water from the device to the well in order to maintain the same volume of water in the wells throughout the experiment (*see* **Note 17**).
12. Record conductivity at each time point. Meanwhile leave the 12-well plate rotating on the tilt shaker.

3.8 Data Representation and Statistical Analysis

1. Plot conductivity in μS/cm as a function of time (Fig. 2).
2. For statistical analysis, compare the conductivity (in μS/cm) of two genotypes at a given time point by a two tailed Student's t-test. For comparison of more than one genotype, use a one-way analysis of variance (ANOVA).

4 Notes

1. While NASC distributes seeds to Europe, the Biological Resource Center (ABRC) based at Ohio State University (USA) delivers seeds to North and South America. Laboratories located in other parts of the world may order stocks from either of both stock centers. Arabidopsis Col-0 accessions carry the resistance (R) genes *RPM1* and *RPS2,* which encode for the NLRs RPM1 and RPS2, respectively. In contrast, *rpm1–3* and *rps2* mutants are not equipped with functional RPM1 and RPS2, respectively [12, 14].
2. *Pto* DC3000 (*avrRpm1*) and *Pto* DC3000 (*avrRpt2*) avirulent strains overexpress the effector molecules avrRpm1 and avrRpt2, respectively. Plant NLRs RPM1 and RPS2 recognize

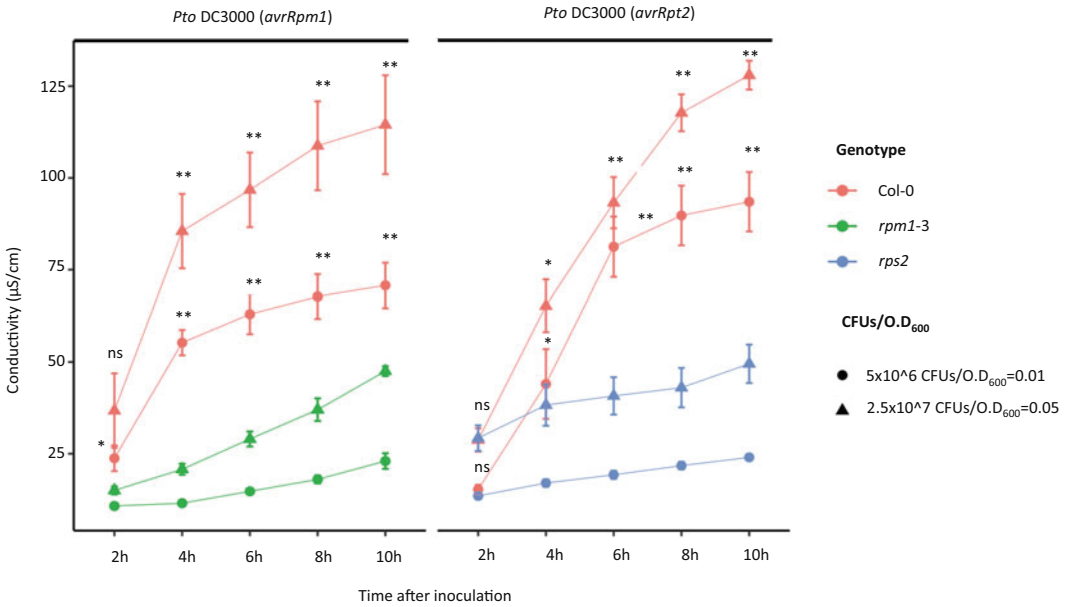

Fig. 2 Electrolyte leakage from Col-0, *rpm1–3* and *rps2* leaf discs after bacterial inoculation. Four- to five-week-old Arabidopsis leaves were syringe-infiltrated with either *Pto* DC3000 (*avrRpm1*) or *Pto* DC3000 (*avrRpt2*) with two independent bacterial titers: 2.5×10^7 CFUs/O.D_{600} = 0.05 (triangles) or 5×10^6/O.D_{600} = 0.01 (circles). Conductivity measurements of electrolyte leakage from dying cells were recorded from 2 to 10 h after inoculation. Standard error bars represent four biological replicates. Asterisks denote significant differences (**, *P* value <0.01 or *, *P* value<0.05, NS, *P* value >0.05) from independent Student's t-tests for comparisons between two genotypes at each time point and O.D_{600}. *NS* non-significant

perturbations in the host cell caused by the aforementioned effectors eliciting an ETI response that is accompanied by HR.

3. For selection of *Pto* DC3000 (*avrRpm1*) and *Pto* DC3000 (*avrRpt2*) in KB media. Kanamycin is added for selection of the construct that carries the *avrRpm1* and *avrRpt2*, whereas resistance to rifampicin comes inherently in *Pto* DC3000. Working concentrations for kanamycin and rifampicin are 50 µg/mL.
4. We recommend including at least eight pots per time point and genotype in the trypan blue experiment to have robust and consistent results when comparing genotypes that show mild differences.
5. We recommend avoiding walk-in chambers for pathogenesis-related experiments in order to avoid stresses from other pathogens (i.e., insect infestations) that can be present in a chamber where other plants are growing or where users come in and out on a regular basis. We suggest a photoperiod of 9 h light/15 h dark that resembles short-day conditions (8 h light/16 h dark) but adds an extra hour of light, allowing plants to be at their optimal stage for infiltration earlier than the classical short-day

photoperiod (in between the 4th and 5th week of growth). This extended short-day cycle is used by many laboratories working on molecular plant pathology.

6. In order to have comparable results between different plants, we always infiltrate the seventh and eighth leaf of the plant [15]. In this way leaves of comparable developmental stages that may respond similarly to the pathogen are chosen for infiltration.
7. The CFUs/O.D.$_{600}$ (OD_{600} = 1.0 correlate to $3.55*10^8$ CFU mL^{-1} determined by serial dilutions and plating) of the bacterial inoculum may be adapted depending on the genotype being infected [16], bacterial strain used in the experiment, or time points at which samples are collected after infection.
8. Gently exert pressure on the abaxial side of the leaf with a needleless syringe and infiltrate the leaf thoroughly. If users are not experienced, we recommend practicing beforehand with water on plants that will not be used in the experiment. Besides including mutants impaired in pathogen effector recognition as negative controls (i.e., *rpm1–3* and *rps2*) when available, we encourage users to include leaves infiltrated with 10 mM $MgCl_2$ as an additional negative control.
9. Pouring trypan blue working solution along with the already stained leaves onto a sieve will allow you to grab the leaves from the petiole and transfer them easily to a new 50 mL tube containing destaining solution.
10. Once leaves are incubated in destaining solution, they need to be handled very carefully to avoid damage. Furthermore, since leaves will lose the green color due to the loss of chlorophyll, it will become harder to identify where the petiole is. As a result, we recommend working always in the same tube, once the destaining solution has been added to the leaves.
11. The abaxial side of the leaf faces the coverslip. Use Optivisor lenses in order to aid vision when handling the leaves.
12. Gently drop the coverslip on top of the leaf very slowly from top to bottom of the leaf by sliding a 1000 μL pipette tip below the coverslip really slowly. Avoiding as many bubbles as possible at this step is critical so that they do not appear in the images and do not affect quantification.
13. Follow the instruction guide for running the cell death processing macro located in the GitHub platform: https://github.com/Celldeathquantification/Cell-death-quantification.
14. When punching out leaf discs, we recommend users to excise the leaf disc from the center part of the leaf. Exerting strong pressure toward a flat surface covered with a fine layer of tissue paper allows neat excision of discs.

15. The first hour of incubation of leaf discs under constant rotation is intended to remove electrolytes leaked from damaged cells on the edges of the leaf discs as a consequence of the excision caused by the cork-borer.
16. Time points selected for conductivity measurements can vary depending on the bacterial inoculum used. We recommend a time series of measurements from 0 h to 10 h once the water from **step 9** has been replaced, with measurements being taken every 2 h.
17. Always clean the sensor of the conductivity meter with Milli Q sterilized water in between samples.

Acknowledgments

Research at CRAG was funded with grants PID2019-108595RB-I00 funded by MCIN/AEI/ 10.13039/501100011033 and AGL2016-78002-R funded by MCIN/AEI/10.13039/501100011033 and by "ERDF A way of making Europe" (NSC), fellowship PID2019-108595RB-I00 funded by Spanish MCIN/AEI/ 10.13039/501100011033 (NSC) and fellowships BES-2017-080210 funded by MCIN/AEI/ 10.13039/501100011033 and by "ESF Investing in your future" (JS-L); and through the "Severo Ochoa Programme for Centres of Excellence in R&D" (SEV-2015-0533 and CEX2019-000902-S funded by MCIN/AEI/ 10.13039/501100011033) and by the CERCA Programme /Generalitat de Catalunya.

References

1. Balint-Kurti P (2019) The plant hypersensitive response: concepts, control and consequences. Mol Plant Pathol 20(8):1163–1178. https://doi.org/10.1111/mpp.12821
2. Pitsili E, Phukan UJ, Coll NS (2020) Cell death in plant immunity. Cold Spring Harb Perspect Biol 12(6). https://doi.org/10.1101/cshperspect.a036483
3. Jones JDG, Dangl JL (2006) The plant immune system. Nature 444(7117):323–329. https://doi.org/10.1038/nature05286
4. Salguero-Linares J, Coll NS (2019) Plant proteases in the control of the hypersensitive response. J Exp Bot 70(7):2087–2095. https://doi.org/10.1093/jxb/erz030
5. Mur LA, Kenton P, Lloyd AJ, Ougham H, Prats E (2008) The hypersensitive response; the centenary is upon us but how much do we know? J Exp Bot 59(3):501–520. https://doi.org/10.1093/jxb/erm239
6. Coll NS, Epple P, Dangl JL (2011) Programmed cell death in the plant immune system. Cell Death Differ 18(8):1247–1256. https://doi.org/10.1038/cdd.2011.37
7. Imanifard Z, Vandelle E, Bellin D (2018) Measurement of hypersensitive cell death triggered by avirulent bacterial pathogens in Arabidopsis. Methods Mol Biol 1743:39–50. https://doi.org/10.1007/978-1-4939-7668-3_4
8. Lema Asqui S, Vercammen D, Serrano I, Valls M, Rivas S, Van Breusegem F, Conlon FL, Dangl JL, Coll NS (2018) AtSERPIN1 is an inhibitor of the metacaspase AtMC1-mediated cell death and autocatalytic processing in planta. New Phytol 218(3):1156–1166. https://doi.org/10.1111/nph.14446
9. Coll NS, Vercammen D, Smidler A, Clover C, Van Breusegem F, Dangl JL, Epple P (2010) Arabidopsis type I metacaspases control cell

death. Science 330(6009):1393–1397. https://doi.org/10.1126/science.1194980

10. Chan LL-Y, Rice WL, Qiu J (2020) Observation and quantification of the morphological effect of trypan blue rupturing dead or dying cells. PLoS One 15(1). https://doi.org/10.1371/journal.pone.0227950
11. Hatsugai N, Katagiri F (2018) Quantification of plant cell death by electrolyte leakage assay. Bio-Protocol 8(5). https://doi.org/10.21769/BioProtoc.2758
12. Bisgrove SR, Simonich MT, Smith NM, Sattler A, Innes RW (1994) A disease resistance gene in Arabidopsis with specificity for two different pathogen avirulence genes. Plant Cell 6(7):927–933. https://doi.org/10.1105/tpc.6.7.927
13. Schindelin J, Arganda-Carreras I, Frise E, Kaynig V, Longair M, Pietzsch T, Preibisch S, Rueden C, Saalfeld S, Schmid B, Tinevez JY, White DJ, Hartenstein V, Eliceiri K, Tomancak P, Cardona A (2012) Fiji: an open-source platform for biological-image analysis. Nat Methods 9(7):676–682. https://doi.org/10.1038/Nmeth.2019
14. Kunkel BN, Bent AF, Dahlbeck D, Innes RW, Staskawicz BJ (1993) RPS2, an Arabidopsis disease resistance locus specifying recognition of Pseudomonas syringae strains expressing the avirulence gene avrRpt2. Plant Cell 5(8): 865–875. https://doi.org/10.1105/tpc.5.8.865
15. Farmer E, Farmer E, Mousavi S, Lenglet A (2013) Leaf numbering for experiments on long distance signalling in Arabidopsis. Protocol Exchange. https://doi.org/10.1038/protex.2013.071
16. Johansson ON, Nilsson AK, Gustavsson MB, Backhaus T, Andersson MX, Ellerstrom M (2015) A quick and robust method for quantification of the hypersensitive response in plants. PeerJ 3:e1469. https://doi.org/10.7717/peerj.1469

CRAG
CENTRE FOR RESEARCH
IN AGRICULTURAL GENOMICS

UAB
Universitat Autònoma
de Barcelona

GOBIERNO
DE ESPAÑA

MINISTERIO
DE CIENCIA
E INNOVACIÓN